DISSERTATION
submitted to the
Combined Faculties for the Natural Sciences and for Mathematics
of the Ruperto-Carola University of Heidelberg, Germany
for the degree of
Doctor of Natural Sciences

Put forward by
Dipl. Phys. Tillmann Kaudse
born in Titisee-Neustadt

Oral examination: 22.01.2014

Noble gases in groundwater of the Azraq Oasis, Jordan, and along the central Dead Sea Transform

Two case studies

Abstract

For the first time, noble gases dissolved in groundwater were applied in Jordan on a larger scale. Two studies are presented where noble gases, especially the ^{3}He/^{4}He ratio, are used in very different contexts. The first project sheds light on the complex groundwater mixing in the Azraq Oasis, where groundwater reserves are heavily exploited and where the creeping salinization of some wells is explained. It is found that the mentioned wells also contain a considerable amount of mantle derived helium, which is interpreted as an upward leakage of deep groundwater into the shallow aquifer. The observed drawdown in the area lead to enhanced abstraction of water from deeper parts of the this aquifer, which is both saline and contains mantle gases according to the presented mixing scheme.

The second study examines the mantle helium component in thermal springs and wells along both the Jordan and the Israeli part of the central Dead Sea Transform, which constitutes the tectonic boundary between the African and the Arabian plates. The collected samples range from almost crustal to clear mantle signature with ^{3}He/^{4}He ratios up to $5\,R_A$. The presented data set contradicts the model published by Torfstein *et al.* [2013], who interpreted their observed increase of mantle influence in Israeli thermal localities to be caused by a progressive decrease of crust thickness. Covering also Jordanian sites, the new data suggest a much more local control by single conductive fractures permitting an ascent of mantle volatiles into shallow groundwaters.

Kurzfassung

Zum ersten Mal wurden in Jordanien gelöste Edelgase umfassend zur Grundwasseruntersuchung eingesetzt. Es werden zwei Studien vorgestellt, in denen Edelgase, insbesondere das ^{3}He/^{4}He-Verhältnis, in völlig verschiedenen Zusammenhängen verwendet werden. Das erste Teilprojekt beleuchtet die komplexen Grundwassermischungvorgänge in der Azraq Oase, einem Gebiet starker Grundwassernutzung und wo einige Brunnen einen seit Jahren steigenden Salzgehalt zeigen. Es wird aufgezeigt, dass genau diese Brunnen einen deutlichen Heliumanteil aufweisen, welcher dem Erdmantel zuzuordnen ist und durch aufströmendes Grundwasser aus großen Tiefen in den flachen Grundwasserleiter gekommen sein muss. Durch die Absenkung des Grundwasserspiegels in der Region entnehmen die genannten Brunnen vermehrt Wasser aus tieferen Zonen des Aquifers, in denen das Wasser nach dem präsentierten Mischmodell sowohl salzhaltig ist als auch Mantelhelium beinhaltet.

In der zweiten Studie werden Thermalquellen und -brunnen sowohl auf der jordanischen als auch auf der israelischen Seite der zentralen Transformstörung, welche die tektonische Plattengrenze zwischen der afrikanischen und der arabischen Platte darstellt, untersucht. Dabei zeigen einige Proben eine krustale, andere eine deutliche Mantelsignatur mit ^{3}He/^{4}He-Verhältnissen von bis zu $5\,R_A$. Es zeigt sich, dass das nur auf Daten von israelischen Thermalwässern beruhende Modell von Torfstein *et al.* [2013] nicht haltbar ist. Bei diesem wird die Zunahme des Manteleinflusses von Süd nach Nord mit einer zunehmend dünner werdenden Erdkruste erklärt. Die präsentierten Daten hingegen legen nahe, dass vielmehr jedes Thermalwasser gesondert zu betrachten ist, wobei einzelne lokale, leitfähige Verwerfungen, welche einen Aufstrom tiefen, heißen Grundwassers ermöglichen, berücksichtigt werden müssen.

Contents

1 Introduction

In terms of water scarcity Jordan ranks, according to the Worldbank [2013], as the fourth poorest country in the world. Wide parts are classified as semi-arid to arid, and considerable rain falls only in a rather small area in the highlands. Due to its geographic position in the Middle East and its political stability, Jordan has been a major target for refugees from Palestine in the 1960s and 70s, from Iraq in the last decade and today for people fleeing the civil war in Syria. The development of new, sustainable water resources, however, lags behind the massive population growth. In consequence, the groundwater reserves are being exploited far beyond the sustainable yield, and a drawdown of the groundwater table is observed in most parts of the country.

Beside the depletion of groundwater reserves, the deterioration of water quality is a major issue [Salameh, 2008]. Pollution by the residents, often in form of sewerage leakage, spoils local groundwater reservoirs, but also natural contamination is possible like the intrusion of saltwater into a high quality groundwater body in consequence of extensive abstraction rates. The latter occurs, for example, in the area around the Azraq Oasis, situated in the desert about 100 km east of the Jordanian capital Amman. Since the 1980s the area is heavily pumped for municipal and agricultural purposes, and the groundwater table fell several tens of meters since then. As a consequence, some wells of the AWSA well field showed a rising salt content over the years. A large-scale survey in 2002 tried to figure out the reason behind the creeping water quality degradation [Al-Momani *et al.*, 2006], but they could not work out a satisfying answer.

The first part of this thesis addresses this salinization phenomenon in the Azraq Oasis by the application of dissolved noble gases to wells of the AWSA well field and the surroundings, which has never been done before in this area. The new data set suggests an upward leakage from deeper layers into the shallow aquifer in combination with an altered abstraction pattern as a consequence of the drawdown.

The second part of the thesis approaches the tectonic setting of the Jordan Valley, which is the central section of the Dead Sea Transform (DST) and constitutes the continental break-up zone of the African and the Arabian plates. Thermal springs and wells on the Jordanian part of the rift valley were sampled by myself, and in the course of the master's thesis of Neta Tsur [2013] also the Israeli side is covered. The samples were analyzed for their noble gas content, especially for their ^{3}He/^{4}He ratio, which is a well established marker for mantle gases from the Earth's interior. The presence of an elevated helium isotope ratio in tectonically active zones is associated with magmatic occurrences or deep, conductive faults facilitating the upstream of mantle fluids. The presented helium isotope data set is the most complete ever reported for this area. It partly contradicts the explanation of mantle helium distribution along the transform given by Torfstein *et al.* [2013], who just recently published ^{3}He/^{4}He

data for thermal waters on the Israeli part of the Jordan Valley. Instead of a clear north–south trend found by these authors, which was interpreted to be the consequence of gradual thinning of the Earth's crust towards the north, the new data proposes a much more local view of each geothermal manifestation including the consideration of single fractures and nearby recent volcanic activity.

This thesis is structured as follows: The basic knowledge about noble gases and other applied groundwater tracers are elucidated in chapter 2, whereas the analytical aspects are treated in chapter 3. Chapter 4 gives an introduction to the geological and hydrogeological background needed for the data interpretation of both studies. Sampling campaigns and procedures are shortly reviewed in chapter 5. Chapter 6 examines the salinization in Azraq, whereas the tectonics of the Dead Sea Transform are dealt with in chapter 7. Chapter 8 briefly summarizes the results of this thesis.

A short note should be made about the transcription of Arabic and Hebrew names of localities into Latin script. As both languages largely omit vowels and some consonants cannot be translated into Latin letters, the writing of names is often ambiguous. For example the Jordanian city Zarqa is also found to be written as Zerqa or Zarka. Therefore, the same locality might be spelled differently in other publications, but voicing the name often helps to find accordances. In Israel and Jordan, there are also different coordinate systems in use. Beside the global WGS84, the Palestine Belt and Palestine Grid systems are commonly used in Jordan. Although the positions of sampling points in this thesis are given in WGS84 coordinates, maps taken from other publications often use local reference systems.

2 Fundamentals

All background information necessary to understand the topics treated in this thesis is compiled in this chapter. First, the basics of hydrology are introduced, followed by a description of the applied physical parameters. The introduction to all environmental tracers applied within the scope of this thesis occupies the majority of this chapter. For a deeper insight, one may consult the literature cited within each section and adequate textbooks.

2.1 The basics of hydrogeology

With respect to groundwater, the subsurface can be divided into an upper zone of aeration and a lower zone of saturation. In the first one, also called *vadose zone*, the soil pores contain mainly soil air and only some water. This zone's thickness can be close to zero or up to several hundred meters in arid regions. Groundwater resides in the zone of saturation, also called *phreatic zone*. Almost no air is found there, the pores are saturated with water. The top of the saturated zone is defined as the groundwater table, which is the water level that establishes in an open borehole. There, the water pressure equals atmospheric pressure. The transition between vadose and phreatic zone is called *capillary fringe*. Its thickness varies from almost zero to up to more than one meter, depending on the pore and grain size of the surrounding rock matrix. As the phreatic zone it is saturated, but by capillary force water is held against gravitational force above the groundwater table. This situation is depicted in figure 2.1. Under natural conditions the groundwater table usually fluctuates due to a temporal variation of recharge events, i. e. one often observes an annual oscillation of the upper boundary of the saturated zone. Due to these fluctuations the uppermost layer contains tiny air bubbles in dead end pores. Hydrologists often name this boundary layer between the saturated and the unsaturated zone the *quasi-saturated zone*.

A permeable layer of water bearing rock or unconsolidated material like gravel or sand is called an *aquifer*. Using a well it is possible to extract groundwater from an aquifer. In contrast, *aquicludes* are rock strata with a very low permeability. Pores are usually filled with water, but no considerable water flow happens. Typically clay and silt strata are non-permeable. *Aquitards* are layers where water flow is possible but low compared to an aquifer.

Aquifers are subdivided into confined and unconfined ones (see figure 2.2). In *unconfined* aquifers the water table equals the hydraulic head or potentiometric surface, which is essentially the water level in an open borehole driven by the hydraulic pressure in the aquifer. Spring discharge occurs at places where the water table of an unconfined aquifer is equal or higher than the land surface. *Confined* aquifer, by contrast, are overlain by an impermeable, i. e. confining, layer. Under confined conditions the water level in an open borehole exceeds
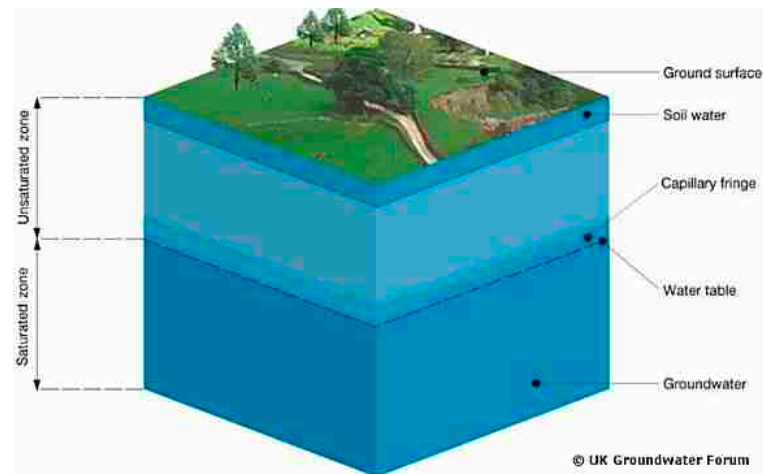
Figure 2.1: Structure of the subsurface related to groundwater. Modified from UK Groundwater Forum [2013].

the upper boundary of the aquifer rock material itself due to its high hydrostatic pressure. In cases where the hydraulic head lies above the land surface, water flows out a borehole without a pump. Such a well is called an *artesian well*.

In many cases there are several permeable and non-permeable layers above each other, hydrologists speak of an aquifer system. Especially in areas of high tectonic activity, however, water exchange between aquifers which are separated from each other by an aquiclude often occurs through fractures and faults.

The natural hydraulic conditions of an aquifer system can severely be changed by man-made pumping. Many regions around the world suffer from a decline of the water table. Such over-exploitation eventually leads to an increase of the water production costs and depletes the groundwater reservoir. Especially in coastal areas a lowering of the groundwater table below the sea surface reverses the natural flow direction of groundwater into the sea. An inflow of saline sea water into the aquifer deteriorates the groundwater quality and is a major threat to the supply with good quality water. But also in inland areas over-pumping can induce a salinization of production wells. The case study in the Azraq Oasis dealt with in the scope of this thesis is an example.

2.2 Physical parameters of groundwater

This chapter gives a short overview of the physical properties as they were recorded in the field as well as implications for the interpretation of these parameters.

Temperature

Groundwater temperature varies with depth in the Earth's crust. In most regions of the world a geothermal gradient of about 30 K/km is present. Groundwater at the bottom of
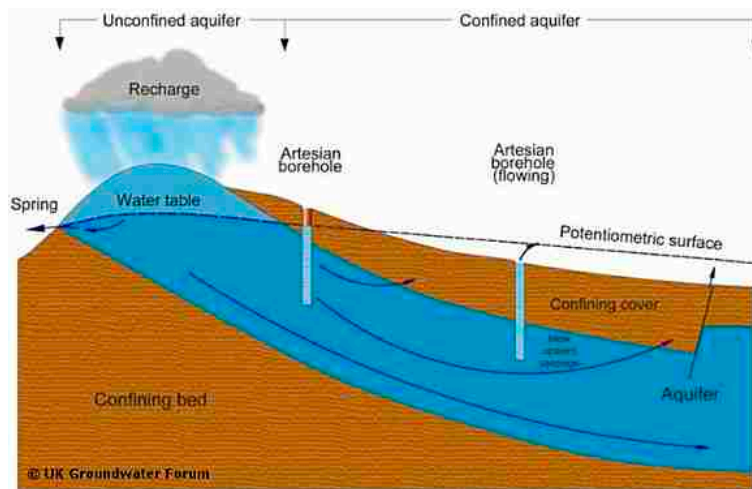
Figure 2.2: Illustration of a simple aquifer with its potentiometric surface. Modified from UK Groundwater Forum [2013].

a 1 km deep borehole, for example, is therefore expected to have a temperature of about 40 °C, given a mean annual air temperature of 10 °C. In regions of geothermal surface activity, however, this gradient can be much higher. In Jordan, geothermal anomalies occur predominantly east of the Dead Sea and in the lower Yarmouk Valley (compare chapter 4.2).

Electric conductivity (E. C.)

Electric conductivity is a measure for the total dissolved solids, i. e. the salinity, of water. These solids are present in ionic form and thus conduct an electric current. As groundwater usually infiltrates with only a few solids dissolved, almost the whole mineralization comes from the interaction of the water with the surrounding rock material. The dissolution of the minerals is, in general, a function of temperature and especially the pH value [Merkel and Planer-Friedrich, 2005]. Major re-precipitation of dissolved minerals can take place only when the conditions change significantly, and therefore it can usually be assumed that the salinity increases monotonic with groundwater residence time.

pH

The pH value is a measure for the acidic or alkaline character of an aqueous solution and expresses the hydrogen ion activity. Pure water has a neutral pH of 7. Water in contact with the soil atmosphere dissolves CO_2 and forms carbonic acid (H_2CO_3), therefore infiltrating groundwater is slightly acidic [Appelo and Postma, 2005]. Dissolution of minerals, especially bicarbonate, increases the pH value. In case of alkali basalt forming the aquifer matrix, the pH of the groundwater is higher as well, because the chemical weathering of the basalt consumes a lot of H^+ ions. This means, that the pH is the governing factor of groundwater–rock interaction, but in turn depends on dissolved solids (and gases, too).

Dissolved oxygen (DO)

Atmospheric oxygen dissolves in water as it precipitates. It is then consumed by biogenic processes in the soil. High oxygen content in groundwater is therefore an indicator of young and shallow, unconfined water. Older groundwater, however, is mostly depleted in oxygen. In some cases the pumping of a well can cause aeration which artificially raises the level of O_2.

2.3 Environmental Tracers

Environmental tracers are properties of a medium or compounds dissolved in it, which allow to "trace" a specific information in the environment. In hydrological systems, chemical substances like dissolved ions or physical properties as isotope ratios or temperature are examples for tracers. They can be of natural or of anthropogenic origin.

Tracers used in this work are the so called stable isotopes deuterium (^{2}H), oxygen-18 (^{18}O), and carbon-13 (^{13}C), the radioactive tritium (^{3}H) and radiocarbon (^{14}C), major dissolved ions, as well as the noble gases helium, neon, argon, krypton, xenon, and radon.

2.3.1 Tritium

The heavy, radioactive isotope of hydrogen, ^{3}H, is called tritium and often denoted with T. It is naturally produced in the upper atmosphere by cosmic radiation [Libby, 1946],

$$^{14}N + n \longrightarrow T + {}^{12}C, \tag{2.1}$$

as well as in the lithosphere, i. e. the rock matrix, where neutron capture of lithium is by far the most prominent production:

$$^6Li + n \longrightarrow T + \alpha. \tag{2.2}$$

The geogenic tritium production is very low compared to cosmogenic production and leads to a tritium content share of about 0.1 TU in groundwater [Clark and Fritz, 1997]. Tritium decays by a β^- process into ^{3}He: $T \longrightarrow {}^3He + e^- + \bar{\nu}_e$, with a half-life $t_{1/2}$ of 12.32 years [Lucas and Unterweger, 2000]. Tritium concentrations are usually reported in tritium units (TU), defined by the relative abundance of tritium:

$$1\,\text{TU} = \frac{\left[^3H\right]}{\left[^1H\right]} \cdot 10^{18}. \tag{2.3}$$

Mainly in the 1960s, thermonuclear bomb tests introduced high amounts of anthropogenic tritium ("bomb tritium") into the atmosphere [Weiss *et al.*, 1979], which was gradually washed out, so that precipitation reached the natural tritium background of 5 to 10 TU today.

The distribution of tritium from bomb tests in precipitation is highly dependent on latitude [Rozanski *et al.*, 1991], the northern hemisphere was much more affected than the southern
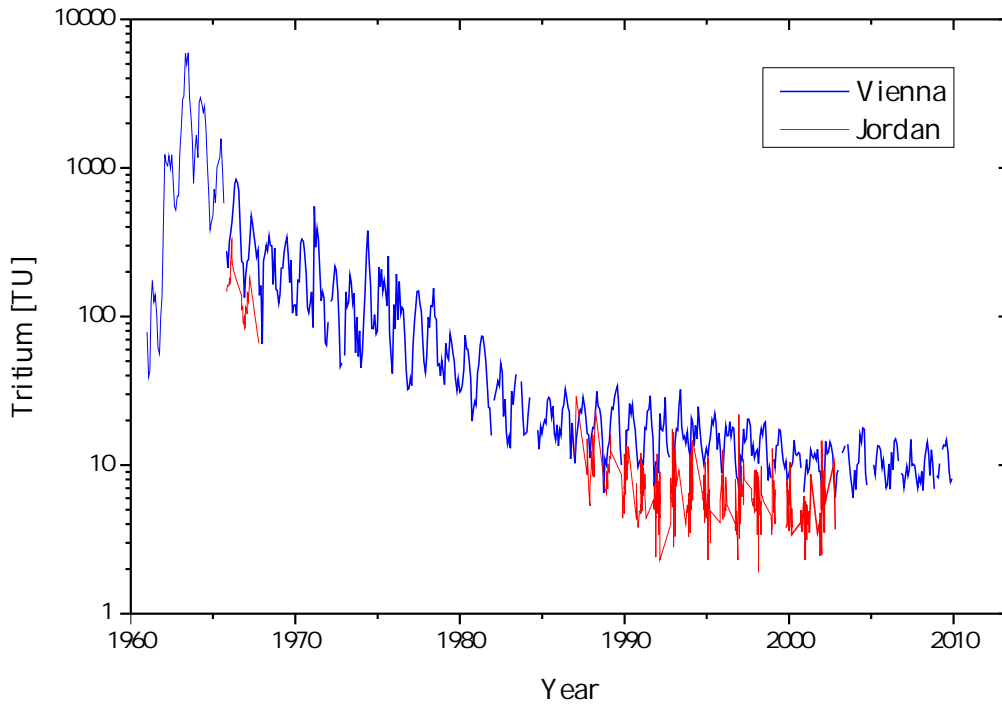
Figure 2.3: Tritium content in precipitation in Vienna (blue) and in Jordan (red). The bomb peak in the 1960 is clearly visible with up to 6000 TU in Vienna. The data from Jordan is compiled from all collection stations in Jordan. No data is available in the 1970s and the first half of the 1980s. Tritium content in Jordan is generally lower than in Vienna. All data from IAEA/WMO [2006].

one. Figure 2.3 shows the tritium content in precipitation in Vienna and in Jordan. Although the available data from Jordan is sparse, the behavior at both locations is similar, but in Jordan the tritium concentration is generally lower than in Vienna at higher latitudes.

Tritium can be employed to date young groundwater up to an age of about 50 years. However, due to the highly seasonally variable input curve and low present day tritium concentrations, the ages derived from tritium data are often ambiguous. The determination of tritiogenic ^{3}He, the daughter nucleus of tritium, helps considerably to enhance the dating potential of tritium, because the sum of tritium and ^{3}He is conserved over time [Schlosser *et al.*, 1988]. T–^{3}He ages, τ, are calculated by

$$\tau = \frac{t_{1/2}}{\ln 2} \cdot \ln \left(1 + \frac{[^3\text{He}]}{[^3\text{H}]} \right), \qquad (2.4)$$

with the concentrations of ^{3}He and tritium in the bracket given in the same unit. The ^{3}He amount, given in ccSTP/g, is converted into TU by the following relation (for pure water):

$$1 \, \text{TU} = 2.488 \times 10^{-15} \, \text{ccSTP/g}. \qquad (2.5)$$

Because ^{3}He gets lost to the atmosphere as long as the water is in contact with the soil air, the T-^{3}He age reflects the duration the water parcel is closed off from the atmosphere – in

contrast to tritium-only ages, which express the time span between precipitation and sampling. The travel time in the vadose zone of infiltrating water can be up to several tens of years [Solomon *et al.*, 1995; Geyh, 2000; Schwientek *et al.*, 2009], depending on the thickness of the unsaturated zone, the soil and rock permeability and the precipitation amount.

When mostly old groundwater is examined – as it is done in this work – tritium often acts as a marker of admixed young groundwater.

2.3.2 Isotope fractionation

The use of isotopic tracers relies on the fact that several mechanisms alter the isotopic composition in a medium. Among these mechanisms are chemical reactions and phase changes (e.g. evaporation). The fundamental principle behind this so-called isotope fractionation is that usually the heavier isotope is less likely to participate in a chemical reaction, rather stays in the more dense phase during a phase change compared to its lighter version, or moves slower in diffusive processes. The explanation of these phenomena comprise two points: First, heavy isotopes move slower than their lighter versions. This causes a slower diffusion velocity as well as a lower chemical reactiveness, because the collision frequency as the primary condition for chemical reactions is reduced. Second, heavier molecules generally have higher intra-molecular binding energies. Thus, $^1H_2^{18}O$ has a lower vapor pressure than $^1H_2^{16}O$, for example, and $Ca^{12}CO_3$ dissolves faster in an acidic environment than $Ca^{13}CO_3$ does. Particularly in an isotope equilibrium between two chemical compounds, the heavy isotope is, in general, enriched in the aggregate with the largest density. As the difference of binding energies of different isotopic compounds becomes smaller at higher temperatures, also the resulting isotope effects diminish.

Fractionating processes can occur at equilibrium (*equilibrium fractionation*) or at transient conditions (*kinetic fractionation*). While the first takes place at conditions which facilitate the establishment of an equilibrium, kinetic fractionation results from irreversible processes like evaporation of water with instantaneous removal of the vapor. Natural processes, however, are a mixture of equilibrium and kinetic fractionation; evaporation is neither a one-way process, because for sure there is also condensation of vapor taking place, nor is it an equilibrium process as there is a net evaporation.

Isotope abundances are described by the *isotope abundance ratio R*, compare Mook [2000]:

$$R = \frac{\text{abundance of rare isotope}}{\text{abundance of abundant isotope}}. \tag{2.6}$$

The isotopic composition in a chemical equilibrium ($A \longleftrightarrow B$) or of a chemical or physical reaction ($A \longrightarrow B$) is described by the *isotope fractionation factor* $\alpha = R_B/R_A$. Because the isotopic variation is generally very small and $\alpha \approx 1$, the use of the *fractionation* ε is more convenient:

$$\varepsilon = \alpha - 1. \tag{2.7}$$

$\varepsilon > 0$ describes an enrichment, $\varepsilon < 0$ a depletion of the rare isotope in B with respect to A and is usually reported in units of per mille.
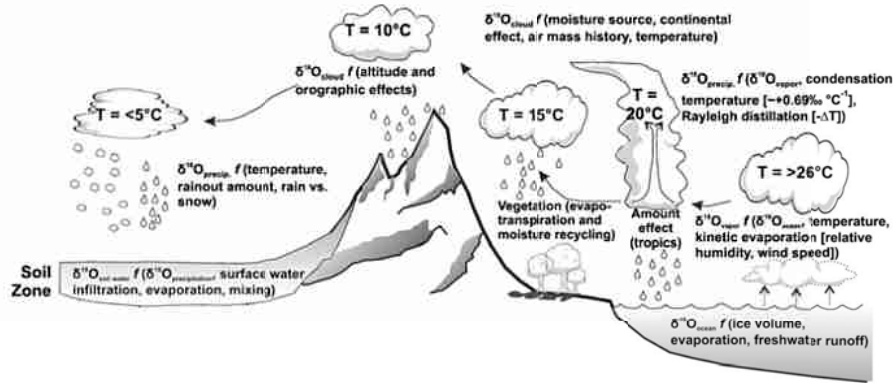
Figure 2.4: Evaporation and vapor formation over the oceans and landmass. In each reservoir the δ^{18}O affecting factors are displayed (f symbolizes that δ^{18}O is a function of the mentioned factors). Adapted from [Lachniet, 2009].

For the purpose of international comparison, isotope abundances are usually indicated as deviations of the sample isotope ratio compared to a reference standard. This is expressed in the delta notation:

$$\delta_{sample/std} = \frac{R_{sample}}{R_{std}} - 1. \tag{2.8}$$

For oxygen-18 this means:

$$\delta^{18}O = \frac{(^{18}O/^{16}O)_{sample}}{(^{18}O/^{16}O)_{std}} - 1. \tag{2.9}$$

δ-values of deuterium and carbon-13 are defined respectively. Like the fractionation ε, δ values are reported in per mille.

In this work the Vienna Standard Mean Ocean Water (VSMOW) is used as the reference standard for δ^2H and δ^{18}O, and Vienna Pee Dee Belimnite (VPDB) for δ^{13}C. The absolute ^{2}H/^{1}H ratio of VSMOW is reported to be $(155.75 \pm 0.08) \times 10^{-6}$ [de Wit *et al.*, 1980], ^{18}O/^{16}O $= (2005.2 \pm 0.45) \times 10^{-6}$ [Baertschi, 1976] and ^{13}C/^{12}C in VPDB equals 0.0112372 [Craig, 1957].

2.3.3 Stable isotopes of water (^{2}H and ^{18}O)

In the hydrologic cycle, water molecules experience several fractionation steps as they evaporate and then condens in clouds. Most evaporation occurs over the oceans, especially in the tropics and subtropics where solar radiation is highest [Peixóto and Oort, 1983]. Due to their vast size, evaporation hardly changes the isotopic composition of the oceans (although there have been changes on geologic timescales, see Wadleigh and Veizer [1992]). Figure 2.4 gives an overview of evaporation and condensation processes over the oceans and continents as well as their influence on δ^{18}O.

In the process of evaporation, equilibrium as well as kinetic fractionation contribute. In a very thin layer above the water surface 100 % humidity prevails and fractionation at equilibrium conditions takes place. As the atmosphere usually has a lower humidity, a net transport of vapor from the water body through a transition zone into the atmosphere takes place. Thus, the different diffusivities of $^1\text{H}_2^{16}\text{O}$, $^1\text{H}^2\text{H}^{16}\text{O}$ and $^1\text{H}_2^{18}\text{O}$ cause kinetic fractionation in a second step. The degree of kinetic fractionation can be estimated from the water surface vapor [Gonfiantini, 1986]. Due to the different fractionation processes, water molecules containing the heavy isotopes of hydrogen and oxygen are stronger enriched in the liquid phase and the influence of kinetic fractionation leads to an excess of deuterium (so called deuterium excess *d*) during evaporation, calculated by

$$d = \delta^2\text{H} - 8 \cdot \delta^{18}\text{O}. \tag{2.10}$$

Condensation is considered to occur at equilibrium conditions because the formation of droplets in clouds takes place only at 100 % humidity. Hence, the deuterium excess is not affected by this process.

The isotopic analysis of stable isotopes in rainfall from all over the world results in the Global Meteoric Water Line (GMWL, see figure 2.5), first empirically delineated by Craig [1961], and later stated more precisely by Rozanski *et al.* [1993], using the data of the Global Network of Isotopes in Precipitation (GNIP) database [IAEA/WMO, 2006]:

$$\delta^2\text{H} = 8.17 \cdot \delta^{18}\text{O} + 10.35\,\text{‰ VSMOW} \tag{2.11}$$

This equation holds for an average world-wide humidity of 85 %. 10.35 ‰ is the average deuterium excess. Local Meteoric Water Lines (LMWL) can differ quite strongly from the GMWL in slope and deuterium excess. The reasons are different origins of the vapor mass, secondary evaporation during rainfall and the seasonality of precipitation.

In the Middle East often the Eastern Mediterranean Water Line (EMWL) [Gat and Carmi, 1970] is applied:

$$\delta^2\text{H} = 8 \cdot \delta^{18}\text{O} + 22\,\text{‰ VSMOW}. \tag{2.12}$$

It is the most common MWL in Israel. The high deuterium excess in precipitation in this region is attributed to the favored storm path coming from the Baltics [Gat, 1987]. At continental conditions, humidity is lower than over the oceans and the effect of kinetic fractionation is enhanced (see references above).

Bajjali [2012] presents a water line derived from Jordanian rainfall only with a significantly smaller slope, the Jordanian Meteoric Water Line (JMWL):

$$\delta^2\text{H} = 6.27 \cdot \delta^{18}\text{O} + 11.40\,\text{‰ VSMOW}. \tag{2.13}$$

The reduced slope of 6.27 can be attributed to highly evaporative conditions in Jordan, i. e. that already during precipitation the rain drops experience evaporation, rendering the drops that reach the surface to be enriched in the heavy isotopes.

The interpretation of stable isotopes in water requires the consideration of several environmental parameters that alter the isotopic composition of water. The ultimate driving force
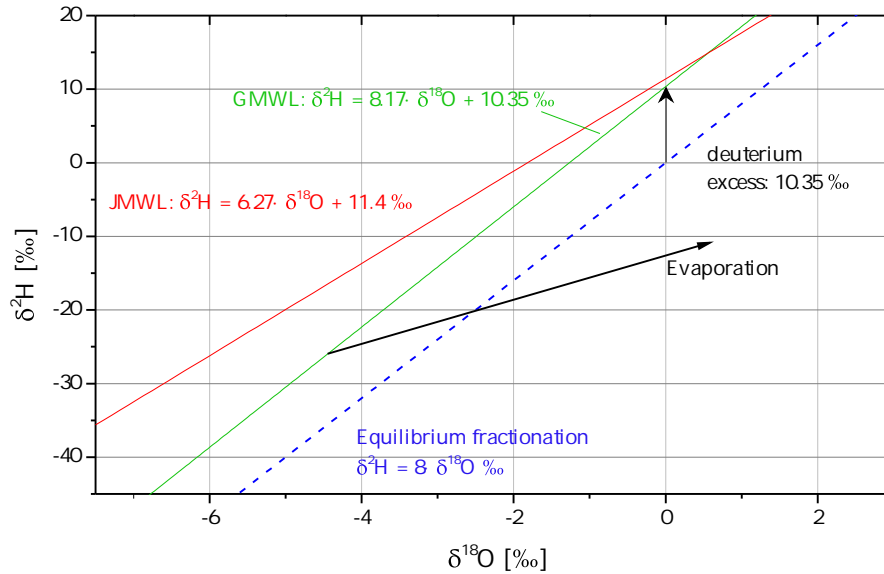
Figure 2.5: The relation of δ^2H and δ^{18}O in global precipitation forms the Global Meteoric Water Line (GMWL), here depicted in green. The Jordan Meteoric Water Line (JMWL) [Bajjali, 2012], which represents the isotopic composition in Jordanian rainfall, is characterized by a smaller slope, indicating an influence of evaporation (red line). Groundwater samples which plot along a line with smaller slope than the local meteoric water line indicate the presence of evaporative processes before the water seeps underground.

behind most of them is temperature. Dansgaard [1964] formulated the global relationship between mean annual temperature T and the average δ^{18}O of precipitation to be

$$\delta^{18}\mathrm{O} = 0.69 \cdot T - 13.6\,‰\ \mathrm{VSMOW}, \tag{2.14}$$

T in °C, but strong variances are observed on regional or local scale [Rozanski *et al.*, 1993]. Having this relation in mind, the following isotope effects can be explained. Clark and Fritz [1997] provide a good overview of these effects.

A rough correlation between latitude and local temperature explains the depletion of heavy isotopes in rainfall at higher latitudes, called *latitude effect*. As vapor masses travel to colder regions the relative humidity rises and finally the vapor condensates and rains out, leaving less enriched vapor behind. Analogous, vapor masses rising to high altitudes cool down adiabatically by approximately 0.5 °C per 100 m [Fairbridge and Oliver, 2005]. This *altitude effect* induces a depletion of heavy isotopes. For ^{18}O in precipitation a change of -0.15 to $-0.5\,‰$ per 100 m is found, but this effect strongly depends on the individual setting [Clark and Fritz, 1997]. The further the vapor masses move inland, the relief forces progressive rainout and, hence, a depletion in heavy isotopes occurs. This effect is called *continental effect* and is illustrated by fig 2.6. The basic principle behind all of these three isotope effects is called *Rayleigh process* or *Rayleigh distillation*. It describes the fact that under progressive rainout the remaining water vapor gets less depleted with time and, hence, also the subsequent condensation leads to isotopically "lighter" rain drops [Mook, 2000].
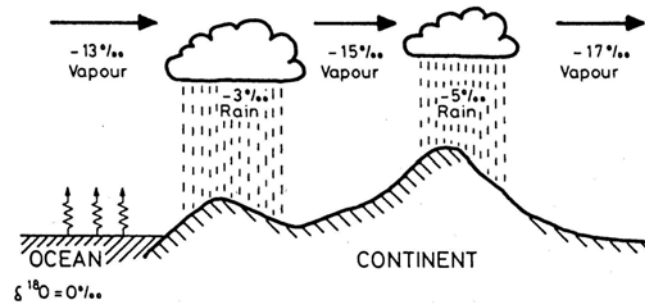
Figure 2.6: Visualization of the continental effect. From Siegenthaler [1979].

Not only the ambient temperature plays a role for the isotopic composition of precipitation, but also its strength. Dansgaard [1964] describes three mechanisms of the *amount effect* which cause a depletion of the stable isotopes in strong rainfall events: 1) Clouds that bring heavy rainfall experience depletion resulting from a progressive cooling, 2) small drops equilibrate faster with the vapor below the cloud which has not yet been exposed to the cooling process, resulting in an enrichment in slight precipitation events, and 3) the effect of re-evaporation from drops while falling down through air masses of less humidity causes an enrichment of heavy isotopes – this effect being, again, weaker in storm events. Clark and Fritz [1997] set the example of Bahrain, where the LMWL shows a slope of 6.3 when all rainfall is considered, but of 7.8 when only rain events with > 20 mm are incorporated in the calculation.

As a result of the latitude effect, the most depleted precipitation is found in the ice shields at the poles as well as in alpine glaciers due to the altitude effect. In times of global cold phases, a significant amount of sea water is bound in these ice volumes and leaves the ocean water more enriched than it is today. This effect is called the *global ice volume effect*. Shackleton and Opdyke [1973] find a δ^{18}O enrichment of 1.2 ‰ in the Last Glacial Maximum (LGM) in an Equatorial Pacific sediment core and calculated a sea level rise of 120 m at the end of the last glacial period. Hence, because precipitation mostly originates from the oceans, paleowaters from the last glacial also show an enrichment in δ^{18}O.

2.3.4 Carbon

Three natural isotopes of carbon exist on Earth: carbon-12, which is by far the most abundant, carbon-13 with an occurrence of 1.11 % and carbon-14, also called radiocarbon, with a relative abundance of 10^{-12}. In groundwater science ^{13}C is usually applied to trace water masses, while ^{14}C is the tool of choice to date old groundwater in the time range of up to 30 000 years [Clark and Fritz, 1997].

The main source of carbon in groundwater is the uptake of highly soluble CO_2 in the soil atmosphere during infiltration. In the subsurface, CO_2 is produced by plant respiration and microorganisms decomposing organic material. Partial pressure of soil CO_2 typically ranges between 0.1 and 10 %, i. e. concentrations can exceed the atmospheric value of around 400 ppm by almost three orders of magnitude [Clark and Fritz, 1997].
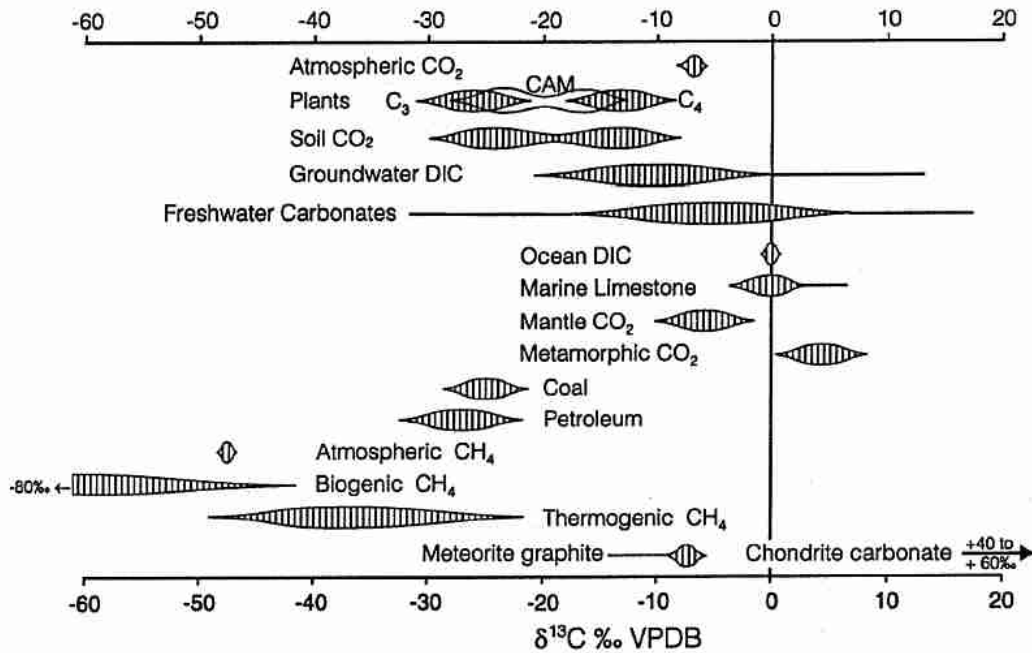
Figure 2.7: Typical variation of δ^{13}C in several natural reservoirs [Clark and Fritz, 1997].

Carbon-13

A lot of factors influence the carbon isotopy in groundwater and give rise to wide range of δ^{13}C values. These effects are described below and figure 2.7 offers an overview.

While atmospheric δ^{13}C is around $-7\,‰$, soil air carbon isotopy is more variable and depends mainly on the type of vegetation present on the surface. Generally, CO_2 fixation processes by plants prefer the lighter $^{12}CO_2$ molecule over the heavier $^{13}CO_2$ to be incorporated into plant material. Hence, the plants are depleted in ^{13}C. Respiration by the plant's roots, in contrast, favors the heavy $^{13}CO_2$ to be emitted to the soil air, but the resulting carbon isotopy of soil CO_2 is still way below the atmospheric value (compare figure 2.7). However, so called C_3 and C_4[1] plants differ from each other by their photosynthesis pathways and hence their CO_2 respiration [Peisker, 1984]. Soil air δ^{13}C values produced by C_4 plants are in the range of -9 to $-19\,‰$ (mostly around $-14\,‰$) and therewith much less fractionated than the ^{13}C isotopy respired by C_3 plants, which falls in the range of -22 to $-40\,‰$ (mostly around $-28\,‰$) [Peisker, 1984; Schulze *et al.*, 2005].

C_3 plants are common in temperate climate and tropical regions, where temperature and sunlight intensity are moderate and sufficient groundwater prevails [Schulze *et al.*, 2005]. They constitute most of the planet's biomass. During photosynthesis C_3 plants loose most of their uptaken water [Raven and Edwards, 2001] and are therefore not fitted to dry climate.

C_4 plants, in contrast, are adapted to arid climate by optimizing their photosynthesis mechanism in respect to water transpiration. In fact, the more efficiently a C_4 plant uses the scarce

---

[1]These plant types are named for the amount of carbon atoms present in the first product of the carbon fixation process, three in case of C_3 plant, four in case of C_4 plants.
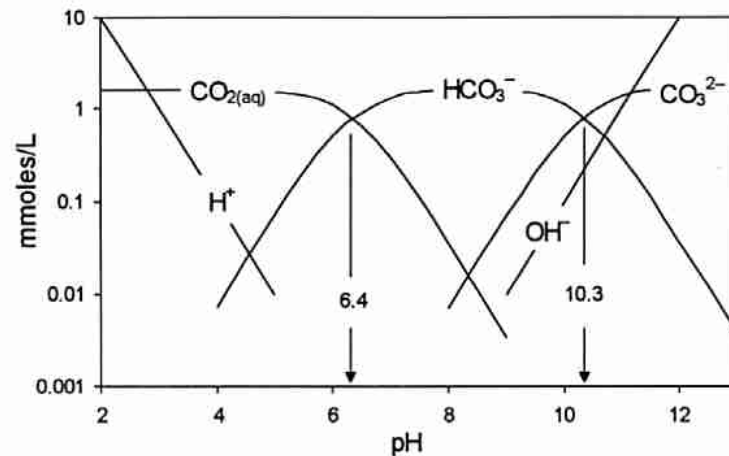
Figure 2.8: Carbon species in water in dependence of pH. Calculated for a DIC content of 1.6 mmoles/L at 25 °C. As sampled groundwaters from Jordan are all in the neutral pH range, HCO_3^- is the dominant species and the total DIC content can easily determined by measuring the alkalinity.[Clark and Fritz, 1997]

water the less it fractionates the carbonate isotopes [Ehleringer *et al.*, 1991].

No broad study on the occurrence of C_3 and C_4 plant in Jordan has been conducted up to now. Al-Eisawi [1996] at least lists some species typical in desert regions present in Jordan, and Sandias [2011] summarizes archeological studies which infer some animals diet mainly on C_4 plants in the desertified areas in Israel and south Turkey, but overall C_3 plants dominate in this region. As most groundwater recharge in Jordan takes place in more fertile areas of the Jordan highlands, most groundwater can be expected to have formed mainly below C_3 plants. However, as recharge in desert wadis occurs, where often grasses and bushes adapted to arid climate grow, some minor groundwater amount recharged in the C_4 plant regime may be found.

In every case, diffusive outgassing of soil CO_2 into the atmosphere leads to an enrichment of the remaining soil $^{13}C/^{12}C$ ratio by about 4 ‰ [Cerling *et al.*, 1991].

Gaseous soil carbon dioxide reacts with infiltrating water and forms carbonic acid, bicarbonate and carbonate, which are all subsumed under the term *dissolved inorganic carbon* (DIC):

$$DIC = [CO_2(aq)] + [H_2CO_3] + [HCO_3^-] + [CO_3^{2-}].$$

These components can change into each other and their distribution depends on the pH. At neutral pH, bicarbonate predominates, whereas dissolved CO_2 prevails at acidic conditions and carbonate in alkaline environments (see also figure 2.8). The transformation from one species into another is accompanied by carbon isotope fractionation. Details about these processes are found in Clark and Fritz [1997].

Interaction with carbonaceous material of the aquifer strongly alters the isotopic carbon composition of groundwater. $CaCO_3$ of marine limestone usually has $\delta^{13}C$ values of (0 ± 1) ‰

[Geyh, 2000]. Dissolution of it therefore enriches the δ^{13}C of the water. The lower the groundwater pH, the more calcium carbonate goes into solution, and even when saturation is reached, δ^{13}C may still alter due to ongoing ion exchange. Hence, the aquifer material plays an important role in coining the carbon isotope discrimination. Geyh and Michel [1982], for example, found that groundwater in a sandstone aquifer is commonly more depleted than water in a limestone aquifer.

Freshwater carbonates include speleothem, travertine and calcrete formations as well as secondary mineralization in soil. Due to the varying genesis conditions, CO_2 degassing in consequence of depressurization, evaporation or freezing of bicarbonate water, the δ^{13}C values cover a wide range, including positive values.

In locations of seismic activity, additional geogenic carbon in form of CO_2 can rise from sources in the the deep crust or the mantle and influence the carbon isotopy of groundwater. Mantle CO_2 has typical δ^{13}C of $-6\,‰$ [Geyh, 2000]. Metamorphic CO_2 originates from deep limestones, which experience a transformation in their physical and/or chemical state under high temperatures and pressure. This decarbonation is often related to magma bodies interacting with the limestone and release preferentially heavy CO_2. Typical δ^{13}C values of metamorphic CO_2 lie in the range of $+5$ to $+10\,‰$[Clark and Fritz, 1997].

Carbon-14

Atmospheric carbon-14 was discovered by Willard Frank Libby in 1946 [Libby, 1946]. He was awarded the Noble Prize in chemistry in 1960 for developing the radiocarbon dating technique, which revolutionized archeology as well as environmental sciences.

Radioactive ^{14}C is naturally produced in the upper atmosphere. Cosmic rays shower the gas particles and generate secondary thermal neutron in spallation reactions. Hitting ^{14}N, these neutrons produce radiocarbon:

$$^{14}\text{N} + \text{n} \longrightarrow {}^{14}\text{C} + \text{p}, \tag{2.15}$$

where n are neutrons and p protons. ^{14}C immediately oxidizes to $^{14}CO_2$ and enters the troposphere where it is assimilated in the biosphere and hydrosphere.

^{14}C disintegrates by β^- decay according to $^{14}\text{C} \longrightarrow {}^{14}\text{N} + \text{e}^- + \bar{\nu}_\text{e}$. Libby determined the half-life of ^{14}C to be 5568 years, which was subsequently corrected to be 5730 ± 40 years [Godwin, 1962], but still today the Libby half-life is often used to keep the comparability to older data.

^{14}C is widely used in archeologic and paleoclimatic studies as an age tracer. Assuming a closed system, which means there is no gain or loss of ^{14}C except of radioactive decay, and that the initial concentration is known, the age t of a sample can be derived from the ratio of the measured activity $A(t)$ and the initial activity A_0:

$$t = -\frac{\tau_{1/2}}{\ln 2} \cdot \ln \frac{A(t)}{A_0}, \tag{2.16}$$

where $\tau_{1/2}$ is the half-life of carbon-14.

[14]C activity is reported in *percent modern carbon* (pmC). 100 pmC are set by convention as 13.56 decays per minute and gram carbon and reflect the activity in the year 1950 AD [Mook, 1980]. Cosmogenic production and the radioactive decay of carbon-14 form a secular equilibrium and the concentration of ^{14}C can indeed be considered as constant over short periods of decades to some centuries.

Over long time periods, however, ^{14}C activity in the atmosphere was found to vary significantly. The examination of carbon isotopes of tree rings [Becker and Kromer, 1993; Muscheler *et al.*, 2008], foraminifera [Hughen *et al.*, 2004, 2006] and corals [Fairbanks *et al.*, 2005] revealed a variation of the atmospheric ^{14}C concentration over the millenia. Its activity varied by over 10 % during the Holocene and was even 40 % higher during the Last Glacial Maximum [Bard *et al.*, 1990]. Crowe [1958] and Stuiver and Quay [1980] revealed a dependency of the ^{14}C production rate on the number of visible sunspots, while Willson and Hudson [1988] and Hoyt *et al.* [1992] correlated the number of sunspots with solar activity measured by the SSM and Nimbus 7 satellites. Beiser [1957] and Damon *et al.* [1989] demonstrated an alteration of the production rate by the variability of the Earth's magnetic field. The latter is the major driving force behind the natural variation [Damon *et al.*, 1989].

The collected ^{14}C activity data in the Earth's atmosphere provide a calibration curve of the atmospheric ^{14}C content over time, summarized by Reimer *et al.* [2009], that is applied to get actual, calibrated sample ages.

Nowadays, ^{14}C activity in the atmosphere has an additional, anthropogenic source. While the combustion of radiocarbon free fossil fuel leads to a dilution of ^{14}C concentration in the atmosphere (Suess effect, see Suess [1955]), nuclear bomb tests in the 1950s and 60s released not only tritium in the atmosphere but increased the carbon-14 concentration as well [Münnich and Vogel, 1958]. In 1963 the activity in the atmosphere was about twice as high compared to 1950, but declined to about 105 pmC at the present day [Levin *et al.*, 2010]. The deviation of modern ^{14}C activity in the atmosphere from that of the year AD 1890, $\Delta^{14}C$ (delineated from 1890 tree-rings, which define the oxalic acid ^{14}C standard, see Stuiver and Polach [1977]), is shown in figure 2.9.

While the radiocarbon method allows dating of archeologic, i.e. biological, samples up to ages of 50 000 years [Kromer, 2007], ^{14}C dating of groundwater is accompanied by several complications. First, all the fractionating effects introduced above apply also for [14]C. Second, and having the strongest influence on the ^{14}C concentration in DIC in groundwater, the effect of artificial aging. By dissolution of carbonaceous aquifer material (which is free of ^{14}C, called *carbon dead*) and ion exchange of DIC dissolved in water with it, the initial ^{14}C content is reduced, which is expressed in a falsely greater groundwater age. For that reason, groundwater ^{14}C dating is generally limited to about 30 000 years [Clark and Fritz, 1997].

Several models were developed to account for the effects altering the initial ^{14}C content using different approaches. The Vogel model takes the ^{14}C activity in young groundwater (containing bomb tritium) to estimate the matrix effects [Vogel, 1967, 1970; Clark and Fritz, 1997]. The Pearson model tries to deduce the ^{14}C dilution by measuring the $\delta^{13}C$ and assuming a two component mixture of soil CO_2 (depending on vegetation) and leeched calcite (usually 0 ‰) [Pearson Jr., 1965]. Others take into account geochemical processes (Tamers
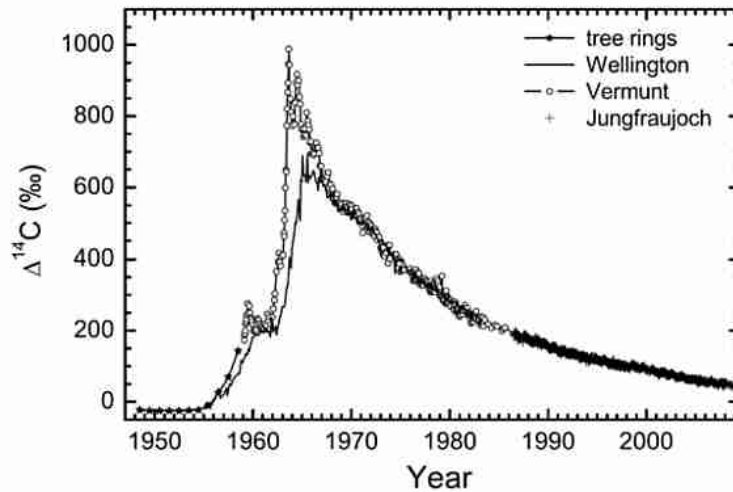
Figure 2.9: Deviation of modern atmospheric ^{14}C concentration from tree-ring data of AD 1890 [Stuiver and Polach, 1977] in the Northern (Vermunt, Austria) and Southern (Wellington, New Zealand) hemisphere [Levin *et al.*, 2010]. The bomb peak in the 1960s is obvious. Negative pre-1950 Δ^{14}C values indicate the influence of the Suess effect [Suess, 1955].

model [Tamers, 1975] and the chemical mass balance model by Clark and Fritz [1997]), or a combination of these indicators [Fontes and Garnier, 1979].

Due to the totally different approach, these models often result in differing groundwater ages [Wieser, 2011]. In this work, however, the exact water age is not so much of interest and only a very few samples are analyzed for radiocarbon. In the Azraq study, for example, mixing of different groundwater sources is assumed and therefore a specific water age makes principally no sense. Hence, ^{14}C data is interpreted in form of its basic analysis result, given in pmC, and is only used as a rough age indicator to discriminate between young samples, old and very old (carbon dead) samples.

2.3.5 Water chemistry in groundwater

Many different solutes are present in groundwater, mainly inorganic ions. A minor part is already present in precipitation [Davis and DeWiest, 1966], but most of the substances result from the dissolution of the aquifer rock during the subsurface flow of the water (compare table 2.1). Generally the most abundant cations are sodium (Na^+), calcium (Ca^{2+}), magnesium (Mg^{2+}) and the most frequent anions are chloride (Cl^-), sulfate (SO_4^{2-}) and bicarbonate (HCO_3^-). They are termed *major ions* and are included in every hydrochemical consideration [Freeze and Cherry, 1979]. Minor constituents include iron, strontium, potassium, carbonate, nitrate, fluoride, boron as well as other trace substances.

The concentration of solutes is usually reported in mg/L or in milligram equivalent per liter (meq/L). The latter is calculated from the first by dividing the concentration in mg/L, C_i^*, by the molar weight m_i and multiplying by the specific charge z_i of the ion i:

Table 2.1: Dissolution reactions and dissolved products of some common minerals, after Fitts [2002].

Salts			
Halite	$NaCl$	$\rightleftharpoons$	$Na^+ + Cl^-$
Sylvite	KCl	$\rightleftharpoons$	$K^+ + Cl^-$
Fluorite	CaF_2	$\rightleftharpoons$	$Ca^{2+} + 2F^-$
Sulfates			
Gypsum	$CaSO_4 \cdot 2\,H_2O$	$\rightleftharpoons$	$Ca^{2+} + SO_4^{2-} + 2\,H_2O$
Anhydrite	$CaSO_4$	$\rightleftharpoons$	$Ca^{2+} + SO_4^{2-}$
Epsomite	$MgSO_4 \cdot 7\,H_2O$	$\rightleftharpoons$	$Mg^{2+} + SO_4^{2-} + 7\,H_2O$
Barite	$BaSO_4$	$\rightleftharpoons$	$Ba^{2+} + SO_4^{2-}$
Carbonates			
Calcite	$CaCO_3$	$\rightleftharpoons$	$Ca^{2+} + CO_3^{2-}$
Aragonite	$CaCO_3$	$\rightleftharpoons$	$Ca^{2+} + CO_3^{2-}$
Dolomite	$CaMg(CO_3)_2$	$\rightleftharpoons$	$Ca^{2+} + Mg^{2+} + 2\,CO_3^{2-}$
Siderite	$FeCO_3$	$\rightleftharpoons$	$Fe^{2+} + CO_3^{2-}$
Silicates			
Quartz	SiO_2	$\rightleftharpoons$	$Si(OH)_4$

$$C_i[\text{meq/L}] = \frac{C_i^*[\text{mg/L}]}{m_i} \cdot z_i. \tag{2.17}$$

The advantage of indicating the ion concentrations in meq/L is to picture the true chemical character of the water, because it converts the substance's weight into the molar abundance and considers the net charge of the ion. As water is electrically neutral, the total equivalents of cations and anions need to be the same. The deviation from this ion balance, the ion balance error (IBE), is a measure of the goodness of the water sample analysis[2]:

$$\text{IBE} = \frac{\sum\limits_{\text{cations}} C_i - \sum\limits_{\text{anions}} C_i}{\sum\limits_{\text{anions}} C_i}. \tag{2.18}$$

A deviation of up to 5 % is usually accepted as a trustworthy analysis, errors of up to 10 % are tolerable in some cases [Knödel *et al.*, 2007]. Large errors may be due to the omission of other relevant inorganic solutes, large fractions of organic ions, contamination during sampling or precipitation of some of the solutes during the time between sampling and measurement in the lab. A small deviation, however, does not generally mean the ion analysis covered all solutes in the sample, since errors of cations and anions may cancel out each other. Nevertheless, this case is rare, and when the IBE is found to be small, the total dissolved solids

---

[2]Other definitions of the IBE exist, but here the most simple form is used.

(TDS) can usually be directly calculated with acceptable uncertainty by summing up all the individual ion concentrations (in mg/L, of course).

Another advantage of giving the concentrations in meq/L lies in the fact that the dissolved ions from a mineral which consists of two components only are present in the same concentration, i. e. plotting the concentrations of these ions against each other, the result is found to lie on the angle bisector. The dissolution of halite (NaCl), for example, leads to the same concentration of Na^+ and Cl^-, given in meq/L. Dissolution of gypsum leads to an equal amount of Ca^{2+} and SO_4^{2-} ions, and so on. Thus, the minerals that influence the considered groundwater can often be identified in this way (table 2.1 lists some of the most common dissolution reactions and their corresponding mineral).

Major ion data can be presented in several ways, compare Zaporozec [1972]. They all work with ion concentrations in meq/L. The most simple graph shows the composition in cations and anions as columns, as first proposed by Collins [1923] and depicted in figure 2.10. The concentration of the major ions are separately piled in two columns whose height is proportional to the total concentration of the cations and anions. It is therefore a graphical visualization of the ion balance calculation, as large IBE result in different heights of the columns. Sometimes the relative contributions of the single ions to the total cations/anions are drawn; thereby the IBE cannot be represented anymore, but the relative ionic composition of two samples can be compared more easily, independent of their total solute content.

The semi-logarithmic Schoeller diagram ([Schoeller, 1955, 1962], cited after Freeze and Cherry [1979]) allows the comparison of several water samples (see figure 2.11). For each sample the concentration of each observed ion is plotted and the dots are connected by a straight line, which gives kind of a footprint of each water. Samples with a similar overall composition have a similar footprint, independent of their total solute content.

A popular way to present major ion data is the trilinear Piper diagram [Piper, 1944; Hill, 1940, both after Zaporozec [1972]], exemplary shown in figure 2.12. Each trilinear diagram can show the composition of three ions, where the ion concentrations are given as percentages, those of the cations in the left triangle, those of the anion in the right triangle. Each apex of a triangle represents water with 100 % composition of one of the three constituents. Commonly, Ca^{2+}, Mg^{2+} and Na^+ (+ K^+) are plotted in the cations triangle, while Cl^-, SO_4^{2-} and HCO_3^- (+ CO_3^{2-}) form the anion triangle.

If only two of the three components are present, the water sample plots on the line between the two corresponding apexes. When all ions are present the analysis falls in the interior of the triangle. In cases of substantial potassium content, the same is added to the sodium concentration and the sum is drawn. The same holds for carbonate, which is grouped to the bicarbonate concentration in the anion triangle when required [Fetter, 2001].

The data point positions in the cation and the anion field are then projected into the central diamond. The resulting point characterizes the water type with respect to both its cations and anions (compare figure 2.13). Data point A in figure 2.12, for example, corresponds to Na-Cl-type water, point B to Ca-Mg-Na-HCO_3 water type. It is also possible to depict the absolute solute concentration of each sample in a piper diagram by varying the size of the data points.
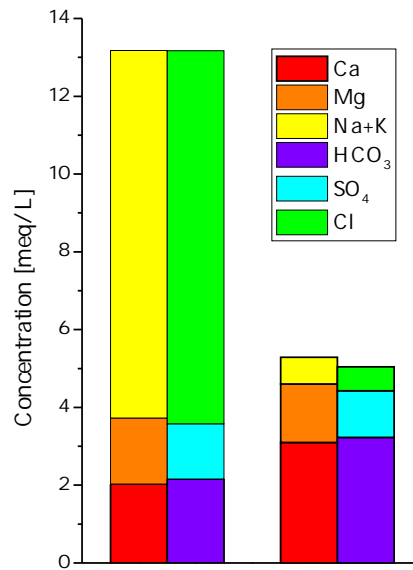
Figure 2.10: Column diagrams for two samples. The left one is typical for Na-Cl type water, the right one an example of Ca-HCO$_3$ water. Obviously, the left sample has higher TDS. The IBE is clearly visible in the visualization of the right sample. The coloration follows the recommendation of Collins [1923].
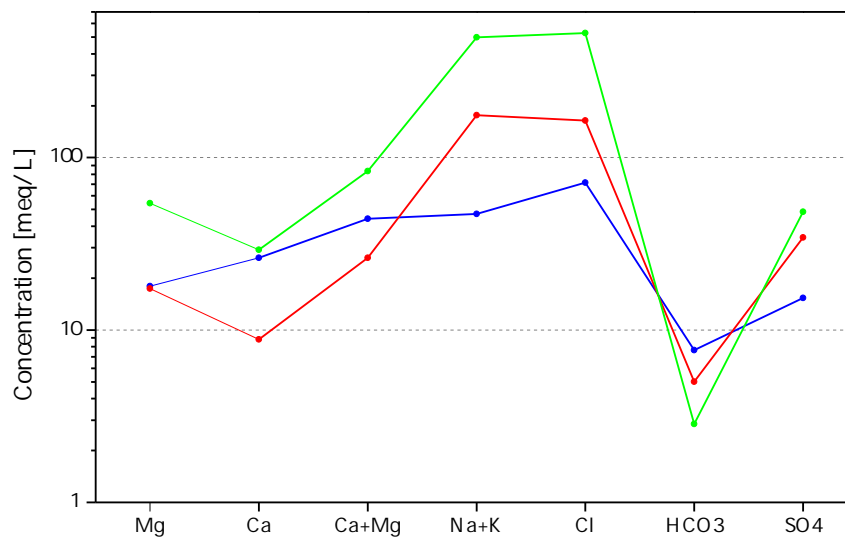
Figure 2.11: The Schoeller diagram allows the fast distinction between different water types. In this example the water samples represented in red and green have a similar footprint, i. e. they are similar in their ionic composition despite an obviously different total amount of solutes, whereas the blue sample represents a different water type (more Ca compared to the Na content).
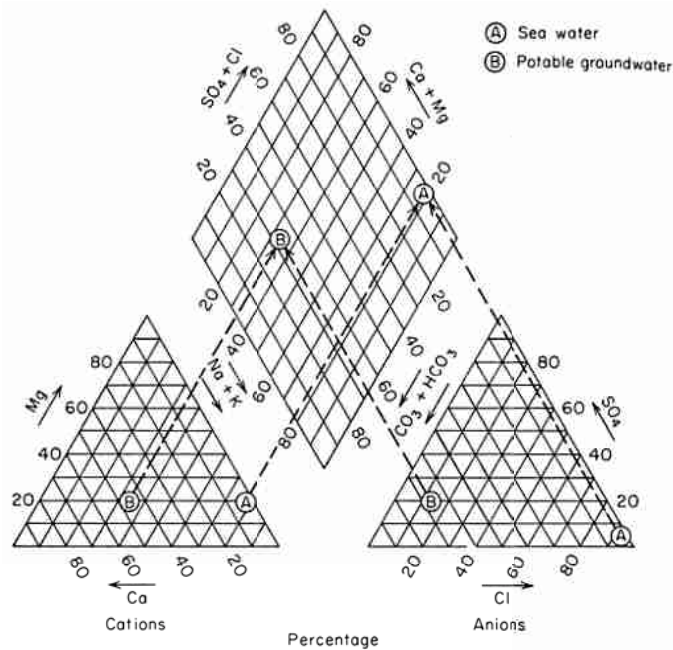
Figure 2.12: The piper diagram is a smart way to illustrate the chemical composition regarding the major ions of many water samples at once. It consists of two trilinear fields, one for cations and one for anions. In each triangle the relative shares of three ions or ion groups are plotted. The data points from the triangles are then projected into the central diamond shaped field, where it represents the chemical composition with respect to all considered ions. Taken from Freeze and Cherry [1979].
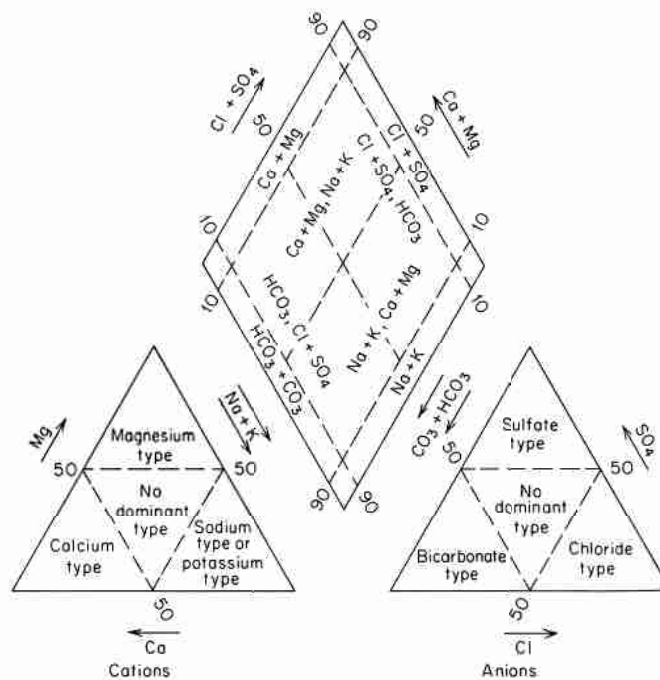
Figure 2.13: Characterization of water types in a piper diagram after Back [1966]. Adopted from Freeze and Cherry [1979].

Because each analysis is represented by a single point only in the diamond-shaped field, waters with very different total compositions can have the same projection in this diagram. Therefore, when investigating groundwater mixing, the two trilinear diagrams offer a much better illustration since the mixture of two different water types plots on a straight line joining the two endmember types.

2.3.6 Noble Gases

Noble gases have proven to be valuable tracers in geosciences [Porcelli *et al.*, 2002] and groundwater science [Kipfer *et al.*, 2002; Aeschbach-Hertig and Solomon, 2013]. Their chemical inertness and low abundance render them ideal tracers in geochemical, cosmochemical and groundwater studies.

Three major noble gas reservoirs exist on Earth: the atmosphere, the largest storage of noble gases, the Earth's crust and its mantle[3]. The different noble gas isotopic composition of these reservoirs enables scientists to separate the influences of these reservoirs and to trace crustal and mantle fluids.

Groundwater draws its noble gas content primarily from the atmosphere, from radioactive decay processes in the crust producing noble gases and, in regions of volcanic activity, also from the mantle reservoir [Ballentine and Burnard, 2002]. In groundwater, atmospheric noble gases originate from the equilibration of precipitating and then infiltrating water with the surrounding gas reservoir and an additional atmospheric component called excess air (EA) (see chapters 2.3.6.1 and 2.3.6.2). Especially within the crust, radioactive production of noble gases takes place. Three different mechanisms are distinguished: radiogenic (α decay in the U/Th decay chains produces ^{4}He), fissiogenic (direct production of Kr and Xe isotopes by spontaneous fission of heavy elements) and nucleogenic production (from the interaction of light elements with α particles or neutrons, like in the reaction ^{18}O $(\alpha, n)^{21}$Ne). These gases are released from the rock matrix and accumulate in groundwater. The Earth's mantle is assumed to bear primordial noble gases [Lupton and Craig, 1981] or input from cosmic dust [Anderson, 1993]. In regions with a thin crust or tectonic activity, these gases can ascend and mix into groundwater [Oxburgh and O'Nions, 1987].

Except for argon, all noble gases are present in the atmosphere only in traces. Table 2.2 gives an overview of atmospheric concentrations as well as relative abundances of stable noble gas isotopes used in this study.

In the following, the noble gases helium, neon, argon, krypton, xenon and radon are introduced. A much more detailed treatment is found in Ozima and Podosek [2002] and Porcelli *et al.* [2002], especially in the chapters of Ballentine and Burnard [2002] and Graham [2002] in the latter book.

---

[3]The oceans comprise dissolved noble gases as well, but those are not relevant within the scope of this thesis.

Table 2.2: Atmospheric noble gas concentrations and the absolute molar abundances of isotopes used in this study as well as the relative abundance in respect to a reference isotope denoted with $\star$ (i.e. the usually used isotope ratios). Data is compiled from Porcelli *et al.* [2002] and references therein as well as other sources mentioned in the text.

Noble gas	Volume mixing ratio	Isotope	Molar abundance [%]	Relative abundance
He	5.24×10^{-6}	^{3}He	1.4×10^{-4}	1.384×10^{-6}
		^{4}He	100	$\star$
Ne	1.818×10^{-5}	^{20}Ne	90.50	9.80
		^{22}Ne	9.23	$\star$
Ar	9.34×10^{-3}	^{36}Ar	0.3364	$\star$
		^{40}Ar	99.60	295.5
Kr	1.14×10^{-6}	^{84}Kr	57.00	
Xe	8.7×10^{-8}	^{132}Xe	26.89	

Helium

Helium is produced in radiogenic and nucleogenic reactions within the Earth's crust and mantle. Desintegration of elements in the U/Th decay chains generates one ^{4}He in almost all α decay reactions (a small fraction induces secondary nucleogenic reactions). The production of ^{4}He in the crust is significantly higher than in the mantle, Yatsevich and Honda [1997] indicate production rates of 4.15×10^{-13} compared to 4.15×10^{-15} ccSTP/(g·year). In the lithosphere ^{3}He originates predominantly from tritium poduced by the capture of thermal neutrons by ^{6}Li in the reaction ^{6}Li (n,α) ^{3}H (β^-) ^{3}He [Morrison and Pine, 1955; Mamyrin and Tolstikhin, 1984]. Also, atmospheric tritium is incorporated into groundwater and subsequently decays into ^{3}He [Cornog and Libby, 1941; Libby, 1946]. The total atmospheric concentration of He is 5.24 ppm [Porcelli *et al.*, 2002] and the atmospheric ^{3}He/^{4}He ratio was found to be $(1.384 \pm 0.006) \times 10^{-6}$ by Clarke *et al.* [1976]. This ratio is commonly named R_A. Due to slightly different solubilities of ^{3}He and ^{4}He the ^{3}He/^{4}He ratio in an air equilibrated water sample is 1.360×10^{-6} [Benson and Krause Jr., 1980].

A constant flux of helium from the Earth interior to the atmosphere was observed by Craig *et al.* [1975] and Oxburgh and O'Nions [1987]. While the heavier noble gases from deep sources accumulate in the atmosphere, He is light enough to overcome the Earth's escape velocity and to vanish into the exosphere [Torgersen, 1989]. The atmospheric He concentration is, thus, considered to be constant due to an equilibrium between inflow from the subsurface and an effluent into space [Torgersen, 1989].

While the atmospheric ^{3}He/^{4}He ratio is R_A, the other reservoirs differ significantly. Since the neutron capture probability of ^{6}Li is very low, the helium production in the Earth's crust is dominated by ^{4}He production from the U and Th decay series. This leads to a crustal ^{3}He/^{4}He ratio of 1 to $3 \times 10^{-8} \approx 0.015\,R_A$ [Mamyrin and Tolstikhin, 1984]. Mantle mate-

rial displays a wide range of ^{3}He/^{4}He ratios. Mid-ocean ridge basalts (MORB) commonly have ratios in the range of 7 to 9 R$_A$ [Graham, 2002], i.e. 1.0 to 1.2×10^{-5}. Much higher ^{3}He/^{4}He ratios of up to 50 R$_A$ [Class and Goldstein, 2005; Graham, 2002] can be associated with hotspot volcanism. The primordial helium composition is estimated to be in the order of 230 R$_A$ [Class and Goldstein, 2005]. These wide variations of ^{3}He/^{4}He ratios render helium to be a great tracer for geochemical studies of mantle fluids.

Other applications of helium in groundwater science include qualitative dating of groundwater [Solomon, 2000; Aeschbach-Hertig *et al.*, 2002], but quantitative dating appeared to be difficult [Torgersen and Clarke, 1985]. Torgersen [1980] revealed that the combination of ^{4}He and ^{222}Rn can improve the dating potential of helium. ^{4}He has been used to trace groundwater discharge from a deep (old, i.e. much ^{4}He) into a shallow reservoir (less radiogenic He) [Gascoyne and Sheppard, 1993; Stephenson *et al.*, 1994; Deshpande and Gupta, 2013]; this possibility of helium data interpretation is applied in the Azraq study of this thesis. Tritiogenic ^{3}He in young groundwater is applied to considerably enhance the precision of the tritium dating method [Schlosser *et al.*, 1988].

The interpretation of helium from different sources in groundwater is often displayed in the three-isotope plot depicted in figure 2.14. The ^{3}He/^{4}He ratio is plotted against Ne/He. Ne is introduced as a measure of additional atmospheric noble gases (excess air, see chapter 2.3.6.2). All three possible helium sources – atmosphere, crust and mantle – are shown in form of their endmembers. Newly formed groundwater "starts" at the atmospheric composition with ^{3}He/^{4}He $= R_A$ and Ne/He ≈ 4.2 (slightly dependent on the mean annual temperature). As it ages, it "moves" along the dashed line towards the radiogenic endmember with ^{3}He/^{4}He $= 0.015\,R_A$ and Ne/He $= 0$. The mantle endmember is assumed as MORB-like with ^{3}He/^{4}He $\approx 8\,R_A$ and Ne/He $= 0$. As a result all water samples with a significant mantle influence scatter above the dashed line. The closer they are to the mantle endmember, the stronger is its influence. One exception from this rule are young groundwaters, which possess tritogenic ^{3}He. These samples are found close to the atmospheric endmember, but above the line.

If tritiogenic ^{3}He can be neglected or determined another way, the atmospheric, crustal and mantle helium contributions to a sample can be calculated. A graphical and an analytical method for that are presented in chapter 2.3.6.3.

Neon

Neon occurs in three stable isotopes, ^{20}Ne, ^{21}Ne and ^{22}Ne, of which ^{21}Ne has not been analyzed in the scope of this thesis. Atmospheric neon has a ratio of ^{20}Ne/^{22}Ne $= 9.80 \pm 0.08$, whereas the Earth's mantle exhibits ratios of up to ^{20}Ne/^{22}Ne $= 13.5$ [Graham, 2002]. There are secondary nuclear reactions that produce neon isotopes [Yatsevich and Honda, 1997], but the yield is very low (about 10^{-7} compared to ^{4}He for both ^{20}Ne and ^{22}Ne [Yatsevich and Honda, 1997]) and affects the isotopic composition in groundwater only if residence times are in the order of many millions of years. Because neon has a very low solubility, excess air or degassing have large effects on its concentration in water. It is often used to roughly estimate the amount of excess air or degassing of a sample (compare chapter 2.3.6.2).
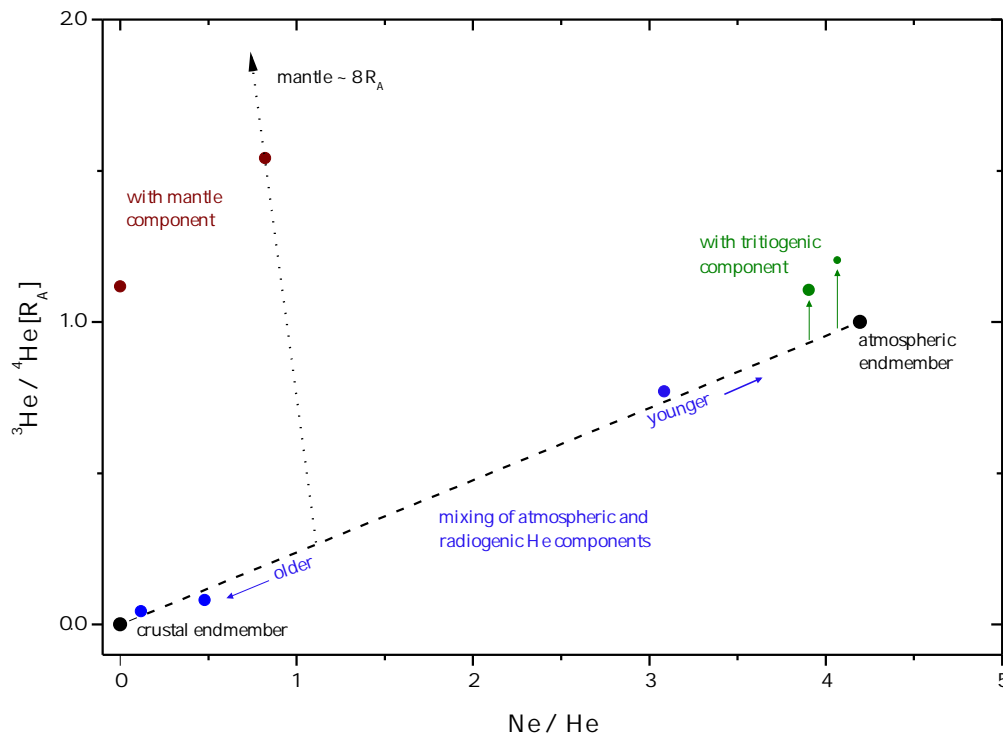
Figure 2.14: Three-isotope plot indicating different sources of He. Newly formed groundwater "starts" with atmospheric composition with $^3\text{He}/^4\text{He} = R_A$ and $\text{Ne}/\text{He} \approx$ 4.2 (depending on the ambient temperature at the time of isolation from the atmosphere). In young groundwater the $^3\text{He}/^4\text{He}$ ratio is increased due to ^3He from bomb tritium decay. When the water gets older, it "moves" towards the radiogenic endmember. An existing mantle component becomes apparent in data points above the atmospheric-radiogenic mixing line, in case tritiogenic origin can be ruled out.

Argon

Argon is by far the most abundant noble gas in the terrestrial atmosphere and has three stable isotopes: ^{36}Ar, ^{38}Ar and ^{40}Ar. The latter is the only one with relevant production on Earth [Sano *et al.*, 2013]. It originates from electron capture and β^- processes of ^{40}K and subsequently degases into the atmosphere. ^{40}K has a half-life of 1.25×10^9 years, but due to its comparatively high abundance in the crust, the ^{40}Ar production is similar to the one of ^4He ($^4\text{He}/^{40}\text{Ar} \approx 5.7$ [Ballentine and Burnard, 2002]). However, because of its high concentration in the atmosphere, radiogenic argon noticeably affects groundwater only in cases of residence times of millions of years.

^{36}Ar has a very low production mainly from β^- decay of ^{36}Cl [Fontes, 1991, cited after Ballentine and Burnard, 2002], but the relative production of it compared to ^{40}Ar is 6.5×10^{-8}. In the time range of groundwater studies, ^{36}Ar can be assumed to be totally primordial. The atmospheric $^{40}\text{Ar}/^{36}\text{Ar}$ ratio is found to be 295.5 [Porcelli *et al.*, 2002].

Krypton and xenon

Six stable isotopes of krypton exist. The main isotope is ^{84}Kr with a relative abundance of 57.00 % [Basford *et al.*, 1973]. Xenon has nine stable isotopes of which ^{132}Xe has a relative abundance of 26.89 % [Basford *et al.*, 1973]. Some isotopes of Kr and Xe experience production by spontaneous fission of several U and Th isotopes, but these processes play a role only in extremely old groundwater (Lippmann *et al.* [2003] dated groundwater in a deep South African gold mine up to 10^8 years by considering several Xe isotopes) or in an exceptional site like the Oklo natural fission reactor in Gabon [Meshik *et al.*, 2004]. In conventional groundwater studies krypton and xenon are assumed to be solely of atmospheric origin.

Radon

Radon has no stable isotopes. From the naturally occurring isotopes only ^{222}Rn is commonly applied in groundwater science, because ^{219}Rn and ^{220}Rn have very short half-lifes. ^{222}Rn is part of the ^{238}U decay chain and, hence, is produced in the lithosphere. Its half-life of 3.82 days enables scientists to estimate groundwater influx into lakes [Kluge *et al.*, 2007] or gas diffusion in soil [Lehmann *et al.*, 2000]. Some people employed radon as a geochemical exploration tool [Gingrich, 1984] or to identify geological features and rock radium content [Choubey and Ramola, 1997]. Radon is also a valueable means when dating groundwater with ^{4}He [Torgersen, 1980]. A good summary of the chemistry and hydrologic applications of radon can be found in DeWayne Cecil and Green [2000].

Due to its rapid decay, radon is not measured at the mass spectrometer in the laboratory in Heidelberg, but directly in the field by a portable radon analysis device (see chapter 3.7 for detailed description).

Noble gases found in groundwater samples are made up of several components. During recharge, the water equilibrates with the surrounding soil air (equilibrium component). An additional atmospheric component originates from entrapped air bubbles in the quasi-saturated zone (excess air component). Terrigenic noble gases, i.e. radiogenic, tritiogenic and mantle gases, are subsumed under the term non-atmospheric component. Except for helium the non-atmospheric component can usually be neglected. Figure 2.15 illustrates the different components for each noble gas.

In order to exploit the different components as proxies for distinct effects, they have to be separated from each other. This is done by inverse modeling as described in chapter 3.6.4.

2.3.6.1 Equilibration

When water and air are in contact with each other, gases are exchanged until an equilibrium between the concentration in the gas phase, C^g, and water phase, C^w, is established. The amount of each single gas i in the water fraction is determined by its partial pressure in the gas phase, the water temperature and its dissolved ions.
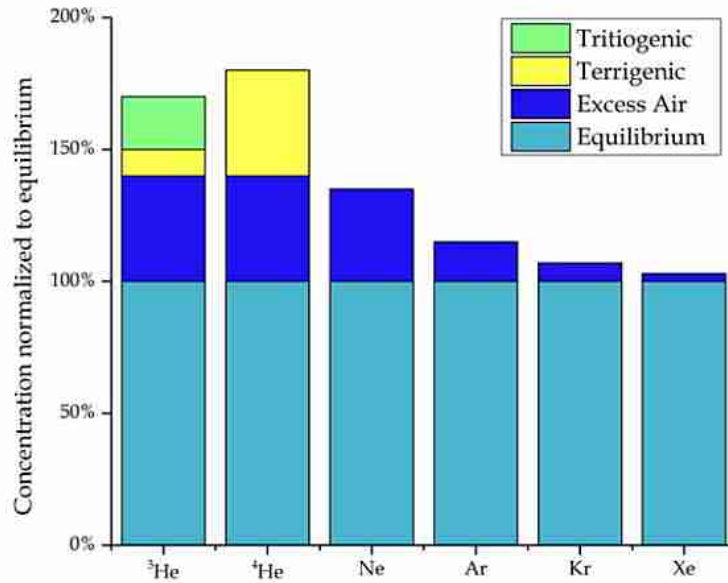
Figure 2.15: The composition of each noble gas in a groundwater sample normalized to the concentration of the equilibrium component. All are affected by excess air, but the influence is less for the heavy noble gases. Only helium is often significantly influenced by terrigenic sources, ^{3}He in young groundwater has a tritiogenic component. Adapted from Kipfer *et al.* [2002].

The solubility of gas i in water is often delineated by the Henry coefficient $H_i(T, S)$ [Henry, 1803] which describes the proportionality of the gas concentrations in the gas and liquid phase in dependence of water temperature T and salinity S:

$$C_i^g = H_i(T, S) \cdot C_i^w. \tag{2.19}$$

Often the concentration in water is correlated with the ambient partial pressure of gas i:

$$p_i = H_i^*(T, S) \cdot C_i^w. \tag{2.20}$$

Partial pressures depend predominantly on the height. This relation is usually approximated by the barometric formula for the total pressure p:

$$p = p_0 \cdot \exp\left(-\frac{h}{h_0}\right). \tag{2.21}$$

p_0 denotes the atmospheric pressure at sea level and h_0 is the scale height which can be assumed to be 8300 m [Aeschbach-Hertig *et al.*, 1999].

Several works have been published that empirically describe the correlation between solubility and temperature respectively salinity. Weiss [1970, 1971] and Weiss and Kyser [1978] list the equilibrium concentrations of helium, neon, argon and krypton in dependence of temperature and salinity. Benson and Krause Jr. [1976] and Krause Jr. and Benson [1989] give solubility-temperature relations of all noble gases except radon, Smith and Kennedy [1983]
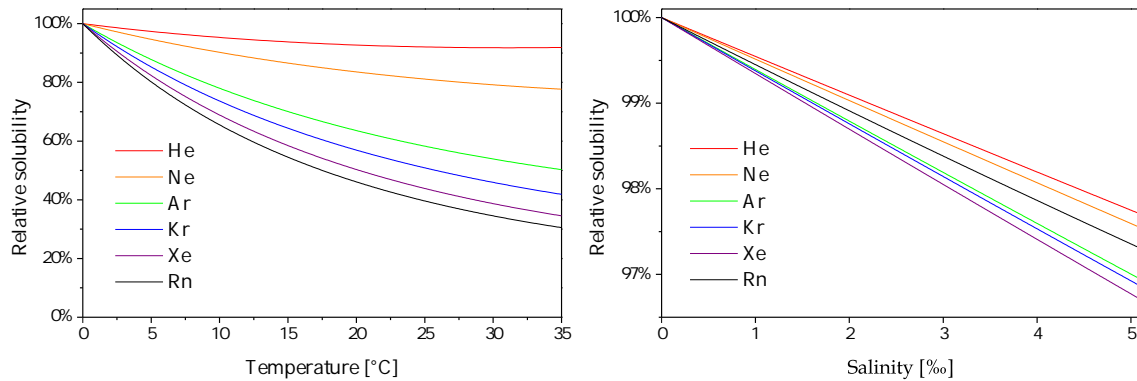
Figure 2.16: The relative solubility of noble gases in water in dependence of temperature (left) and salinity (right). For the temperature dependence pure water (i. e. 0 ‰ salinity) is assumed. Salinity dependence is given for a fixed temperature of 18 °C. The data is plotted according to the equations in appendix A.1, citations and more details are found there as well. The salinity dependence of radon seems to be inaccurate at low dissolved salt content, because the shown solubility behavior originates from a fit on solubilities at salinities between 12 and 362 g/kg, i. e. much higher concentration than the other gases, which in turn are optimized for the salt content range of sea water.

also determined the solubility dependence of temperature and salinity. Clever [1979a,b, 1980] compiles solubility data of all noble gases, too. Figure 2.16 depicts the temperature effect on solubility for all noble gases, including radon.

Aeschbach-Hertig *et al.* [1999] and Beyerle *et al.* [2000] compare the different solubility data sets in the temperature range of 0 to 40 °C and find deviations in the order of 1 %, which is in the range of typical measurement errors. As Aeschbach-Hertig *et al.* [1999] conclude, the solubilities of Weiss for He to Kr are used in this work and those of Clever for Xe. For meteoric water the salinity is usually taken to be zero, as the effect of dissolved ions is small compared to the temperature effect and forming groundwater usually exhibits no high salinity. A more detailed treatment of these solubilities is given in appendix A.1.

The temperature dependent solubility of noble gases was applied in paleotemperature studies for 40 years [Mazor, 1972] and developed into a reliable tool to reveal a substantial temperature increase at the end of the last glacial 11 ka ago (for example Andrews and Lee [1979]; Stute *et al.* [1995]; Aeschbach-Hertig *et al.* [2002] and many others, compare Kipfer *et al.* [2002] and Aeschbach-Hertig and Solomon [2013]).

Noble gas temperatures (NGTs), i. e. the temperatures reconstructed from the equilibrium component of the dissolved noble gases in groundwater, reflect the mean temperature at the groundwater table at the place of recharge. This corresponds quite well to mean annual air temperature [Stute and Schlosser, 1993; Smith *et al.*, 1964], unless the water table is very close to the surface (imprint of seasonal temperature variations) or a deep (> 30 m) unsaturated zone is prevalent, as ambient temperatures at the groundwater table in this case are higher due to the geothermal gradient.

In many areas in Jordan, the unsaturated zone is quite thick, several hundred meter in some ares. An influence of the geothermal gradient can, therefore, not be neglected in general. Because wide parts of Jordan experienced volcanic activity in the recent past, the mostly assumed gradient of 30 K per km needs to be scrutinized.

2.3.6.2 Excess air

Already the first noble gas studies on groundwater detected a gas content which exceeded the expected atmospheric equilibrium gas content. Andrews and Lee [1979] attributed this finding to an entrainment of air bubbles as the groundwater flows, and soon after Heaton and Vogel [1981] coined the term "excess air" (EA) for this phenomenon. During infiltration of precipitation, the water table rises and small air bubbles are entrapped in tiny dead-end pore spaces of the quasi-saturated zone. The increasing hydrostatic pressure causes these bubbles to dissolve, at least partly [Faybishenko, 1995; Holocher *et al.*, 2002, 2003] and therefore leads to an enrichment of noble gas concentrations above the equilibrium.

Some studies examined the air content of the quasi-saturated zone in different soils. Seymour [2000] for example found 3 to 15 % of the pore volume of a sandy soil filled with air after wetting under laboratory conditions. More studies on the air content in the quasi-saturated zone are listed in Sakaguchi *et al.* [2005].

To describe the additional noble gases in groundwater, several excess air models were introduced. The assumed processes behind those models introduced below are visualized in figure 2.17.

UA model

The **U**nfractionated **A**ir (UA) model is the simplest excess air model. It assumes a total dissolution of the entrapped air bubbles [Heaton and Vogel, 1981] and describes the noble gas concentration C_i in groundwater according to

$$C_i^{\mathrm{UA}} = C_i^{eq} + A'x_i = C_i^{eq}(1 + AH_i). \tag{2.22}$$

Thereby, A' is the fraction of entrapped air bubbles with respect to the water volume and x_i is the atmospheric mole fraction of gas i. The alternative form on the right [Aeschbach-Hertig *et al.*, 2008] emphasizes the proportionality of the excess air to the equilibrium component. A' and A are related by $A'x_i = Ac_i^{\mathrm{air}}$. Many subsequent studies found this first excess air model to be not satisfying, because often an enrichment of the heavy noble gases was found compared to atmospheric equilibrium. Thus, a couple more models were developed, of which the most important are described below.

PR and PD model

Stute *et al.* [1995] try to explain excess air patterns in a noble gas record from Brazil assuming **p**artial **r**e-equilibration (PR) with the soil air after total dissolution of the air bubbles. Due
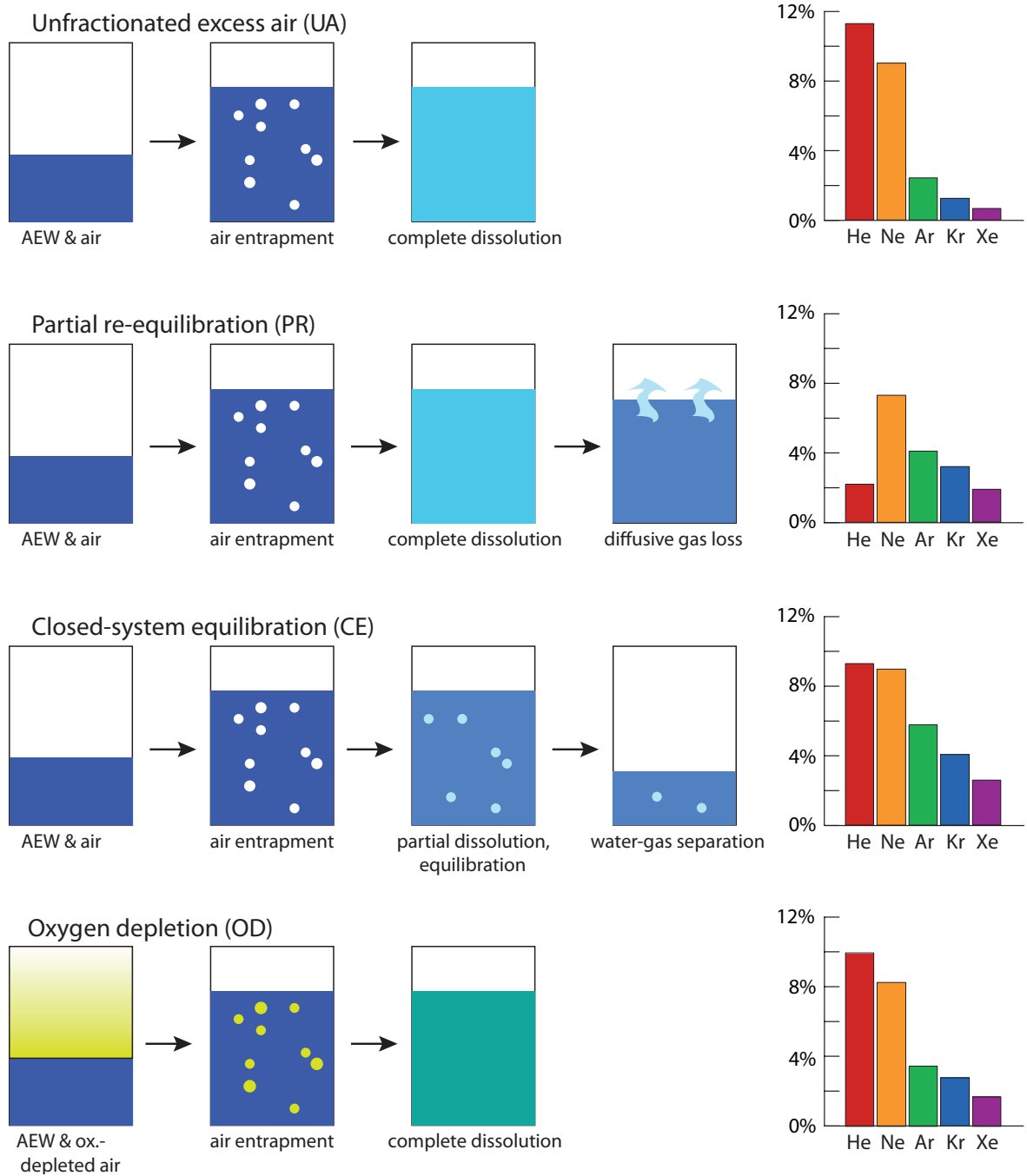
Figure 2.17: Visualizations of the assumed physical processes behind the most common excess air models. On the right the individual excess air pattern of each model is given. Adapted from Wieser [2011], who was inspired by Kipfer *et al.* [2002].

to the higher diffusion coefficients of He and Ne, a stronger depletion of these elements is expected. This situation can be described by [Aeschbach-Hertig *et al.*, 2008]:

$$C_i^{\mathrm{PR}} = C_i^{eq} \left[1 + AH_i \cdot \exp\left(-F_{\mathrm{PR}} \left(\frac{D_i}{D_{\mathrm{Ne}}} \right)^{\beta} \right) \right]. \tag{2.23}$$

F_{PR} describes the degree of excess air loss by re-equilibration processes, D_i are the diffusion constants of the noble gases in water and β is a modeling parameter from the gas transfer theory and can attain values between 0.5 and 1 [Holmén and Liss, 1984; Aeschbach-Hertig *et al.*, 2008].

Since in the PR model only the excess component is affected by diffusive degassing, it is not able to handle cases of degassed water, i.e. cases where gas bubble formation depletes the total noble gas amount in groundwater. This issue is attended to by the **P**artial **D**egassing (PD) model, which is similar to the PR model, but the diffusive term applies to the total gas concentration [Lippmann *et al.*, 2003; Aeschbach-Hertig *et al.*, 2008]:

$$C_i^{\mathrm{PD}} = C_i^{eq}(1 + AH_i) \cdot \exp\left(-F_{\mathrm{PD}} \left(\frac{D_i}{D_{\mathrm{Ne}}} \right)^{\beta} \right). \tag{2.24}$$

Degassing in groundwater occurs when the total dissolved gas pressure is higher than the hydrostatic pressure [Fry *et al.*, 1997], which often is the case when denitrification takes place [Blicher-Mathiesen *et al.*, 1998] or deep thermal waters supersaturated with CO_2 discharge in surface springs [Chiodini *et al.*, 1995].

CE model

A different approach to explain the excess air is the **C**losed-system **E**quilibration (CE) model, proposed by Aeschbach-Hertig *et al.* [2000]. Observations of entrapped air in soils have shown that considerable amounts of excess air is formed in the upper most meters [Faybishenko, 1995], where hydrostatic pressure is not sufficiently high to completely dissolve the air bubbles. Instead, of the initial air amount A only a fraction is dissolved, resulting in a smaller amount B remaining in the gas phase. The model in the formulation of Aeschbach-Hertig *et al.* [2008] is reflected by

$$C_i^{\mathrm{CE}} = C_i^{eq} \frac{1 + AH_i}{1 + BH_i} = C_i^{eq} \left(1 + \frac{(1-F)AH_i}{1 + FAH_i} \right). \tag{2.25}$$

The latter formulation introduces the fractionation factor $F = B/A$, which was used in the first formulation of the CE model. $F < 1$ delineates excess air in groundwater, while the CE model can also be applied to characterize degassing in the case of $F > 1$ [Aeschbach-Hertig *et al.*, 2008; Blaser *et al.*, 2010].

OD model

All above models start from the premise that the noble gas composition of soil air corresponds to atmospheric composition, which does not hold in regions with biological activity

where oxygen is consumed by root respiration and the decomposition of organic material to produce CO_2. Under aerobic conditions the equimolar reactions do not change the partial pressure of the other gases. However, CO_2 may be washed out due to its higher solubility in water [Weiss, 1970, 1974] compared to oxygen. This would lead the other gases to compensate for the gas loss, i. e. the partial pressure of all other gases would increase. Although Stute and Schlosser [1993] ruled out this effect qualitatively, Hall *et al.* [2005] found noble gas concentrations in an aquifer in Michigan which they attributed to **o**xygen **d**epletion with subsequent CO_2 wash-out and termed this excess air model OD model. The mathematical formulation of the OD model was published by Sun *et al.* [2008], introducing an oxygen depletion factor P_{OD} which reflects the partial pressure rise of the other gases in consequence of oxygen depletion:

$$C_i^{OD} = C_i^{eq} P_{OD} + A' x_i = C_i^{eq} (P_{OD} + A H_i)^4. \tag{2.26}$$

Obviously the OD model resembles the UA model, but a modified soil air composition is assumed. Since a maximum of 21 % of oxygen can by replaced in soil air, P_{OD} is limited to values between 1 and 1.26. Because increasing the partial pressure is analogues to an equilibration in lower altitudes, P_{OD} is usually considered to be constant for an aquifer to avoid high colinearities in the inverse modeling. The NGTs derived by application of the OD model tend to be lower than the actual ground temperatures due to the elevation of noble gas partial pressures.

The OD model and its consequences are vividly discussed recently. The effect of oxygen depletion on noble gas concentrations is investigated by Freundt *et al.* [2013] in boreholes under natural and artificial precipitation conditions. While the sum of oxygen and carbon dioxide is lowered to a minimum of 16.5 %, an increase of noble gas concentrations of up to 6.4 % above the atmospheric mixing ratio is observed. Whether this effect is visible right above the groundwater table or in groundwater itself, is subject of current research in our group and data has not been published yet.

A couple of other excess air models exist and are compiled by Aeschbach-Hertig and Solomon [2013], most of them are derivations of the above listed ones. Just recently Sun *et al.* [2010] published a comparison of several models on synthetical and real data sets. The quintessence is that these models produce an offset in absolute noble gas temperatures compared to the local mean annual air temperature, but agree remarkably well when estimating temperature differences. In paleoclimate studies it is therefore essential to stick to one excess air model for each data set.

The decision which excess air model is chosen should depend on which one describes the physical situation best. Since none of the current models can explain all available noble gas data sets adequately, the processes behind those models do not seem to be fully understood. The most likely explanation is that the physical mechanisms are much more complex than

---

[4]The fact that in the model formulation of Sun *et al.* [2008] the P_{OD} factor acts on the equilibrium concentration only might be disturbing at a first glance, as formed air bubbles need to be assumed to consist of the deviated soil air composition as well. According to the modelling (A resp. A' seen as model parameter) this fact can be ignored, but one needs to have in mind, that A and A' in the OD formulation are not the same as in the UA model formulation: $A'_{OD} = P_{OD} \cdot A'_{UA}$ and $A_{OD} = P_{OD} \cdot A_{UA}$

the lumped-parameter type models reflect. Obviously this issue needs further research. In the meanwhile, if no additional information is available, the accuracy of the fit is the best possible decision criteria. A good start is to use the UA model to distinguish between over and undersaturated samples regarding their noble gas content. In a mixed data set, this helps to identify samples that should be fitted by the CE model in degassing mode (i.e. $F > 1$).

Although in most noble gas studies excess air has been considered as a disturbing or concealing factor, it seems that EA itself is a paleoclimate proxy. A change in precipitation patterns can affect the water table fluctuations and, thus, the formation of excess air. Several studies connected the amount of excess air in groundwater to a change in local recharge patterns or amounts. A measure for the excess air amount is the so called neon excess, ΔNe, defined as the ratio of excess neon concentration to the calculated equilibrium Ne concentration and is usually reported in %:

$$\Delta \text{Ne} = \frac{C_{\text{Ne}}^{exc}}{C_{\text{Ne}}^{eq}} = \left(\frac{C_{\text{Ne}}^{meas}}{C_{\text{Ne}}^{eq}} - 1 \right). \tag{2.27}$$

Positive ΔNe values indicate an excess air component, whereas negative values signal degassing. Especially in (semi) arid regions or regions of intermittent rainfall, water table fluctuations can vary widely and imprint different excess air amounts [Beyerle *et al.*, 2003; Kulongoski *et al.*, 2004; Klump *et al.*, 2008] but the effect can also be found in temperate climate [Ingram *et al.*, 2007]. Kulongoski *et al.* [2009] correlate a temporal change of excess air in California with prolonged El Niño-like conditions during the Pleistocene, Zhu and Kipfer [2010] interpret their data to reflect the passing of the southern branch of the jet stream over Arizona between 14 and 17 ka BP. More studies on paleohumidity with the excess air proxy are referenced in Aeschbach-Hertig and Solomon [2013].

2.3.6.3 Component separation of helium

The endmembers of the atmospheric, crustal and mantle components in groundwater span a triangle in the ^{3}He/^{4}He–Ne/^{4}He space of the isotope plot in figure 2.14, as displayed in figure 2.18. It forms a trilinear plot in which the relative abundances of ^{4}He (which is essentially identical to the total He) of the three components can be graphically delineated [Pyle, 1993]. Each component has its own scale on one side of the triangle, and the proportion of it can directly be read off (an example is given in the caption of figure 2.18).

As Aeschbach-Hertig [2005] demonstrated, the crustal and the mantle share of a water sample can also be separated by a simple, but more precise calculation. He realized this for the case of old groundwater, i.e. a negligible atmospheric component. Following, I will delineate a similar way to calculate the fraction of crustal and mantle He in a sampled water in case of a non-negligible atmospheric component.

The helium isotope ratio, R, of a sample (S) can be expressed as a mixture of crustal (C), mantle (M) and atmospheric (A) helium:

$$R_S = \frac{^3\text{He}_S}{^4\text{He}_S} = \frac{^3\text{He}_C + ^3\text{He}_M + ^3\text{He}_A}{^4\text{He}_C + ^4\text{He}_M + ^4\text{He}_A}. \tag{2.28}$$
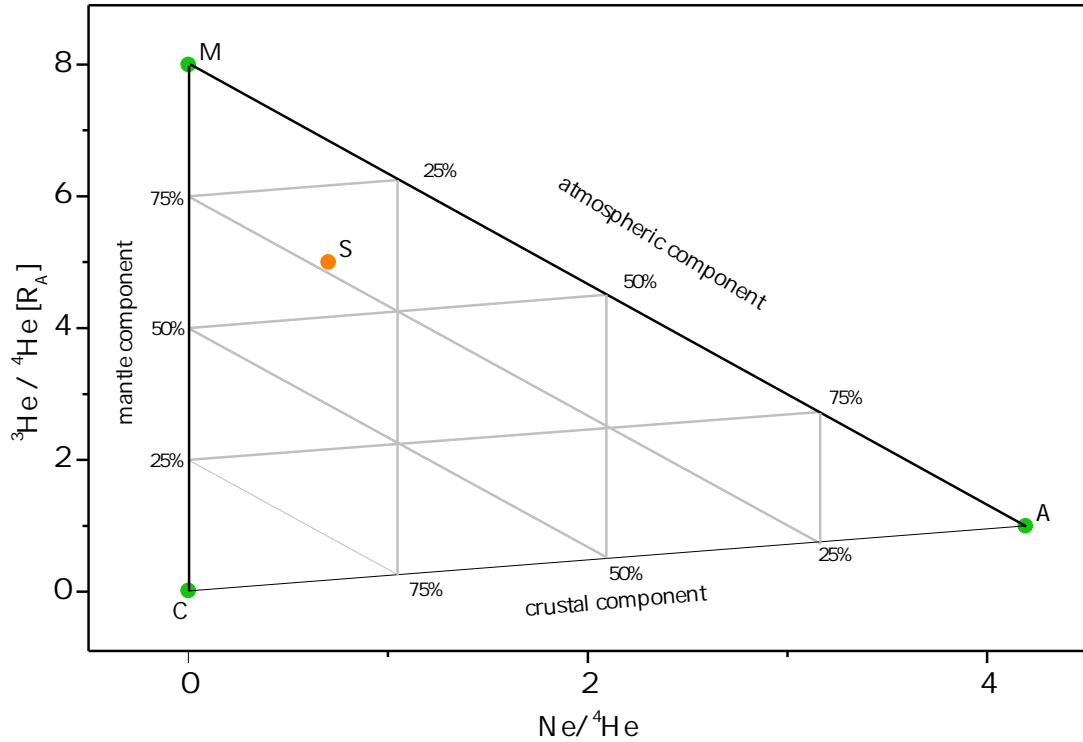
Figure 2.18: The three endmembers of the atmospheric (A), crustal (C) and mantle (M) component span a trilinear plot in the ^{3}He/^{4}He – Ne/^{4}He diagram. The relative contribution of the three reservoirs to the helium composition of a sample (S) can directly be read off from the scale at the sides of the triangle. The helium composition of the data point shown, for example, consists of roughly $X_A = 17\,\%$ atmospheric, $X_C = 23\,\%$ crustal and $X_M = 60\,\%$ mantle derived helium.

Using the ^{3}He/^{4}He ratios for the single components, R_C, R_M and R_A, equation 2.28 can be rewritten as:

$$R_S = \frac{^4\mathrm{He}_C R_C + {}^4\mathrm{He}_M R_M + {}^4\mathrm{He}_A R_A}{^4\mathrm{He}_S} = X_C R_C + X_M R_M + X_A R_A, \qquad (2.29)$$

with X_i being the relative share of $^4\mathrm{He}_i$ in the single fractions. Thus, $X_C + X_M + X_A = 1$, and the crustal share, X_C, can be expressed by the other ^{4}He fractions: $X_C = 1 - X_M - X_A$. Equation 2.29 is then:

$$R_S = (1 - X_M - X_A)R_C + X_M R_M + X_A R_A. \qquad (2.30)$$

Solving equation 2.30 for the mantle derived ^{4}He fraction X_M yields:

$$X_M = \frac{R_S - R_C - X_A(R_A - R_C)}{R_M - R_C}. \qquad (2.31)$$

The proportion of atmospheric ^{4}He, X_A, in the sample is obtained by inverse modeling using all other noble gases (see chapter 3.6.4).[5] Equation 2.31 can now be solved using $R_C = 2 \times 10^{-8}$, $R_M = 1 \times 10^{-5}$ and $R_A = 1.384 \times 10^{-6}$. In the limiting case of a negligibly small atmospheric component, i.e. $X_A \to 0$, equation 2.31 reduces to the one deduced by Aeschbach-Hertig [2005] for the case of a two-component mixing between mantle and crustal helium components.

X_M characterizes the relative fraction of mantle derived ^{4}He in the sampled water. The obtained X_A, therefore, is the fraction of atmospheric ^{4}He, and the fraction of crustal ^{4}He is $X_C = 1 - X_M - X_A$. Due to the huge difference of the helium isotope composition of the three reservoirs, the relative contributions regarding ^{3}He, Y_i, differ from the X_i significantly and are calculated by:

$$Y_i = \frac{^3\text{He}_i}{^3\text{He}_S} = \frac{^4\text{He}_i R_i}{^4\text{He}_S R_S} = X_i \cdot \frac{R_i}{R_S}. \tag{2.32}$$

---

[5]For a rough calculation, X_A can also be obtained as the relative Ne/^{4}He ratio of the sample compared to the atmospheric one: $X_A = (\text{Ne}/^4\text{He})_S / (\text{Ne}/^4\text{He})_A$. This estimation yields a correct result in case of both mixing components having the same amount of excess air. Even when the EA amount varies greatly, the deviation from the correct value of X_A lies within a few percent.

3 Methods

This chapter outlines the applied measurement systems. Some parameters were recorded in the field, but most tracers were analyzed in the laboratories in Heidelberg. For a more detailed description it is referred to the respective references in each section.

3.1 Multiparameter probe

Physical parameters are recorded with a WTW multi-parameter probe (WTW GmbH, Weilheim, Germany), equipped with sensors for temperature, electric conductivity, pH and dissolved oxygen. Temperature and electric conductivity are measured with a TetraConc©325 sensor. Its precision is 0.2 K for temperature and 1 µS/cm for signals below 2 mS/cm and 10 µS/cm above this value. While the temperature sensor needs no calibration, the conductivity sensor is calibrated once a day with a one-point calibration solution. pH is determined by a SenTex©41 sensor, which has an accuracy of 0.01. A two-point calibration is performed every day with solutions of pH-values of 4.01 and 7.00. A CellOx©325 clark cell sensor is used to determine dissolved oxygen with an accuracy of 0.01 mg/L. It is calibrated each day in a vessel that ensures atmospheric oxygen concentration in a water saturated humidity. The maximum working temperature of this sensor is 50 °C, thus, there are no data of dissolved oxygen in some thermal waters. As this sensor consumes O_2 it needs to be constantly fed with fresh water.

3.2 Water chemistry

Samples of the 2010 and 2012 field trips are analyzed for their ionic composition at the laboratories of the geological institute, Heidelberg University. The cations Al, Ca, Fe, K, Mg, Mn, Na and Sr are measured on a Varian Vista MPX (Agilent Technologies, California, USA), while the anions F, Cl, Br, NO_3, SO_4 are analyzed on a ICS 1100 (Dionex, Sunnyvale, California, USA) using a 25 µL loop, a separating column AS23, eluent solvent containing 4.5 mmol Na_2CO_3 and 0.8 mmol $NaHCO_3$.

Alkalinity, i. e. the sum of HCO_3^- and CO_3^{2-}, is measured in the field by titration using the test kit by Salifert (Duiven, The Netherlands). In the pH range of the sampled waters almost exclusively HCO_3^- is present (compare figure 2.8), so only this species is incorporated in the ion balance (see chapter 2.3.5). The alkalinity test is stated to have an accuracy of ± 0.07 meq/L,

the resolution is 0.1 meq/L. Above an alkalinity of 3.9 meq/L the result may deviate by approximately 0.1 meq/L. If the alkalinity exceeds 5.6 meq/L, the test was repeated with half the amount of water to extend the range of the test by a factor of two.

Nitrate content is also determined in the field by a titration kit by Salifert, but the resolution of the nitrate test is quite coarse. As nitrate was only tested for to get a rough idea if the water is of recent origin this test was sufficient.

3.3 Stable isotopes

Oxygen and hydrogen isotopy of samples from the 2009 and 2010 field trips are measured on a Finnigan MAT 252 mass spectrometer (Thermo Scientific, Waltham, Massachusetts, USA). Oxygen isotopy is determined by first equilibrating 5 ml of sample water with a CO_2 atmosphere and then measuring the CO_2 isotopy. Fractionation in the equilibrating process is taken into account [Neubert, 1998].

Hydrogen analysis requires only 2 μL of water, which is reduced to H_2 gas by a reaction with chromium at 850 °C [Keck, 2001] and then measured in the mass spectrometer. Since all water molecules are reduced no fractionation between D and H occurs [Florkowski, 1985].

The absolute precision of the hydrogen analysis is 0.26 ‰ [Keck, 2001] and 0.05 ‰ [Neubert, 1998] for the oxygen analysis.

Due to a break down of the stable isotope mass spectrometer at our institute the stable isotope samples from the 2012 campaign are analyzed on a Picarro L2120-i (Picarro, Sunnyvale, California, USA) in the labs of the Federal Institute for Geosciences and Natural Resources (BGR) in Hannover, Germany. Its precision is given by the manufacturer to be less than 0.1 ‰ for $\delta^{18}O$ and less than 0.5 ‰ for δ^2H.

3.4 Tritium

Tritium content is determined by low level counting at the IUP, as described in Grothe [1992]. 9 ml of sample water is heated at 600 °C with magnesium chippings to be reduced to H_2. This gas is measured for 48 h. The detection limit of the proportional counting chamber is 2 TU and the error is ±1 TU. This accuracy is too poor for good quantitative tritium results, but in the scope of this thesis tritium is only employed as a tracer for the presence of recent meteoric water at the sampled sites.

3.5 Carbon

Both carbon-13 and radiocarbon analysis require the isolation of DIC from the water sample. The carbon extraction line was built by Unkel [2006] and Kreuzer [2007] and is depicted in figure 3.1. Hydrochloric acid is used to bring the carbon into gas phase. No fractionation

AMS - ^{14}C water extraction device

Diagrammatic plan
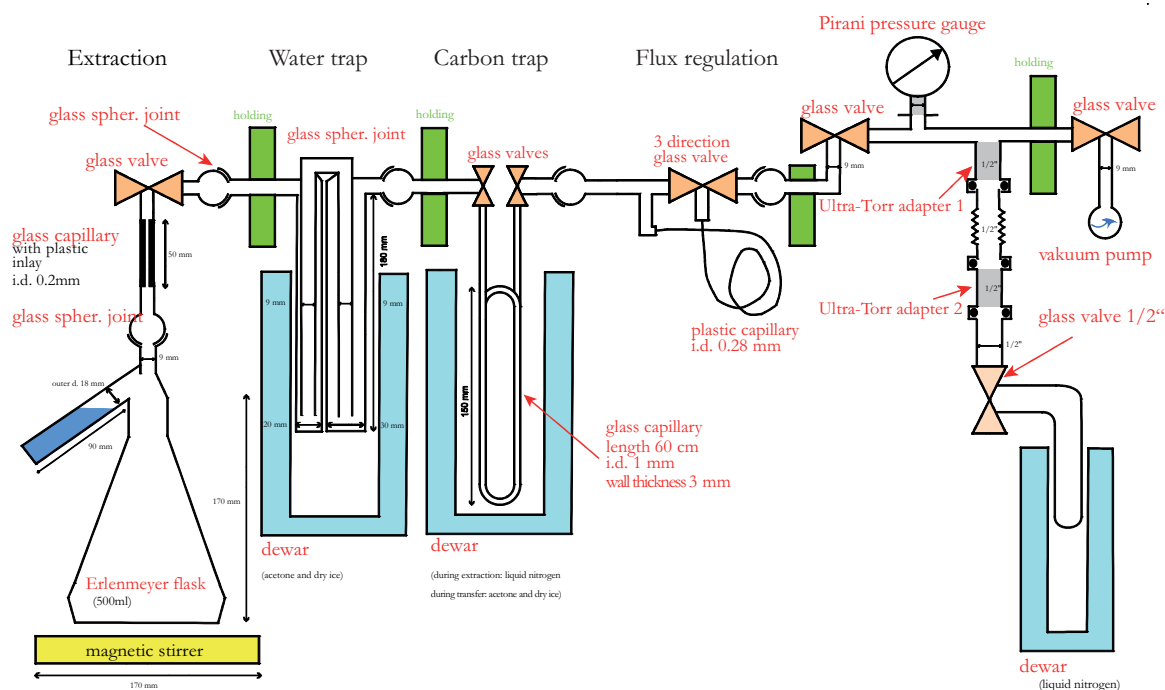
Figure 3.1: The carbon extraction line. The resulting CO_2 is measured for ^{13}C isotopy and radiocarbon (from Wieser [2011], who adapted it from Kreuzer [2007]).

is expected since all DIC should convert into CO_2. In contrast to Kreuzer [2007] no iodine needs to be added to the sample water, because the sample is treated with silver nitrate instead of sodium acide. The extraction process is well summarized by Wieser [2011].

For the isotopic analysis of ^{13}C the extracted CO_2 is measured in the same MAT 252 as the stable isotopes of water. Despite its break down it was still possible to analyze the 2012 campaign ^{13}C isotopy with this mass spectrometer. The analytical error for δ^{13}C measurement is ± 0.03 ‰.

Since ^{14}C is very rare and has the same mass as ^{14}N and ^{12}CH$_2$ it cannot be measured in a normal mass spectrometer. However, an accelerated mass spectrometer (AMS) as described by Wölfli *et al.* [1983] is capable of separating ^{14}C from the other species. DIC needs to be carbonized to be present in solid state for the AMS measurement. The catalytic reduction of CO_2 with H_2 at $575\,°C$ leads to pure carbon and water: $CO_2 + 2H_2 \longrightarrow C + 2H_2O$.

In an AMS the solid carbon is ionized by a sputter ion source and a pre-selection of masses takes place in a normal mass spectrometer. The ions with mass 14 are then accelerated in a tandem accelerator and the electrons are then stripped off in a capillary filled with N_2 gas. In a second mass spectrometer the ion beam is cleaned from fragments of other molecules before the carbon ions are detected [Wölfli *et al.*, 1983; Wölfli, 1987].

3.6 Noble gases

3.6.1 Mass spectrometer

Noble gas samples are analyzed on a MM 5400 mass spectrometer from GV Instruments (Manchester, UK, today Thermo Fisher, Waltham, Massachusetts) at the IUP, which is optimized for measuring noble gases in static mode. This sector field spectrometer is described in detail by Friedrich [2007].

Samples are processed in several stages. First the sample water is degassed and dried from water vapor in a trap filled with zeolith granules with 3 Å pore diameter. Argon, krypton and xenon as well as the permanent gases are frozen to a stainless steel trap (SST) at 25 K (compare Lott [2001]), while helium and neon are adsorbed on an activated charcoal trap (ACT) at 10 K.

Because the noble gases are analyzed one after another they are separated from each other by exploiting their different freezing points. First, He is released by heating the ACT to 42 K. Because He concentrations in samples can differ by several orders of magnitude, the gas amount is checked in a quadrupole mass spectrometer and diluted until a concentration is reached which the detectors of the MM 5400 can handle. While measuring He, Ne is released at 140 K and experiences the same procedure. In the meanwhile the Kr and Xe from the SST are being separated from Ar and the permanent gases. They are measured in the order Xe, Kr, and Ar last. Before each single analysis the detectors are tested for short-time sensitivity fluctuations by measuring a small gas amount from a (almost) pure gas reservoir. These so-called fastcals are analysized in exactly the same way as the samples.

The initial extraction and preparation procedure is explained in detail by Friedrich [2007], further improvements are given by Wieser [2011]. In the following I will describe only the progress in the preparation and analysis procedures compared to Wieser [2011].

Samples up to run 62 (see appendix A.6 for an overview of all measurement runs) are analyzed with the "interim procedure" described in Wieser [2011]. However, as a minor change in run 60 to reduce to measurement time span the amount of measuring points of Xe is reduced to 15, each lasting 23 s (before it was 21 times 23 s) and of Kr from 27 times 2 s to 22 times 2 s. At the same time the ^{4}He analysis is slightly modified: Hitherto one data point for ^{4}He was recorded, then the ^{3}He measurement was done and last another seven points of ^{4}He were recorded. Due to the good reproducibility of ^{4}He the first ^{4}He data point is now omitted.

In run 62 the Kr analysis procedure is optimized again to consists of 15 data points of 15 s each. This prolongs the duration but reduces to measurement error significantly from around 1.9 % in run 60 to 1.3 % in run 62. Also the He procedure is optimized for ^{3}He analysis to obtain better ^{3}He-^{3}H dating and ^{3}He/^{4}He ratios. While both He isotopes were analyzed at the same time before, from now on ^{3}He is analyzed first and a small gas portion is retained in a volume close to the inlet of the mass spectrometer and analyzed in a second inlet step for ^{4}He. This eliminates the possibility to obtain ^{3}He/^{4}He ratios from the mass spec data

directly but facilitates to analyze bigger ^{3}He amounts since the He splitting threshold can be increased. This results in a slightly better ^{3}He resolution especially for samples which contain a lot ^{4}He and need to be split up.

The method described by [Stanley *et al.*, 2009] which prevents the trapping of He and Ne in the matrix of frozen gases on the SST is introduced in run 65. As in the previous routine all degassed gases are transmitted to the SST for 20 min. Before opening the ACT the SST is closed completely and heated to 60 K and then re-cooled to 25 K. After this step the ACT is opened for 20 min to separate He and Ne from the heavy noble gases.

The Stanley procedure is modified in run 71 by opening the ACT for 5 min after the 20 min freezing to the SST. Then the SST is closed and heated as described above. This modification aims at hindering He and Ne to be trapped in the matrix of frozen gases in the re-cooling SST again by transporting most of the light gases into the ACT beforehand.

3.6.2 Data evaluation

The noble gas data evaluation aims at calculating the individual noble gas amounts of a sample from the measured signals (a voltage in case of the faraday cup detector and counts per second in case of the electron multiplier detector). This is done by comparing the measured signal of the sample with the signal of a known calibration gas standard. Due to a gas amount dependent signal strength of the detectors a nonlinearity correction has to be done. Therefore, calibration gas amounts of different sizes, usually between 0.2 and 5 cm^3, are measured to cover the gas amount range of all noble gases in the analyzed samples[1]. To account for short time detector sensitivity fluctuations a so-called fastcal measurement is performed directly before each single measurement to test the detector as well as prepare it for the coming measurement. The detected signal of a sample or a calibration is considered in relation of these fastcals signals. Sample and calibration signals are corrected for background signal which is derived from blank analyses. An in-depth description of the measurement and analysis process is found in [Friedrich, 2007].

The software Wucem, written by Michael Jung from our group, simplifies the data evaluation in comparison to the formerly used Wincalc and Calc5400[2]. In the first window of the program the raw data from the spectrometer is checked and outliers are deleted. In case of the ^{3}He, Kr and to a minor extent also the Xe multiplier measurement occasionally show a sensitivity adjustment in the first few data points, before a linear decay is visible (compare figure 3.2). This usually happens at high count rates. These first points are deleted as well. A little instability of the faraday detector is observed frequently in the neon and ^{4}He measurements for which no explanation is found so far (see figure 3.3).

For each single fastcal and sample/calibration measurement a linear fit is set to the data points to extract the signal at the time of the gas inlet, i. e. at $T = 0$ s. Wucem is also capable

---

[1]The gas pressure in the calibration gas vessel is about 1 atm in the beginning, as it is filled with atmospheric air at the air pressure present in the moment of filling. Each gas amount taken from this reservoir is regarded by the measurement software Prepline5400; therefore the gas pressure in the vessel is known at every time. From time to time the vessel has to be refilled.

[2]Wucem is an acronym for the German phrase *Wincalc- und Calc5400-Ersatz von Michael*.
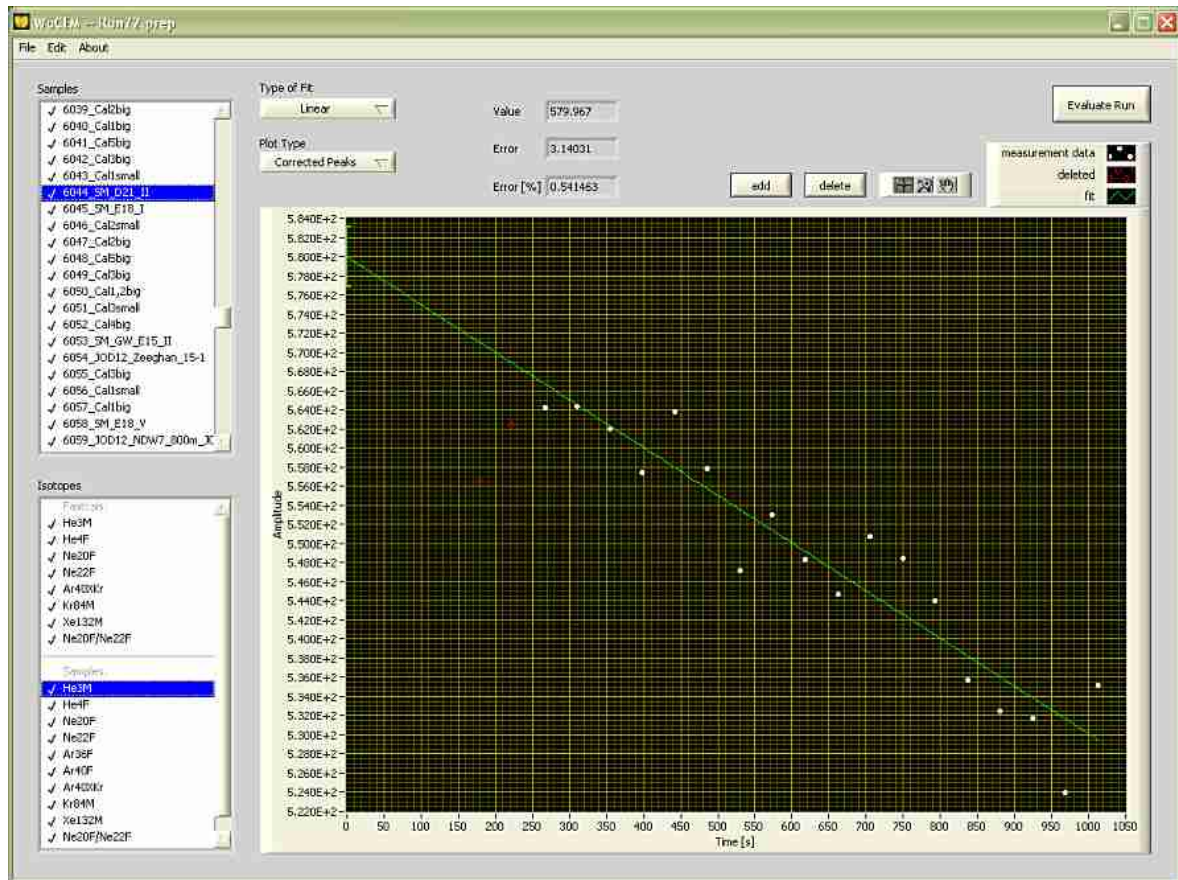
Figure 3.2: Especially at higher count rates the multiplier detector needs some time to adapt to it. The first signal points are hence systematically too low and are deleted (red circles on the left side).

of calculating isotope ratios from the raw data. Several routines are implemented in WUCEM, two of them are applied to the Jordan samples: "next neighbors" interpolates a value between two data points of isotope 1 and determines the ratio to the data point, measured in between, of isotope 2 at the same position, and vice versa (used for the calculation of the ^{20}Ne/^{22}Ne ratio). "mean of isotope 1" relates all data points of isotope two to a linear fit through the isotope 1 data points. This routine is applied when the data points are not recorded in an alternating way, but with a pattern like first some data points of isotope 1, then some points of isotope 2, again some point of isotope 1 and so on. This is the case of the ^{3}He/^{4}He ratio (up to run 60) and the ^{40}Ar/^{36}Ar. Finally one gets a ratio distribution for each isotope ratio, which is fitted by a constant fit (despite Ne ratios show a trend sometimes).

Usually each measurement is corrected with its own fastcal. If for any reasons the fastcal measurement has not worked, WUCEM offers several methods to handle this issue. In another window all fastcals are plotted against time and are fitted with different polynomials. For a specific measurement the fastcal correction can be changed. However, in the scope of this work all measured fastcals are suitable.
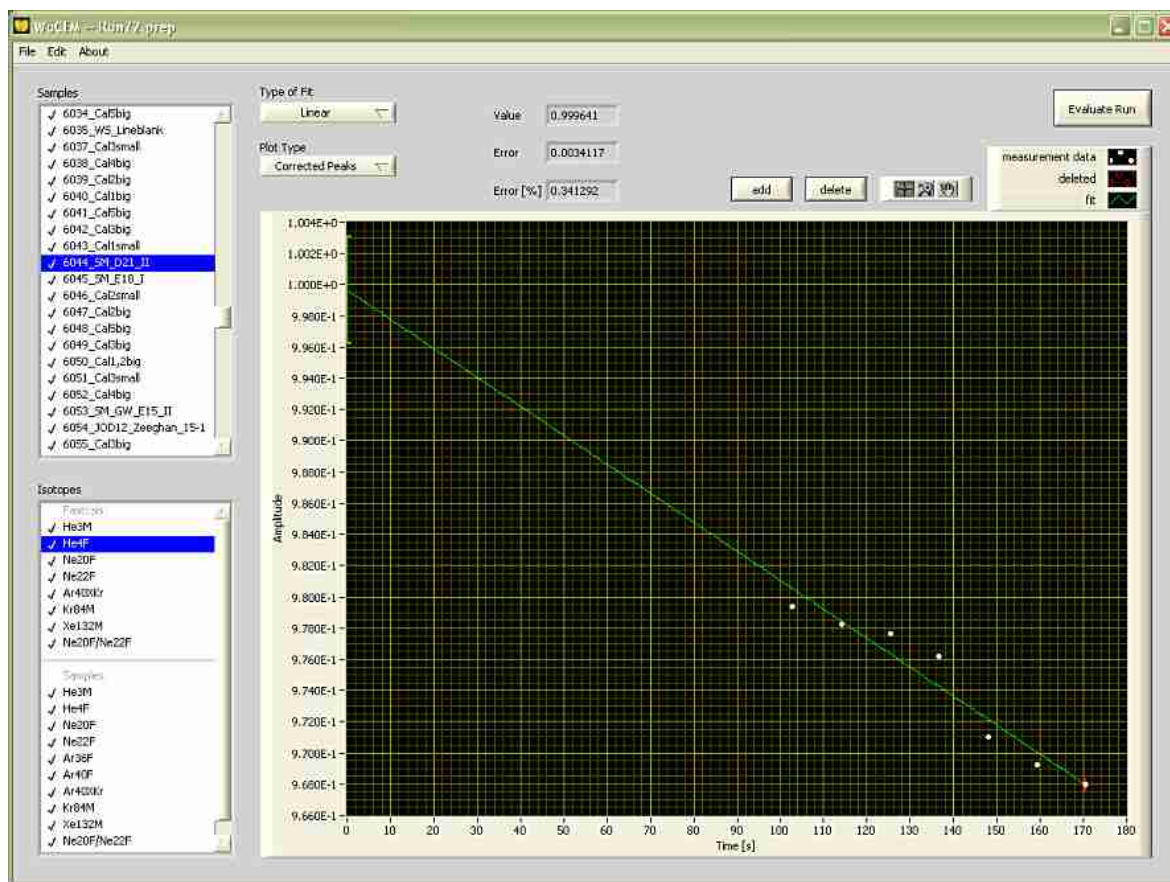
Figure 3.3: Occationally the faraday cup detector shows some instabilities, which often express in two branches. In case of the neon measurements these instabilities can usually be observed in both isotopes. This can sometimes help to decide which branch is more likely to be the correct one. If this does not work all data points are considered for the fit.

Since there is no fastcal for argon, artificial fastcal are assembled in a way that the temporal trend in the argon calibrations (due to the dilution of the calibration gas reservoir) is balanced out. In most measurement runs a correction with a linear trned of the artificial fastcals is sufficient. Only Run 65 needed a second order function fitted through the artificial fastcals to correct for the reservoir dilution effect.

In the next WUCEM window the blanks are plotted. Outstanding high blank values can usually be attributed to leakage and are excluded from the further analysis. The average of all remaining blank measurements (i. e. a constant fit) is taken for the background correction.

The last step of the WUCEM analysis is to calculate the gas amounts in a sample by comparing the measured signals to signals of aliquots of the known standard gas. The samples (vertical blue lines in figure 3.4) spread over the calibrations' distribution and the amount of the respective isotope is calculated by comparing the fastcal corrected signal with a polynomial fit function laid through the calibrations.
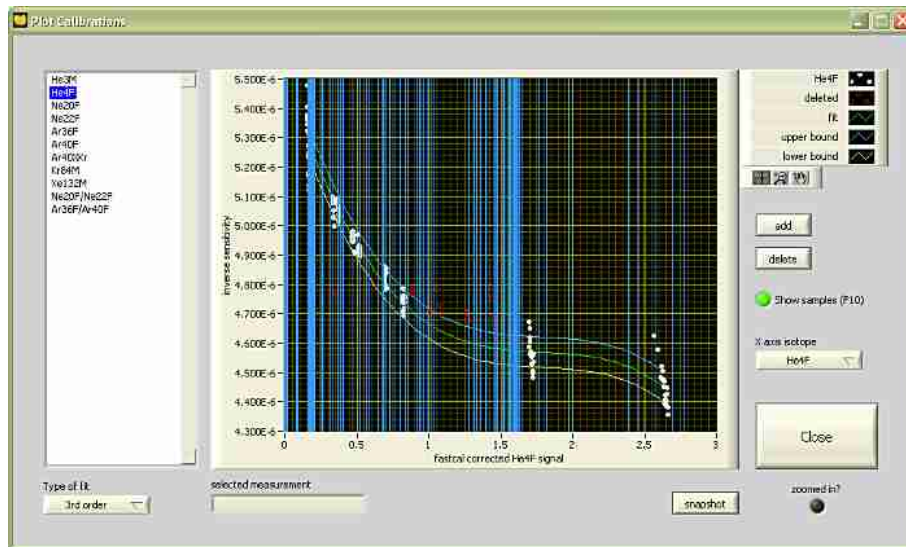
Figure 3.4: The non-linearity of the detectors is taken into account by calibrating the samples' gas amounts with different aliquot sizes of the calibration standard gas. The inverse sensitivity (details behind this concept is found in Friedrich [2007]) of the calibration measurements is plotted against the fastcal corrected signal. Samples are drawn in vertical blue lines. Samples gas signals are compared to interpolated values of the polynomial calibration fit to calculate the samples gas amounts.

In case of samples with extreme ^{3}He/^{4}He ratios some ^{3}He samples lie far beyond the calibration spectrum. An evaluation with a polynomial fit as all the other samples would in general result in unrealistic gas amounts and high uncertainties due to the extreme behavior of the fit function outside its fitting range. The best way to cope with this issue is to take the two biggest calibrations and fit them constant or linear, as exemplified in figure 3.5.

In cases of isotopes where the samples do not cover the whole range of calibrations usually only the relevant calibrations are considered in the evaluation. This is especially the case for krypton and xenon where an unexplainable nonlinearity between 1big and 2big calibrations is observed. Since all samples are located in the range of calibrations bigger than 1big, only these are taken as a basis (figure 3.6).

A bit more complicated is the case of ^{40}Ar. Calibrations of the small pipette resemble another branch as the calibrations of the big pipette (figure 3.7). In some cases both branches could be chosen. The only criteria which helps to decide is the fact that AEWs agree much better with theoretical value when only the calibrations of the big pipette are considered. Unfortunately one has to extrapolate a little bit to evaluate all argon ^{40}Ar measurements with the big pipette calibrations.

The final output format gives the total noble gas amount of the samples in ccSTP. In order to get the concentration one has to divide it by the weight of the sampled water to get the results in a comparable unit of ccSTP/g water.
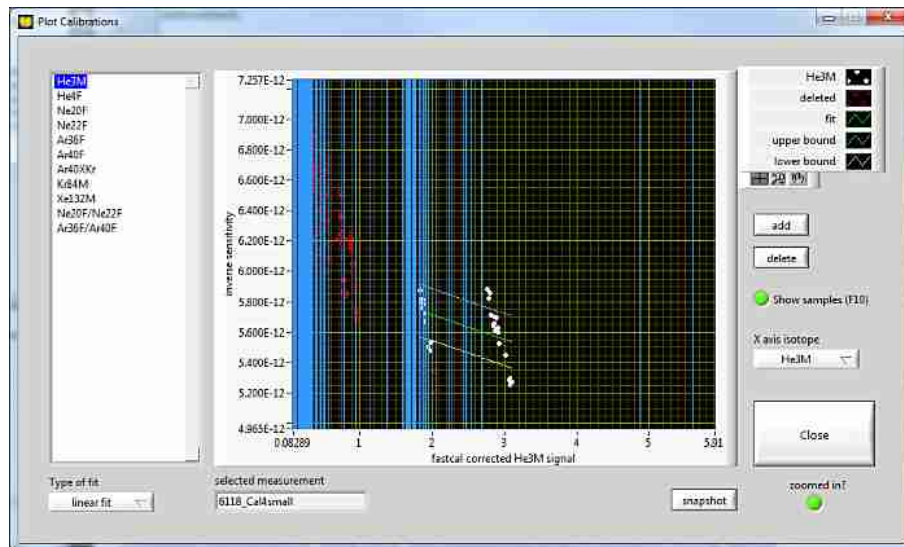
Figure 3.5: In cases of ^{3}He concentration falling outside the range covered by the different calibration sizes, a constant or linear fit is applied using the biggest cals.
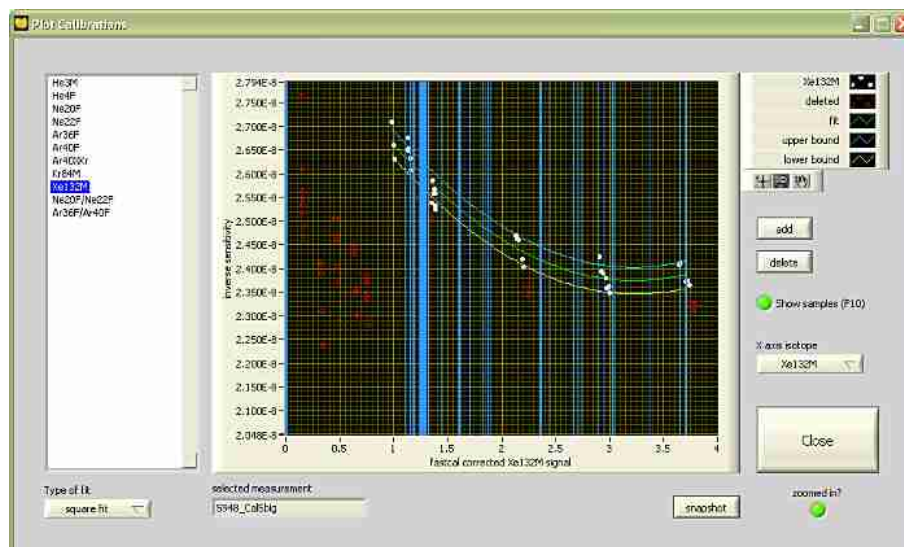
Figure 3.6: Xenon exhibits a strongly nonlinear behavior. As all samples, except strongly degassed ones, match calibrations bigger than 1big, only those calibrations are considered in the evaluation of xenon.
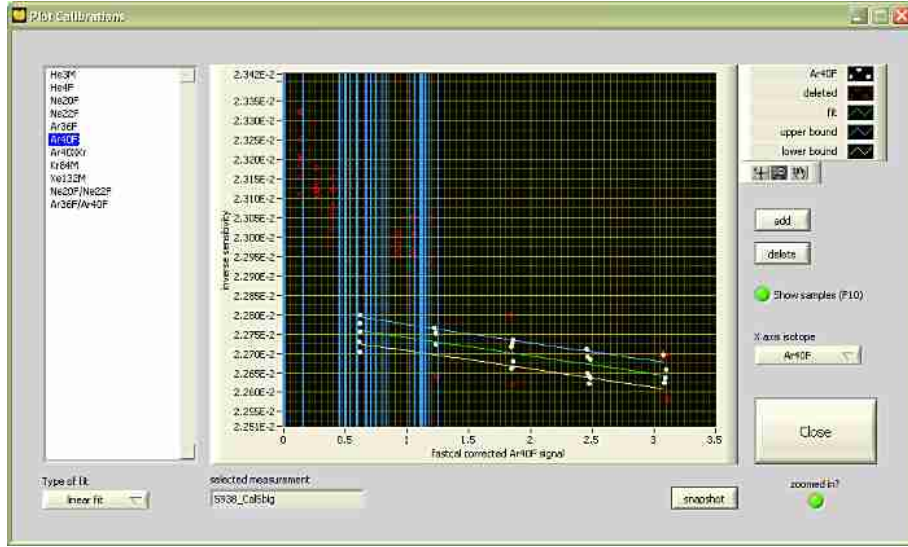
Figure 3.7: Ar calibrations of small and big pipettes form two different branches. Because Ar concentration of AEWs agree much better with theoretical values when evaluated with the lower branch (i. e. the calibrations from big pipettes) this one is chosen for the interpretation of all samples.

3.6.3 Evaluation of diffusion samplers

While the WUCEM output for water samples directly gives the gas concentration in ccSTP/g water, the gas content of diffusion samplers is only an image of the concentration in water and, thus, needs to be converted [Wieser, 2006]. Starting from the noble gas amount in ccSTP, v^i, the molar amount n^i of the noble gas i is calculated:

$$n^i = \frac{v^i}{V_{mol}},\tag{3.1}$$

with $V_{mol} = 22\,414\,\text{cm}^3$ being the molar Volume. By use of the ideal gas law the molar amount is converted into the partial pressure p^i as it prevailed in the sampler at time of sampling:

$$p^i = n^i \cdot \frac{R \cdot T}{V_S}.\tag{3.2}$$

The volume of the sampler, V_S, is calculated from its length l: $V_S = 0.13583 \cdot l - 0.12284$ [Wieser, 2006]. $R = 83.1446$ is the universal gas constant in units of $\text{cm}^3\,\text{atm}\,\text{mol}^{-1}\,\text{K}^{-1}$. T denotes the ambient temperature during equilibration of the diffusion sampler. As this quantity was not accessible at the sampling spots, a temperature of $20\,^\circ\text{C}$ is assumed for the shallow wells in Azraq ($\approx$ the average annual temperature). In the deep boreholes a common geothermal gradient of $3\,\text{K}$ per $100\,\text{m}$ is assumed.

According to the solubility equations of Weiss [1970, 1971], Weiss and Kyser [1978] and Clever [1979b] the noble gas concentrations in ccSTP/cm^3 of the water surrounding the diffusion samplers is calculated by

$$C^i_{\frac{ccSTP}{cm^3}} = \beta^i(T,S) \cdot p^i.\tag{3.3}$$

The solubility of gas i is represented by the Bunsen coefficient $\beta^i(T,S)$, which is dependent on temperature T and salinity S and is calculated with equations A.1 and A.2 in the above mentioned publications.

The final step to compare noble gas concentrations from diffusion samplers with normal water samples is to convert the concentrations in ccSTP/cm^3 into ccSTP/g water using the density correlation found by Gill [1982]:

$$C^i_{\frac{ccSTP}{g}} = C^i_{\frac{ccSTP}{cm^3}} \cdot \frac{1000\,\text{cm}^3\,\text{L}^{-1}}{\rho(T,S)}, \tag{3.4}$$

with $\rho(T,S)$ being the density of water in dependence of temperature, T, and salinity, S.

3.6.4 Fitting noble gas temperatures

In order to compute noble gas temperatures (NGTs), first the total amount of each noble gas has to be calculated. Total Ne is received by dividing the sum of the concentrations of ^{20}Ne and ^{22}Ne by a factor of 0.9973, which corresponds their molar abundance. Total atmospheric Ar is usually calculated in the same way by taking the sum of ^{36}Ar and ^{40}Ar, divided by the factor 0.999364. Only in cases of very old water, i. e. when the ratio ^{40}Ar/^{36}Ar deviates from 295.5, atmospheric Ar is calculated from ^{36}Ar only, using a factor of 0.003364. The latter case is applied when the ^{40}Ar/^{36}Ar ratio of a sample is higher than 302. Total Kr results from ^{84}Kr by division with 0.57 and total Xe from ^{132}Xe using a factor of 0.2689. Helium is omitted in the NGT analysis due to its non-atmospheric component.

Noble gas temperature (NGT) fitting is performed by inverse modeling [Ballentine and Hall, 1999; Aeschbach-Hertig *et al.*, 1999], using a weighted least-square routine, with the software PANGA written by Michael Jung (a short description is given in Jung [2013], the corresponding paper is in preparation). The fitting routine uses a Levenberg-Marquardt least square algorithm [Levenberg, 1944; Marquardt, 1963] to inverse fit model parameters of several excess air models to measured data. The tool is also capable of performing Monte Carlo calculations. In cases of difficulties to fit the excess air model parameters to the measured noble gas concentrations the Monte Carlo method offers the chance to achieve better fit results as well as enables one to trace the reason of fitting problems [Jung *et al.*, 2013]. The basis of the Monte Carlo algorithm is to vary measured noble gas concentrations randomly within their error margins and perform a fit with each concentration combination. In many cases this helps to find "reasonable" fitting results (i. e. concentration combinations) and evaluate a sample which does not deliver a sound combination of the fitting parameters temperature T, excess air A and other parameters of the respective excess air model in the normal fitting routine. Since inverse fitting especially of the CE model bears some risk of unreasonable convergence, the Monte Carlo routine can be of great benefit for the analysis of groundwater samples.

The goodness of fit is described by its χ^2 value, which is defined as the sum over all input parameter i (i. e. the noble gas concentrations, usually neon, argon, krypton and xenon) of the
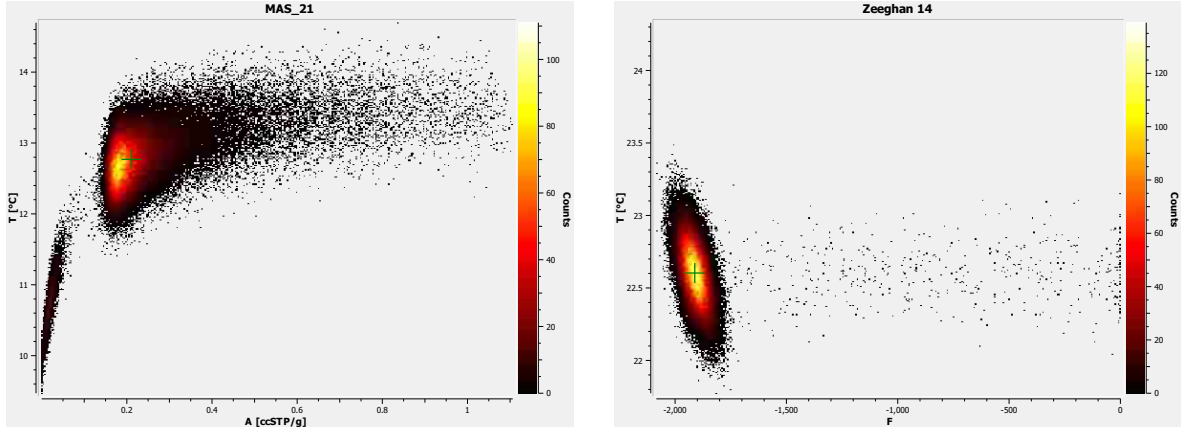
Figure 3.8: Examples of the limiting cases of the CE model described in the text. The left graph shows a MC analysis, where one part of the simulations resulted in low *A* and a lower NGT, and a second fraction with higher temperature, but unrealistically high excess air values. The latter block is therefore rejected in a MC analysis. The example on the right exhibits a small fraction of simulations with *F* values close to zero, and another one around $F = -2000$. The latter belong to MC simulations where $F \cdot A$ becomes neglectible small and is considered a quasi-UA case. However, the resulting noble gas temperatures are almost the same.

squared, error weighted deviations of the modeled to the measured noble gas concentrations C_i,

$$\chi^2 = \sum_i \left(\frac{C_i^{\text{mod}} - C_i^{\text{meas}}}{\sigma_i} \right)^2 \tag{3.5}$$

where σ_i is the standard deviation of the measured noble gas concentration. In case of a Gaussian error distribution and if the free model parameter (T, A and F in case of the CE model) are independent, the estimated value of χ^2 is the same as the degrees of freedom [Aeschbach-Hertig *et al.*, 1999], i. e. equals one in case of the CE model (four input noble gas concentrations and three model parameters). χ^2 values higher than the degrees of freedom are indicative of collinearities between the model parameters, which worsen the goodness of fit [Oehsen von, 2008]. Very low χ^2 may be a result of overestimation or correlation of experimental errors or of overparametrisation in the context of the small number of degrees of freedom of these calculations [Aeschbach-Hertig *et al.*, 1999].

As Jung *et al.* [2013] found, the Monte Carlo simulations of the CE model sometimes exhibits two mathematically possible solution: Reasonable parameter combination with $A < 0.1$ and a solution for higher *A*, accompanied by higher noble gas temperatures (compare the left diagram in figure 3.8). The latter, unrealistic solution is attributed to the limiting case of large *A*, where the CE model transforms into a pure OD model (i. e. only an excess in pressure, but no excess air). Monte Carlo simulations of this kind are discarded in the analysis of the respective samples.

Another limiting case of the CE model parametrization revealed by Monte Carlo calculations appears for extremely small values of *A*, accompanied by large values of *F* (with positive or

negative sign). When the product of *A* and *F* becomes very small, the CE model transforms into a quasi-UA model:

$$\lim_{FA \to 0} \left[C_i^{eq} \left(1 + \frac{(1-F)AH_i}{1 + FAH_i} \right) \right] = \lim_{FA \to 0} \left[C_i^{eq} \left(1 + \frac{AH_i - FAH_i}{1 + FAH_i} \right) \right] = C_i^{eq}(1 + AH_i). \quad (3.6)$$

Despite the fact that *F* gains unphysical values, in combination with the tiny *A* values the Monte Carlo results in such cases yield reasonable solutions for the temperature *T* and can therefore be trusted. An example is shown in the right panel of figure 3.8. A paper about this phenomenon is in preparation by M. Jung.

3.7 Radon

Radon samples were measured in the evening or the next morning after a sampling day. The used RAD7 (Durridge, Billerica, Massachusetts, USA) radon detector is only capable of detecting alpha decays in a gas phase. Therefore, the water sample has to be degassed using a glass frit (compare figure 3.9). The gas phase is dried by a Drierite cartridge (W. A. Hammond DRIERITE Co. LTD, Xenia, Ohio, USA) below 10 % relative humidity, the working range of the RAD7. A detailed description of the RAD7 device is found in Durridge [2000], the extraction setup RAD-H$_2$O is treated in Durridge [2001], Kluge *et al.* [2007] and Reichel [2009].

Instead of counting the radon-222 decays directly the RAD7 alpha spectrometer detects the disintegration of its daughter nucleus polonium-218. In a closed system the activities of radon-222 and polonium-218 are in secular equilibrium after about 20 minutes. Thus, before each run a 20 min equilibration cycle is performed. To account for background radiation a measurement with an empty sample bottle is done. Due to limited time in the evenings often the background determination of the first and sometimes more analyses was omitted. In case of the first samples of a day the background is defined as the average background signal of all other background measurements that are recorded before the first sample analysis of the respective day. As the background error the maximum of these background measurements is assumed. The same background values are assumed for samples which are measured after a low-signal analysis (Zarqa Ma'in 1 and 2 and Wadi Ibn Hammat 2). In case of the AWSA 16 and the Zeeghan 15-1 sample the preceding Radon signal is significantly higher and, thus, the average of the background signals of Wadi Ibn Hammat 1 and Manshiyeh 1 is assumed as they are measured after samples of comparable background signal. The resulting error is about twice as high as for the first-of-the-day samples but still ≈ 0 within the error margins.

When the water temperature is higher than the surrounding temperature, small air bubbles form inside the radon sampling bottles due to contraction of the water with lower temperatures. This causes a little loss of radon when the bottle is connected to the RAD7 instrument.
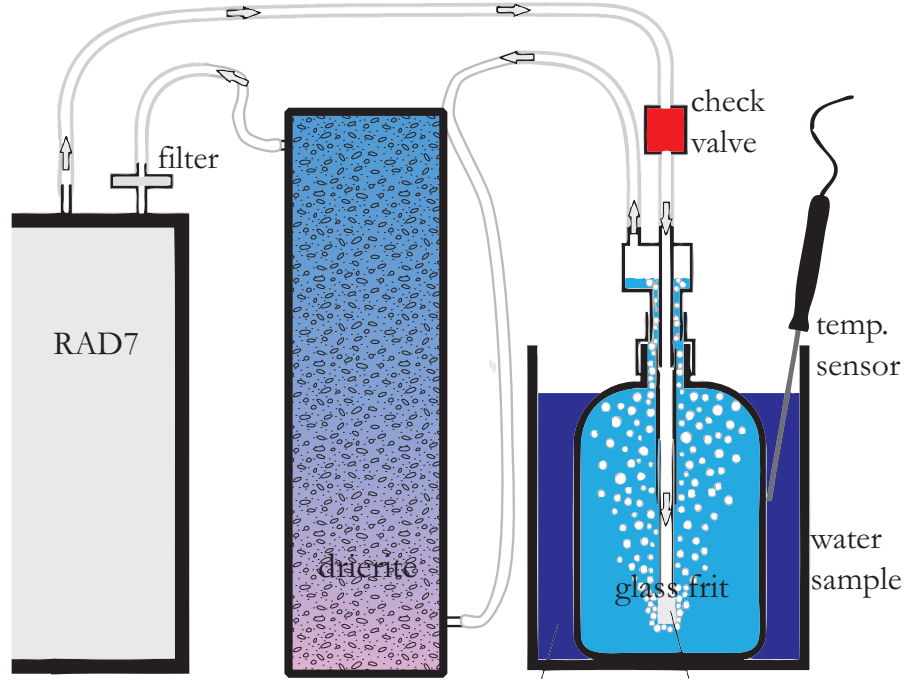
Figure 3.9: Setup of radon analysis with the RAD7 radon alpha detector. From Wieser [2011].

The background corrected activity in the gas phase, A_{gas}, is converted into the activity in the water sample at the time of analysis, A_{water}, by

$$A_{water} = A_{gas} \cdot \left(\frac{V_{gas}}{V_{water}} + a(T) \right) \cdot K_S, \tag{3.7}$$

with V_{water} being the water sample volume ((242.44 ± 0.06) mL due to displacement of some water by the glass frit), V_{gas} the volume of the gas circuit (1720.0 ± 5.5) mL and $a(T)$ the Ostwald solubility $a(T) = 0.105 + 0.405 \cdot \exp(-0.0502 \cdot T)$ [Weigel, 1978], and K_S the relative solubility correction due to salinity according to Clever [1979b], compare appendix A.1. Except of the Zeeghan samples, where the salinity correction is around 7 %, the salt influence is negligible small.

The water temperature of the sample during measurement, T, has not been recorded and is considered to be (15 ± 5) °C. This temperature range implies all possible ambient temperatures and, thus, sample temperatures at the time of analysis. The influence of the sample temperature at the time of analysis is less than 1 % for the assumed error of ± 5 °C and hence much smaller than the statistical error of the measurement. To get the radon activity at the time of sampling, the calculated activity is finally corrected by the radioactive decay law.

4 Geographical and geological setting

4.1 Jordan and its water situation

Jordan, officially the Hashemite Kingdom of Jordan, is situated in the north-western part of the Arabian peninsula. It is bordered by Israel and the Westbank in the west, Syria in the north, Iraq in the east and Saudi Arabia in the south and southeast. Jordan can be divided from west to east into three major landscapes: The Jordan Rift Valley, the Jordan Highlands and the eastern deserts [Margane *et al.*, 2002].

The *Jordan Rift Valley* stretches from the depression of Lake Tiberias (Sea of Galilee) in the north to the Gulf of Aqaba in the south. The deepest point of the rift valley is occupied by the Dead Sea, its coast forming the deepest surface area of the world, currently about 423 m below sea level. The part between Lake Tiberias and the Dead Sea is called the Jordan Valley, the most fertile and, hence, most heavily tilled stripe of land in Jordan. South of the Dead Sea the rift valley continues under the name Wadi Arava.

Along the rift valley's eastern side a mountain range ascends, the *Jordan Highlands*. They elevate up to 1600 m and consist of several plateaus, separated by deeply cut wadis (valleys that often carry water only seasonal).

Beyond the mountain range the landscape dips gently towards the east and forms the *eastern desert*. Different outcropping lithology forms varying stone desert types, only in the very south some sand dunes are found. Large parts in the north are covered by a thick basalt shield called Harrat ash-Shaam originating from the extinct volcano Jabal ad-Druze in Syria. Just bordering the basalt desert, about 100 km east of the capital, the former oasis al-Azraq forms the center of the Azraq-Wadi Sirhan depression, which stretches in southeastern direction into Saudi Arabia. The picturesque landscape of the mountains of Tubeiq and Wadi Ram with its bizarre sandstone formations on top of the granite bedrock reaching up to 600 m above the surrounding plain forms the border region to Saudi Arabia.

Jordan has three perennial rivers. The Jordan River flows from Lake Tiberias into the Dead Sea, forming the border between Jordan and Israel, respectively the West Bank. The Yarmouk River originates from Jabal ad-Druze in Syria and is the border between Syria and Jordan downstream. The Yarmouk is the main tributary to the Jordan River. The Zarqa River emanates northeast of Amman and feeds the Jordan River as well. Some small streams in side wadis of the Jordan Valley are fed by perennial springs, but they do not contribute significantly to the Jordan water budget. A lot more rivers and streams exist throughout the country, but they are active only during the rainy winter season.
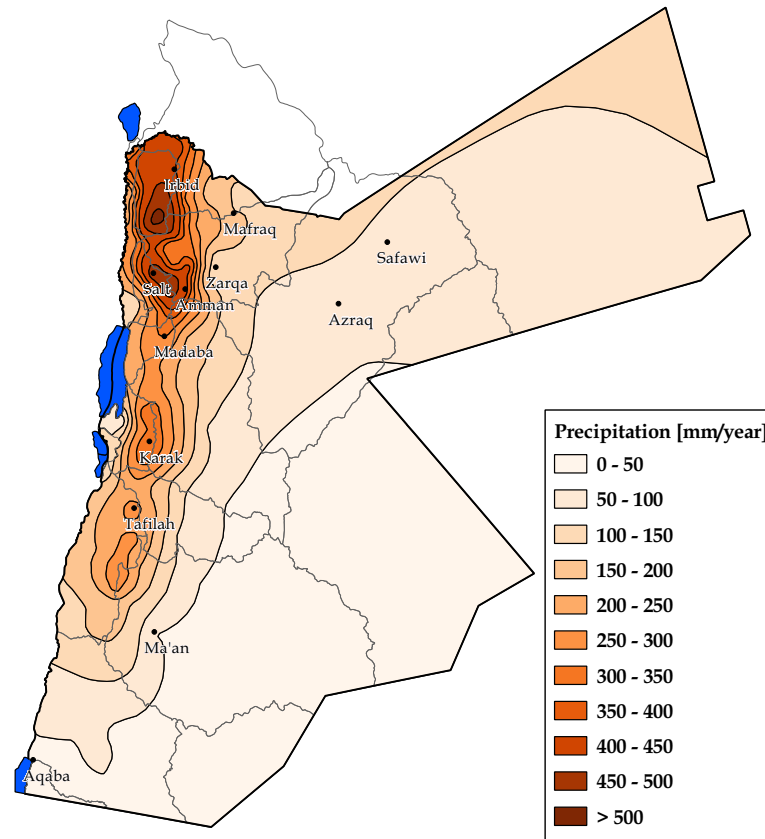
Figure 4.1: Precipitation distribution in Jordan. While the highlands receive considerable rain amounts, most of the country is semi-arid to arid. Also the surface water basins are shown in this map. All data from WAJ [2010], precipitation pattern map created by Thomas Bonn [2013].

The climate in Jordan is coined by Mediterranean influence and is characterized by hot, dry summers and cool winters. Temperatures in the highland occasionally fall below the freezing point. Practically all precipitation happens in winter. In figure 4.1 the precipitation distribution in Jordan is shown. By far the most rain falls in the highlands, reaching more than 500 mm per year in the North, around Ajloun, and decreases to about 300 mm per year on the Karak plateau, southeast of the Dead Sea. Rainfall diminishes fast towards the east, with large parts of the country receiving less than 100 mm a year, rendering two thirds of the country to be semi-arid to arid. The aridity is also reflected by high evaporation: About 92 % of the total rainfall of 8215 MCM (Million cubic meters) evaporates, only 5 % recharges the groundwater reserves [MWI, 2009b].

Jordan is considered as one of the most water scarce countries in the world. The annual per capita water availability in 2007 was only 145 m^3/year [MWI, 2009c], far below the 500 m^3/year limit for absolute water scarcity according to the Falkenmark water stress in-

dex [Falkenmark *et al.*, 1989]. The development of new water resources lags behind the massive population growth of about of about 2.5 % per year. This high growth rate is owed to the reduced mortality rate and the large influx of refugees from Palestine in the 1960s and 70s, from Iraq in the last decade and today from people fleeing the civil war in Syria.

Agriculture in Jordan depends on irrigation in most parts of the country, only in the Highlands between Karak and Irbid rainfed farming is possible. In the Jordan Valley the water of the Jordan and Yarmouk rivers is used for irrigation. The heavy utilization of the Jordan River water by Israel and Jordan is the cause of the steady shrinkage of the Dead Sea. Its surface level drops by about 1 m each year [IOLR, 2013]. Yet, the amount of surface water does not satisfy the high agricultural demand in the Jordan Valley, and groundwater is used for irrigation purposes as well. In the desert areas, especially in Azraq and in south Jordan, agriculture depends totally on irrigation with groundwater.

To provide enough drinking water to the capital, groundwater is abstracted all around the country and pumped to Amman. Several well fields and pumping stations cluster around the city, and a big part of the Amman drinking water originates from the AWSA well field in Azraq.

An estimated nation-wide annual deficit of 104 MCM in the groundwater budget is the consequence [MWI, 2009b], but large uncertainties come from the fact that many private wells are run illegally [Chebaane *et al.*, 2004; Daoud *et al.*, 2006]. This deficit results in a depletion of the Jordanian groundwater reserves. The water table of the most employed aquifer, the B2/A7 limestone aquifer, drops between one and two meters annually, and the water table of the B4 aquifer in the Azraq area is lowered by about 1 m per year.

The Jordan government reacts to these threats and develops new water resources. Just in 2013 the Disi conveyance project finished, which draws fossil groundwater from the Disi aquifer in the very south of Jordan and pumps it more than 300 km to Amman and Zarqa. This project aims at relieving the pressure on the most heavily used groundwater basins in Amman-Zarka and Azraq [MWI, 2009a]. Another option being discussed is a connection between the Red Sea and the Dead Sea, the so-called "Red-Sea-Dead-Sea" canal. Not only could the decent to the Dead Sea be exploited to generate electricity but also the Dead Sea rescued and preserved as a tourist destination. About 50 % of the water is planned to be desalinized and used for irrigation and drinking purpose. The World Bank certifies the feasibility in principle [World Bank, 2013]. But due to the high investment costs the Jordan Government recently decided to drop the project in favor of smaller, less cost intense ventures [Jordan Times, 2013].

4.2 Tectonic setting

This chapter covers mainly the tectonics of the Jordan Rift Valley, often considered the Dead Sea Transform (DST), between Israel and Jordan. This area is treated in detail on both sides of the transform to offer a background for the thermal waters study. Other faulting zones are
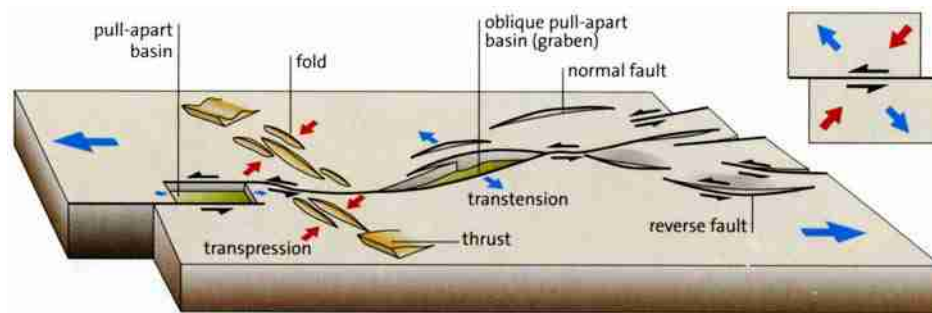
Figure 4.2: Sketch of the formation of a pull-apart basin. Lateral motion along offset faults leads to subsidence of the surface in between. From Frisch *et al.* [2011].

addressed only briefly, insofar as they are important for the interpretation of the mixing processes in the Azraq Oasis. The textbook of Horowitz [2001] treats the geologic and tectonic issues of the DST in very detail. This chapter bases mainly on this source.

The most prominent geotectonic feature in this area is the Dead Sea Transform. It constitutes the plate boundary between the Arabian plate and the Sinai microplate, an appendage of the African plate. The DST is part of the 6000 km large Syrian–African Rift system, which runs from central Africa through the Red Sea, and continues to the Taurus mountains in Turkey (compare figure 4.3). As the Arabian plate rotates couterclockwise with respect to the Siani sub-plate [Girdler, 1990; Klinger *et al.*, 2000], the same kinematics that are responsible for the opening of the Red Sea require a left-lateral displacement between the two plates, which is found in the DST. Therefore, the terms *rift* or *graben* do not describe the Jordan Valley formation correctly, as those characterize tensional spreading zones where the plates move away from each other [Kashai and Croker, 1987]. Transverse separation varies along the DST, but is of minor magnitude (Garfunkel and Ben-Avraham [1996] assess it to be less than 5 % of the lateral motion); however, it seems to have increased with time [Garfunkel, 1981].

In contrast, the Gulf of Aqaba/Eilat, the Dead Sea, Lake Kinneret and the Hula Lake area form so-called pull-apart basins [Frisch *et al.*, 2011]. This kind of depression develops when a shear system of several parallel, but offset faults moves laterally and therefore causing transtensional structures, as illustrated in figure 4.2. The relief of the DST is depicted in figure 4.3, where also the major fault lines are shown. Obviously the Wadi Arava Fault (WAF) and the Jordan Valley Fault (JVF) are offset at the present day Dead Sea, and in combination with the left-lateral shear motion pull apart the Dead Sea depression. Similar processes are taking place at the other mentioned pull-apart basins. Therefore, the term *transform zone* is more adequate to describe the tectonic setting of the Jordan-Arava Valley. However, the terms rift and graben are still widely employed. The map in figure 4.4 shows the regional tectonic activity, where the plate motion relative to Eurasia is indicated by arrows. The inset shows detail along the DST.

This horizontal shift between the two plates in the DST was determined by the comparison of geologic units and structures to be 105 km [Quennell, 1958; Freund *et al.*, 1970]. While the spreading of the Red Sea started in the Mid Cenozoic [Garfunkel, 1981], i. e. about 30 Ma ago, Garfunkel and Ben-Avraham [1996] found the first igneous activity along the transform to
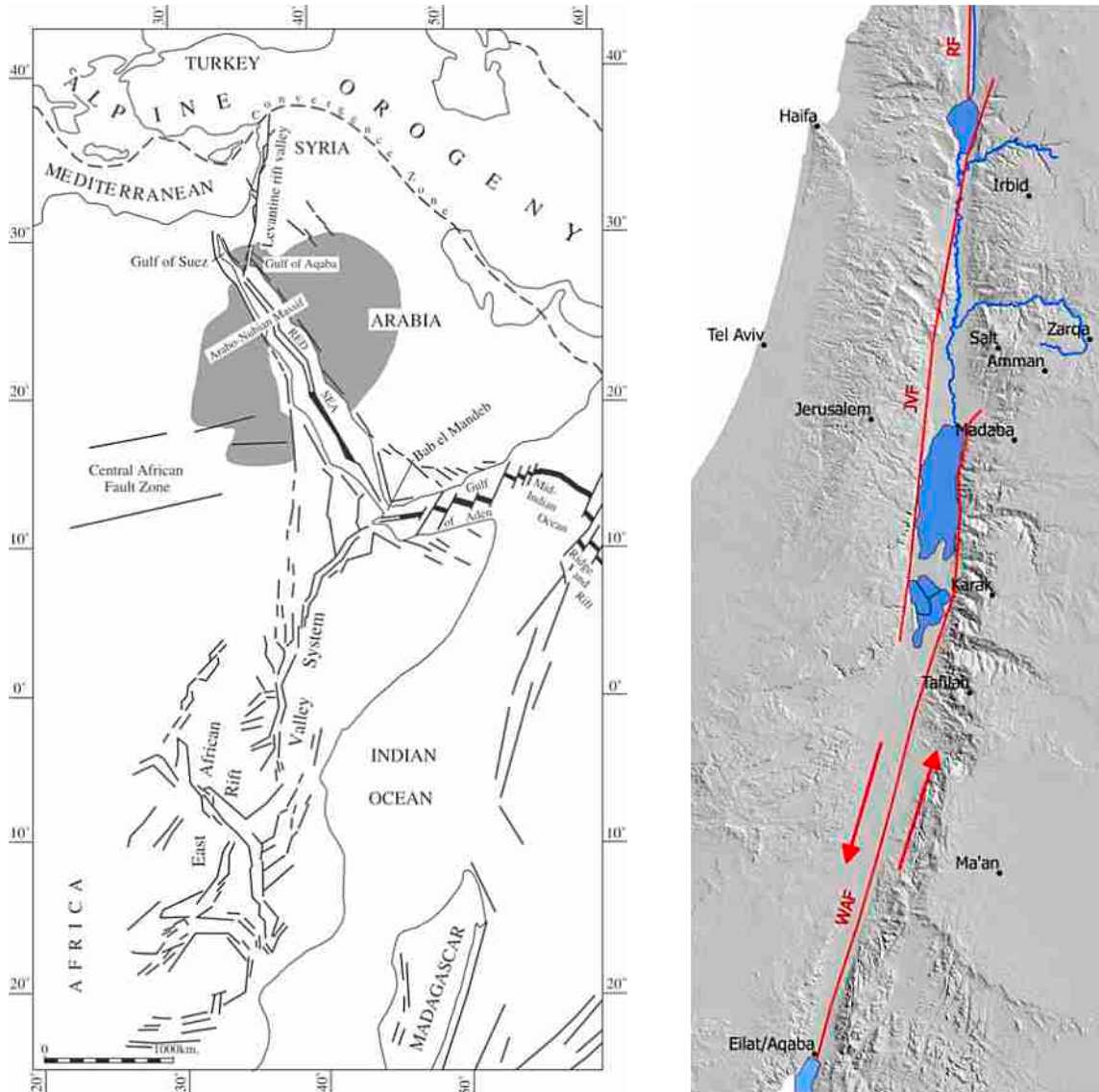
Figure 4.3: Left: The Dead Sea Transform as the northernmost part of the huge Syrian-African Rift system. From Horowitz [2001]. **Right**: The relief of the Dead Sea Transform. The dominating faults are shown in red (WAF: Wadi Arava Fault, JVF: Jordan Valley Fault, RF: Rachaiya Fault). The left-lateral displacement is depicted by the two red arrows. The offset between the WAF and the JVF leads to the Dead Sea pull-apart basin. Elevation data base on Aster DEM 30 m, downloaded from the DEM Explorer [Han *et al.*, 2012]. Faults are drawn after Marco [2007], other data from WAJ [2010].

55
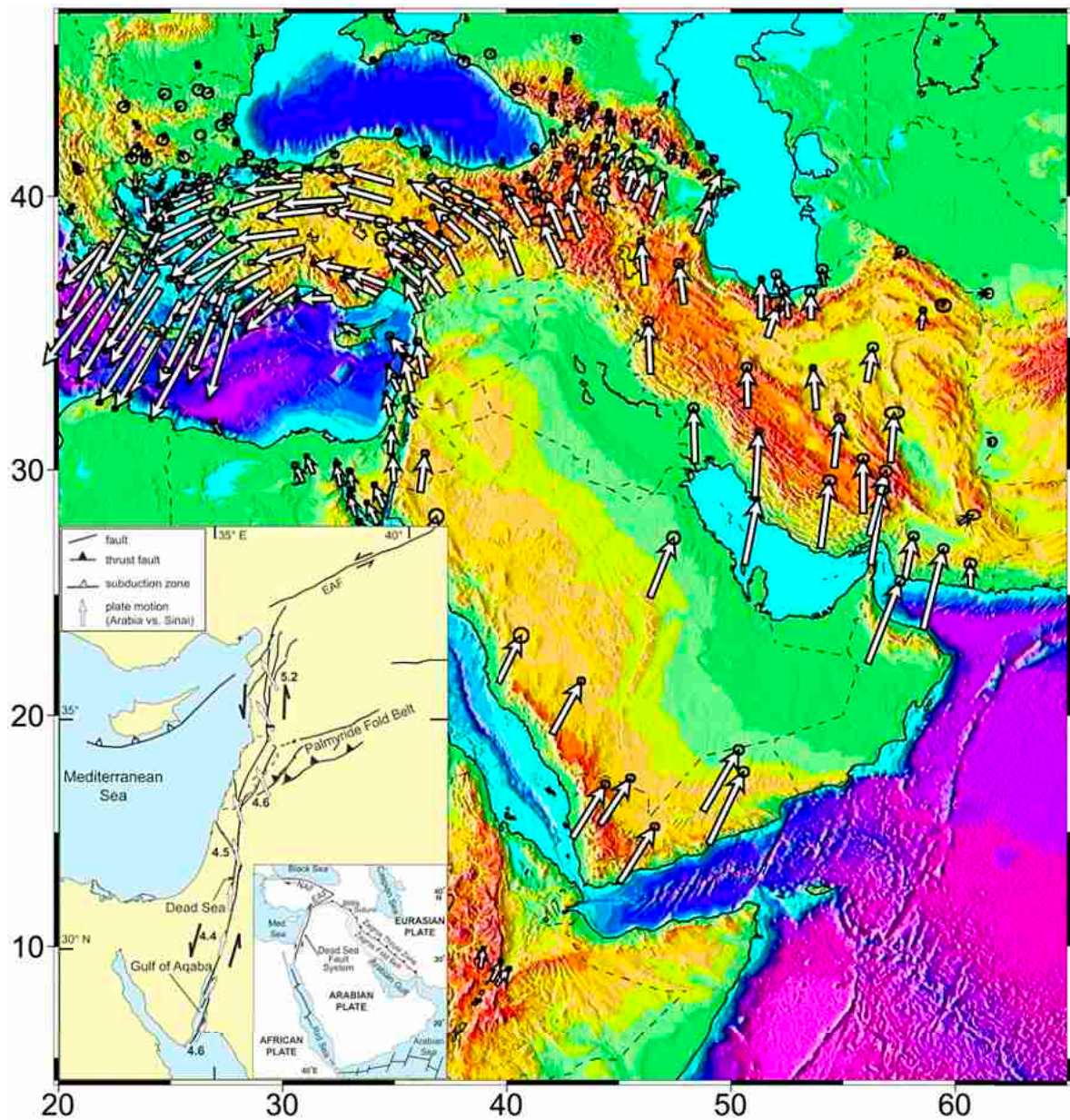
Figure 4.4: The regional tectonic setting in the Middle East. The Arabian plate moves with a counterclockwise rotation towards Eurasia. Arrows indicate the direction and velocity relative to Eurasia. The inset zoomes to the Dead Sea Transform and shows the major fault lines in this system as well as the speed and direction of movement of the Arabian plate relative to the Sinai sub-plate. Numbers indicate relative velocities in mm/year. The main map is from Reilinger *et al.* [2006], the inset is adapted from Gomez *et al.* [2007], but bases on the same data set.

be 18 Ma old. Yet, most basalt outpourings along the Jordan Valley, especially at the eastern escarpment south of the Dead Sea and Wadi Arava, on the Golan heights and around lake Kinneret, are of Pleistocene age [Bender, 1968; Watts *et al.*, 2004]. However, the lateral motion was not uniform. Freund *et al.* [1970] recognized two phases of accelerated tectonic activity. An early one took place between 25 and 14 Ma ago and displaced the plates about 60–65 km, and a later movement took place during the last 4.5 Ma [Zak and Freund, 1981]. Recent estimates for the current relative slip velocity are (4 ± 2) mm/a, calculated from the offset of Pleistocene alluvial fans in the wadi Arava [Klinger *et al.*, 2000], and more recently Gomez *et al.* [2007] found shear velocities of 4 to 5 mm/a, determined using GPS based monitoring (see inset of figure 4.4).

The dominating longitudinal faults, which are responsible for the pull-apart, are accompanied by normal faults which extend along the basin margins. The latter faults cause the slight plate separation motion and therefore are responsible for the thinning of the crust beneath the transform and hence caused its subsidence [Garfunkel and Ben-Avraham, 1996]. The marginal zone of normal faulting is 4 to 5 km wide on the western side, but only 2 km east of the pull-apart. This leads to an asymmetric structure along the Dead Sea-Jordan Valley depression in longitudinal cross-sections [Garfunkel and Ben-Avraham, 1996]. Accompanying the formation of the Jordan Valley Depression, the flanks experienced uplifting of about 1 km, in some place considerably more [Garfunkel and Ben-Avraham, 1996].

As Galli [1999] outlines, the transform is still active along the Jordan Valley Fault and also north of Lake Kinneret, and Horowitz [2001] notes, one would expect strong seismic activity along a recently shaped rift. However, the Dead Sea Fault Zone is pretty quiet with only few earthquakes in the last century, mainly distributed in the Gulf of Aqaba and north of the Dead Sea [Ambraseys, 2006; Grünthal and Wahlström, 2012]. Historical seismic activity over the past two millenia was considerably higher [Ambraseys, 2006].

The sedimentary fill of the rift valley is very thick in most parts. The deepest borehole in the Jordan Rift Valley fill, Sedom Deep 1, located just south of the Dead Sea, reaching 6448 m below the surface, does not reach the basement [Horowitz, 2001]. Ginzburg and Ben-Avraham [1997], among others, deduce a 6 km deep sedimentation north of the Dead Sea, which increases to roughly 14 km south of it from seismic refraction. Several salt diapirs evolved especially south of the Dead Sea (Lisan and Sedom diapir), which reach thicknesses of several kilometer [Garfunkel and Ben-Avraham, 1996].

Much of this sediment fill today contains saline water bodies, which developed from leaching of saline lacustrine depositions arising from the evaporation of the predecessors of the Dead Sea, the freshwater Lake Samra (~135 to 75 ka ago, see Waldmann *et al.* [2009]) and the saline Lisan Lake (~70 to 15 ka ago, compare Bartov *et al.* [2002]), which both extended north to present day Lake Tiberias. The thickness of the resulting deposits ranges from 40 to several hundred meters [Salameh, 2001]. Figure 4.5 shows a geologic cross-section in W–E direction across the DST just south of the Dead Sea.

Crustal structure is revealed by seismic refraction studies to be different on both sides of the transform [El-Isa *et al.*, 1987b]. The crust in southern Israel is about 35 km thick and thins towards the north, where it is only roughly 25 km thick. The crustal basement under Jordan reaches a maximum of 40 km in the east and thins to 35 km along the rift valley [El-Isa *et al.*,
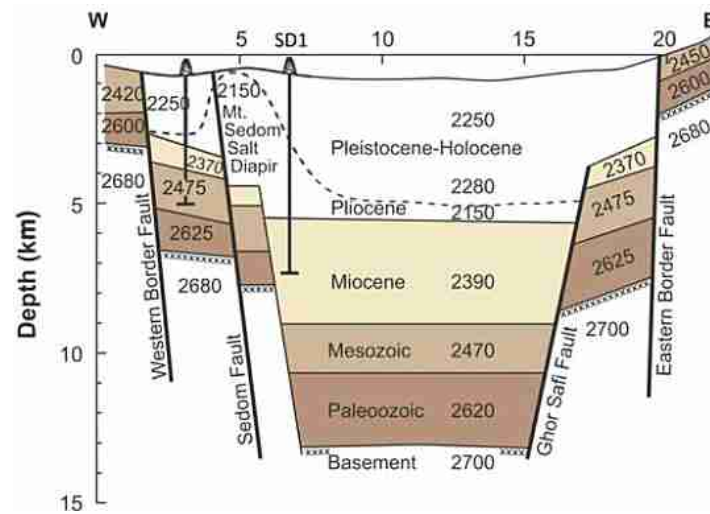
Figure 4.5: W–E cross-section across the DST just south of the Dead Sea. The deep fill with sediments is obvious. The Sedom Deep 1 borehole mentioned in the text is indicated as SD1. Numbers are densities in kg/m^3. From Ben-Avraham *et al.* [2008].

1987b]. Most notable, the crust in northwestern Jordan reaches a thickness of 35 km [El-Isa *et al.*, 1987a] and is much thicker than its counterpart at the same latitude on the western side of the rift valley. Segev *et al.* [2006] suggest that the thickness of 35 km continuous under the Golan heights, whereas Koulakov and Sobolev [2006] and Weber *et al.* [2009] find a thin crust (29 km) under the northern Jordan highlands and about 31 km below the Golan heights from the regional earthquake and seismological network.

Gravity modeling along the Jordan Valley by ten Brink *et al.* [1993] yielded no major intrusion of upper mantle material into the lower crust under the rift. Opposing, Frieslander and Ben-Avraham [1989] find a strong magnetic anomaly close to Wadi Zarqa Ma'in on the eastern Dead Sea shore, indicating young basaltic flows. This interpretation is confirmed by borehole temperature profiles yielding geothermal gradients of up to 175 K/km in the Zara and Zarqa Ma'in hot springs area [Galanis Jr. *et al.*, 1986]. Other minor geothermal anomalies are found by the same author in the Yarmouk Valley and the northern Wadi Arava (both between 30 and 40 K/km), a discovery supported by Shalev *et al.* [2013], who found significantly elevated heat flux exceeding 100 mW/m^2 in the Yarmouk area. It should be noted that Bajjali *et al.* [1997] calculated a thermal gradient in the Yarmouk location of only 25 K/km, but his underlying data is rather vague. The basal heat flow in Israel is 40 to 45 mW/m^2 [Shalev *et al.*, 2013], that in Jordan is given by Galanis Jr. *et al.* [1986] as 53 mW/m^2, whereas Förster *et al.* [2007, 2010] state a slightly higher average heat flow of 60 mW/m^2 in Jordan. Heat maps of Jordan [Gharaibeh, 2008] and Israel [Shalev *et al.*, 2013] are included in the appendix on page 178 and 179, respectively.

Continuities of magnetic anomalies across the western fault at the Dead Sea basin indicate the faulting along the western margin of the DST is mostly normal. On the eastern margin, however, magnetic contours are discontinuous, suggesting different types of crust meet and hence the strike-slip motion of the DST occurs at the eastern faults in the Dead Sea basin [Frieslander and Ben-Avraham, 1989].
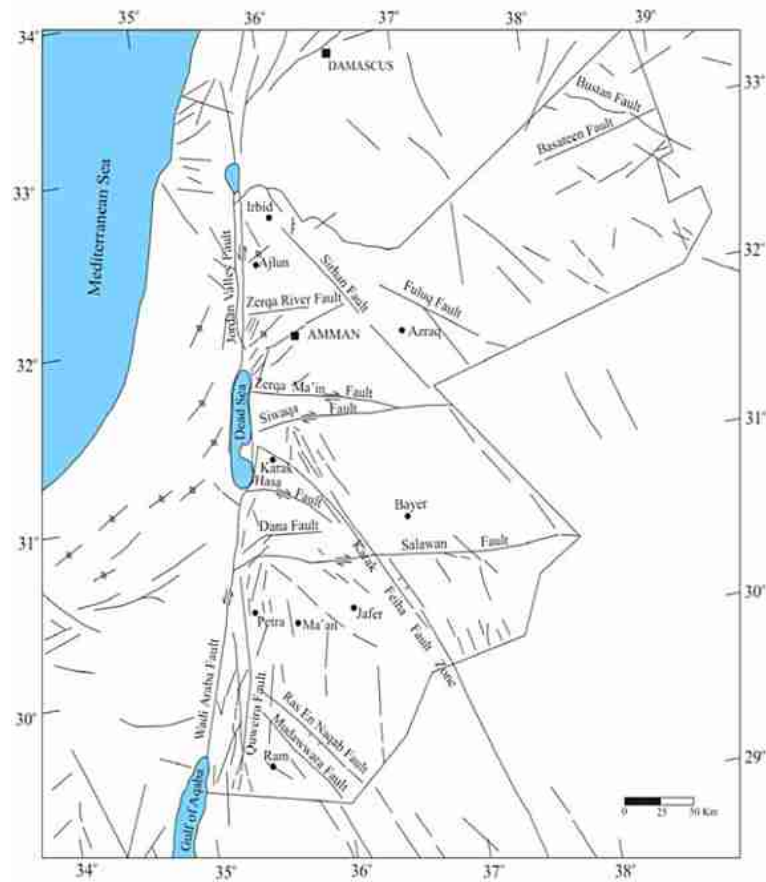
Figure 4.6: Structural map of Jordan. The country is permeated by a lot of faults, most notable the Jordan Valley Fault. From Sawarieh [2005], who adapted it from Diabat [2004].

Associated with the rift formation a lot of other faults evolved. The sediments in the valley are fractured in many places, with some of the lineaments having considerable vertical displacement (compare for example Horowitz [2001] or Ben-Avraham *et al.* [2008]). The Jordan plateau is traversed by several fracture zones, as shown in figure 4.6. The most striking one is the Karak-Feiha Fault which extends from the Karak plateau in southeastern direction. The Sirhan Fault elongates from Wadi Sirhan in Saudi Arabia in NW-SE direction. Almost parallel to it runs the Fuluq Fault. These two faults constitute the margins of the Hamza Graben, whose formation caused the subsidence of the Azraq depression. Other prominent faults are the Swaqa Fault, leading from the Dead Sea towards east into Saudi Arabia and the ESE striking Zarqa Ma'in Fault, the elongation of the Wadi Zarqa Ma'in. Many more structural elements are present and can influence the hydrodynamic patterns in Jordan.
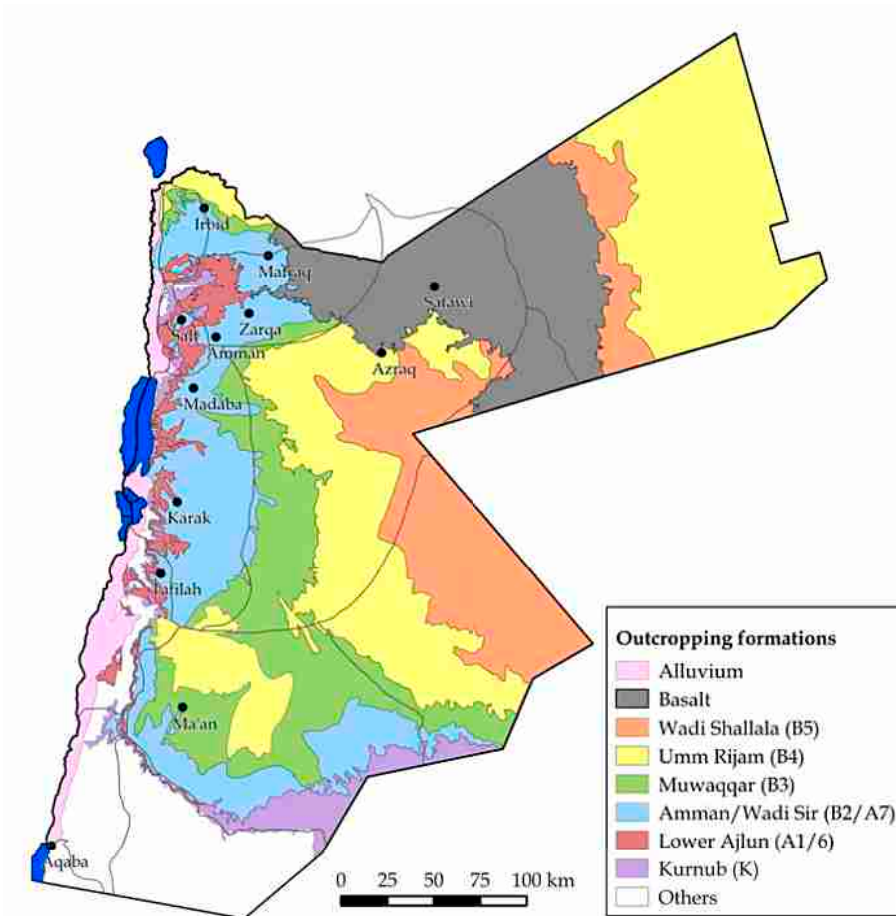
Figure 4.7: Map of the major outcropping hydrogeological units. Also the groundwater basins in Jordan are shown. Drawn based on data from WAJ [2010].

4.3 Hydrogeology of Jordan

A lot of literature has been published about the geology and hydrogeology of Jordan. Still today the book of Friedrich Bender [1968] is the reference regarding geologic aspects. A superb summary of hydrogeologic information in Jordan with a focus on the northern half of the country is found in Margane *et al.* [2002]. The description of the hydrogeologic setting in Jordan in this thesis follows mainly this publication.

Jordan is divided into 12 groundwater basins (depicted in figure 4.7), where the Amman-Zarqa, the Azraq and the Jordan Valley basins are the most heavily exploited ones [Margane *et al.*, 2002; USAID, 2012]. The same map displays the outcropping major hydrogeologic units, which are described in the following.

Over geologic timescales several sedimentary layers have deposited in Jordan. Generally spoken, the stratigraphy in Jordan dips gently towards the east and the north (compare figure 4.8). Especially along the escarpment of the Jordan Rift Valley the sequence of lithologi-

Figure 4.8: A generalized cross section of the hydrogeologic pattern in central Jordan, from west to east. Aquifers are displayed in white, aquitards are shaded. From Salameh and Udluft [1985].

cal sequence is well revealed. Figure 4.9 displays the geologic classification of rock units in Jordan. The Precambrian basement outcrops only in the southwest around Aqaba, whereas in the Yarmouk River area the depth to the bedrock is assumed to be more than 4000 mbsl [Margane *et al.*, 2002].

Three aquifer systems are present in Jordan, often termed the deep, middle and shallow aquifer. Above the Precambrian bedrock lies the sandstone aquifers of the Ram group of Cambrian to Ordovician age, which underlie almost whole Jordan and extend far into Saudi Arabia (where it is termed the Saq aquifer). It outcrops in wide areas of southern Jordan, where the main present-day recharge area is along the escarpment of the Wadi Araba (in more pluvial periods recharge also took place to the Saudi part of the aquifer system [UN-ESCWA and BGR, 2013]). The flow direction is generally towards the northwest. The Ram aquifer discharges at the lower escarpments of the Jordan Valley and into the Dead Sea [Salameh and Udluft, 1985; Mallast *et al.*, 2013]. The surface of the deep sandstone aquifer reaches a depth of more than 3500 m below surface in the Hamza oil field area southeast of the Azraq Oasis [HSI, 1994, cited after Ayed [1996]]. The term Disi aquifer is equivalent to the Ram group aquifer and is widely used among hydrogeologists.

In central Jordan, the Lower Cretaceous Kurnub sandstone aquifer (K) lies directly on top of the Ram group, both are thus considered as one aquifer complex. However, in south Jordan the aquitards of the Khreim group and in north Jordan those of the Zarqa group separate these two aquiferous layers. The thickness of the Kurnub group decreases towards the east and is 100 to 200 m in the Azraq area. The Kurnub outcrops along the slopes of the rift escarpment from the Zarqa River to the south and at several domal structures northwest of Amman. The Kurnub sandstone recharges on the slopes of the Sharaa mountain range between Tafilah and Petra, from where the water flows in northeast direction to Azraq and then turns towards the Jordan Rift Valley again [Salameh, 1996]. UN-ESCWA and BGR [2013] suggest an additional inflow from the south and southeast and across the Iraqi border. The Kurnub aquifer in the Azraq Oasis is under artesian conditions [Ajamieh, 1998; Galanis Jr. *et al.*, 1986]. The deep aquifer system, consisting of the Ram and the Kurnub aquifer, is exploited mostly

SYSTEM	EPOCH	GROUP	FORMATION	SYMBOL	LITHOLOGY	THICKNESS	AQUIFER UNIT
QUATERNARY	Holocene	JORDAN VALLEY (JV)	Alluvium	Qal	clastics		ALLUVIUM (AQUIFER)
	Holocene		Lisan	JV3	marl, clay, evaporites	>300 m	
	Pleistocene		Samra		conglomerate with silicious cement.	100-350 m	BASALT (AQUIFER)
TERTIARY	Pliocene / Miocene / Oligocene		Neogene	JV1-2	sand, gravel		
	Eocene	BELQA (B)	Wadi Shallala	B5	chalky and marly limestone with glauconite	0-555 m	
	Paleocene		Umm Rijam	B4	limestone, chalk, chert	0-311 m	B4/5 (AQUIFER)
	Maastrichtian		Muwaqqar	B3	chalky marl, limestone, chert	80-320 m	B3 (AQUITARD)
UPPER CRETACEOUS	Campanian		Amman-Al Hisa	B2	limestone, chert, chalk, phosphorite	20-140 m	A7/B2 (AQUIFER)
	Santonian		W. Umm Ghudran*	B1	dolomitic marly limestone, marl, chert, chalk	20-90 (*)	
	Coniacian	AILUN (A)	Wadi as Sir	A7	limestone, dolomitic limestone, chert, marl	60-340 m	
	Turonian		Shuayb	A5/6	marl, limestone	40-120 m	
	Cenomanian		Hummar	A4	limestone, dolomite	30-100 m	A1/6 (AQUITARD)
			Fuheis	A3	marl, limestone	30-90 m	
			Naur	A1/2	limestone, dolomite, marl	90-220 m	
LOWER CRETACEOUS		KURNUB (K)	Subeihi	K2	sandstone, shale		KURNUB (AQUIFER)
			Aarda	K1	sandstone, shale	120-350 m	
JURASSIC		ZARQA (Z)	Azab		siltstone, sandstone, limestone	0->600 m	ZERQA (AQUITARD)
TRIASSIC			Ramthu		siltstone, sandstone, shale, limestone, anhydrite, halite	0->1250 m	
PERMIAN			Hudayb		siltstone, sandstone, limestone	0->300 m	
SILURIAN		KHREIM (KH)	Alna		siltstone, sandstone, shale	0->1000 m	KHREIM (AQUITARD)
			Batra		mudstone, siltstone	0->1600 m	
			Trebeel		sandstone	0-130 m	
ORDOVICIAN			Umm Tarifa		sandstone, siltstone, shale	0->1200 m	
			Sahl as Suwwan		mudstone, siltstone, sandstone	0-200 m	
			Amud		sandstone	0->1500 m	
CAMBRIAN		RAM (D)	Ajram		sandstone	0-ca. 500 m	RAM SANDSTONE (DISI) (AQUIFER)
			Burj		siltstone, dolomite, limestone, sandstone	ca. 120 m	
			Salib		arkosic sandstone, conglomerate	0->750 m	
PRECAMBRIAN			Unassigned clastic unit		sandstone, argillaceous, siltstone, claystone	0-1000 m	BASEMENT COMPLEX
			Saramuj		conglomerate, sandstone	up to 420 m	
			Crystalline Basement				

Figure 4.9: Geologic and hydrogeologic classification of rock units in Jordan. From Margane *et al.* [2002].

62

in south Jordan due to generally great depths of the strata and often high mineralization in the northern parts of the country.

The Kurnub aquifer is overlain by the formations of the Lower Ajloun group, A1/6. These marl and limestone units are considered to act as an aquitard in most parts of the country, although the A1/2 and A4 form aquifers of local importance in some parts of the northern highlands. These layers separate the sandstone aquifer complex from the Ammen Wadi Sir aquifer (B2/A7), which is exploited most extensively for municipal and agricultural purpose of all aquifers in Jordan. Its enormous extent, relatively high permeability and good water quality makes it the primary groundwater resource in the Jordan highlands. Although present in whole northern Jordan, usage of the B2/A7 is limited to the western part, because under confined conditions the water quality is mostly poor due to a high salinity. The B2/A7, often named middle aquifer in the Azraq area, consists mainly of limestone and chert of Upper Cretaceous age. As this aquifer crops out in the Jordan highlands, it is recharged there. The difference in hydraulic head drives the groundwater to flow in eastern and northeastern direction towards the center of the Azraq basin (figure 4.10), except in the most western parts, where it discharges into side wadis of the rift valley. The B2/A7 reaches a thickness of more than 3000 m close to the Fuluq Fault and thins rapidly to the west.

The Maastrichtian to Paleocene Muwaqqar formation (B3) confines the B2/A7 aquifer system in the eastern and northeastern area. It consists mostly of marl and bituminous marl and its thickness increases to the east up to more than 400 m in the Azraq area, close to the Fuluq Fault. It's low permeability renders it to act as an aquitard.

Above the B3 formation lies the shallow aquifer system, which is made up of three subunits: the Paleocene Umm Rijam (B4) chalky limestone, the Eocene Wadi Shallala (B5) formation, and the basalt shield (B) in the north, which are all hydraulically connected. In wadis and particularly in the central Azraq depression Quaternary sediments overlie the other members of the shallow aquifer and are accounted to it as well. The B4 and B5 are exposed widely in the Azraq basin and increase in thickness from west towards the Fuluq Fault, where more than 300 m is reached. In wide parts of northern Jordan the Harrat Ash-Shaam basalt shield, which extends from the Golan Heights and Jabal al-Druze in Syria into northern Saudi Arabia, overlies the sedimentary layers. It reaches a thickness of more than 400 m at the Syrian border and may reach 1500 m at the mountain Jabal al-Druze [Wolfart, 1966]. The basalt covers an area of 11 414 km^2 [Guba and Mustafa, 1988] and is formed from Oligocene to recent times [Ilani *et al.*, 2001; Krienitz *et al.*, 2007]. Several basalt layers can be distinguished, which are locally separated by 2 to 20 m thick clay layers [Boom, 1968]. The chemical analysis of Boom [1968] classifies the basalt as olivine rich alkaline basalt.

The shallow aquifer system is recharged primarily at the slopes of Jabal ad-Druze, and some recharge takes place in the wadis and the central playa of the Azraq Oasis after storm events. The flow direction of this aquifer system in the Azraq basin is generally towards the central depression (compare figure 4.11), where once several springs used to be the natural discharge area. About 85 % of the groundwater in the Azraq basin comes from northern to northeastern direction [Ayed, 1996].

The B4 and the basalt are considered as generally good aquifers. Ayed [1996], citing Humphreys and Sons [1982], reports hydraulic transmissivities in boreholes of the AWSA well
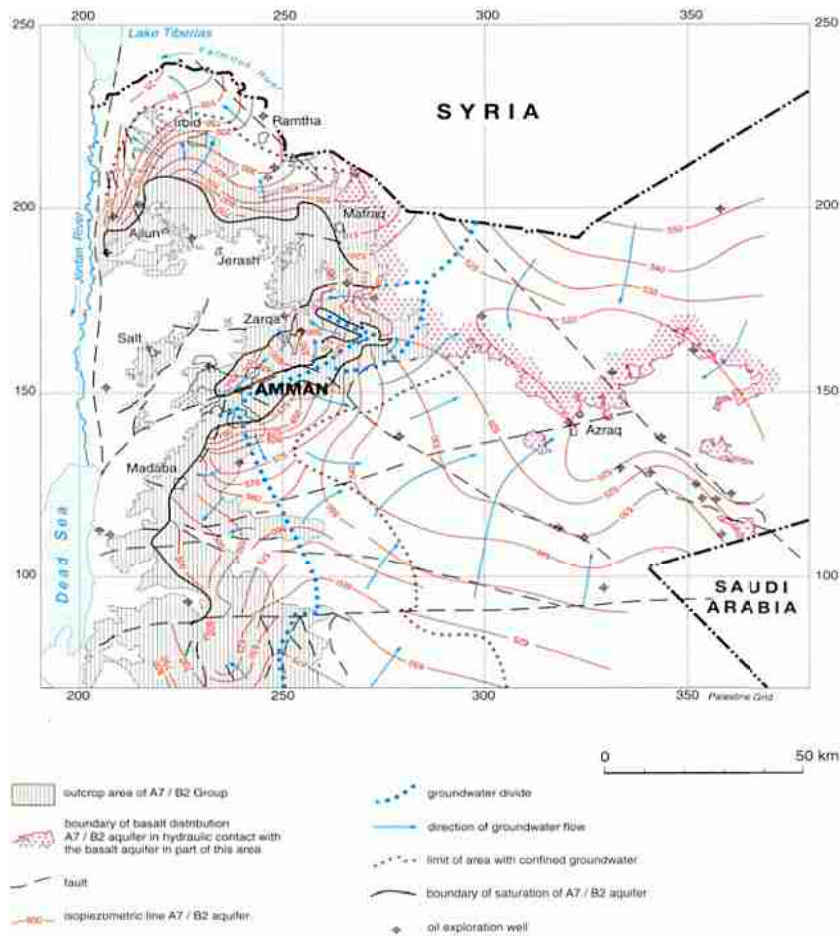
Figure 4.10: Groundwater flow direction of the B2/A7 aquifer in north Jordan. The general flow is from the recharge area in the Jordan highlands towards the Azraq Oasis. Taken from Margane *et al.* [2002].

field in Azraq to be between 23 and $660\,m^2/d$ in the B4 unit and between 54 and $65\,664\,m^2/d$ in the basalt aquifer, with an average of $11\,000\,m^2/d$ over the whole well field. Transmissivities are found to be a bit less in the northern part of the well field, on average $4500\,m^2/d$. The wide range of transmissivities of the basalts and the B4 are characteristic for fractured aquifers. The B5 is termed an aquifer in the northern part of the Azraq basin, but acts locally as an aquitard, especially in the AWSA well field area, where it consists of a 70 m thick layer of marl, clay and marly limestone and separates the overlaying basalts from the B4.

Alluvial deposits add to the shallow aquifer complex in the Azraq basin. The wadis leading water masses during storm events towards the central playa of the Azraq depression are filled with sand and clay. The playa itself is covered with sediments of Quaternary age called the Sirhan formation [El-Waheidi *et al.*, 1992]. It is divided into two subunits: the youngest consists of wadi deposits, gravels and silts of the mud flat; the second unit comprises cemented lacustrine sediments [El-Waheidi *et al.*, 1992]. The circumstance of highly saline water above a fresh water body within the Sirhan formation lead El-Waheidi *et al.*
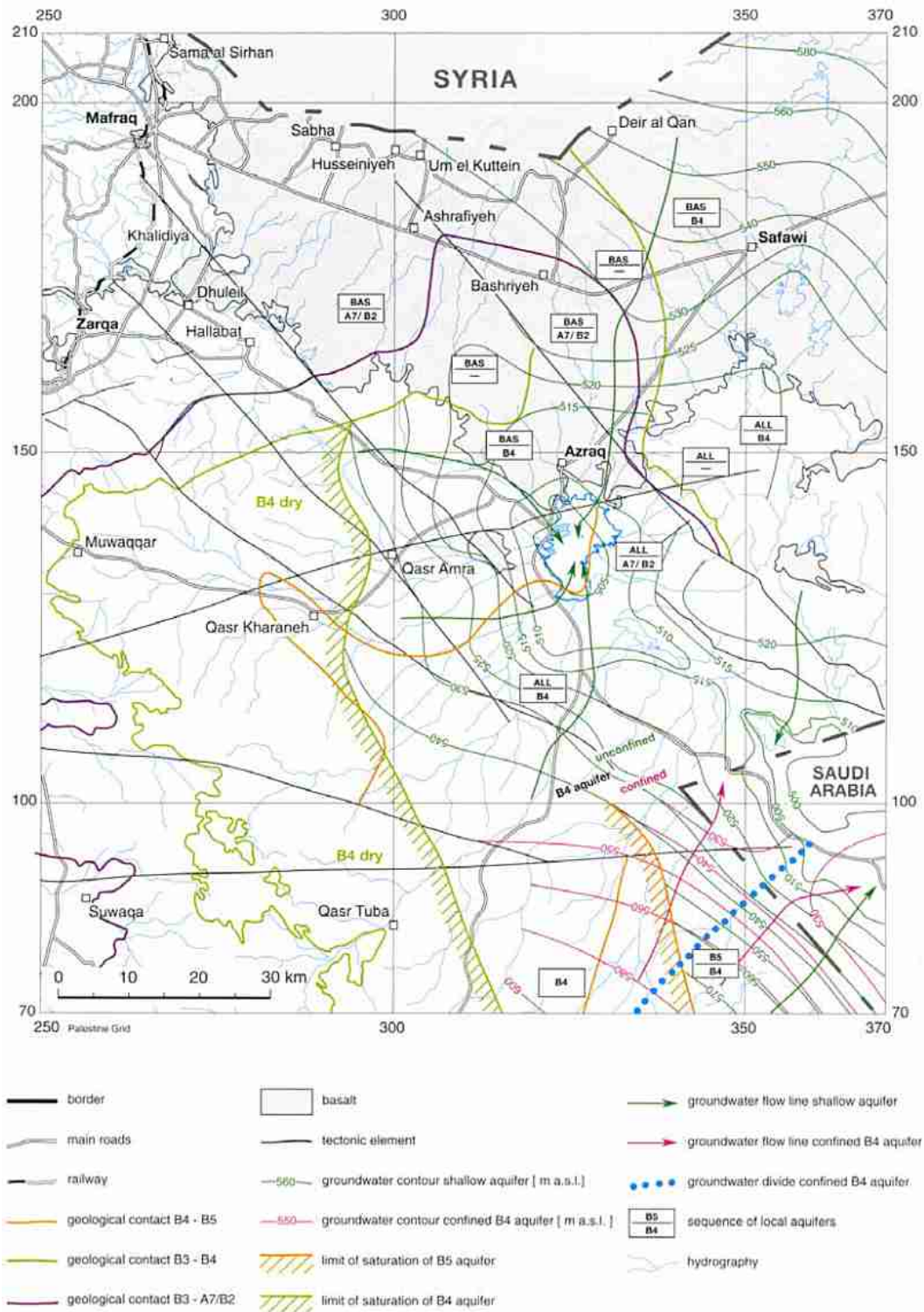
Figure 4.11: Groundwater contour lines and resulting flow directions of the shallow aquifer in north Jordan. Groundwater flow is from all directions towards the central playa in Azraq. Taken from Margane *et al.* [2002].

[1992] to the assumption of an impermeable layer in between. The presence of basaltic material below the sediments of the playa is yet unknown [Yogeshwar *et al.*, 2013]. There are no boreholes in the Sabkha and geoelectric methods do not penetrate deeper than about 70 m.

The shallow aquifer complex is extensively pumped in Azraq for over three decades and the groundwater reserves have significantly depleted in consequence. The issue of water quality deterioration resulting from the exploitation is addressed in chapter 6.

5 Sampling

5.1 Sampling and measurement procedures

Samples for tritium and stable isotopes were collected in 50 ml glass bottles. The water for the anionic and cationic composition analysis were filtered with a 0.22 µm filter before being bottled in 50 ml glass bottles each. The cation sample was acidified with 150 µl of concentrated nitric acid to a pH below 2 to prevent any precipitation of solute, because this might affect the measurement weeks later in the laboratories in Heidelberg. Radiocarbon samples were collected in 500 ml glass bottles and treated with 0.1 g silver nitrate to avoid any alteration of the carbonate isotopic composition by living organisms. In all samples a little head space was left for safe transportation by air cargo.

Radon samples were collected in 250 ml glass bottles without any contact to the atmosphere to prevent any gas exchange which would alter the radon content of the sample. This was performed by filling the bottles under water inside a bucket, flushing the bottle with fresh water for a while and then putting the cap onto the bottle underwater with no air bubble residing inside the bottle. The cap has a flexible diaphragm to be able to compensate for volume changes of the water due to temperature variation.

Radon samples were measured during the campaign between working days, mostly in the evening. As described in chapter 3.7 each measurement starts with a 20 min equilibration phase, followed by the actual sample measurement with a duration between 40 min and more than two hours, the last sample each day usually performing a longer analysis. The water temperature during the measurement has not been recorded. Thus, a reasonable evening temperature at the winter garden of the German Protestant Institute in Amman, where the radon measurements were conducted, of $(15 \pm 5)\,°C$ is assumed for the evaluation.

Noble gas samples were collected in copper refrigeration tubes mounted on aluminum racks, which can be sealed vacuum tight by stainless steel clamps on both sides [Beyerle *et al.*, 2000]. In general they were connected by hoses and a fast locking coupling directly to a threaded opening at the well head. This was possible at almost all pumped wells except two of the farming wells in Azraq were a rubber plug connected to a hose was used instead to get the water through the copper tube without air contact. Since groundwater is usually stored under high hydrostatic pressure it is important to avoid degassing during sampling. To prevent the dissolved gases to degas at the end of the copper tube a second PVC hose was connected there to move the point of a rapid pressure decay away from the sampling container. Attention was payed to a reasonably high water pressure. This was tested by checking the distance the water sprayed after leaving the copper tube and a careful check for air bubbles inside the sampling hose. Before closing the container a tool was knocked

repeatedly against it to make any bubbles that stuck in the pipe flush away. The copper tube was closed by two steel clamps at its ends of which the one on the exit side of the copper tube was closed first to keep up the water pressure.

Sampling thermal springs sometimes needed a little variation in the sampling procedure described above. In some cases where there was a little downward slope the hose feeding the copper tube is moved as far as possible into the spring opening so that the water has only a minimum of atmospheric contact. The water then flows through the hose and the copper tube,which was then closed in the same manner like at pumped wells, but with only the gradient as a source of pressure. This usually caused no problem as the water ran out of the rock without any pressure – if any degassing happened, it already occurred before sampling.

In other cases there was no exploitable downward gradient, or the thermal spring discharged below the surface into a pool. In these cases one of the two hoses connected to the copper tube was placed as close as possible to the spring's discharge spot (occasionally a weight had to be attached to the hose to lower it into the spring's pool, see appendix A.3). On the hose at the other end of the copper tube one had to suck the water until the water surface was at least a little bit above the copper tube. It was then first closed at the water entry side (in contrast to the usual sampling procedure). After the first clamp was closed, the sucking stopped and the remaining water column generated a little pressure. When sampling a hot spring alone, the vertical height was at most half a meter. With the help of an assistant, more than two meters vertical height were possible. One may argue that the sucking induced an negative pressure, but degassing due to this should only happen above the copper tube within the water column in the hose. Diffusion of degassed water into the copper tube can be neglected if one works quickly.

Some hot springs showed an obvious degassing, as bubbles of H_2S (detected by its smell) or other gases ascended in the spring's pool. These ascending bubbles strip (noble) gases from the water and one has to make sure this effect is kept as small as possible [Kennedy *et al.*, 1988]. The best way of avoiding this impact is to take samples as close as possible to the bottom or the discharge opening of the pool. However, if bubble formation already occurs below the pool's floor, non-degassed samples are hardly possible to obtain. Sometimes also wells are subject to degassing. In this study, the thermal wells in the Abu Zeeghan well field showed a massive degassing during sampling. In both cases, springs and wells, the samples showed extremely low radon concentrations.

In the case of a deep pool (Himma spring) water samples in bottles were taken close to the surface, but as deep as possible. This holds also for extremely hot springs where it was not possible to go deep into the pool with ones hands (especially at Zerqa Ma'in spring I).

Physical parameters were analyzed on site[1] with the WTW multi-parameter probe introduced in chapter 3.1. In cases of a water flow through the copper tube (i. e. all pumped wells

---

[1]In a few cases of extreme hurry at sampling points in Azraq electric conductivity and pH were recorded in the evening of the same day. Due to a failure of the sensors at the NDW wells pH and electric conductivity were measured back in Heidelberg on bottled water from these wells. No oxygen and temperature were taken in these cases. See description of the individual sampling procedure in appendix A.3.

Figure 5.1: Two sets of diffusion samplers used in this study. The lower ones are the normal diffusion samplers, consisting of two separate copper tubes connected by a PVC tube. The upper version of diffusion samplers was constructed to withstand the high hydrostatic pressure in the deep boreholes.

and some springs) the outlet water is filled into a bucket and the parameters are recorded under permanent water flow. In all other cases the sensors were hung directly into the spring's pool and were stirred a little bit to feed to oxygen sensor with fresh water. Finally alkalinity and nitrate values were determined in the field.

5.2 Diffusion samplers and deep sampler

Wells without a working pump had to be sampled in a different way. So-called diffusion samplers (DS) facilitate to collect noble gas samples from water without actually collecting the water. A diffusion samplers is a closed volume with a gas-permeable membrane. Located in water gases diffuse through the membrane until an equilibrium between in gases inside the diffusion sampler and the surrounding water is established. After enough time for equilibration the samplers are closed with a pneumatic pliers.

Passive diffusion samplers where first used by Sanford *et al.* [1996] to collect gas samples from water without disturbing it. Sheldon [2002] first used a copper tube design similar the one used in this study.

Two different versions of diffusion samplers were used in Jordan and are shown in figure 5.1. The lower version is the normally used one which was introduced by Wieser [2006]. They consist of two copper refrigeration tubes, 6 mm in diameter and 1 mm wall thickness, connected by a PVC tube (Thomafluid$^{®}$ tube, 6 mm outer diameter, 0.5 mm wall thickness, from Reichelt Chemietechnik GmbH + Co., Heidelberg, Germany) which acts as the permeable membrane. The outer ends of the copper tubes are closed. A steel spring prevents the PVC tube from being squeezed under hydrostatic pressure and a sealing ring supports the tube to inhibit water leakage to the sampler's inner volume.

Wieser [2006] comprehensively characterized this kind of diffusion samplers, especially in terms of equilibration duration. Due to the opposing factors of diffusion coefficients and

Figure 5.2: The deep sampler used to get water samples from open borehole without a pump. It is depicted in its open state. A weight is sent down along the cable enables to close the sampler at the desired depth.

solubility in water, neon needs the longest equilibration time of all noble gases, but 75 hours turned out to be sufficient for 99.9 ‰ equilibration.

Because this type of diffusion sampler has never been tested under high hydrostatic pressure the upper, a "strong" version was invented during this thesis to use it in deep boreholes. It comprises of one copper tube only which is perforated at one end. The same PVC tube is pulled over this perforated part and acts as the membrane, but the total surface where gases can diffuse to the interior is smaller, thus, equilibration time is expected to be longer than for the normal DS. The reduction of the area where diffusion occurs is about a factor of 10, so this type of diffusion sampler needs approximately 20 days to equilibrate. The assumed advantage of this design is that the PVC tube does not cover the edges of the copper tubes and rupture due to deformation under high pressure appears less likely. However, the normal diffusion sampler design proved to be more sturdy. As this study is the first of our working group where diffusion samplers are were applied under field trip conditions, especially in deep boreholes, the gained experiences are summarized in appendix A.2.

All diffusion samplers located in one borehole were fixed to a single string. In NDW 5 a fishing line was used, in all other wells a stronger plastic string. Both ends were tied to the string to prevent the samplers to get stuck in the borehole in case they can freely move. The closed ends were packed into duct tape because they are sharp and could cut through the string. An additional weight was used drag the string down. The lowering of the samplers was conducted slowly and the string finally bound fast at the well head.

Retrieval of the DS was done as fast as possible to avoid much re-equilibration with shallower water and the atmosphere. The copper tubes were immediately closed tight using pneumatic pliers. Because the inner volume is changed by the first sealing-off, it is important to note the sequence in which the copper tubes were closed.

At every sampling depth at least two diffusion samplers were located to reduce the risk of loosing the sample due to a rupture of the PVC tube (except the deepest sample from NDW 7, only one normal DS was used here, as nobody exspected any sampler to survive this depth). The "strong" design samplers were used in depth starting from 300 m coupled with a normal sampler. The experience gained from the application of both types of diffusion samplers is summarized in appendix A.2.

In order to collect water from the non-pumped wells, a so-called deep sampler, provided by the Water Authority, was used. This device, shown in figure 5.2, is lowered in to the borehole and fills with water. It can then be closed by a weight which is sent down along the cable. It has a volume of 500 ml, which means that the sampler had to be used twice at every sampling depth. The cable provided a scale the depth could be set precisely. The deep sampler was also used to determine the water table in the borehole. It gave an acoustic signal when it came in contact with water.

This way samples for stable isotope, tritium, ionic composition and carbon-14 were filled into the according bottles and treated afterwards, as explained above. Because the deep sampler could reach a maximum of 250 m no water samples from greater depths in the NDW wells in Azraq could be obtained. No radon sample was taken in these cases since the deep sampler cannot be considered gas tight and the results would have been questionable. Also the water temperature could not be recorded, but pH and conductivity were noted.

5.3 Sampling Campaigns

Three sampling campaigns were conducted in the scope of this thesis. In total 51 wells and 9 springs were sampled, some of them several times. A detailed description of all sampling sites is given in the appendix A.3.

Campaign 2009

The first field trip took place in late September/October 2009 over three and a half weeks. Beside getting to know the general situation of Jordan regarding water issues, this field trip aimed mainly to find a local partner in Jordan. With the Water Authority of Jordan (WAJ) a trustful and helpful cooperation partner was found and a cooperation agreement was signed.

The initial plan of taking noble gas samples from the Disi aquifer in southern Jordan was not possible at this time due to restrictions by the Ministry of Water and Irrigation (MWI). Instead, the Azraq basin was found as a substitute and first samples were collected: Three wells (two governmental and one private farming well) in the northern part of the groundwater basin and six wells of the AWSA well field (all governmental) in the basin's center were sampled.

On this campaign samples for stable isotopes of hydrogen, tritium and noble gases were collected. In the field temperature and dissolved oxygen were measured. The limitation of recorded parameters is owed to the uncertainty of the outcome of the search for field partners and, thus, only the most necessary equipment was shipped to Jordan.

Campaign 2010

The second field trip of four weeks duration took place between mid-September and mid-October 2010. Ten wells in the AWSA well field were examined to support the findings from

the 2009 campaign. As a second study 20 governmental wells in the Karak area were sampled in order to estimate the local groundwater recharge rate in this agricultural dominated region. The wells stretched from close to Karak town along the supposed eastward groundwater flow direction to the town Swaqa. The Karak study aimed at calculating the local recharge rate from groundwater age depth profiles and their spatial distribution. However, most waters appeared to be too old to be dated by the ^{3}He-^{3}H method. Therefore, this study is not included in this thesis, but at least the measured noble gas isotope concentrations and the most important isotope ratios are compiled in table A.8 in the appendix on page 186.

All wells were sampled for stable isotopes, tritium, radiocarbon and noble gases. Physical parameters recorded in the field are temperature, pH, electric conductivity and dissolved oxygen. The alkalinity and nitrate content were determined using chemical test kits at the sampling sites.

As it was decided that the ionic composition of the waters in Azraq is of importance, it was analyzed for it on the leftover of the tritium and stable isotope water samples. Obviously, these samples had not been filtered and treated with nitric acid and, therefore, the results may show deviations from the original values. However, the ion balance confirmed that no major ions were precipitated in significant amounts.

Campaign 2012

In March and April 2012 the final sampling took place with a duration of about six weeks. For the Azraq study wells which penetrate the B2/A7 aquifer as well as shallow farming wells were sampled in order to have water samples of both possible sources of salinity of the AWSA well field detected in the previous campaigns. There are no pumped wells of the B2/A7 in this area due to high salt content in this aquifer in the Azraq basin. Therefore, diffusion sampler were used in two exploration wells. In each of them they were positioned at several depth. Also some farming wells which are not in use anymore due to the salty water were sampled with diffusion samplers.

Thermal waters in 8 springs and 7 wells along the Jordan Valley were collected. The northernmost spring was the Himma spring in the Yarmouk Valley, the southern-most spring the Afra spring in the Wadi Hasa.

Despite the information stop about the Disi project it was possible to sample four wells in the Disi area during this campaign. Since the well drilling was still in progress it was only possible to take samples during the pumping test following the drilling. In the time period of the field trip two newly drilled wells were sampled. Additionally one well from 1992 was sampled which today provides drinking water to the construction camp site. However, due to restriction by the MWI the data of these well is not allowed to be published.

The same physical parameters were recorded as in the 2010 campaign, as well as the same chemical test have been conducted. Additionally samples for the ionic composition (major anions and cations) were collected and treated as described in chapter 5.1. Radon was measured for all samples of the thermal waters and the Disi studies as well as for some wells in Azraq.

6 Azraq

Azraq is situated in the northeastern desert, about 80 km east of Amman. Azraq used to be an oasis, with an extensive system of lakes and marshland, fed by the two large springs Shishan and Druze.

The first traces of habitation in the area of the Azraq Oasis date back to the Lower Paleolithic, i. e. 0.3 to 2.6 Ma BP, and people settled there during all major prehistoric periods [Stanley Price and Garrard, 1975]. It can be assumed that this region reacted sensitive on climate variation. Garrard *et al.* [1985] report a period of extreme drought during the last glacial maximum and the total disappearance of the lakes, and the return of moist conditions about 12 000 years BP, where the lake grew to cover an area of 700 km^2 with 20 m depth. During the Holocene the size reduced to about 7 km^2. Newer studies support these findings and determine the driest and most inhabitable period in Azraq to last during the Bølling-Allerød warming (14.7 – 12.8 ka BP) as there was no sediment deposition in Qa'a Azraq at this time [Jones and Richter, 2011].

The Azraq Oasis had a vivid ecosystem with a large number of species inhabiting the swamps around the pools [Nelson, 1985] and it was an important stop-over for many migrating birds on their journey to the south.

However, the springs dried up in 1991 in the wake of large increase of groundwater abstraction rates (see figure 6.1, left panel), and the area of the former lake forms a wasteland now. Shallow groundwater was used for agricultural purposes for decades, and about 3.3 MCM per year was pumped to Irbid since 1963 [Nelson, 1985]. In the early 1980s, however, the AWSA[1] well field was drilled close to the oasis to supply the urban areas of Amman and Zarqa with good quality drinking water. This additional groundwater abstraction and an increasing water demand for irrigation purposes caused the groundwater table to drop by about 1 m per year since then, as illustrated in the right panel of figure 6.1. This is due to the wide discrepancy between the estimated safe yield of the Azraq basin of 24 MCM/year [USGS, 1998] to the actual abstraction rate of 59.3 MCM/year [Raddat, 2005, data from 2004].

To diminish the ecologic disaster and resettle some of the native species in Azraq (including the endemic Azraq Killifish *Aphanius sirhani*), an artificial wetland reserve was established by the Royal Society for the Conservation of Nature (RSCN), but it covers only a small part of the original lake area [RSCN].

Not only is overpumping a hazard for the Azraq ecosystem, but also the threat of deteriorating groundwater quality grows. Some shallow agricultural wells already show high salinization, rendering the groundwater useless for irrigation in some parts of the Azraq

---

[1]Amman Water and Sewage Authority
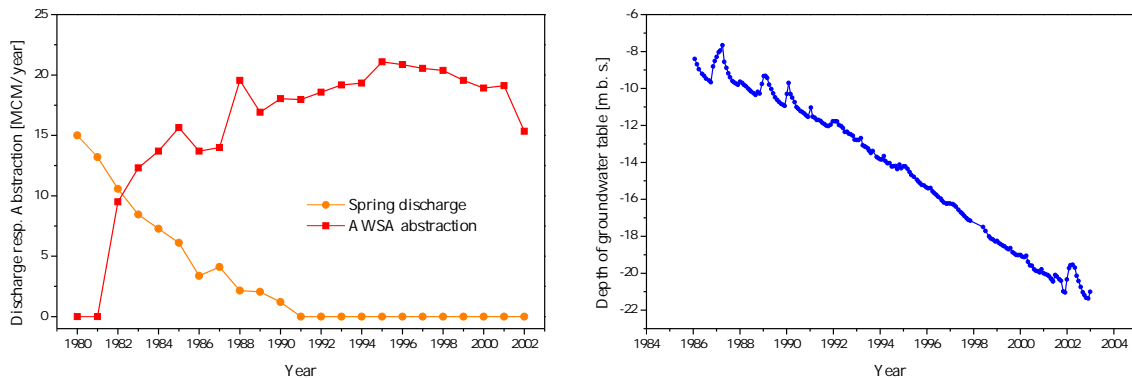
Figure 6.1: Left: Spring discharge (orange) of the Azraq springs and the groundwater abstraction rates in the AWSA well field (red). Both given in million cubic meter (MCM) per year. **Right**: As a result of overpumping the groundwater table dropped by about 1 m per year (data is shown for the AZ 12 observation well, which is situated in the center of the AWSA well field). Data courtesy of the WAJ.

area. While the AWSA well field produced high quality drinking water with little mineralization in the first years of operation, some of its wells show a rising salt content over the years [Al-Momani *et al.*, 2006]. It is particularly interesting that, although the wells lie close to each other, wells in the middle of the well field are affected by saltwater intrusion rather than those on its edges.

The map in figure 6.2 gives an overview of the setting around the Azraq Oasis and the location of the sampled wells in this area. The farm land surrounds the central mud pad, which is more symbolized in this map, because the extent to the south is not known. The basalt cover extending north of the oasis is also shown. The boundary between salty water in the center and fresh water in the surroundings is indicated by the orange, dotted line. The underlying data from geoelectric surveys is extracted from El-Waheidi *et al.* [1992, green lines], El-Naqa [2010, brown lines] and Yogeshwar *et al.* [2013, blue lines]. The lines indicate the direction of the respective georadar profiles. By far the most precise boundary locations are those from Yogeshwar *et al.* who created very high resolution profiles. The locations indicated after El-Waheidi *et al.* and El-Naqa are only rough positions between two distant measurement points. Northwest of Azraq town the AWSA well field is situated, where wells with an elevated salt content are depicted in orange, whereas from the salt unaffected wells are red. The observation well AZ-12 in the well field is yellow; data of depth to the groundwater table shown in figure 6.1 originates from this well. The middle aquifer wells NDW5 and NDW7 are printed blue, the shallow farm wells are green. Furthermore, the extensive network of faults is presented. The major ones are displayed as thick, black lines and labeled by the names stated by the geologic map prepared by Ibrahim [1993]. Many more lineaments are known or inferred beneath superficial deposits, they are indicated by grey lines. The wells sampled in the northern part of the basin lie 30 to 40 km north of the map section.

Figure 6.2: Overview of the vicinity of the Azraq Oasis. In brown the central mud pan (Sabkha) is displayed, the farm land in green and the basalt shield in grey. The AWSA wells are indicated by orange or red dot, whether they are affected by rising salinity or not. Farm wells are green, the middle aquifer wells blue. The approximate boundary of the salt water body in the center is show as an orange, dotted line, direction of the georadar profiles is indicated by short, colored lines (data sources El-Waheidi *et al.* [1992, green], El-Naqa [2010, brown] and Yogeshwar *et al.* [2013, blue]). The major faults are named and thick, black lines, other lineaments are displayed as grey lines. The Sirhan and the Fuluq Faults margin the Hamza Graben structure, forming the Azraq depression. Compiled using data of WAJ [2010], road data base on OpenStreetMaps.

6.1 Hydrology and Hydrogeology of the Azraq basin

The Azraq Oasis is situated in the depression of the Azraq basin, a 12 800 km^2 large surface catchment. About 94 % of this basin belongs to Jordan, 5 % is situated in Syria and about 1 % in Saudi Arabia. The elevation of the central mud pan (Qa'a or Sabkha in arabic) in its deepest point is 505 m above sea level. The surface profile rises in all directions, most prominently to the north, where the basin reaches its highest point at the mountain Jabal ad-Druze (1803 m) in Syria.

Rain falls in winter only and its amount decreases from more than 300 mm per year in the northern part to less than 50 mm per year in the southeast of the basin [Ayed, 1996]. In Azraq town it averages to 66 mm per year [Margane *et al.*, 2002]. The basin has no perennial rivers, but during storm events wadis transport much water into the central playa, where most of it evaporates.

The economy of Azraq town relies largely on agriculture. Due to the precipitation scarcity, the farmers depend almost exclusively on irrigation with groundwater, since the springs dried up.

All three aquifer systems described in chapter 4.3 are present in the Azraq basin. The principle hydrogeologic setting is sketched in figure 6.3. The Azraq oases lies in the depression of the Hamza Graben. To the north the basalt shield forms the slopes of Jabal ad-Druze, where by far the most precipitation falls and where the major recharge area of the shallow aquifer is. The aquifers and aquitards (striped) are shown in this figure as well as the four well types: The northern wells, abstracting the most recently formed groundwater from the basalt aquifer, the wells in the AWSA well field, drilled through the basalt and almost to the bottom of the B4 aquifer, the shallow farm wells around the Sabkha and the deep wells NDW5 and NDW7. The Fuluq Fault and the Sirhan Fault are indicated in the sketch, as is the groundwater table, illustrated by the blue, dotted line. Its deepest point is located in the central depression.

The formation of the Azraq depression, where the Azraq Oasis is situated in the deepest part, is closely related to the development of the Hamza Graben system which runs in NW – SE direction. Its eastern boundary is the Fuluq Fault, the most striking tectonic feature in Azraq, with a maximum vertical displacement of more than 3000 m [Margane *et al.*, 2002]. The Sirhan Fault, indicated in the cross-section in figure 6.3, constitutes the western boundary of the graben. Plenty of other faults and minor lineaments are present, witnesses of a turbulent geologic past. Yet, none of them has a displacement comparable to the Fuluq Fault.

The displacement at the Fuluq, however, varies largely along fault. Margane *et al.* [2002] published a geologic cross-section in W–E direction, which exactly runs through the Azraq Oasis and crosses the Fuluq Fault, where its maximum displacement is assumed (see the top cross-section in figure 6.4). The cross-section of Dottridge and Abu Jaber [1999], also displayed on page 78, runs from the Azraq Oasis in NE direction and passes the Fuluq about 10 km north of where the one of Margane *et al.* [2002] runs through it. There, the displacement is considerably smaller. The exact location of the two cross-sections is shown in figure A.13 on page 176.
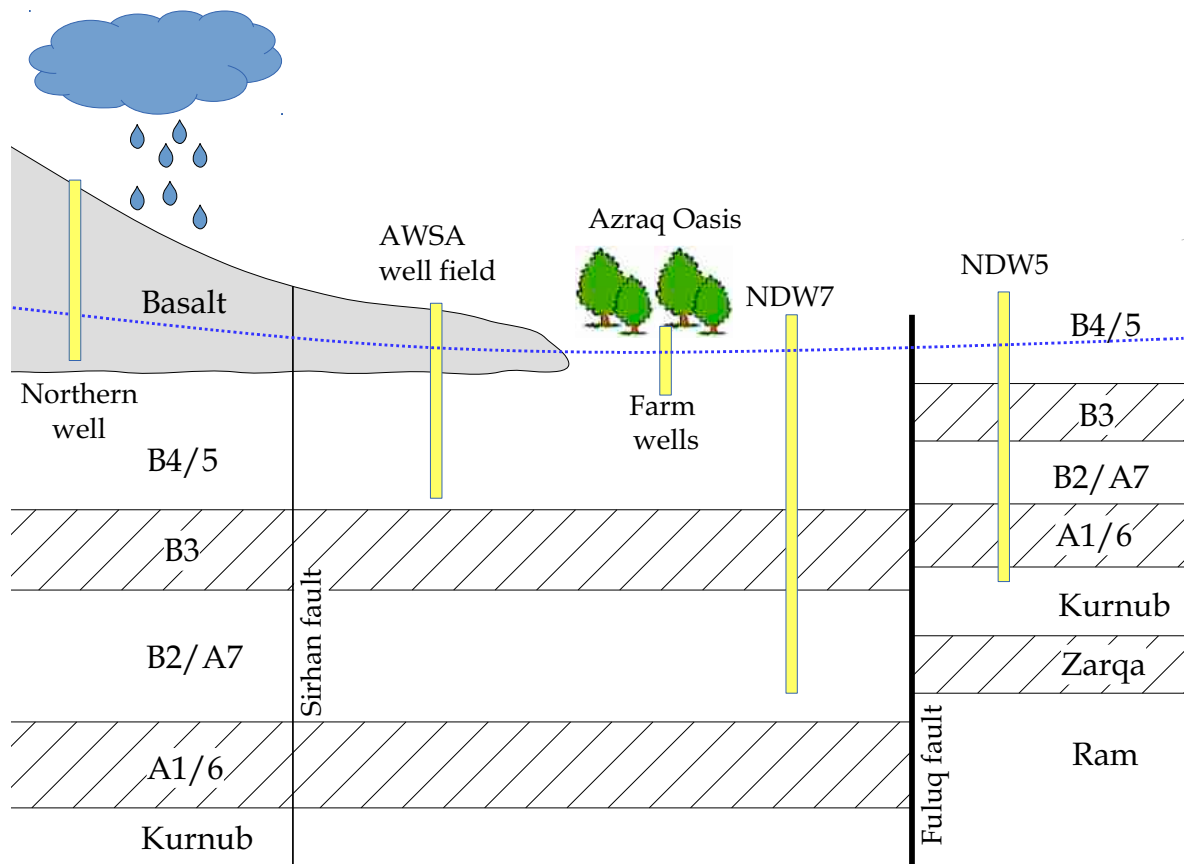
Figure 6.3: Sketch of the hydrogeologic setting around the Azraq Oasis. Aquitards are shown as striped layers, aquifers are left white. The Fuluq Fault causes a vertical displacement of the strata. East of the Fuluq the thickness of the geologic units is smaller. Other faults are present, like the Sirhan Fault, but none has a displacement comparable to the Fuluq Fault. Precipitation falls mainly at the northern mountains. All four types of wells are displayed: The northern wells, the AWSA well field, the shallow farm wells and the deep wells NDW5 and NDW7. The groundwater table is indicated by the blue, dotted line.

This strong locality of the vertical displacement induces a very local "contact plane" between the different rock layers on both sides of the fault. Whereas more south [Margane *et al.*, 2002] the shallow aquifer to the west connects to the Kurnub on the eastern side of the fault and the middle aquifer is connected with the Ram sandstone, some kilometers north the western middle aquifer is in contact with the Kurnub on the eastern side, while the shallow aquifers have no contact at all (within the saturated zone).

In order to get an impression of the geologic settings close to the surface around the Sabkha, the detailed cross-sections found in Ibrahim [1993] are reproduced in figure A.14 on page 177. There it is evident that most of the other faults have rather small (vertical) displacements.

The data published about hydraulic heads in the three aquifer systems in the Azraq Oasis disperse. The upper aquifer's head reduced from 510 masl at steady state conditions to
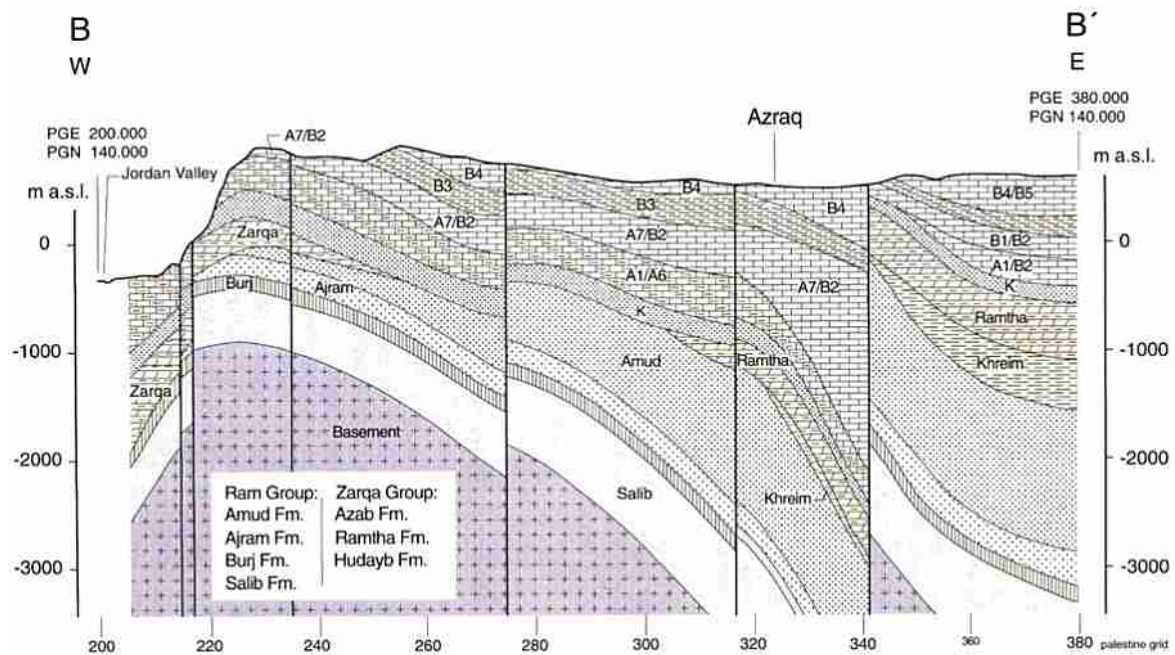
(a) Cross-section of Margane *et al.* [2002]
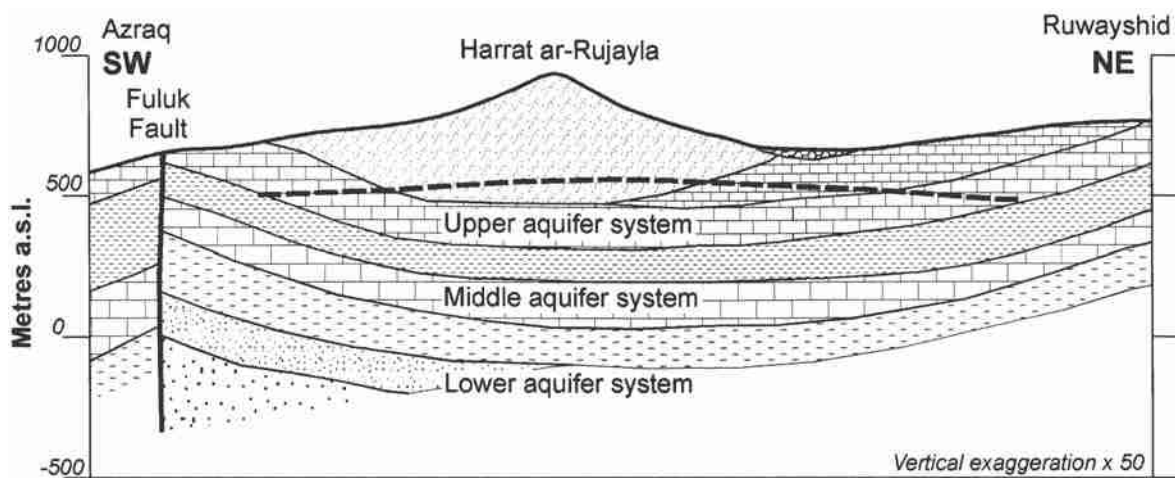
(b) Cross-section of Dottridge and Abu Jaber [1999]

Figure 6.4: Top: Geologic cross-section published by Margane *et al.* [2002], which runs from the Jordan Rift Valley in eastern direction through the Azraq Oasis and the Fuluq Fault. **Bottom:** The cross-section of Dottridge and Abu Jaber [1999], which starts at the Azraq Oasis and runs in NE direction. It passes the Fuluq Fault about 10 km further north than the one of Margane *et al.*. The map in figure A.13 on page 176 illustrates the exact locations of both cross-sections.

495 masl in 2002 [Al-Momani *et al.*, 2006], and extrapolation of the almost constant ground-water level decline suggests a present day level of about 488 masl in the well field area. Own measurements, comparing the depth to the water table in open boreholes to the altitude taken from Ibrahim [1993], resulted in the farming wells F3960 and Moh in a groundwater level at 493 masl. Al-Momani *et al.* [2006] state the piezometric head of the middle aquifer in Azraq to be 520 masl, which would promote an upward flow into the shallow aquifer; the same information is found in Salameh and Bannayan [1993]. However, an own measurement at the open borehole of NDW7 resulted in much lower water level of 484 masl. The only borehole in the Azraq Oasis that penetrates the deep aquifer is the AZ-1 well (1299 m, taps the uppermost 40 m of the Kurnub aquifer). According to Ajamieh [1998] it has an artesian flow rate of 45 m^3/h and its piezometric head is 7 m above the ground surface (i. e. 519 masl). If conductive zones are present, the deep aquifer water would discharge into the middle and the shallow aquifer.

The water of the upper aquifer is in general of good quality and, hence, largely exploited in the basin, mostly in the northern parts and in the farm area around the central playa for agricultural, but also for domestic purposes. Only in shallow depths in the central farming area a groundwater body with high salinity is found. It is assumed that the dissolved minerals originate from the S1 subunit of the Sirhan formation, which deposited in a brackish lake environment in Miocene times [Andrews, 1992, cited after Ayed [1996]]. El-Waheidi *et al.* [1992] find the thickness of the saline groundwater body in the Sabkha to be about 60 m and a freshwater body below. They deduce that a non-permeable layer needs to prevent the more dense saline water to descend into deeper layers.

6.2 The salinization problem and previous studies

When the AWSA well field was drilled in the early 1980s the mineralization of all wells was low (E. C. mostly in the range of 300 to 400 µS/cm). But in the mid-90s, AWSA 12 and 15 experienced an increase of salinity, AWSA 3 joined around 2005, and AWSA 13 kept a higher mineralization level over the years, but showed a steep rise in 2012. The data suggest that also AWSA 11 will get more saline in the coming years[2]. All other wells keep the low mineralzation they had since they were drilled (figure 6.5). This difference in behavior is surprising because most wells are drilled to almost to the same depth of about 200 m and they are located within a few kilometers from each other. In addition, the wells with a rising E. C. are not all situated at one edge of the well field, which would suggest the movement or expansion of the salt body in the Sabkha towards the well field. However, the salty wells are tendentially located in the south of the well field, but surrounded by low-saline wells. The map in figure 6.2 displays the well field, where the orange dots represent the salty wells and the red dots those with a more or less constant salt content.

Three possible mechanisms of the increasing salinization of those affected wells in the AWSA well field are discussed [Al-Momani *et al.*, 2006; El-Naqa *et al.*, 2007] (both publications base on almost the same data set from 2002):

---

[2] According to Al-Momani *et al.* [2006], AWSA well No 1 had a rising salt content, too, but it could not be sampled in this project and is, thus, neglected.
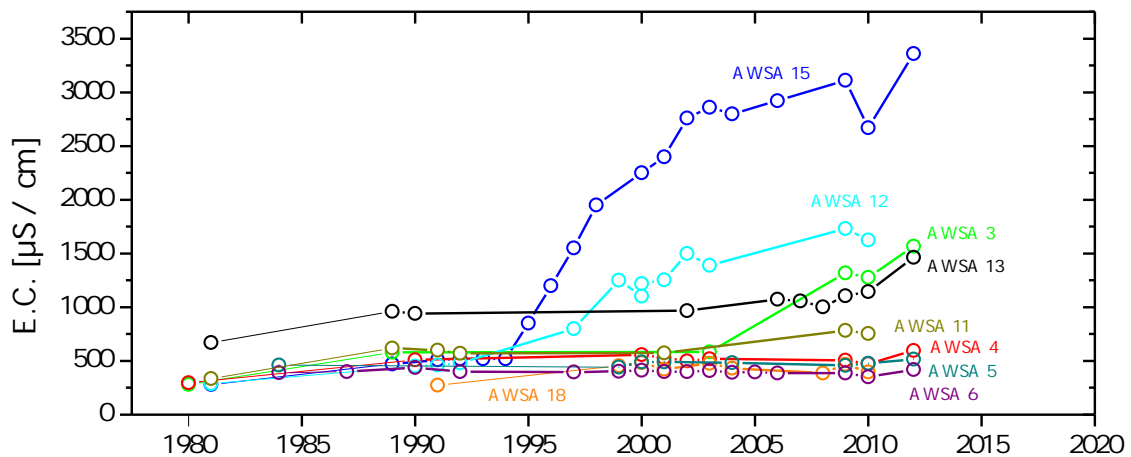
Figure 6.5: The temporal development of the salinity in most of the sampled AWSA wells; those neglected are all constant over time. Most of the wells remained below 500 µS/cm, but AWSA wells No 3, 12, 13 and 15 increase in E.C. for a couple of years. Also AWSA 11 tends slightly to higher salinity for the last years. The early data is courtesy of the WAJ, data from 2009, 2010 and 2012 is own data.

1. As a result of the continuous pumping in the AWSA well field the hydraulic gradient changed and a back-flow of saline groundwater from the Sabkha began.

2. Due to the reduction of the groundwater table in the shallow aquifer the hydrostatic pressure is reduced and induces an upward leakage from the middle aquifer (B2/A7) and the B3 aquitard.

3. Changes in the local hydrodynamic situation lead to different hydrological and geochemical processes (dissolution in the aquifer matrix) which cause a different chemical composition.

The first possibility is ruled out by the above mentioned studies because the hydraulic head gradient at the time of data collection (in 2002) is very low, but still drives the groundwater to generally flow from the well field area towards the Qa'a Azraq. This fact is confirmed by El-Naqa [2010]. According to Al-Momani *et al.* [2006] and El-Naqa *et al.* [2007] the third explanation seems to be the most likely where the transient condition in the upper aquifer led to a significant change in the groundwater geochemistry. This assumption is supported by the fact that the increase of some constituents is not accompanied by a change of stable isotopes, i.e. it seems to be unlikely that water from other sources admixes into the well field. The possible upstream of the brackish water from the middle aquifer through faults, however, could not be ruled out by this study.

Apart from the [Al-Momani *et al.*, 2006; El-Naqa *et al.*, 2007] study, the complex behavior of the groundwater in the upper aquifer system in the Azraq basin has been extensively studied. Several groundwater models were applied to describe the groundwater flow, the groundwater balance and piezometric head distribution and decrease [Holden, 1998; Abdulla *et al.*, 2000; Al-Kharabsheh, 2000; Aljazzar, 2003; Abu-El-Sha'r and Rihani, 2007]. The

Federal Institute for Geosciences and Natural Resources (BGR), Germany, established in co-operation with the Ministry of Water and Irrigation (MWI) a groundwater model of entire Jordan, where the Azraq basin is incorporated [Schmidt *et al.*, 2008]. Most of these models are constrained to describe only the upper aquifer or the upper and the middle aquifer (except the model of the BGR, which covers all three aquifer systems in Jordan). All mentioned models have in common that they describe the change of the piezometric head distribution quite well under different groundwater abstraction schemes, but none of them is capable to delineate the movement and interaction of the several groundwater species around the Qa'a Azraq. This may result from the fact that mixing processes take place on a relatively small spacial scale, while all models employ a more or less coarse grid resolution. In addition, the more complex a system is, the more input data a computational simulation needs to properly describe it. Knowledge of the groundwater behavior in the Qa'a is still insufficient, especially regarding the deep and middle aquifer complexes and in the farm land around the playa. Although there are hundreds of wells, most of them were drilled illegally and thus not much information of the subsurface geology is known. Therefore, models essentially lack information they would need to describe the present state and predict the future conditions of the shallow aquifer in detail.

Geoelectric surveys shed light on the salt water/fresh water interface in the Sabkha as well as adding information about the structure of the Sirhan formation below alluvial deposits. According to El-Waheidi *et al.* [1992], El-Naqa [2010] and Yogeshwar *et al.* [2013], the boundary between the highly and low conductive zone is quite sharp and was found to be several kilometers away from the well field (compare the orange line depicting the salt water/fresh water interface in figure 6.2). El-Naqa [2010] estimated the saltwater regime to need 500 to 2000 years to reach the well field at present abstraction rates.

In 1985, Rimawi and Udluft published data of 50 wells from the shallow aquifer in the Azraq basin and clustered them in four distinct water groups according to their ionic composition and total salinity.

Group 1 is characterized by sodium being the major cation with about 70 % and chloride the dominant anion. Average E. C., $\bar{x}$, is 1363 µS/cm with a standard deviation, s, of 316 µS/cm.

Group 2 cations are also dominated by sodium (about 68 %). Regarding the anions, chloride and bicarbonate dominate. $\bar{x} = 676$ µS/cm with s = 125 µS/cm.

Group 3 shows a sodium concentration that equals that of calcium and magnesium together. Chloride is the dominating anion (46 %), but in this group the sulphate ion is the second most abundant with 28 %. The calcium content of this water is higher than the bicarbonate, which is the main difference to group 1 and 2 waters. The salinity is quite high with $\bar{x} = 2043$ µS/cm and s = 564 µS/cm.

Group 4 is brine water which is dominated by sodium (91 %) and chloride (86 %). Only two wells of this type were sampled.

The Collins bar diagram and the Schoeller diagram of these groups is shown in figure 6.6. Rimawi and Udluft [1985] further conclude a progressive water genesis. Freshly recharged rain water interacts with clayey beds in the basalt aquifer on its travel from Jebel ad-Druze
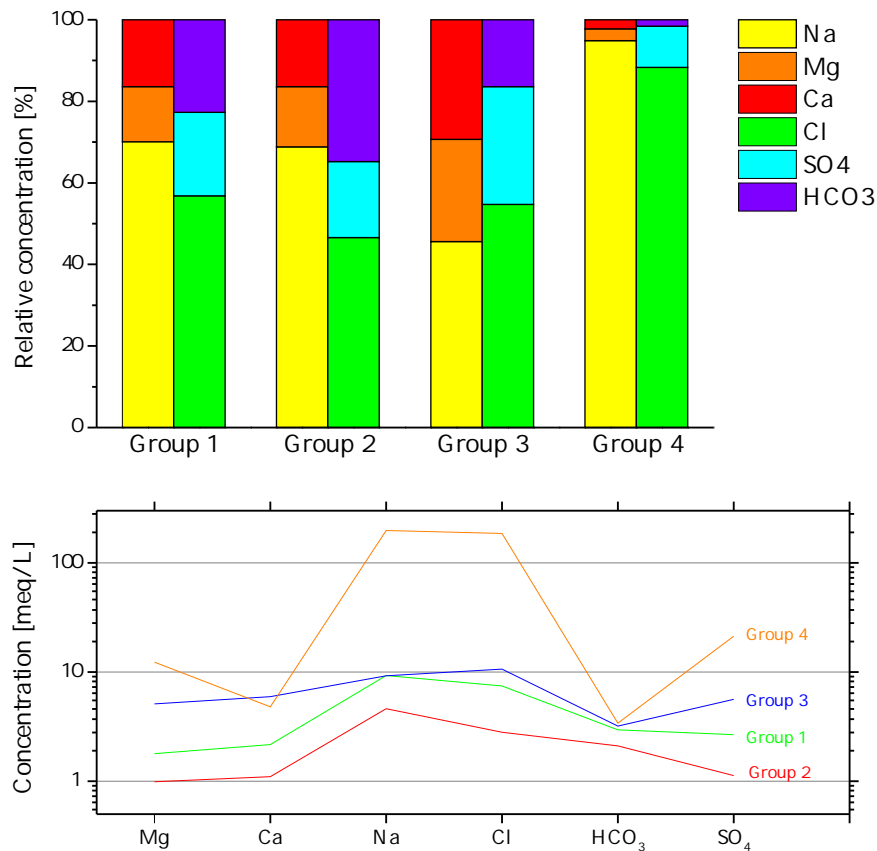
Figure 6.6: Collins bar diagram and Schoeller diagram of the water groups in Azraq after Rimawi and Udluft [1985]. For each group the average ion concentration of each ion is used for the plots. The illustration of group 4 in the Schoeller diagram is reduced by 10 to better fit into the diagram.

southwards. Consequently the water changes to group 1 type by the interaction with a carbonate aquifer, where mainly calcium and magnesium are dissolved and the Ca + Mg exceeds HCO_3 content. This water further develops into group 3 type water by interaction with carbonates and evaporites, until Ca > HCO_3 and Cl > Na. Group 4 water evolves from type 3 water by an extensive interaction with evaporites in the Sabkha area. Type 3 water is by far the most abundant in the Azraq Oasis area, only a few wells of the other groups are present close to the southern rim of the basalt shield.

Only very few data regarding the deep and middle aquifer is published, most data originates from the drilling records of the NDW wells, two of which are also sampled in this study. Al-Momani [1994] presents the pump test data and calculate a geothermal gradient for the Azraq basin of (35 ± 6) K/km, which indicates a possibly slightly elevated gradient in this area. Water temperature of NDW5 is given as 39.3 °C and NDW7 as 45 °C. They found no ^{14}C in the middle aquifer wells, but 3.7 to 80 pmC in shallow groundwater. Al-Momani *et al.* [2006] measured 5 to 6.5 pmC in most AWSA wells, except for AWSA 11 (23.3 pmC), AWSA 15 (39 pmC) and AWSA 18 (27 pmC). Shallow farm wells were determined to have between 3

and 80 pmC [Al-Momani, 1994]. Tritium has not been detected in AWSA wells [Al-Momani, 1994; Al-Momani *et al.*, 2006], only in some shallow wells close to wadis tritium was detected [Al-Momani, 1994]. Salinities of the middle aquifer vary widely, with a maximum reported for NDW7 of about 24 mS/cm [Al-Momani, 1994].

6.3 Description of the sampled wells in Azraq

This chapter aims at presenting the basic information about the sampled wells in the Azraq basin as well as illustrating the depth profiles of the AWSA wells regarding the hydrogeologic formations they penetrate. The well specific sampling conditions and procedures are not addressed here, this information is found in appendix A.3.

The AWSA well field is located at the basalt part of the desert and has an extent of about 6 x 3 km². All wells have no casing installed, i. e. they can abstract groundwater from all depths. Some basic information about the sampled wells is compiled in table 6.1, including pump test results from the time the wells were drilled [Ayed, 1996]. The hydrogeologic units these wells penetrate are listed in table A.2 and, more convenient, displayed in figure 6.7.

The wells tapping the middle aquifer, NDW5 and NDW7, are closed in the upper layers and the screen opens only within the B2/A7. NDW5 also taps the deep sandstones, which is much closer to the surface east of the Fuluq Fault. The spudded geological units are listen in table A.2 as well.

Not much information on the farm wells is obtainable, because no drill log exist, since most of them were drilled illegally and were later legalized. The coordinates are found in table 6.1.

Information about the northern wells is rare, but essentially not needed within this thesis. The unsaturated zone is very thick in this part of the country, in case of KM140 the water level is at 275 m (statement of the well caretaker).

6.4 Results

This section summarizes the results of all wells sampled in Azraq during all three field campaigns. The wells are grouped according to their function in this study. In order to facilitate an immediate recognition in the presented plots, each group is assigned a characteristic color:

- Group 1: wells in the northern part of the Azraq basin (purple)
- Group 2: AWSA wells affected by salt (orange)
- Group 3: not affected AWSA wells (red)
- Group 4: Farm wells (green)
- Group 5: Deep wells (blue)

Table 6.1: Basic information about the sampled wells in the Azraq basin. The drawdown and transmissivity information was recorded when the wells were drilled. The observation well AZ-12, referred to in figure 6.1, is listed, too. Well locations noted myself, well depth and information about the base of the basalt shield from WAJ [2010]. Pump test data from Ayed [1996].

Name	ID	Eastern	Northern	Altitude [masl]	Depth [m]	Initial drawdown [m]	Initial transmissivity [m²/day]	Base of basalt [masl]
AWSA wells								
AWSA 3	F1030	36°49'8.8"	31°55'53.2"	521	210	4	17539	457
AWSA 4	F1031	36°48'58.2"	31°56'29.7"	536	206	19	842	462
AWSA 5	F1032	36°48'34.4"	31°56'37.3"	541	204	33	268	444
AWSA 6	F1033	36°48'57.6"	31°56'45.2"	549	206	3	6782	464
AWSA 11	F1038	36°49'18.5"	31°55'30.3"	517	62	1	35165	463
AWSA 12	F1039	36°48'51.0"	31°54'47.0"	528	209	7	65664	474
AWSA 13	F1040	36°48'31.5"	31°55'5.2"	532	205	1	7485	473
AWSA 15	F1042	36°48'30.0"	31°54'18.5"	524	210		469	472
AWSA 16	F4166	36°48'25.0"	31°55'38.1"	539	160	26		
AWSA 18	F3222	36°48'0.9"	31°57'8.4"	553	171			494
AWSA 20	F4205	36°48'2.1"	31°54'14.1"	533	117			
Farm wells								
F3731	F3731	36°51'40.4"	31°52'57.4"	514				
F3975	F3975	36°49'27.5"	31°49'16.7"	509				
F3741	F3741	36°55'39.6"	31°49'43.8"	513				
F3960	F3960	36°53'25.0"	31°51'50.2"	509				
Moh	?	36°54'54.4"	31°50'20.8"	513				
Deep wells								
NDW5	F1354	36°56'6.1"	31°59'14.8"	598	733			
NDW7	F1350	36°54'43.9"	31°50'49.2"	515	970			
Northern wells								
Mkeifteh 2	F3524(2)	36°39'45.4"	32°17'6.1"	921	550			
F1381	F1381	36°41'34.3"	32°9'57.4"	777	575			
KM140	F3935	36°53'0.7"	32°8'2.9"	803	421			
Observation well								
AZ-12	F1043	36°49'19"	31°55'36"	519	255			462
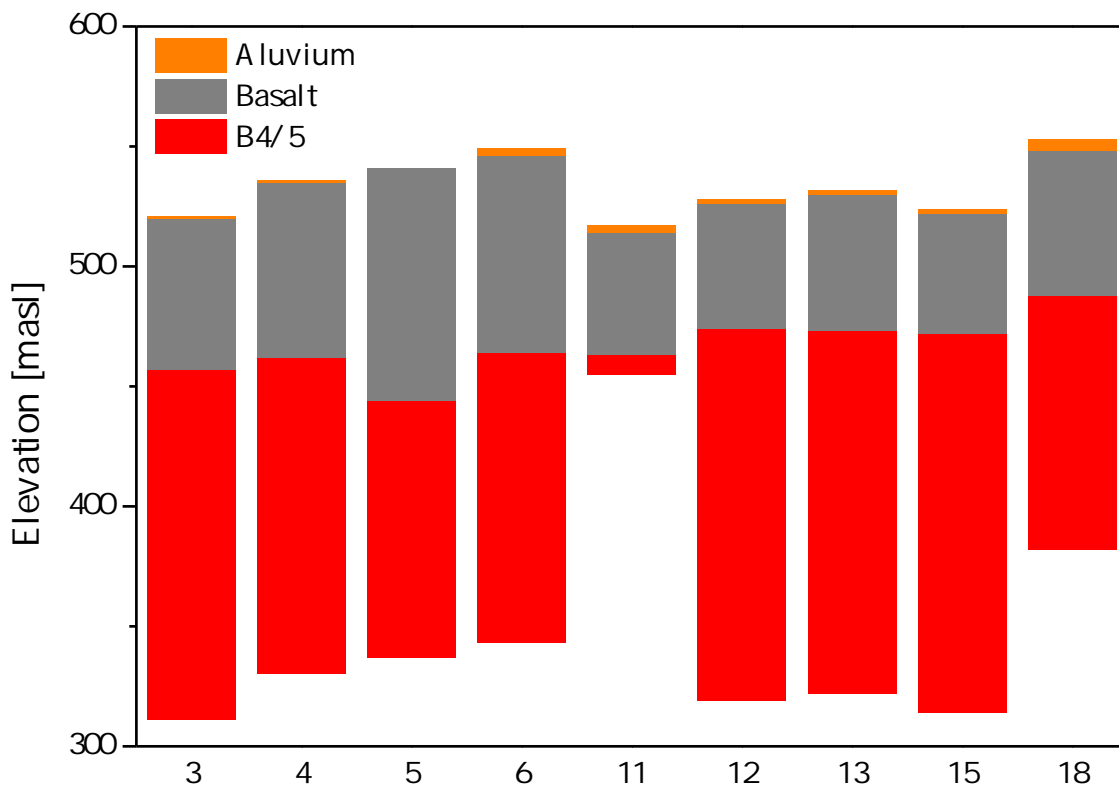
Figure 6.7: Lithologic profiles of the sampled AWSA wells. The depth scale is in meters above sea level, which allows a comparison of absolute depths. AWSA 16 and 20 are missing, since no lithologic description could be obtained. The underlain data is from WAJ [2010] and is compiled in table A.2 on page 180.

The color code is the same used for the overview map in figure 6.2. Furthermore, the sampling year is discerned by the symbol as well as the color the labels are written:

- 2009: rhombus with green labels

- 2010: triangle with cyan labels

- 2012: circle with black labels

Data points in plots are labeled with a short form of the wells' names to keep the plot clear. In the following the according short names are introduced:

- Northern wells: Mk = Mkeifteh 2, KM = KM140, Jordan Modern Farm well = F1381

- AWSA wells are abbreviated just by their number

- Farm wells are labeled with their well ID, Moh refers to a well owned by Mohammed where I could not figure out the well ID

- The deep well NDW-5 is labeled with N5 and NDW-7 with N7, followed by a number referring to the sampling depth
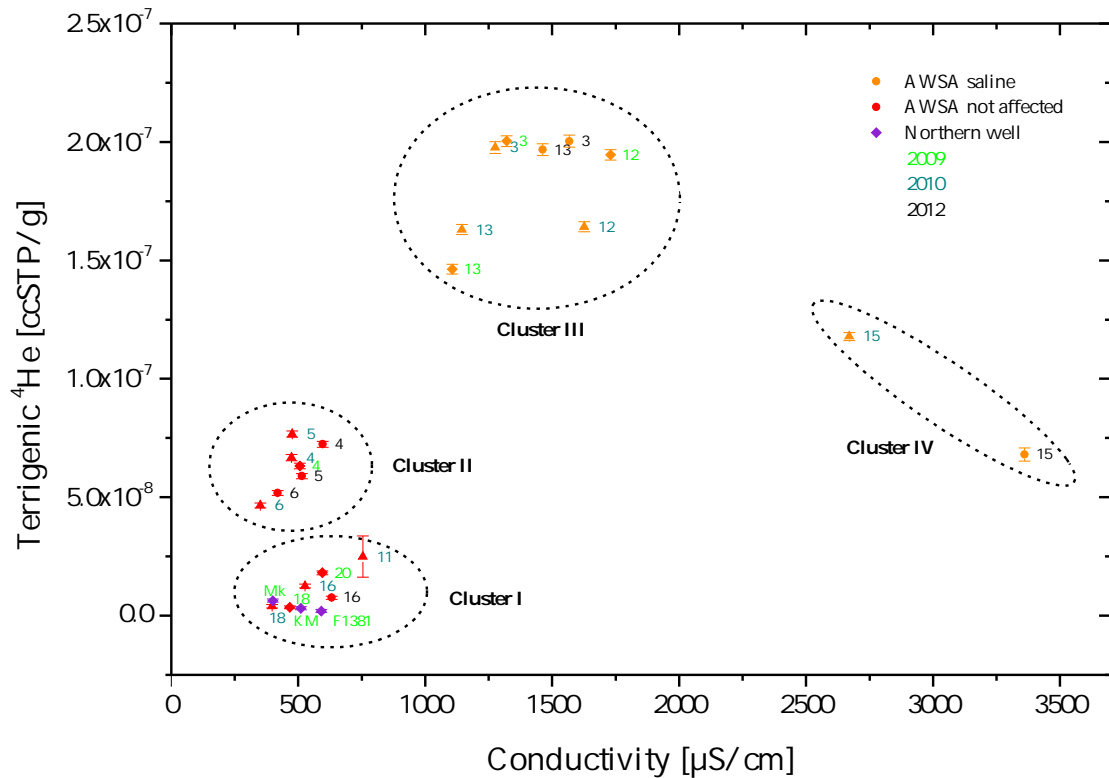
Figure 6.8: The relation between terrigenic ^{4}He. Four clusters can be distinguished, as described in the text.

6.4.1 Physical parameters

This chapter deals with the physical parameters recorded directly at the well head. It concentrates on the wells of the AWSA well field, as for the other wells no data was recorded. For all wells sampled with the deep sampler no (trustworthy) pH, water temperature and O_2 could be measured, and when sampling the farm wells the multiparameter probe refused to function. An overview of the data discussed in this chapter is presented in table 6.2.

Electric conductivity

The salinity behavior of the AWSA wells is already described in the introducing chapter 6.2 on the salinization problem. Yet, it is found that the amount of terrigenic ^{4}He correlates with E.C. and the helium content is favorable over the salinity itself to interpret the following data presentation. The relation between the salt content of the water and the amount of terrigenic produced ^{4}He is displayed in figure 6.8: all those wells with an increased salinity also show an elevated terrigenic He content. In total, four cluster can be distinguished:

- Cluster I: low salinity and low terrigenic ^{4}He (AWSA 11, 16, 18 and 20)

- Cluster II: low salinity, but elevated terrigenic ^{4}He (AWSA 4, 5 and 6)

Table 6.2: Compilation of the recorded physical parameters of all sampled wells in the Azraq basin of all field trips alongside the corresponding content of terrigenic ^{4}He.

Well	Year	E. C. [µS/cm]	O$_2$ [mg/L]	pH	Sampling Temp. [°C]	Terr. ^{4}He [ccSTP/g]	Terr. ^{4}He err [ccSTP/g]
AWSA well field							
AWSA 3	2009	1320	–	–	28.8	2.004E-07	2.270E-09
	2010	1276	0.52	7.57	28.4	2.011E-07	4.619E-09
	2012	1568	–	8.07	27.2	2.003E-07	8.372E-09
AWSA 4	2009	506	–	–	29.1	6.319E-08	1.175E-09
	2010	474	2.32	7.77	29.2	6.673E-08	2.180E-09
	2012	596	–	8.20	28.2	7.227E-08	2.670E-09
AWSA 5	2010	476	0.94	7.82	28.7	7.691E-08	2.310E-09
	2012	515	–	8.26	28.3	5.883E-08	5.882E-09
AWSA 6	2010	351	0.75	7.81	28.8	4.619E-08	1.755E-09
	2012	419	–	8.23	28.0	5.147E-08	4.334E-09
AWSA 11	2010	755	12.00	7.90	26.2	2.436E-08	9.548E-09
AWSA 12	2009	1730	–	–	27.9	1.946E-07	2.226E-09
	2010	1626	1.34	7.67	28.0	1.669E-07	3.957E-09
AWSA 13	2009	1107	–	–	27.0	1.463E-07	2.061E-09
	2010	1144	0.76	7.72	27.7	1.657E-07	3.932E-09
	2012	1463	–	8.03	26.8	1.967E-07	7.949E-09
AWSA 15	2010	2670	3.62	7.65	26.5	1.193E-07	3.070E-09
	2012	3360	–	7.77	21.3	6.772E-08	2.798E-09
AWSA 16	2010	526	7.73	8.03	24.7	1.188E-08	1.291E-09
	2012	631	–	8.43	23.9	7.522E-09	7.555E-09
AWSA 18	2009	467	–	–	25.4	3.548E-09	6.310E-10
	2010	397	7.43	8.20	25.3	3.372E-09	1.065E-09
AWSA 20	2009	595	–	–	24.6	1.812E-08	7.972E-10
Farm wells							
F3731	2012	8580	1.65	6.65	–	-5.087E-10	8.363E-10
F3975	2012	19750	–	7.40	–	7.070E-08	3.127E-09
F3741	2012	16960	–	7.03	–	2.766E-07	6.875E-09
F3960	2012	6880	–	7.10	–	2.876E-08	2.827E-09
Moh	2012	50200	–	7.22	–	1.452E-07	9.601E-09
Deep wells							
NDW5 684m	2012	1179	–	8.19	–	2.194E-06	4.758E-08
NDW7 50m	2012	7310	–	7.20	–	4.211E-07	1.134E-08
NDW7 100m	2012	7310	–	8.53	–	5.716E-07	1.572E-08
NDW7 150m	2012	7300	–	8.81	–	6.827E-07	1.502E-08
NDW7 200m	2012	7660	–	8.85	–	9.402E-07	2.194E-08
NDW7 250m	2012	7360	–	8.00	–	1.293E-06	2.974E-08
Northern wells							
Mkeifteh 2	2009	400	–	–	30.6	6.375E-09	6.552E-10
KM 140	2009	510	–	–	30.5	3.155E-09	6.218E-10
JMF	2009	591	–	–	35.2	1.968E-09	6.337E-10

- Cluster III: medium salt content and high terrigenic ^{4}He (AWSA 3, 12 and 13)

- Cluster IV: highest salinity, but only medium terrigenic ^{4}He content (AWSA 15)

One should recall, that the terrigenic ^{4}He content is an indicator of groundwater age. As Cluster I and II are both lowly mineralized, terrigenic ^{4}He is a better indicator than E. C. to trace the processes taking place in the well field. Therefore, in the following the other physical parameters are related to the terrigenic ^{4}He instead of E. C.

pH

The pH of the sampled water has only been noted on the 2010 and 2012 campaigns and is compiled in table 6.2 and visualized in the terrigenic ^{4}He-vs.-pH plot in figure 6.9. Apparently, the pH values of these campaigns are shifted against each other, which is likely due to the usage of different calibration solutions. However, a general pattern is discernible: all wells affected by salinization have a significantly lower pH value than the other wells. Also the clusters introduced above can be differentiated. This trend may be an indicator that water from the saline wells originates from a different aquifer material. The basalt aquifer is made up of alkaline magmas, as described in chapter 4.3. This trend in pH therefore suggests that those wells containing only little terrigenic He are stronger influenced by water from the basaltic regime of the shallow aquifer than the wells with elevated terrigenic ^{4}He, which implies a correlation between water age and pH.

Temperature

The water temperatures at the time of sampling show a similar pattern, as displayed in figure 6.9. All those wells with an elevated He amount are significantly warmer than those with almost no terrigenic ^{4}He. Again, the clusters are clearly visible. Cluster II water is as warm as cluster III water, although it is not affected by an increased salinity, but has an elevated He concentration. The AWSA 15 sample of 2012 is much colder than all other samples. At the time of sampling this well showed huge air bubbled by shoves. Presumably the pump sucked soil air, which affected the water temperature as well as the pH (and other parameters). Higher water temperatures argue for a deeper origin of the respective water.

Dissolved oxygen

Data for dissolved oxygen in the AWSA wells is only available for the 2010 sampling trip. As figure 6.9 shows, all wells with a higher He content are depleted in dissolved oxygen. In the case of AWSA 11 the notably high O_2 concentration can be attributed to some air bubbles in the measurement bucket, as the pump apparently drew some air. As a low oxygen content is mostly found in old groundwater, this finding again supports the greater age indicated by the elevated helium content, and older water usually exists in greater depths.
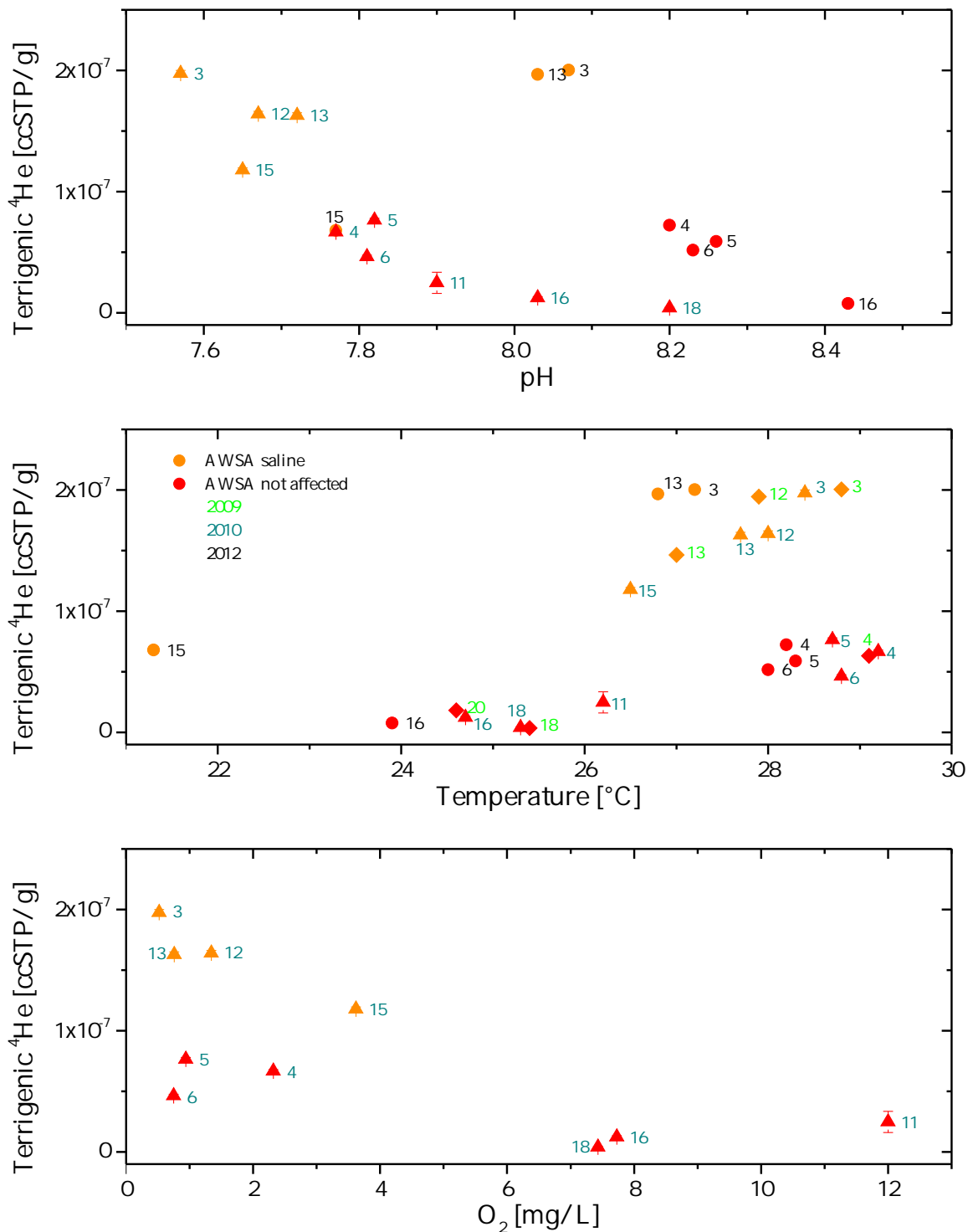
Figure 6.9: The Terrigenic ^{4}He is plotted against the physical parameters pH, water temperature and oxygen content. Although split into two branches it is obvious that those wells containing an elevated amount of terrigenic helium have lower pH values. Higher pH may indicate water originating from the alkaline basalt aquifer. A similar trend is visible in the temperature diagram, where those wells with higher helium are significantly warmer and, hence, suggest to origin from deeper layers. The depleted oxygen content in the high-helium wells argues for older water, i.e. coming from deeper layers, too.
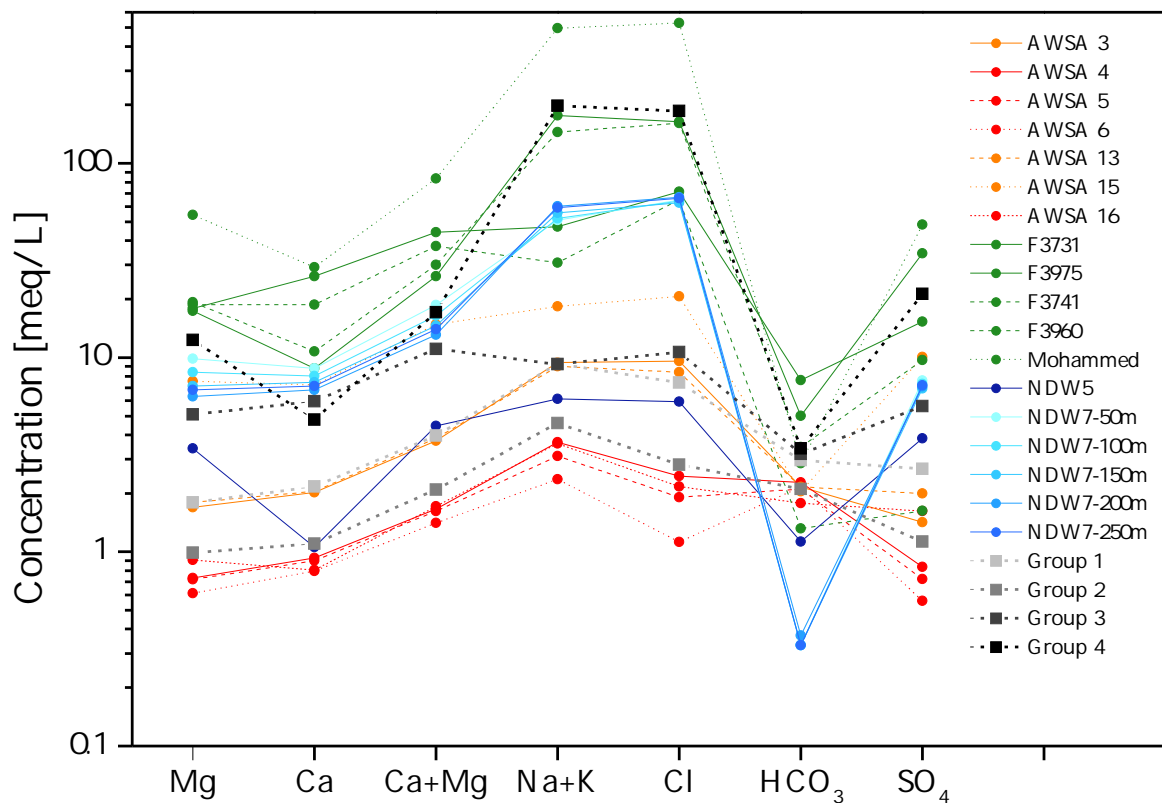
Figure 6.10: The Schoeller diagram of all sampled wells of 2012 in Azraq. The data of the water groups regarding Rimawi and Udluft [1985] is plotted as well. Red are the unaffected AWSA wells, those with elevated salt content are coded in orange. The shallow farm wells are green, NDW5 is dark blue, while NDW7 is displayed in different shades of blue, according to the sampling depth.

6.4.2 Water chemistry

The samples of the 2012 campaign were analyzed for their major ion content. Table A.4 in the appendix on page 182 lists all data together with the total sum of the cations and the anions. The calculated ion balance error (IBE) is given in the last column. All samples except AWSA 4 and 16 fall into the exceptable range of the IBE of 5 %. AWSA 4 and 16 are handled like the other samples in the further analysis, but one has to keep in mind that they might contain another substance not tested for, or at least experienced analytical trouble. Figure 6.10 compiles all data in a Schoeller diagram. Based on this diagram the wells in Azraq are assigned to the water groups introduced by Rimawi and Udluft [1985] and which are described above on page 81:

Group 1 AWSA 3 and 13

Group 2 AWSA 4, 5, 6 and 16

Group 3 AWSA 15, (F3731) and (F3960)

Group 4 F3975, Moh, NDW7 and (F3741)

(a) Group 1

(b) Group 2

(c) Group 3

(d) Group 4
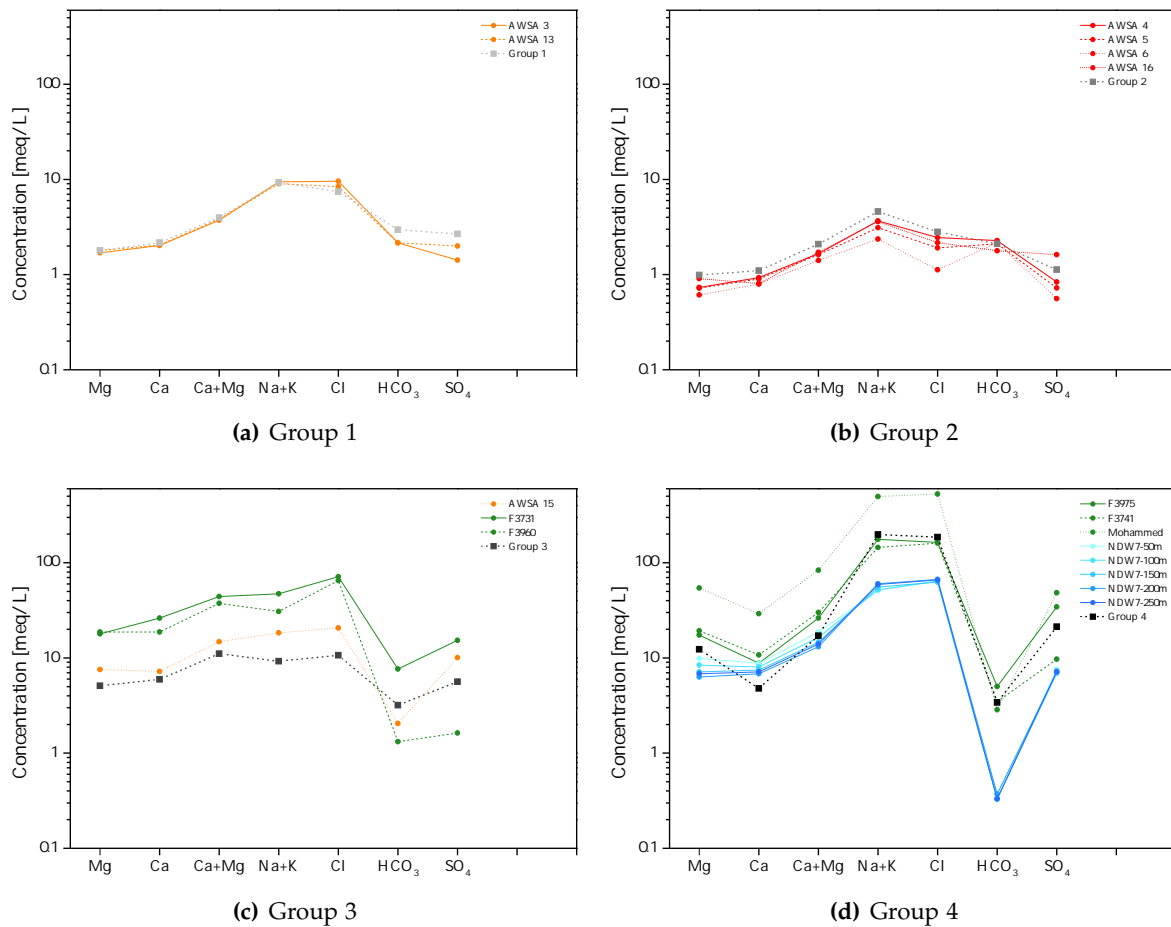
Figure 6.11: The Schoeller diagrams for the 2012 Azraq samples separated according the four water groups of Rimawi and Udluft [1985] found in the Azraq basin.

In figure 6.11 the Schoeller diagram in figure 6.10 is split up into the individual water groups to justify this assignment. The wells in brackets do not fit into that scheme that well and show particular deviations from the water group definitions. F3731 is closest to group 3, but the salinity is much higher. F3741 seems to be a mixture of groups 3 and 4, but group 4 water dominates the pattern. F3960 is most similar to group 3 water, but has a high salinity and Mg, Ca, Na and Cl are a bit too high, whereas HCO_3 and SO_4 are a bit lower. However, one may consider that for the definition of the water groups the mean concentration of each ion is employed, but within each group quite large deviations are accepted (compare the standard deviations by Rimawi and Udluft [1985] given on page 81). The NDW5 sample does not fit in this scheme at all. Its ion pattern is similar to group 4 water, but the total mineralization is far too low for Na–Cl brine water. This type of water may not be covered by the typecast of Rimawi and Udluft [1985], because they considered only water samples from the shallow aquifer in the Azraq basin.

The relative shares of cations and anions is presented in the Piper plot in figure 6.12. Regarding the cations the AWSA wells cluster very close to each other, with AWSA 3 and 13 lying
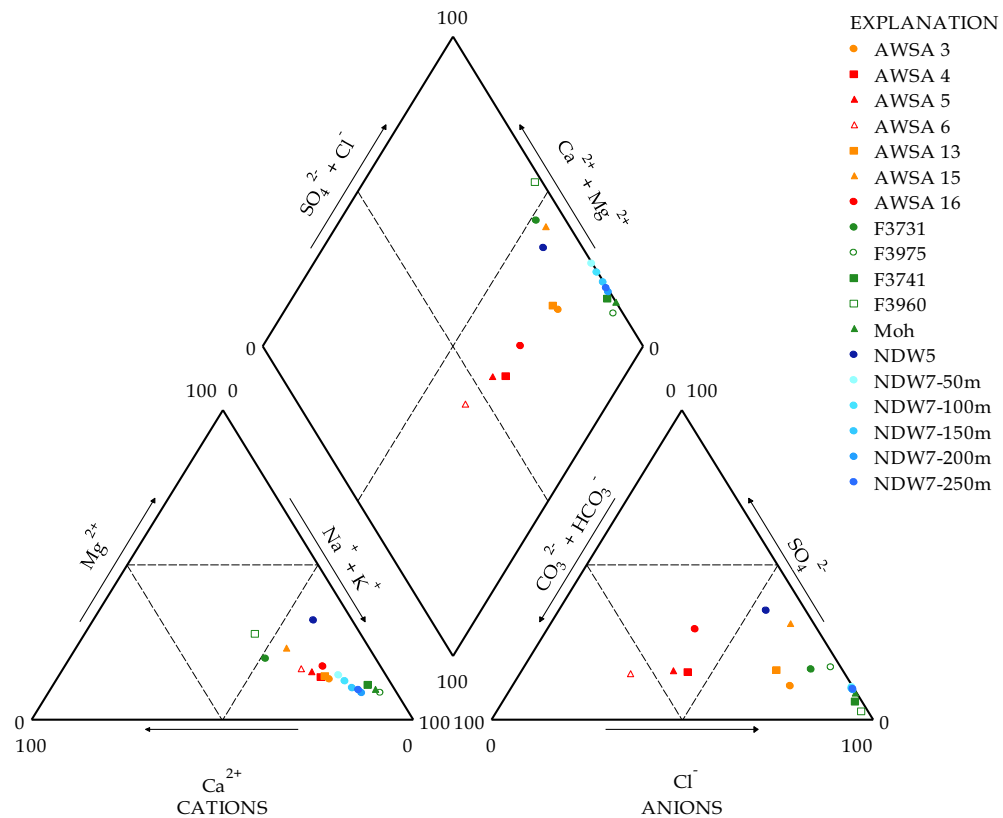
Figure 6.12: Piper diagram of the 2012 Azraq samples. As usual, the colors indicate the water group defined in the beginning of this chapter. A description is found in the text.

slightly more towards Na/K type water (see figure 2.13 for a description of the water types distinguishable in a Piper diagram); only well No 15 is a bit apart from the cluster and positioned opposite the other salinity affected wells. The picture is totally different respective the anions, where the AWSA wells are widely spread from bicarbonate to chloride type water. Although the differences in salinity between the unaffected AWSA wells (red) are small, the basic trend is also visible with AWSA 6 having the lowest salt content. All wells influenced by increasing salinity, however, are clearly shifted from the unaffected wells towards more relative chloride content which indicates admixing with water similar to F3731 and F3975. It therefore looks like an admixing of water with a higher Cl content into these AWSA wells. Both AWSA 15 and 16 contain considerably more SO_4 than the other AWSA wells.

The farm wells form two distinct clusters in the cation triangle and lie in a mixing line including the AWSA wells. In this plot it seems that AWSA 15 is influenced by water found in the shallow wells F3731 and F3960, which, indeed, are the northernmost of the sampled farm wells. Moreover, these two wells are the two farm wells assigned to water group 3, while the other farm wells are attributed to group 4. The anion plot locates all farm wells in the chloride dominated corner, where F3731 and F3975 are less governed by Cl than the others. It has to be mentioned that the grouping of farm wells in the anion triangle differs from that of the cation plot.

NDW7 shows a trend with sampling depth towards more Na + K type water, which is surprising, because this well has a closed casing in the depth range in which water samples were collected using the deep sampler and water should origin from the depth where the screen opens (upper A7 formation). Additionally, the total salinity is almost constant in all NDW7 samples. Regarding the anions, the different depths of NDW7 plot more or less identical, with practically no bicarbonate, but strong chloride influence. NDW5 obviously is different from all other water types, as it plots rather separated in the cation as well as the anion triangle.

The results from both triangle plots unite in the central diamond shaped diagram. The trends of both the AWSA wells and within the deep NDW7 well are transferred. Also the two farm well groups regarding the cations are translated into the diamond. It becomes apparent that all farm wells, both deep wells and AWSA 15 fall into the regime of Cl + SO$_4$ type water, while the two northernmost farm wells F3731 and F3960 show considerably more Ca and Mg than the other farm wells. All other AWSA wells spread in the wide field of Na + K, Ca + Mg type water, with AWSA 3 and 13 reaching almost into the Cl + SO$_4$ regime.

In order to trace the minerals the ion composition originates from, all possible ion combination were plotted against each other, but only a few yielded interesting information, which is presented in the following. As the dominant ions are Na and Cl, the dissolution of halite is obvious. Figure 6.13(a) shows that most wells fall onto the angle bisector which confirms this assumption. Dedolomitization, i. e. the weathering of dolomite (CaMg(CO$_3$)$_2$), is examined in figure 6.13(b). The AWSA wells are well described by this process, as they all lie on the angle bisector, but one has to keep in mind that the strongest influence on most of these waters is still their Na and Cl content. AWSA 15 is far more influenced by dolomite products than its salinity would suggest, which indicates that this well is additionally influenced by a source with higher dedolomitization imprint. The samples from different depths of the NDW7 well show a trend also in this consideration, but are not so well explained by dedolomitization contributing to their ion composition. The farm wells, however, scatter quite far a round the angle bisector and cannot be well described by dedolomitization.

Gypsum dissolution results in an 1:1 ratio of sulphate and calcium ions. Similar to the dolomite dissolution plot, the AWSA wells lie on the angle bisector, with the gypsum products disproportionately emphasized in AWSA 15 (figure 6.13(c)). This may be explained by gypsum lenses found in the very bottom of AWSA 15 during the drilling [Al-Momani *et al.*, 2006]. Another quite strong correlation is found between SO$_4$ and Mg, which is indicative of epsomite dissolution (figure 6.13(d)). Even the farm wells, except for F3960, plot close to the angel bisector, but no epsomite is reported from the Azraq basin.

A correlation of He and Cl is often applied as an indicator, that the weathering of Cl containing minerals also causes the release of stored radiogenic helium. Among the Azraq wells a very rough correlation is visible, though the picture is not that clear, see figure 6.14. Moreover, leaching of local minerals to explain the elevated total helium content would not explain also a higher ^{3}He content. Radiogenic production of ^{3}He originates from the decay of ^{6}Li (compare chapter 2.3.1). However, no elevated lithium content is reported for the Azraq basin. Generally, high lithium content is mainly found in granitic rock [James and Palmer, 2000], whereas in Azraq several kilometers of sediments have accumulated on top

(a) Halite dissolution

(b) Dolomite dissolution

(c) Gypsum dissolution

(d) Epsomite dissolution
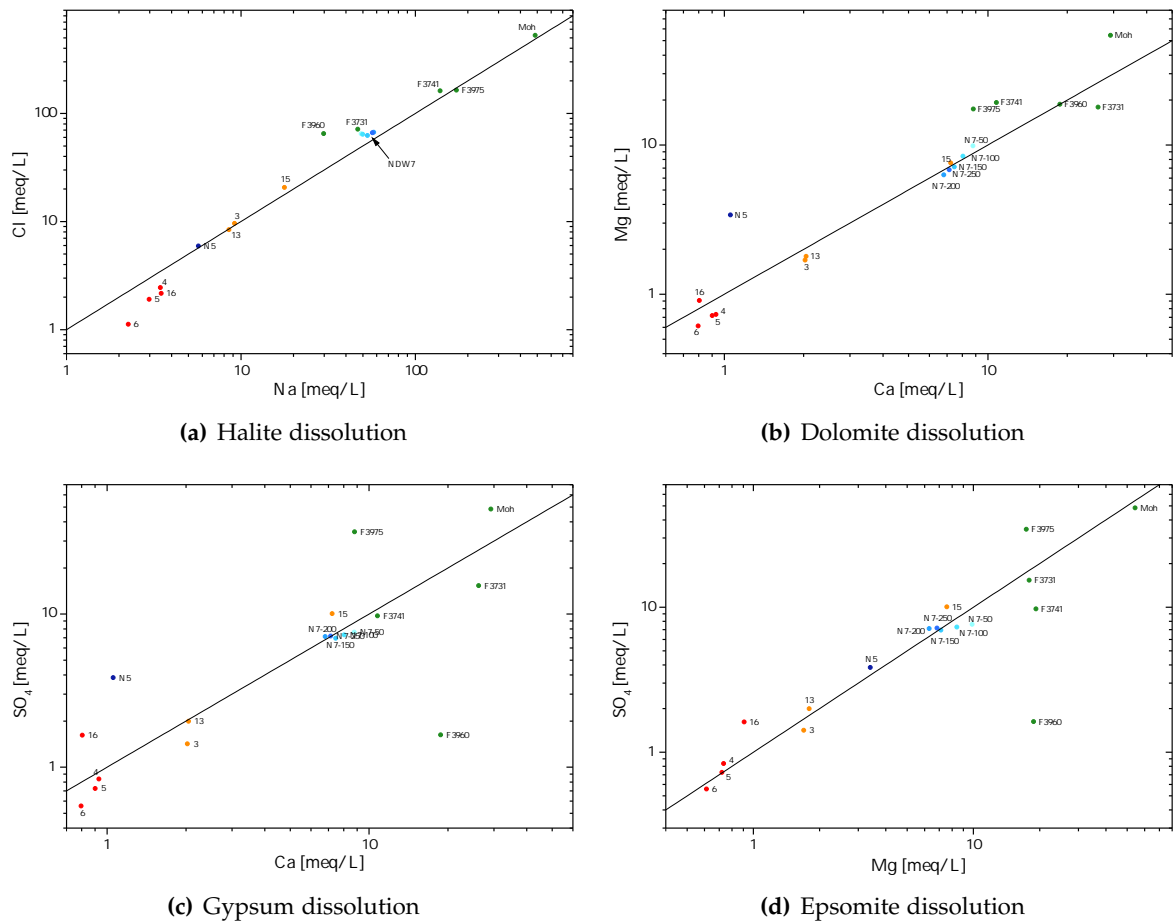
Figure 6.13: The relations of specific ion combinations indicate the dissolution of a certain mineral.

of the crystalline basement. Therefore, a matrix source of ^{3}He is rather unlikely in the Azraq depression.

Concluding, halite dissolution is the dominant cause of the salinity in most of the wells, but other weathering processes play a role in the ion composition as well.

In order to test the salinization scenarios introduced by Al-Momani *et al.* [2006], a simple three component mixing model based on the water chemistry data is applied. Thereby, the ionic patterns of AWSA 3, 13 and 15 are attempted to be characterized as mixture of middle aquifer water (D), shallow water from the Sabkha (S), and of water originating from the north (N). Regarding every tracer, the following equation has to be fulfilled:

$$c_W = x_D \cdot c_D + x_S \cdot c_S + x_N \cdot c_N, \tag{6.1}$$

where c_W is the concentration of ion i found in the respective AWSA well, c_D, c_S and c_N the concentrations of the same ion in the reservoirs D, S and N. The x_S are the relative contributions of the respective source to the final ion content abstracted from the well. As $\sum x \equiv 1$,
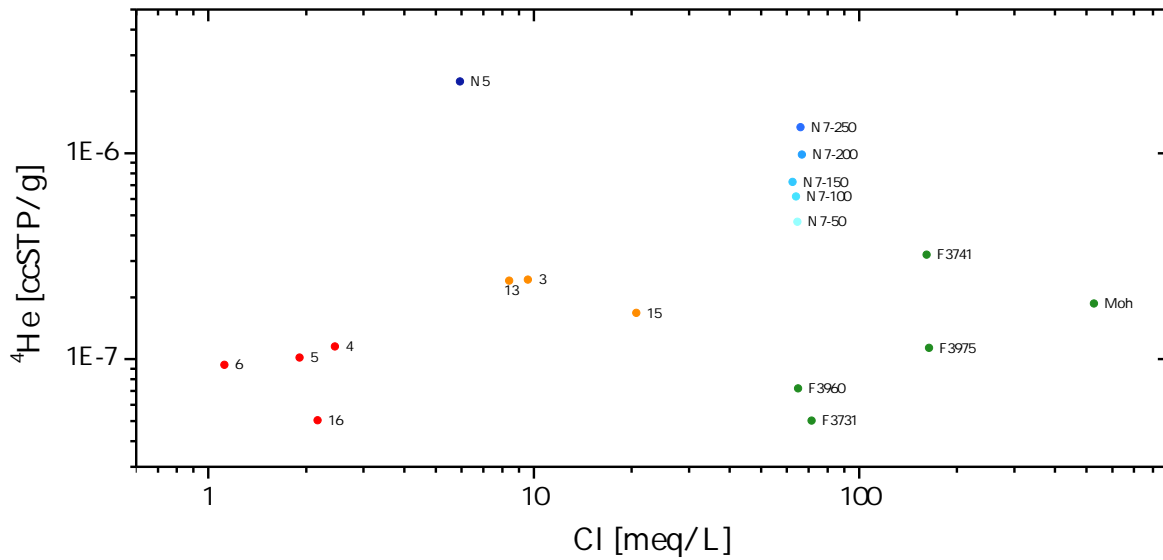
Figure 6.14: Only a very rough correlation between total He content and chloride within the AWSA well field is observed. Together with the high ^{3}He content found in the saline wells it is very unlikely that matrix dissolution is the source of radiogenic helium.

one can eliminate one of the x_S:

$$c_W = x_S(c_S - c_D) + x_N(c_N - c_D) + c_D \tag{6.2}$$

A combination of two ions leads to two equations, having two variables and therefore results in an unambiguous result for the relative contributions.

The deep reservoir concentration, c_D, is defined as the average of the 200 and 250 m depth samples of NDW7. The unaffected AWSA water (c_N) reaching the well field from the north is considered to be the water of AWSA 11 as the only member of cluster I sampled in 2012. Representative of the shallow Sabkha water ion content, c_S, the average of the wells F3731 and F3960 is assumed, because these two wells are closest to the well field. Besides, both belong to group 3 water after Rimawi and Udluft [1985], while the other farm wells are better described by group 4.

The result for several combinations of dissolved ions is presented in table 6.3. Combinations including SO_4 and HCO_3 resulted generally in impossible contribution of the three reservoirs, i. e. when some source supplies less than zero or more than 100 %. Thus, these ions are omitted.

The admixing proportions of the three basic reservoirs of the AWSA 13 ion pattern reproduces very well with different ion combinations, as does AWSA 3 if the Ca/Mg combination is disregarded. AWSA 15, however, is not possible to interpret as a result of mixing of the defined water species. The resulting contributions vary strongly, and two ion combinations even did not yield possible contributions. This reflects the position of AWSA 15 in the anion triangle of the piper plot, where this well locates outside the range, where any mixture be-

Table 6.3: Results of the three component mixing calculations using different combination of dissolved ions. Means values and standard deviations are listed as well. All value given in %. In case of AWSA 15, the ion combinations Ca/Mg and Mg/Cl yield impossible amounts with one reservoir having very negative values. Thus, they are left blank. Also the presented ion combination Ca/Cl exhibits a slightly negative share of deep water.

Tracer combination	AWSA 3			AWSA 13			AWSA 15		
	x_S	x_N	x_D	x_S	x_N	x_D	x_S	x_N	x_D
Na/Cl	1.4	88.1	10.4	-0.2	89.9	10.3	5.2	71.1	23.8
Na/Mg	2.1	87.9	10.0	3.3	88.7	8.0	38.0	59.6	2.4
Na/Ca	2.7	87.7	9.6	3.2	88.7	8.1	26.7	63.5	9.7
Ca/Mg	5.4	94.5	0.1	2.7	87.4	9.9			
Ca/Cl	2.9	88.2	8.9	3.7	90.0	6.2	30.0	71.7	-1.7
Mg/Cl	2.2	88.2	9.6	4.0	90.0	5.9			
Mean value	2.8	89.1	8.1	2.8	89.1	8.1	25.0	66.5	8.6
s. d.	1.4	2.7	4.0	1.5	1.0	1.9	14.0	5.9	11.2

tween the three water species would plot. This well seems to be influenced by an additional mineral source which is not covered by these simple three component mixing calculations.

6.4.3 Tritium, carbon and radon

Tritium data was measured for every well and all campaigns. As shown in table 6.4 the tritium content is below the detection limit of 2 TU in almost all wells in 2009 and 2010. However, in 2012 most of the AWSA wells have significantly higher tritium content compared to the previous campaigns. This fact is attributed to measurement problems during the analysis run of these samples. Hence the tritium data of the farm wells and the deep wells is also questionable. Some tritium content in the shallow farm wells, however, would not be surprising due to possible local recharge of surface runoff gathering in the Sabkha during storm events. The wells in the northern part of the Azraq basin, where young groundwater might be expected due to local precipitation, show no tritium content as well.

The carbon isotopy has only been analyzed for some selected AWSA wells of the 2010 sampling trip (see table 6.4). Although this data set is incomplete, the wells of clusters III and IV (AWSA 12, 13 and 15) are slightly less depleted than those of cluster I and II (AWSA 4, 5, 11 and 18). This may be a hint that the first-mentioned wells draw water which is in contact with different aquifer rock material than the latter ones.

The carbon-14 content has been determined on very few samples, too. AWSA 4, 5 and 12 can be considered as practically ^{14}C free, i.e. their water is several ten thousands of years old. AWSA 15, however, has a ^{14}C activity of almost 28 pmC. This is in accord with the data published by Al-Momani *et al.* [2006], who found elevated ^{14}C activity only for AWSA 11 (23 pmC) and AWSA 15 (38 pmC), sampled earlier than 2002. This strongly suggests that

Table 6.4: Tritium and carbon data of all sampled wells in the Azraq basin. The tritium data of 2012 are questionable due to analytic problems. Negative tritium values are due to background correction and the waters can be considered tritium free. Analysis for $\delta^{13}C$ and ^{14}C have only been done for some selected wells of the AWSA well field.

Well	Year	Tritium TU	Δ Tritium	$\delta^{13}C$ ‰	$\Delta\delta^{13}C$ ‰	^{14}C pmC	$\Delta^{14}C$ pmC
AWSA well field							
AWSA 3	2009	-0.40	0.95	–	–	–	–
	2010	-0.12	0.94	–	–	–	–
	2012	3.08	0.94	–	–	–	–
AWSA 4	2009	0.89	0.95	–	–	–	–
	2010	-0.12	0.87	-11.40	0.10	2.81	0.04
	2012	1.83	0.93	–	–	–	–
AWSA 5	2010	1.43	0.97	-11.63	0.10	2.48	0.04
	2012	1.13	0.95	–	–	–	–
AWSA 6	2010	0.20	0.87	–	–	–	–
	2012	1.40	0.88	–	–	–	–
AWSA 11	2010	0.94	0.90	-11.04	0.10	–	–
AWSA 12	2009	-0.44	0.87	–	–	–	–
	2010	0.53	0.96	-10.41	0.10	2.03	0.04
AWSA 13	2009	-0.97	0.95	–	–	–	–
	2010	0.62	0.97	-8.56	0.10	–	–
	2012	6.45	1.02	–	–	–	–
AWSA 15	2010	1.89	0.97	-10.12	0.10	27.62	0.13
	2012	4.16	1.02	–	–	–	–
AWSA 16	2010	1.19	0.96	–	–	–	–
	2012	-2.37	0.95	–	–	–	–
AWSA 18	2009	-0.24	0.86	–	–	–	–
	2010	2.05	0.98	-11.98	0.10	–	–
AWSA 20	2009	-0.57	0.90	–	–	–	–
Farm wells							
F3731	2012	1.87	0.92	–	–	–	–
F3975	2012	0.58	0.80	–	–	–	–
F3741	2012	2.65	0.95	–	–	–	–
F3960	2012	3.40	0.93	–	–	–	–
Moh	2012	2.57	0.94	–	–	–	–
Deep wells							
NDW5 250m	2012	2.11	0.95	–	–	–	–
NDW7 50m	2012	1.09	0.95	–	–	–	–
NDW7 250m	2012	-0.42	0.85	–	–	–	–
Northern wells							
Mkeifteh 2	2009	-0.93	0.89	–	–	–	–
KM 140	2009	-0.85	0.89	–	–	–	–
JMF	2009	1.13	0.95	–	–	–	–

AWSA 11 and 15 draw younger water or at least admixed young groundwater into the old water that mainly prevails in the AWSA well field. According to this data AWSA 15 draws less young water today compared to > 10 years ago, which needs to be compensated by older water.

The radon concentration in groundwater is an indicator of the radium content of the surrounding rock matrix. Three AWSA wells were analyzed for their radon activity on the 2012 field trip: AWSA 13 $(14\,801 \pm 836)$ Bq/m^3, AWSA 15 $(41\,010 \pm 1141)$ Bq/m^3 and AWSA 16 (1589 ± 409) Bq/m^3. The much lower activity in the unaffected well AWSA 16 is another hint that this well feeds from a different reservoir than the two saline wells.

6.4.4 Stable isotopes

The stable isotopes data of all sampled wells in Azraq is compiled in table 6.5 and is displayed in the δ^2H vs. δ^{18}O plot in figure 6.15 alongside the Jordanian meteoric water line (JMWL) [Bajjali, 2012] and the global meteoric water line (GMWL). The measurements of the AWSA well field water forms three obvious groups, according to their year of sampling. It is quite unlikely that the water of the well field shifted in total over the years. Probably there were some complications in the deuterium measurements (especially as the 2012 samples were analyzed in a different laboratory with another measurement principle, see chapter 3.3), as the δ^{18}O values correspond with each other over the years. For the interpretation of admixing in the AWSA wells, deuterium is therefore only in the 2012 samples considered in the following analysis, which is not a big disadvantage because the farm wells and the deep wells as possible contributors are also just analyzed in the 2012 campaign. However, a potential temporal trend in the stable isotope data between 2009 and 2012 is veiled behind those analytical problems.

In general, all sampled wells are shifted from the local meteoric water line (JMWL) towards the right. This indicates a more or less strong influence of evaporation after the rainwater reaches the land surface for all water found in the Azraq basin. The shallow farm wells in the central mud pan are evidently most affected by evaporation processes, as they lie far away from the local meteoric water line and on an evaporation line which also includes the AWSA groundwater. This evaporation line (drawn only for the 2012 samples) intersects the JMWL at an isotopic composition of δ^{18}O $\approx -7.5\,‰$ and δ^2H $\approx -36\,‰$. Meteoric water in Azraq has a composition of δ^{18}O $= -5.16\,‰$ and δ^2H $= -24.56\,‰$ [Bajjali, 2012]. The only precipitation gauge stations in Jordan, which measure a similar isotope concentration, are Ras Munif (close to Irbid, 1150 masl, δ^{18}O $= -6.86\,‰$, δ^2H $= -30.38\,‰$) and Shoubak (south Jordan, close to Petra, 1475 masl, δ^{18}O $= -6.71\,‰$, δ^2H $= -30.35\,‰$) [Bajjali, 2012]. This indicates that water in the AWSA wells originates from high altitudes. More interesting, however, is the fact that also the groundwater abstracted by the shallow farm wells originates to a great extent from high altitudes. Recharge by local precipitation, therefore, plays a minor role in the Azraq Oasis. Most of the local recharge comes from flash floods forming at Jabal ad-Druze and rushing to the central depression, where the water needs some time to seep away through the badly permeable mud pan surface and experiences strong evaporative influences.

Table 6.5: Stable isotope data of all sampled wells in the Azraq basin. Deuterium excess, *d*, is calculated according to equation 2.10.

Well	Year	^{18}O ‰	Δ^{18}O ‰	^{2}H ‰	Δ^{2}H ‰	d ‰	Δd ‰
AWSA well field							
AWSA 3	2009	-6.25	0.05	-30.75	0.26	19.25	0.66
	2010	-6.28	0.05	-32.29	0.26	17.95	0.66
	2012	-6.26	0.05	-33.52	0.07	16.60	0.48
AWSA 4	2009	-6.37	0.05	-30.58	0.26	20.38	0.66
	2010	-6.41	0.05	-32.22	0.26	19.06	0.66
	2012	-6.35	0.03	-33.14	0.04	17.63	0.29
AWSA 5	2010	-6.41	0.05	-32.54	0.26	18.74	0.66
	2012	-6.35	0.05	-33.13	0.13	17.68	0.53
AWSA 6	2010	-6.33	0.05	-31.56	0.26	19.08	0.66
	2012	-6.31	0.04	-32.83	0.27	17.65	0.60
AWSA 11	2010	-6.24	0.05	-31.11	0.26	18.81	0.66
AWSA 12	2009	-6.34	0.05	-31.05	0.26	19.67	0.66
	2010	-6.29	0.05	-32.50	0.26	17.82	0.66
AWSA 13	2009	-6.32	0.05	-30.46	0.26	20.10	0.66
	2010	-6.34	0.05	-32.18	0.26	18.54	0.66
	2012	-6.38	0.03	-33.65	0.10	17.36	0.31
AWSA 15	2010	-6.16	0.05	-31.11	0.26	18.17	0.66
	2012	-6.16	0.04	-32.93	0.11	16.37	0.42
AWSA 16	2010	-6.19	0.05	-30.99	0.26	18.53	0.66
	2012	-6.16	0.02	-32.02	0.14	17.25	0.33
AWSA 18	2009	-6.17	0.05	-29.27	0.26	20.09	0.66
	2010	-6.09	0.05	-30.57	0.26	18.15	0.66
AWSA 20	2009	-6.12	0.05	-30.51	0.26	18.45	0.66
Farm wells							
F3731	2012	-5.80	0.05	-31.90	0.32	14.48	0.68
F3975	2012	-5.47	0.04	-31.47	0.08	12.32	0.44
F3741	2012	-3.62	0.04	-25.32	0.06	3.67	0.41
F3960	2012	-5.28	0.05	-30.72	0.10	11.55	0.48
Moh	2012	-3.87	0.06	-26.98	0.11	3.97	0.59
Deep wells							
NDW5 684m	2012	-4.77	0.05	-31.19	0.09	6.99	0.52
NDW7 50m	2012	-5.16	0.05	-31.99	0.19	9.33	0.61
NDW7 100m	2012	-5.30	0.02	-32.84	0.08	9.54	0.21
NDW7 150m	2012	-5.31	0.03	-33.53	0.07	8.93	0.30
NDW7 200m	2012	-5.45	0.07	-34.07	0.20	9.53	0.75
NDW7 250m	2012	-5.41	0.02	-33.89	0.29	9.35	0.46
Northern wells							
Mkeifteh 2	2009	-6.07	0.05	-27.53	0.26	21.03	0.66
KM 140	2009	-6.34	0.05	-30.46	0.26	20.26	0.66
JMF	2009	-6.51	0.05	-30.36	0.26	21.72	0.66
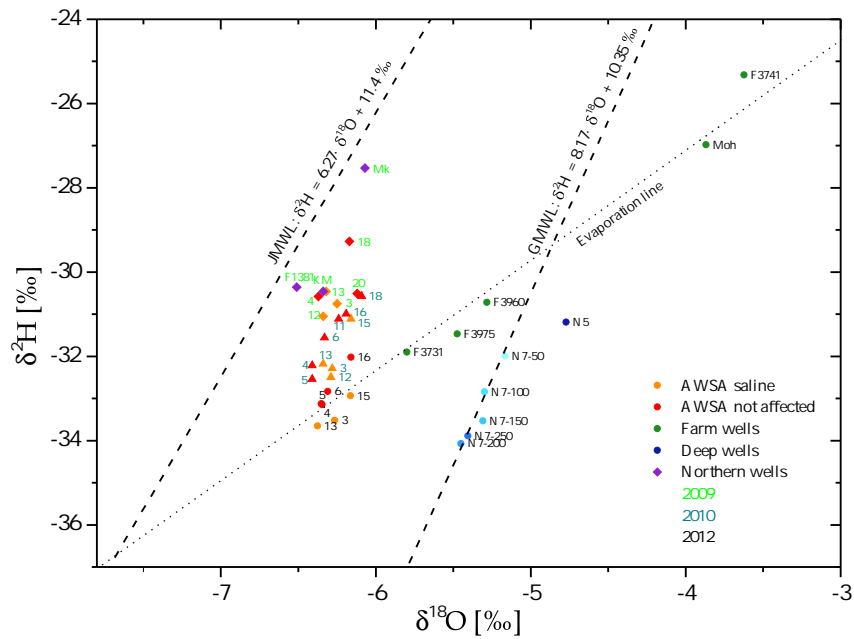
Figure 6.15: Stable isotope data of all sampled wells in the Azraq basin. All wells in Azraq show signals of evaporation. The shallow farm wells and the AWSA wells fall on the same evaporation line. The AWSA wells are shifted in their deuterium isotopy according to the year of sampling (see text for explanation). The shallow farm wells are obviously strongly influenced by evaporation. Samples from different depth of NDW-7 scatter along the GMWL and indicate leakage of shallow groundwater from the Sabkha into the deep well. NDW-5 plots a little bit off the GMWL. Error bars are omitted for more clarity.
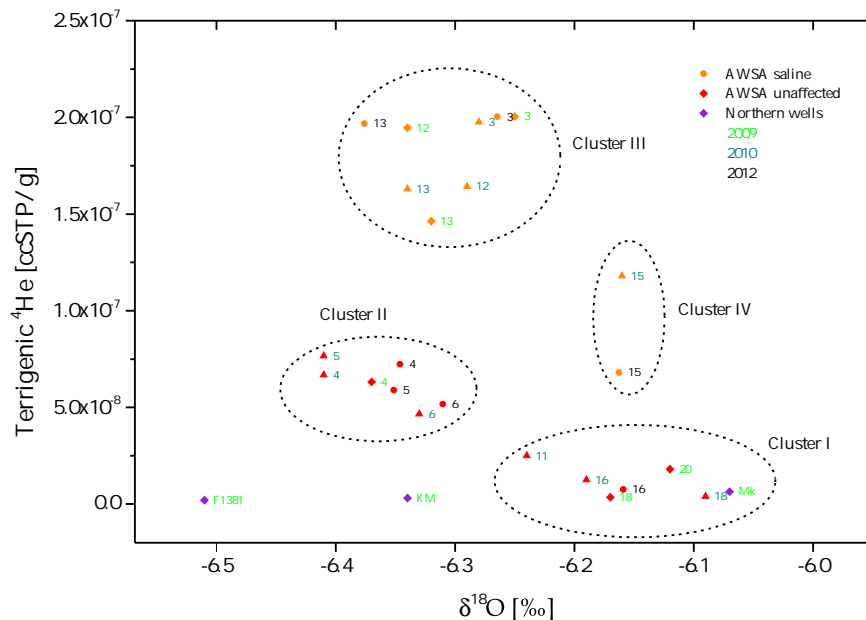
Figure 6.16: Those wells which have an elevated ^{4}He content (cluster II and III) are slightly more depleted than the unaffected wells (cluster I). Although affected by salinization, well No 15 plots a bit away from the other saline wells. Error bars are omitted for clearity reasons.

The samples collected from different depth of the NDW-7 borehole line up along the GMWL. The deeper the water sample is from, the more depleted it is in stable isotopes. This trend may indicate leakage of shallow groundwater into the deep well, where the infiltrating water has an isotopy of about $\delta^{18}O \approx -4.8\,‰$ and $\delta^2H \approx 29.5\,‰$, i.e. where the GMWL and the evaporation line intersect. This might explain the trend with depth observed in other tracers as well. The NDW-5 sample is a bit less depleted than all NDW-7 samples, especially in $\delta^{18}O$ which shifts it a bit to the right. Corresponding to the position of the NDW-7 samples close to the GMWL, the δ^2H excess is close to $10\,‰$.

Two of the northern wells (F1381 and especially KM140) have a very similar isotopic signature to the unaffected AWSA wells. This describes the fact that the groundwater found in the AWSA well field originates from the slopes of Jabal ad-Druze in the north. Only Mkeifteh 2 is distinctly enriched in deuterium compared to the AWSA wells.

Despite the analytical problems, within all groups of AWSA data it can be recognized, that those wells influenced by rising salinity and as well as those wells of cluster II are a bit more depleted in deuterium compared to the wells of cluster I. This suggests that the terrigenic ^{4}He carrying water is slightly more depleted in deuterium. AWSA 15 may be an exception.

It can also be seen, that within each sampling year those AWSA wells which have an increased He content are a little bit more depleted in $\delta^{18}O$ than the unaffected wells. This correlation is well recognizable in figure 6.16, where the terrigenic ^{4}He is plotted against the oxygen isotopy. Clusters I wells plot less depleted than cluster II and III. However, AWSA 15 as the only member in cluster IV is enriched as well although it exhibits a high mineralization.

6.4.5 Noble gases

In 2009 and 2010, for each sampled well two copper tube samples were collected and analyzed. The 2009 samples were measured in Run 53 and Run 55 (compare the overview of measurement runs in appendix A.6). Run 55, however, suffered from several incidents and the obtained data is partly questionable. Therefore, only the data of Run 53 is considered for the analysis of the 2009 samples. Similarly, the 2010 samples were measured in Run 60 and Run 65, but the first one was interrupted several times and the properness of the results is doubtful, i.e. only the Run 65 data is used for the further analysis. The sole exception is AWSA well No 11, which was measured in Run 60 only because the double sample broke. But, to make it clear, the results of two measurement runs deviate only little. The 2012 samples were measured only once, in Run 72 (and a few samples in Run 71, which was terminated accidentally), and only in cases the data looked fishy a double sample was analyzed.

Noble gas raw data is treated like described in chapter 3.6.2 using the group's own software WUCEM. The final noble gas isotope concentrations are given in table 6.6.

Noticeable are two samples with distinctly high noble gas content: AWSA 11 from 2010 and the 2012 sample of AWSA 15. Both show a typical, but very strongly pronounced, excess air pattern in their heavy noble gases, i.e. the relative excess is highest in neon and lowest

Table 6.6: Concentration of all measured noble gas isotopes of the samples from the Azraq basin including their analytical errors, given in ccSTP/g.

	³He	Δ³He	⁴He	Δ⁴He	²⁰Ne	Δ²⁰Ne	²²Ne	Δ²²Ne	³⁶Ar	Δ³⁶Ar	⁴⁰Ar	Δ⁴⁰Ar	⁸⁴Kr	Δ⁸⁴Kr	¹³²Xe	Δ¹³²Xe
2009																
AWSA 3	2.742E-13	1.115E-14	2.422E-07	1.979E-09	1.544E-07	7.872E-10	1.578E-08	7.872E-11	8.466E-07	2.796E-08	2.582E-04	8.479E-07	3.238E-08	5.833E-10	2.020E-09	3.455E-11
AWSA 4	8.548E-14	3.673E-15	1.061E-07	9.250E-10	1.544E-07	7.748E-10	1.575E-08	7.748E-11	8.824E-07	2.938E-08	2.618E-04	8.760E-07	3.210E-08	5.718E-10	2.014E-09	3.501E-11
AWSA 12	2.592E-13	1.009E-14	2.367E-07	1.936E-09	1.555E-07	7.686E-10	1.584E-08	7.748E-11	8.793E-07	2.800E-08	2.604E-04	8.558E-07	3.236E-08	5.848E-10	2.075E-09	3.596E-11
AWSA 13	1.409E-13	5.662E-15	1.908E-07	1.807E-09	1.577E-07	8.089E-10	1.613E-08	8.089E-11	8.946E-07	2.892E-08	2.701E-04	9.114E-07	3.465E-08	5.855E-10	2.118E-09	3.532E-11
AWSA 18	6.371E-14	2.934E-15	4.563E-08	3.755E-10	1.547E-07	7.047E-10	1.623E-08	9.279E-11	9.279E-07	2.892E-08	2.757E-04	9.177E-07	3.435E-08	6.166E-10	2.139E-09	3.736E-11
AWSA 20	6.080E-14	2.786E-15	6.141E-08	5.134E-10	1.583E-07	9.449E-10	1.583E-08	9.655E-11	9.655E-07	2.871E-08	2.837E-04	9.827E-07	3.580E-08	6.103E-10	2.233E-09	3.879E-11
F1381	6.528E-14	2.858E-15	4.492E-08	3.698E-10	1.550E-07	7.108E-10	1.581E-08	7.923E-11	8.832E-07	2.876E-08	2.572E-04	8.482E-07	3.211E-08	5.772E-10	2.067E-09	3.529E-11
KM 140	6.327E-14	2.698E-15	4.468E-08	3.674E-10	1.477E-07	6.848E-10	1.518E-08	8.040E-11	7.876E-07	2.963E-08	2.382E-04	7.796E-07	2.935E-08	5.474E-10	1.851E-09	3.204E-11
Mkeifieh 2	6.656E-14	2.700E-15	4.792E-08	3.952E-10	1.553E-07	6.897E-10	1.553E-08	8.023E-11	8.976E-07	2.795E-08	2.644E-04	8.520E-07	3.456E-08	6.017E-10	2.122E-09	3.633E-11
2010																
AWSA 3	2.840E-13	1.077E-14	2.398E-07	2.087E-09	1.524E-07	8.999E-10	1.555E-08	1.055E-10	9.013E-07	2.118E-08	2.553E-04	8.723E-07	3.191E-08	8.299E-10	1.844E-09	7.234E-11
AWSA 4	9.166E-13	3.781E-15	1.082E-07	8.690E-10	1.509E-07	9.388E-10	1.501E-08	1.777E-10	8.242E-07	2.541E-08	2.560E-04	8.963E-07	3.168E-08	8.470E-10	1.962E-09	7.388E-11
AWSA 5	7.836E-14	2.938E-15	1.192E-07	9.606E-10	1.539E-07	1.024E-09	1.573E-08	1.024E-10	8.607E-07	2.123E-08	2.589E-04	7.662E-07	3.266E-08	8.888E-10	2.008E-09	7.977E-11
AWSA 6	6.377E-14	2.756E-15	8.729E-08	6.994E-10	1.472E-07	9.892E-10	1.501E-08	2.272E-10	8.305E-07	1.941E-08	2.485E-04	7.799E-07	3.121E-08	7.799E-10	1.934E-09	7.490E-11
AWSA 11	8.648E-13	5.356E-15	5.537E-07	4.214E-09	1.719E-06	7.613E-10	1.758E-07	4.368E-10	1.295E-06	1.295E-08	1.055E-03	3.429E-06	1.501E-07	1.223E-09	4.356E-09	1.223E-10
AWSA 12	2.145E-13	7.961E-15	2.065E-07	1.791E-09	1.532E-07	1.086E-09	1.546E-08	1.086E-10	8.877E-07	2.560E-08	2.582E-04	7.587E-07	3.178E-08	8.395E-10	2.081E-09	8.454E-11
AWSA 13	1.543E-13	5.933E-15	2.054E-07	1.755E-09	1.541E-07	8.647E-10	1.574E-08	8.647E-11	8.647E-07	2.630E-08	2.630E-04	9.113E-07	3.332E-08	8.198E-10	2.213E-09	8.931E-11
AWSA 15	9.598E-14	3.562E-15	1.602E-07	1.327E-09	1.586E-07	1.088E-09	1.586E-08	1.088E-10	8.877E-07	2.666E-08	2.666E-04	9.391E-07	3.412E-08	8.052E-10	1.962E-09	8.018E-11
AWSA 16	6.243E-14	2.467E-15	5.772E-08	4.613E-10	1.642E-07	9.034E-10	1.678E-08	1.071E-10	9.620E-07	2.231E-08	2.765E-04	9.589E-07	3.523E-08	8.771E-10	2.288E-09	9.116E-11
AWSA 18	5.545E-14	2.039E-15	4.506E-08	3.517E-10	1.508E-07	8.709E-10	1.541E-08	1.089E-10	8.786E-07	2.240E-08	2.658E-04	9.727E-07	3.436E-08	8.965E-10	2.115E-09	8.331E-11
2012																
AWSA 3	2.906E-13	1.097E-14	2.435E-07	2.342E-09	1.554E-07	6.190E-10	1.586E-08	8.702E-11	8.702E-07	1.226E-08	2.553E-04	8.225E-07	3.224E-08	4.335E-10	2.037E-09	4.388E-11
AWSA 4	1.026E-13	3.647E-15	1.152E-07	1.028E-09	1.544E-07	6.184E-10	1.576E-08	8.616E-11	8.616E-07	1.026E-08	2.545E-04	8.196E-07	3.191E-08	4.281E-10	1.976E-09	3.995E-11
AWSA 5	7.459E-14	2.836E-15	1.018E-07	8.994E-10	1.543E-07	6.164E-10	1.575E-08	8.607E-11	8.607E-07	1.007E-08	2.544E-04	8.228E-07	3.187E-08	4.525E-10	1.975E-09	3.977E-11
AWSA 6	7.565E-14	2.715E-15	9.373E-08	8.247E-10	1.519E-07	5.961E-10	1.548E-08	8.416E-11	8.416E-07	1.279E-08	2.547E-04	8.317E-07	3.201E-08	4.726E-10	2.051E-09	4.248E-11
AWSA 13	1.839E-13	6.690E-15	2.402E-07	2.302E-09	1.569E-07	6.130E-10	1.602E-08	8.631E-11	8.631E-07	1.348E-08	2.589E-04	8.700E-07	3.244E-08	4.128E-10	2.099E-09	4.125E-11
AWSA 15	1.616E-13	5.834E-15	1.676E-07	1.560E-09	1.602E-07	6.794E-10	1.183E-08	1.183E-10	8.791E-07	1.333E-08	3.491E-04	1.130E-06	3.930E-08	5.402E-10	2.402E-09	4.947E-11
AWSA 16	6.149E-14	2.305E-15	5.040E-08	4.336E-10	1.566E-07	7.073E-10	1.593E-08	9.152E-11	9.152E-07	1.056E-08	2.692E-04	8.791E-07	3.450E-08	4.769E-10	2.141E-09	4.724E-11
F3731	6.484E-14	2.456E-15	5.020E-08	4.309E-10	1.841E-07	7.542E-10	1.879E-08	1.043E-10	3.022E-06	1.148E-08	3.022E-04	9.749E-07	3.792E-08	5.145E-10	2.314E-09	4.812E-11
F3975	7.285E-14	2.692E-15	1.135E-07	1.021E-09	1.568E-07	6.248E-10	1.598E-08	9.088E-11	2.723E-06	1.335E-08	2.723E-04	8.877E-07	3.457E-08	4.608E-10	2.201E-09	4.514E-11
F3741	1.273E-13	4.659E-15	3.211E-07	3.116E-09	1.639E-07	6.440E-10	1.674E-08	7.204E-11	2.883E-06	1.134E-08	2.883E-04	9.398E-07	3.726E-08	4.874E-10	2.345E-09	4.943E-11
F3960	8.511E-13	3.626E-15	7.215E-08	8.924E-10	1.607E-07	1.279E-09	1.635E-08	1.328E-10	2.914E-06	1.210E-08	2.914E-04	2.220E-06	3.699E-08	5.476E-10	2.306E-09	5.250E-11
Mohammed	1.079E-13	3.947E-15	1.865E-07	2.176E-09	1.557E-07	1.294E-09	1.588E-08	9.793E-11	9.793E-07	1.186E-08	2.893E-04	2.205E-06	3.699E-08	5.665E-10	2.363E-09	4.932E-11
NDW5 684m	2.239E-12	9.090E-14	2.230E-06	4.154E-08	1.268E-07	2.084E-09	1.294E-08	7.119E-11	7.119E-07	1.344E-08	2.119E-04	2.623E-06	2.623E-08	5.461E-10	1.602E-09	4.343E-11
NDW7 50m	1.469E-13	5.740E-15	4.654E-07	9.185E-09	1.634E-07	2.067E-09	1.671E-08	9.945E-11	9.945E-07	1.907E-08	2.947E-04	3.723E-06	3.723E-08	6.127E-10	2.289E-09	5.842E-11
NDW7 100m	1.673E-13	6.612E-15	6.162E-07	1.325E-08	1.640E-07	2.416E-09	1.674E-08	2.012E-08	2.012E-06	3.963E-08	3.963E-04	6.701E-07	6.701E-08	5.759E-10	2.269E-09	5.759E-11
NDW7 150m	1.785E-13	1.399E-14	7.268E-07	1.382E-08	1.635E-07	2.388E-09	1.663E-08	1.001E-06	1.001E-06	2.035E-08	2.933E-04	3.727E-08	3.727E-08	6.732E-10	2.336E-09	6.331E-11
NDW7 200m	1.790E-13	1.381E-14	9.872E-07	2.095E-08	1.735E-07	2.971E-09	1.768E-08	1.037E-06	1.037E-06	2.285E-08	3.084E-04	7.524E-08	3.789E-08	7.524E-10	2.395E-09	6.628E-11
NDW7 250m	1.572E-13	1.414E-14	1.339E-06	2.878E-08	1.698E-07	2.905E-09	1.731E-08	1.041E-06	1.041E-06	2.288E-08	3.070E-04	4.906E-06	3.756E-08	7.492E-10	2.505E-09	7.316E-11
NDW7 300m	1.568E-13	1.461E-14	3.070E-06	6.921E-08	1.592E-07	2.775E-09	1.599E-08	1.102E-06	1.102E-06	2.406E-08	3.237E-04	5.153E-06	4.090E-08	8.331E-10	2.530E-09	6.722E-11
NDW7 544m	1.671E-13	6.941E-15	2.889E-06	5.454E-08	1.373E-07	2.276E-09	1.400E-08	1.023E-06	1.023E-06	1.966E-08	3.005E-04	4.933E-06	3.917E-08	8.127E-10	2.394E-09	6.526E-11
NDW7 569m	1.344E-13	5.964E-15	2.793E-06	5.198E-08	1.386E-07	2.260E-09	1.411E-08	9.208E-07	9.208E-07	1.709E-08	2.731E-04	4.403E-06	3.470E-08	7.263E-10	2.076E-09	5.296E-11
NDW7 ca450m	7.458E-14	3.630E-15	1.438E-06	2.691E-08	7.491E-08	1.291E-09	1.411E-08	9.134E-09	9.134E-07	2.321E-08	1.398E-04	1.761E-08	1.761E-08	3.837E-10	1.159E-09	3.035E-11

in xenon (compare figure 2.17). This expresses also in the extremely high neon excess values of AWSA 11 and 15 (2012), which are listed in table 6.7. Such high ΔNe values, defined in equation 2.27, can not be attributed to the normal excess air formation described in chapter 2.3.6.2, but are credited to air bubble formation during sampling. Indeed, AWSA 11 showed air bubbles in the sampling tubes, which mostly vanished under increased water pressure, but possibly still influenced the water. At the time of sampling AWSA 15 (2012) often had short interruptions with almost no water running anymore, where the pump seemed to run dry (it possibly did not hang deep enough in the water). Getting a sample without disturbing air bubbles was virtually impossible. KM 140, F3731 and NDW5-684m have rather low noble gas concentrations and consequently negative ΔNe values, which indicate degassing (within the aquifer or during sampling).

Table 6.7 lists the basic noble gas isotope ratios relevant for this study. The ^{3}He/^{4}He ratio of the 2009 samples is calculated by WUCEM using the "mean of isotope 1" routine, whereas it is determined by the division of the final ^{3}He and ^{4}He concentrations for the 2010 and 2012 samples, as those two isotopes are analyzed in separate steps since then (compare the description of different measurement procedures in chapter 3.6.1). ^{20}Ne/^{22}Ne is calculated by the "next neighbors" routine of WUCEM, while for ^{40}Ar/^{36}Ar the "mean of isotope 1" routine is applied.

The ^{20}Ne/^{22}Ne ratio of almost all samples matches the atmospheric value of 9.80. Only four samples differ from that. While NDW7-300m was measured, a leak occurred in the preparation line, which explains the high ^{20}Ne/^{22}Ne ratio. KM 140 and F3731 have a slightly lower ^{20}Ne/^{22}Ne ratio, which is associated with a lower total noble gas concentration (as described above). AWSA 15 (2010) has a lower ^{20}Ne/^{22}Ne ratio as well, but is inconspicuous apart from that.

A high ^{40}Ar/^{36}Ar ratio is generally a sign of very old groundwater, i.e. the presence of a substantial radiogenic ^{40}Ar amount. In those cases the total Ar concentration (needed for the inverse modeling) is calculated from ^{36}Ar only, as mentioned in chapter 3.6.4. The chosen threshold is an argon ratio of 302, which exceeds the atmospheric ratio of 295.5 by about 2 %. Only two samples exhibit ^{40}Ar/^{36}Ar ratios above this threshold: the 2010 samples of AWSA 4 and 18. However, these samples are obviously not old groundwater, as radiogenic ^{40}Ar production is always accompanied by distinct radiogenic ^{4}He production, which is not the case here. The high argon ratio, therefore, needs to be ascribed to measurement inaccuracies, although the data preparation with WUCEM did not exhibit any abnormity. Nevertheless, total Ar is calculated from ^{36}Ar for those two samples.

The final noble gas concentrations are compiled in table A.5 on page 183 and are used to determine the noble gas temperatures (NGTs) by inverse modeling using the software PANGA, as introduced in chapter 3.6.4. In the course of the calculation, each noble gas content is separated into its equilibrium and excess air component, and, in case of helium, the non-atmospheric amount.

The applied excess air model is the CE model, as it is the most versatile of all excess air models and can handle also cases of degassing. Because the Azraq samples prove to not allow a straight-forward modeling, all samples are analyzed using Monte Carlo simulations. A modeling run with 100 000 Monte Carlo simulations is performed for each sample. In

Table 6.7: The noble gas isotope ratios of all measured Azraq samples. The ³He/⁴He ratio is given in absolute value and relative to the atmospheric ratio R_A, indicated by the index *atm*. The ΔNe values are listed, too.

	³He/⁴He	Δ³He/⁴He	(³He/⁴He)$_{atm}$	Δ(³He/⁴He)$_{atm}$	²⁰Ne/²²Ne	Δ²⁰Ne/²²Ne	⁴⁰Ar/³⁶Ar	Δ⁴⁰Ar/³⁶Ar	Ne/He	ΔNe/He	ΔNe	Δ(ΔNe)
2009												
AWSA 3	1.148E-06	3.643E-08	0.830	0.026	9.802	0.004	299.78	4.66	0.701	0.007	5.35%	0.54%
AWSA 4	7.945E-07	2.496E-08	0.574	0.018	9.803	0.004	290.42	4.99	1.600	0.016	4.36%	0.58%
AWSA 12	1.089E-06	3.375E-08	0.787	0.024	9.796	0.005	296.23	4.45	0.722	0.007	5.67%	0.55%
AWSA 13	6.998E-07	2.375E-08	0.506	0.017	9.793	0.005	297.63	4.50	0.908	0.010	4.86%	0.54%
AWSA 18	1.347E-06	4.257E-08	0.974	0.031	9.786	0.005	291.80	4.67	3.727	0.035	1.85%	0.53%
AWSA 20	9.320E-07	2.960E-08	0.673	0.021	9.822	0.005	294.55	4.40	2.835	0.028	3.00%	0.58%
Mkeifteh 2	1.408E-06	4.298E-08	1.017	0.031	9.794	0.004	295.12	4.36	3.494	0.033	2.92%	0.50%
KM 140	1.355E-06	4.265E-08	0.979	0.031	9.756	0.004	297.09	5.28	3.636	0.034	3.80%	0.51%
F1381	1.404E-06	4.374E-08	1.014	0.032	9.792	0.004	294.25	4.74	3.791	0.036	5.79%	0.52%
2010												
AWSA 3	1.184E-06	4.606E-08	0.856	0.033	9.771	0.005	284.18	4.23	0.702	0.007	4.21%	0.69%
AWSA 4	8.474E-07	3.560E-08	0.612	0.026	9.810	0.012	302.39	4.57	1.537	0.016	3.39%	0.94%
AWSA 5	6.573E-07	2.521E-08	0.475	0.018	9.787	0.006	291.81	4.49	1.427	0.014	4.64%	0.65%
AWSA 6	7.306E-07	3.211E-08	0.528	0.023	9.803	0.006	299.51	4.44	1.863	0.019	1.20%	0.64%
AWSA 11	1.562E-06	9.746E-08	1.129	0.070	9.808	0.006	290.44	7.19	3.431	0.029	1178.93%	58.07%
AWSA 12	1.039E-06	3.959E-08	0.750	0.029	9.799	0.006	287.33	4.96	0.819	0.009	4.03%	0.65%
AWSA 13	7.513E-07	2.959E-08	0.543	0.021	9.801	0.006	300.25	4.50	0.829	0.009	3.94%	0.66%
AWSA 15	5.992E-07	2.279E-08	0.433	0.016	9.746	0.006	293.25	5.18	1.066	0.011	3.47%	0.67%
AWSA 16	1.082E-06	4.360E-08	0.782	0.032	9.796	0.006	289.94	4.43	3.143	0.031	9.18%	0.64%
AWSA 18	1.231E-06	4.626E-08	0.889	0.033	9.806	0.006	304.47	4.81	3.699	0.036	0.69%	0.84%
2012												
AWSA 3	1.188E-06	4.541E-08	0.858	0.033	9.795	0.004	295.85	2.32	0.704	0.007	6.11%	0.40%
AWSA 4	8.921E-07	3.190E-08	0.645	0.023	9.793	0.004	295.22	2.08	1.480	0.014	5.57%	0.41%
AWSA 5	7.370E-07	2.816E-08	0.533	0.020	9.792	0.004	300.92	2.93	1.674	0.016	5.54%	0.41%
AWSA 6	8.116E-07	2.928E-08	0.586	0.021	9.797	0.004	298.62	2.83	1.789	0.017	3.63%	0.39%
AWSA 13	7.614E-07	2.812E-08	0.550	0.020	9.794	0.004	293.66	2.12	0.720	0.007	6.60%	0.40%
AWSA 15	9.605E-07	3.510E-08	0.694	0.025	9.802	0.004	297.51	2.09	2.125	0.021	113.24%	1.46%
AWSA 16	1.230E-06	4.628E-08	0.888	0.033	9.789	0.004	294.98	2.03	3.431	0.032	4.51%	0.41%
F3731	1.301E-06	4.947E-08	0.940	0.036	9.772	0.004	294.45	2.02	4.054	0.037	20.41%	0.87%
F3975	6.452E-07	2.399E-08	0.466	0.017	9.788	0.004	300.92	2.39	1.525	0.015	4.23%	0.40%
F3741	3.957E-07	1.467E-08	0.286	0.011	9.791	0.004	295.83	2.19	0.563	0.006	6.83%	0.42%
F3960	1.202E-06	5.182E-08	0.869	0.037	9.819	0.004	296.08	2.03	2.458	0.036	4.61%	0.91%
Mohammed	5.788E-07	2.174E-08	0.418	0.016	9.810	0.004	294.84	2.09	0.921	0.013	0.74%	0.83%
NDW5 684m	9.982E-07	4.403E-08	0.721	0.032	9.811	0.004	298.20	2.05	0.063	0.002	-9.18%	1.54%
NDW7 50m	3.157E-07	1.382E-08	0.228	0.010	9.809	0.012	293.87	4.49	0.388	0.009	7.56%	1.61%
NDW7 100m	2.715E-07	1.222E-08	0.196	0.009	9.796	0.012	295.88	4.52	0.294	0.008	7.05%	1.68%
NDW7 150m	2.455E-07	1.981E-08	0.177	0.014	9.800	0.012	291.02	4.43	0.248	0.006	6.26%	1.64%
NDW7 200m	1.813E-07	1.451E-08	0.131	0.010	9.812	0.012	297.91	4.50	0.194	0.005	12.78%	2.08%
NDW7 250m	1.174E-07	1.086E-08	0.085	0.008	9.793	0.012	292.71	4.41	0.140	0.004	9.60%	2.00%
NDW7 300m	5.106E-08	4.895E-09	0.037	0.004	9.976	0.012	293.88	4.43	0.057	0.002	-0.39%	1.76%
NDW7 544m	5.861E-08	2.626E-09	0.042	0.002	9.810	0.004	295.58	2.03	0.052	0.001	-13.01%	1.48%
NDW7 569m	4.879E-08	2.310E-09	0.035	0.002	9.823	0.004	296.47	2.01	0.055	0.001	-8.53%	1.53%

most cases the Monte Carlo analysis results in a smaller error for the NGTs and the other output parameters. Above all, Monte Carlo analysis reveals samples where the traditional noble gas fitting routine results in bad NGTs, accompanied by unrealistic values for the parameters A and F. The details of the Monte Carlo evaluation is given in appendix A.8, including information about which part of the simulations is considered in the analysis and which ones are discarded.

A check using the UA excess air model revealed no cases of degassing among the Azraq samples from all campaigns. Hence, as initial parameters for the fitting routine the following values are chosen for all samples: Excess air factor $A = 0.01$, temperature $T = 19\,°C$, salinity $S = 0\,mg/L$ and the fractionation factor $F = 0.5$. The air pressure at the groundwater table in the infiltration area is quite tricky to guess for the Azraq basin. The shallow aquifer is mainly recharged at the slopes of 1500 m high Jabal ad-Druze. No information about the depth to the water table could be obtained for this mountain. However, thicknesses of the unsaturated zone of over 400 m are reported from close to the Jordan/Syrian border [Margane *et al.*, 2002], which would correspond to a groundwater table at about 700 masl. It is therefore assumed that the average altitude of the water table is 800 masl, which corresponds to an air pressure $p = 920\,mbar$ at the water table. The middle aquifer is recharged in the Jordan highlands, mainly in altitudes between 700 and 1100 masl. The static water level in wells in the highlands varies between a few 10 meters and more than 100 m below the surface [WAJ, 2010]. Hence, due to the lack of more information about exact groundwater flow lines, an assumed groundwater table altitude of 800 masl, too, seems to be acceptable. Eventually, the assumed groundwater table altitude in the recharge area influences the resulting noble gas temperature (i. e. if a too high altitude is assumed, the NGTs are calculated to be colder). However, since the main results in this chapter concern the non-atmospheric helium content of the samples and the fact that the helium solubility depends only slightly on the recharge temperature, a biased NGT determination would only have a very little effect on the amount of non-atmospheric helium.

Table 6.8 lists the resulting NGTs and the corresponding values of the fit parameters A and F. The values presented are means of all selected Monte Carlo simulations, the respective errors are the standard deviations of the same set of simulations. Also the mean and standard deviation of the distribution of χ^2 values is given. The new fitting routine implemented in PANGA reveals that many samples are described as quasi-UA type, identifiable by the extreme values of the fit parameter $|F|$. Although these numbers do not have a physical explanation, they lead to reasonable NGT and, hence, F is only seen as a fit parameter. More details about this issue is given in chapter 3.6.4. χ^2 as a measure of goodness of the fit is in an acceptable range for all analyses. In addition, table 6.8 presents the modeled atmospheric ^{3}He and total helium concentrations beside the non-atmospheric components (i. e. atmospheric component subtracted from the total measured signal).

The noble gas temperatures found in the Azraq basin seem to be quite reasonable. Elevated NGTs found in the AWSA well field reflect the deep unsaturated zone, where the ambient temperature at the groundwater table, where equilibration between water and soil air takes place, is considerably higher than the mean annual air temperature. The farm wells have NGTs between 20 and 23 °C, suggesting local recharge in the Sabkha. Recharge temperatures from the NDW7 well range from around 21 °C in the uppermost 250 m, around

Table 6.8: The modeled parameters NGT, A and F together with the resulting modeled atmospheric content (i. e. equilibration plus excess air component), ^{3}He^{mod} and He^{mod}, the calculated non-atmospheric components, Δ^3He$^{non\text{-}atm}$ and ΔHe^{ter}, and the χ^2 values. High values of $|F|$ indicate the quasi-UA limiting case, as explained in chapter 3.6.4.

Sample	NGT [°C]	ΔNGT [°C]	A [ccSTP/g]	ΔA [ccSTP/g]	F	ΔF	^{3}He^{mod} [ccSTP/g]	Δ^3He^{mod} [ccSTP/g]	He^{mod} [ccSTP/g]	ΔHe^{mod} [ccSTP/g]	^{3}He$^{non\text{-}atm}$ [ccSTP/g]	Δ^3He$^{non\text{-}atm}$ [ccSTP/g]	He^{ter} [ccSTP/g]	ΔHe^{ter} [ccSTP/g]	χ^2	$\Delta\chi^2$
2009																
AWSA 3	25.81	0.25	4.72E-04	2.46E-03	-1223.02	373.95	5.844E-14	3.631E-16	4.287E-08	2.609E-10	2.158E-13	1.152E-14	2.005E-07	2.250E-09	4.09	3.53
AWSA 4	25.76	0.42	7.37E-03	1.08E-02	-478.85	560.16	5.775E-14	3.435E-16	4.237E-08	2.471E-10	2.773E-14	4.016E-15	6.322E-08	1.166E-09	1.47	1.80
AWSA 12	25.37	0.22	6.02E-05	4.79E-04	-1352.70	243.99	5.872E-14	3.827E-16	4.307E-08	2.752E-10	2.005E-13	1.048E-14	1.946E-07	2.219E-09	5.80	4.37
AWSA 13	24.00	0.28	1.44E-03	4.70E-03	-986.87	509.59	5.669E-14	3.599E-16	4.288E-08	2.585E-10	8.247E-14	6.02E-15	1.464E-07	2.051E-09	4.04	4.04
AWSA 18	22.74	0.30	8.40E-03	1.20E-02	-73.73	400.94	5.669E-14	3.505E-16	4.163E-08	2.544E-10	7.019E-15	2.544E-15	3.604E-08	6.266E-10	1.91	1.92
AWSA 20	21.77	0.36	1.08E-02	1.30E-02	-268.56	417.38	5.762E-14	3.563E-16	4.230E-08	2.577E-10	3.186E-13	3.284E-15	1.827E-08	7.642E-10	1.25	1.67
Mkeifteh 2	23.73	0.20	8.71E-05	1.07E-03	-854.26	180.23	5.719E-14	3.430E-16	4.197E-08	2.470E-10	9.370E-15	3.043E-15	6.422E-09	6.460E-10	9.33	5.77
KM 140	30.06	0.23	2.76E-05	3.13E-03	-1028.37	113.39	5.699E-14	3.431E-16	4.158E-08	2.469E-10	6.575E-15	3.041E-15	3.258E-09	6.157E-10	10.73	6.23
F1381	26.03	0.22	1.60E-05	1.49E-03	-1371.69	114.16	5.866E-14	3.559E-16	4.302E-08	2.560E-10	6.617E-15	3.214E-15	2.062E-09	6.271E-10	10.26	6.08
2010																
AWSA 3	26.77	0.40	3.52E-03	6.93E-03	-493.73	457.65	5.884E-14	4.392E-16	4.225E-08	3.170E-10	2.264E-13	1.121E-14	1.976E-07	2.404E-09	2.85	3.02
AWSA 4	27.40	0.88	2.93E-04	2.57E-03	-548.40	292.61	5.848E-14	5.443E-16	4.178E-08	3.903E-10	3.473E-14	4.325E-15	6.641E-08	1.259E-09	4.38	3.70
AWSA 5	25.92	0.33	1.66E-03	5.72E-03	-827.05	392.29	5.798E-14	4.301E-16	4.253E-08	3.096E-10	2.038E-14	3.368E-15	7.668E-08	1.270E-09	2.71	2.69
AWSA 6	27.53	0.25	3.89E-04	2.67E-03	-317.10	247.40	5.849E-14	4.389E-16	4.073E-08	3.163E-10	8.282E-15	3.195E-15	4.656E-08	1.016E-09	3.19	2.92
AWSA 11	39.50	6.97	1.38E-01	7.48E-03	0.02	0.00	5.804E-13	5.804E-15	5.301E-07	4.251E-09	1.351E-12	5.937E-14	2.362E-08	8.464E-08	1.66	2.15
AWSA 12	25.95	0.30	1.62E-03	5.22E-03	-742.78	368.90	5.757E-14	4.413E-16	4.224E-08	3.177E-10	1.569E-13	8.402E-15	1.643E-07	2.108E-09	3.32	3.07
AWSA 13	24.82	0.28	8.09E-04	1.15E-02	-898.99	200.42	5.768E-14	4.560E-16	4.232E-08	3.282E-10	9.662E-14	4.014E-15	1.631E-07	2.083E-09	6.23	4.57
AWSA 15	23.81	0.34	2.40E-03	5.90E-03	-432.27	396.36	5.763E-14	4.513E-16	4.230E-08	3.259E-10	3.835E-14	4.014E-15	1.179E-07	1.653E-09	3.78	3.78
AWSA 16	22.93	0.24	7.75E-05	5.24E-04	-1528.27	303.28	6.159E-14	4.592E-16	4.515E-08	3.296E-10	8.387E-16	2.926E-15	1.257E-08	7.909E-10	4.62	3.79
AWSA 18	23.46	0.79	6.32E-06	1.06E-04	-151.41	174.69	5.580E-14	4.928E-16	4.097E-08	3.535E-10	-3.553E-16	2.532E-15	4.085E-09	7.052E-10	4.18	3.52
2012																
AWSA 3	26.69	0.21	6.63E-06	7.01E-04	-1351.60	83.09	5.884E-14	3.106E-16	4.315E-08	2.233E-10	2.307E-13	1.103E-14	2.005E-07	2.544E-09	11.38	6.44
AWSA 4	26.86	0.24	5.52E-04	1.21E-02	-1254.73	249.11	5.848E-14	3.105E-16	4.288E-08	2.231E-10	4.431E-14	3.872E-15	7.233E-08	1.242E-09	5.81	4.41
AWSA 5	26.91	0.22	1.76E-04	1.23E-03	-1216.12	262.97	5.846E-14	3.090E-16	4.287E-08	2.221E-10	1.654E-14	3.098E-15	5.888E-08	1.114E-09	5.33	4.18
AWSA 6	26.61	0.21	2.30E-05	2.51E-03	-961.26	91.16	5.929E-14	2.982E-16	4.199E-08	2.146E-10	1.882E-13	2.960E-15	5.171E-08	1.032E-09	11.17	6.39
AWSA 13	25.98	0.21	2.20E-06	9.27E-05	-1441.07	78.24	5.929E-14	3.070E-16	4.347E-08	2.207E-10	1.238E-13	6.840E-15	1.969E-07	2.502E-09	12.46	6.78
AWSA 15	22.21	0.78	4.79E-03	1.02E-03	-0.60	0.26	1.376E-13	1.850E-15	9.960E-08	1.200E-09	2.340E-14	7.545E-15	6.806E-08	2.746E-09	1.56	2.06
AWSA 16	23.62	0.22	3.24E-04	2.22E-03	-1066.98	269.06	5.835E-14	3.197E-16	4.281E-08	2.299E-10	3.577E-15	2.590E-15	7.554E-09	6.599E-10	5.89	4.43
F3731	20.81	0.82	6.46E-03	8.30E-03	-210.38	723.81	5.058E-14	5.333E-16	5.058E-08	3.605E-10	-3.771E-14	2.952E-15	-4.203E-10	7.878E-10	2.99	3.13
F3975	23.00	0.22	5.30E-04	2.99E-03	-1016.81	297.35	5.828E-14	3.104E-16	4.276E-08	2.231E-10	1.496E-14	2.954E-15	7.075E-08	1.235E-09	4.12	3.57
F3741	20.41	0.25	6.64E-04	2.94E-03	-1295.29	484.55	6.055E-14	3.279E-16	4.441E-08	2.345E-10	6.666E-14	4.879E-15	2.770E-07	3.368E-09	4.64	3.87
F3960	20.32	0.52	1.34E-02	1.43E-02	-321.19	562.50	5.903E-14	5.739E-16	4.334E-08	2.773E-10	2.773E-14	4.158E-15	2.882E-08	1.302E-09	1.12	1.55
Mohammed	19.54	0.37	2.95E-03	8.48E-03	-147.96	379.11	5.655E-14	6.388E-16	4.154E-08	4.615E-10	5.146E-14	4.498E-15	1.451E-07	2.625E-09	1.76	1.92
NDW5 684m	33.80	0.68	-2.14E-07	1.91E-04	-1667.17	1852.64	4.820E-14	9.514E-16	3.542E-08	6.881E-10	2.179E-12	9.005E-14	2.196E-06	4.215E-08	3.00	2.83
NDW7 50m	21.56	1.04	-7.83E+00	2.52E-03	-94.70	394.06	6.025E-14	8.958E-16	4.424E-08	6.524E-10	8.668E-14	6.636E-15	4.212E-07	9.837E-09	2.64	2.71
NDW7 100m	20.49	0.70	1.20E-02	1.39E-02	-444.35	787.50	6.079E-14	1.042E-15	4.462E-08	7.536E-10	1.065E-13	7.654E-15	5.716E-07	1.401E-08	1.69	2.28
NDW7 150m	20.00	0.63	7.65E-03	1.22E-02	-788.59	859.66	6.024E-14	1.077E-15	4.421E-08	7.769E-10	1.182E-13	1.507E-14	6.826E-07	1.459E-08	1.44	1.83
NDW7 200m	19.97	0.89	1.90E-02	1.41E-02	-231.10	740.76	6.420E-14	1.289E-15	4.711E-08	9.289E-10	1.148E-13	1.510E-14	9.401E-07	2.188E-08	1.33	1.79
NDW7 250m	19.07	0.79	1.35E-02	1.36E-02	-461.71	883.30	6.243E-14	1.292E-15	4.581E-08	9.302E-10	9.478E-14	1.543E-14	1.293E-06	2.971E-08	3.54	3.40
NDW7 300m	15.51	0.46	8.81E-06	4.78E-04	698.14	349.07	5.591E-14	8.917E-16	4.109E-08	6.437E-10	1.008E-13	1.550E-14	3.029E-06	6.986E-08	12.16	6.98
NDW7 544m	16.97	0.51	1.58E-06	4.20E-05	3187.47	417.73	4.831E-14	9.823E-16	3.558E-08	7.120E-10	2.112E-13	7.876E-15	2.857E-06	5.515E-08	11.97	6.66
NDW7 569m	22.16	0.54	3.39E-07	2.65E-08	2259.14	361.95	5.051E-14	9.997E-16	3.715E-08	7.233E-10	8.592E-14	6.941E-15	2.759E-06	5.260E-08	9.38	5.65

16 °C in depth of 300 and 544 m, and again reaching 22 °C at 569 m. This may indicate the groundwater recharge took place at different climatic conditions, the two colder samples being recharged during a cold stage. A NGT of 33.8 °C found in NDW5 is quite unlikely to reflect real recharge conditions, but as this sample seems to be degassed, the high temperature may also be caused by a bad fitting of the CE model.

As mentioned before, the samples AWSA 11 and AWSA 15 (2012) exhibit extremely high ΔNe values. In cases of such high additional air it is difficult for excess air models to reliably separate the excess from the equilibrium component. In fact, the NGT modeled for AWSA 11 is unrealistically high (39.5 °C), indicating the CE model attributed too much gas to the excess air component, leaving too less for the equilibrated share, which results in such a high temperature. On the calculated non-atmospheric helium components, however, this has only a minor influence, because the solubility of helium is only slightly dependent on the ambient temperature and the sample can nevertheless be used in this study. The NGT yielded for AWSA 15 (2012), in contrast, is within the range of the other wells of the well field and therefore trustworthy.

Many samples show a significant non-atmospheric ^{3}He content. As outlined in chapter 2.3.6, this non-atmospheric ^{3}He may origin from the decay of tritium and/or from deep mantle sources. As much of the Azraq groundwater is from shallow depth, above all the farm wells around the Sabkha, tritiogenic ^{3}He is likely to be found. In order to exclude a pure tritiogenic source, the samples are dated by the ^{3}H-^{3}He method and the results checked for plausibility. To be reasonable, the resulting apparent age needs to fall in the range of the bomb tritium in the atmosphere, and the calculated initial tritium content needs to be in harmony with the tritium input concentration at the time of recharge (the tritium input curve is displayed in figure 2.3). At times where not data for tritium in precipitation in Jordan is available, the concentration is estimated from the Vienna input curve, as both curves suggest to run more or less parallel. The results are presented in table 6.9, the numbers which contradict the mentioned requirements are colored red. For the interpretation one has to keep in mind several constraints. First of all, most of the tritium data is below the detection limit. Nevertheless, a ^{3}H-^{3}He age is calculated, although the tritium concentrations should be considered as zero in this case. Second, there may be several years between the rainfall and the water reaching the groundwater table (the ^{3}H-^{3}He ages state the time span between closure from the soil atmosphere and the moment of sampling. And, third, mixing of different groundwater types in this area is expected, which would render a single water age meaningless. Yet, the results clearly reveal that the ^{3}He content of almost all samples cannot be explained by tritiogenic production alone. Exceptions are the 2012 samples of AWSA 13 and 15 and farm well F3960. The two first mentioned samples have considerably higher tritium content compared to samples from the previous year, which is attributed to analytical problems (compare chapter 6.4.3). The farm well F3960 possibly received young groundwater from local recharge in the Sabkha, so it is not clear if its ^{3}He is from tritium decay only or mantle derived, or if both sources contribute. In the following, however, the ^{3}He content of all wells is being considered as purely mantle derived.

Figure 6.17 presents the ^{3}He/^{4}He vs. Ne/He plot, which is elucidated in the caption of figure 2.14. The ^{3}He/^{4}He ratio is given in multiples of R_A. The samples that plot close to the

Table 6.9: ^{3}H-^{3}He ages of all Azraq wells as a test, if the ^{3}He content is explainable by tritium decay only, with the resulting year of recharge and the calculated tritium concentration of the water at the time of recharge. Inconsistencies are marked red. The employed tritium concentration is found in table 6.4 and the non-atmospheric ^{3}He content in table 6.8. n. c. means "not calculable", which is the case when the measured tritium concentration is below zero, or if the modeled atmospheric ^{3}He component is negative, as in the 2012 sample of AWSA 16.

	^{3}H-^{3}He age [years]	Δ^3H-^{3}He age [years]	year of recharge	^{3}H at recharge [TU]
AWSA 3	61.18	1.26	1951	96.25
AWSA 4	42.12	1.97	1970	19.57
AWSA 5	33.91	3.10	1978	7.62
AWSA 6	32.68	2.30	1979	8.80
AWSA 13	38.58	0.63	1973	56.52
AWSA 15	21.30	1.19	1991	13.79
AWSA 16	n. c.			
F3731	n. c.			
F3975	42.78	5.35	1969	6.44
F3741	42.82	1.41	1969	29.48
F3960	25.03	1.01	1987	13.90
Mohammed	39.08	1.41	1973	23.16
NDW5 250m	107.29	1.90	1905	882.80
NDW7 50m	62.13	3.58	1950	35.93
NDW7 250m	n. c.			

atmospheric endmember can be divided into a set of wells with a slightly higher ^{3}He/^{4}He ratio than the atmospheric ratio, which could be explained by bomb tritium (the northern wells, AWSA 11 and AWSA 18 (but only from 2009)). Other samples close to the atmospheric endmember lie on or close to the crustal mixing line (AWSA 16 and 20, Farm well F3731), but show no significant tritiogenic ^{3}He component. All other AWSA wells, however, show a clear mantle helium component, with AWSA 3, 12 and 13 having the most distinct ones. Also the remaining farm wells exhibit some mantle helium. The samples of the middle aquifer well NDW7 show a trend: the deeper, the more crustal the helium signature. NDW5, however, situated east of the Fuluq Fault, has a strong mantle imprint and proves that in general mantle helium is present in the vicinity of the Azraq Oasis.

Interestingly, the clusters of AWSA wells (compare the beginning of this chapter and figure 6.8) are mirrored in this isotope plot, signaling that the distinct clusters are also differently influenced by mantle helium.

While it is quite simple to visually identify samples with a mantle helium influenced noble gas signature from this isotope plot, the absolute amount of ^{3}He and ^{4}He originating from the Earth's mantle is only vaguely possible to determine using the triangular extension of this plot introduced in figure 2.18 [Pyle, 1993]. A calculation after the approach described in chapter 2.3.6.3 yields much more precise results. Table 6.10 presents the relative fractions of ^{4}He and of ^{3}He originating from the reservoirs atmosphere (A), mantle (M) and crust (C). The underlying ^{3}He and ^{4}He concentations and their respective atmospheric amount
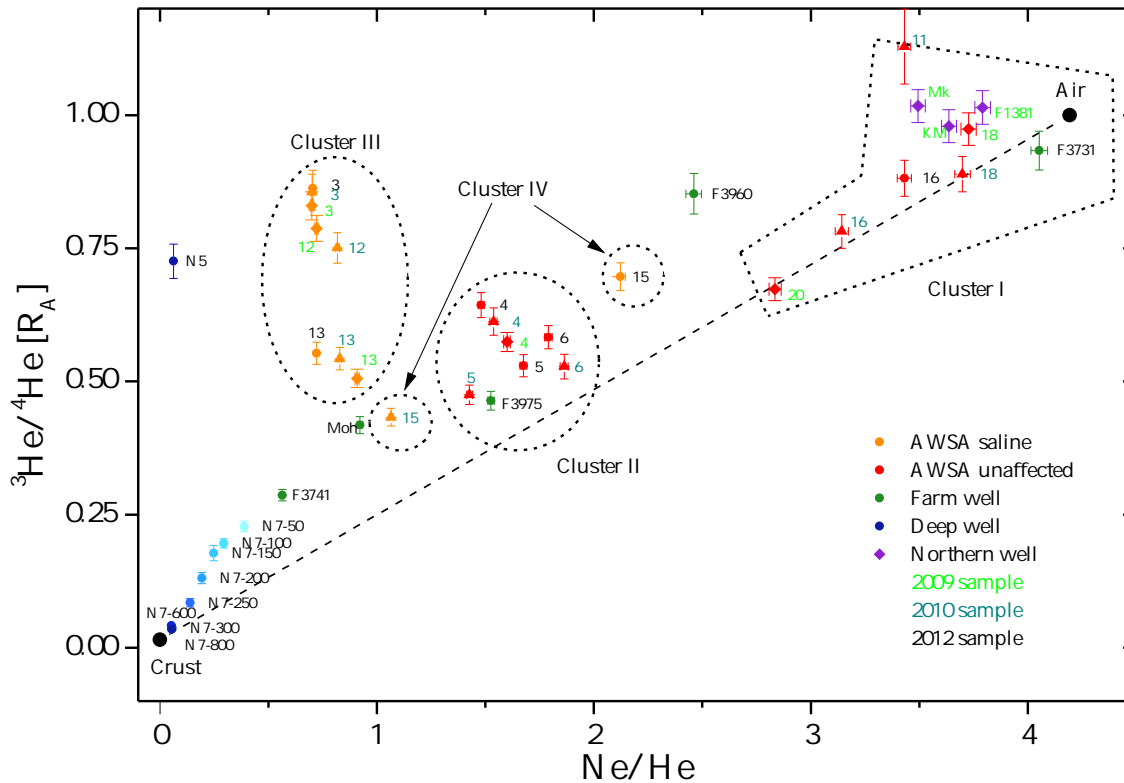
Figure 6.17: The ^{3}He/^{4}He vs. Ne/He plot of the Azraq samples. Again, the different water groups regarding the AWSA wells, defined in the beginning of this chapter (see figure 2.14), are found. This plot bases on the data given in table 6.7.

from inverse modeling, which are needed for the calculations, are listed in table A.3 on page 181.

A better overview of the total helium concentrations allows the ^{3}He vs. ^{4}He plot in figure 6.18. The three straight lines indicate isotopic helium concentrations of either atmospheric, crustal or mantle signature. An air equilibrated water sample in a pure crustal environment, i.e. no mantle or tritiogenic influences, "starts" at equilibrium concentrations of ^{3}He $= 5.44 \times 10^{-14}$ ccSTP/g and ^{4}He $= 3.99 \times 10^{-8}$ ccSTP/g (at $T = 25\,°C$, 920 mbar pressure and no salinity) and then "moves" along the curve, here called crustal evolution curve, that "converges" to the straight line corresponding to crustal helium isotopy. This curve is described by the equation $f(x) = 2 \times 10^{-8} \cdot (x - 3.99 \times 10^{-8}) + 5.44 \times 10^{-14}$, i.e. a straight line going through the start point with a slope of 2×10^{-8} indicating the ratio of crustal ^{3}He and ^{4}He production; the curved character is due to the logarithmic scale used in the plot, in reality it is parallel to the line indicating the crustal helium ratio. Samples locating above this crustal evolution line exhibit ^{4}He components from other sources, i.e. tritium or mantle (whereas tritiogenic ^{3}He has been excluded for the Azraq wells above).

The unaffected AWSA wells scatter quite close to the origin of the crustal evolution curve, as do the northern wells. The fact that they lie a bit above the curve can be attributed to

Table 6.10: The relative fractions of helium isotopes from the reservoirs atmosphere (A), mantle (M) and crust (C) for the 2012 samples. All values are calculated by the procedure demonstrated in chapter 2.3.6.3. Results for the 2009 and 2010 samples are very similar.

	^4He_A	Δ^4He_A	^4He_M	Δ^4He_M	^4He_C	Δ^4He_C	^3He_A	Δ^3He_A	^3He_M	Δ^3He_M	^3He_C	Δ^3He_C
AWSA 3	17.71%	0.19%	8.49%	0.40%	73.80%	0.59%	20.53%	0.83%	78.23%	4.78%	1.24%	0.05%
AWSA 4	37.19%	0.38%	3.31%	0.25%	59.50%	0.63%	57.80%	2.20%	40.87%	3.43%	1.34%	0.05%
AWSA 5	42.08%	0.43%	1.26%	0.21%	56.65%	0.64%	79.48%	3.21%	18.98%	3.19%	1.55%	0.06%
AWSA 6	44.96%	0.46%	1.58%	0.21%	53.46%	0.67%	77.10%	2.95%	21.58%	3.03%	1.32%	0.05%
AWSA 13	18.09%	0.20%	4.54%	0.24%	77.37%	0.43%	32.70%	1.28%	65.27%	4.21%	2.02%	0.08%
AWSA 15	59.33%	0.89%	1.23%	0.22%	39.45%	1.10%	85.17%	3.42%	14.01%	2.53%	0.82%	0.04%
AWSA 16	84.89%	0.86%	0.38%	0.32%	14.73%	1.18%	96.30%	3.83%	3.46%	2.89%	0.24%	0.02%
F3731	100.61%	1.12%	-0.92%	0.32%	0.30%	1.44%	107.81%	4.36%	-7.82%	-2.72%	0.00%	0.02%
F3975	37.64%	0.39%	0.99%	0.17%	61.37%	0.57%	81.19%	3.20%	16.90%	3.04%	1.91%	0.07%
F3741	13.83%	0.16%	1.71%	0.12%	84.46%	0.27%	48.27%	1.91%	47.47%	3.73%	4.26%	0.16%
F3960	59.98%	0.96%	3.11%	0.36%	36.91%	1.32%	70.37%	3.32%	29.01%	3.57%	0.63%	0.04%
Mohammed 53m	22.29%	0.35%	2.32%	0.16%	75.39%	0.51%	53.32%	2.21%	44.07%	3.47%	2.61%	0.10%
NDW5 684m	1.59%	0.04%	8.77%	0.40%	89.64%	0.45%	2.19%	0.11%	96.02%	6.16%	1.79%	0.08%
NDW7 0m	97.97%	1.54%	0.24%	0.36%	1.79%	1.90%	98.08%	4.54%	1.89%	2.84%	0.03%	0.03%
NDW7 50m	9.48%	0.24%	1.52%	0.10%	89.01%	0.34%	41.56%	2.10%	52.80%	4.07%	5.64%	0.25%
NDW7 100m	7.19%	0.20%	1.40%	0.09%	91.42%	0.29%	36.63%	1.94%	56.64%	4.33%	6.73%	0.30%
NDW7 150m	6.07%	0.16%	1.30%	0.16%	92.63%	0.32%	34.21%	2.90%	58.24%	8.60%	7.55%	0.61%
NDW7 200m	4.76%	0.14%	0.88%	0.11%	94.36%	0.25%	36.36%	3.10%	53.24%	8.18%	10.41%	0.83%
NDW7 250m	3.42%	0.10%	0.46%	0.09%	96.12%	0.19%	40.26%	3.91%	43.37%	9.04%	16.37%	1.51%
NDW7 300m	1.37%	0.04%	0.11%	0.04%	98.52%	0.08%	37.20%	3.75%	24.21%	8.78%	38.59%	3.70%
NDW7 600m	1.23%	0.04%	0.19%	0.02%	98.58%	0.05%	29.44%	1.58%	36.48%	4.09%	34.07%	1.55%
NDW7 800m	1.33%	0.04%	0.09%	0.02%	98.58%	0.05%	38.22%	2.11%	20.82%	3.93%	40.96%	1.97%
NDW7 ca500m	1.48%	0.04%	0.11%	0.02%	98.41%	0.06%	39.52%	2.31%	22.54%	4.36%	37.94%	1.98%
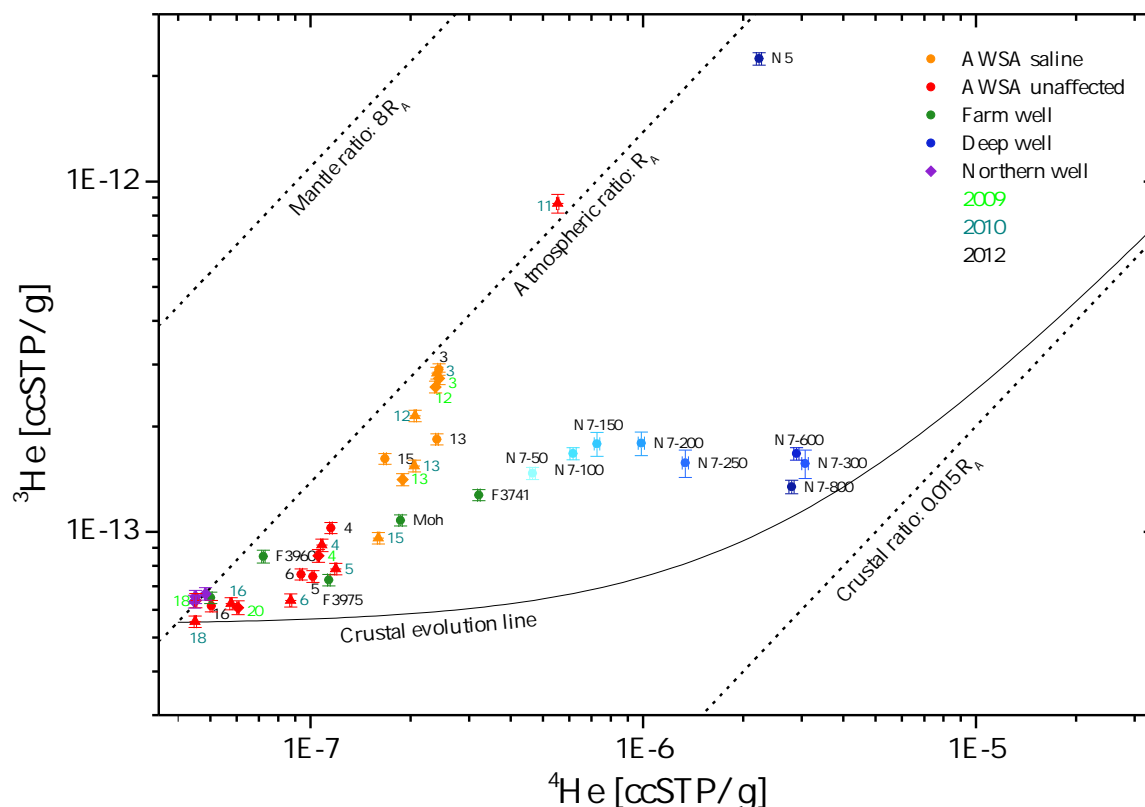
Figure 6.18: The absolute ^{3}He and ^{4}He concentraions are plotted against each other. The three parallel lines indicate ^{3}He-^{4}He combinations corresponding to atmospheric, mantle and crustal ^{3}He/^{4}He ratios. An air equilibrated sample, exposed to a pure crustal environment, will "move" along the crustal evolution line which converges to the crustal line.

excess air, which is not corrected for in this plot like it is done in the isotope plot in figure 6.17. Obviously the saline AWSA well's water contains much more ^{3}He as well as ^{4}He than the unaffected ones, and the ^{3}He concentration emphasized over the ^{4}He content, as these wells plot far away from the crustal evolution line. The wells of cluster II (AWSA 4, 5 and 6) plot in between, but clearly exhibit mantle helium, too.

The northern wells are close to the equilibrium helium ratio, as expected. The farm wells scatter widely, with all of them containing more or less ^{3}He attributed to a mantle source. AWSA 11 is an exception, as it plots on the atmospheric ratio line, but with much higher helium content as it would be possible to explain by excess air. In combination with the fact that AWSA 11 is found to be a young sample in figure 6.17 (located close to the atmospheric endmember) and that is exhibits a very high ΔNe, it is clear that during sampling of this well a lot of additional air contaminated the sample.

The trend with depth of NDW7 observed in many of the previous plots is well resolved in this diagram. Remarkably, the content of ^{3}He is almost constant over depth, while the deeper samples contain much more ^{4}He. This is surprising as all water in shallower depths of this

borehole originates from the top A7 formation, where the casing is screened. This trend in ^{4}He concentration could be attributed to progressive degassing, as warmer water from the depth rises within the borehole and therefore eventually exchanges with the atmosphere. But this effect would affect all other noble gases, notably ^{3}He. This trend, which is visible in most other tracers as well, is not fully understood. The most likely explanation is that the well casing, though quite sturdily constructed, corroded over the past 20 years and other water leaks into the borehole.

Deep well NDW5 behaves totally different from NDW7. It locates far off the evolution line, having the highest ^{3}He content of all sampled wells in the Azraq basin. Together with its high ^{4}He concentration this well is obviously mantle influenced.

6.5 Discussion and conclusion

The three salinization scenarios investigated by Al-Momani *et al.* [2006] and which are introduced in chapter 6.2 are reviewed with respect to the new data presented in this work.

The first scenario, where the change of the hydraulic gradient causes a reverse flow of groundwater towards the AWSA well field, is already rejected by these authors, as, at the time of the study (2002), the affected wells already had a rising salinity, although the gradient still drove the groundwater from the well field area towards the Sabkha. The helium pattern of the shallow farm wells support the discard of this salinization scheme, as admixing of Sabkha water can not explain the high ^{3}He concentrations of AWSA 3, 12, 13 and 15 (compare figure 6.18).

The second scenario, i.e. the upward leakage from the middle aquifer into the shallow one, which could not be excluded in the study of Al-Momani *et al.* [2006], is also disproved by noble gases. The amount of ^{3}He in NDW7, being constant over the total depth, is considerably lower than that found in AWSA 3 and 12. The same results from the ^{3}He/^{4}He ratio (figure 6.17). A mixture of middle aquifer water, which is very close to the crustal endmember, and water found in the unaffected AWSA wells (which locate near the atmospheric endmember) would result in a noble gas signature plotting along the dashed crustal-atmospheric mixing line in the plot in figure 6.17. Cluster II, III and IV water can, therefore, not be explained by upstreaming B2/A7 water in the well field area.

A new mineral leaching scheme as a result of a changed groundwater flow pattern in consequence of the intense groundwater abstraction in Azraq, as proposed by the third scenario and which is the favored salinization explanation of Al-Momani *et al.* [2006], could only explain the observations, if the minerals at the bottom of the B4 aquifer (or the underlying B3 aquitard) would also contain high amounts of lithium. As ^{6}Li is the parent of tritium, significant concentrations of it could be a geogenic source of ^{3}He, which is not related to a mantle source. However, no extraordinary lithium content is reported for the Azraq basin. In general, mainly granitic rock types contain high lithium concentrations [James and Palmer, 2000], but the proposed location of saline water is within a several kilometer thick sequence of sedimentary rock, so an unusual high lithium content is unlikely to be found in Azraq. Therefore, a changed rock weathering scheme can not explain the presence of

high ^{3}He/^{4}He ratios found in the saline wells, too. Regarding the dissolved noble gases, the water would essentially be the same independent from any change in mineral dissolution processes.

As a consequence, a new hypothesis of hydrogeologic circumstances is proposed, which can explain all findings presented in the previous chapter.

Mantle helium distribution

The finding of mantle helium in the shallow aquifer, while at the same time the underlying aquifer exhibits crustal character, is, indeed, surprising. The fact that exactly those wells affected by salt are the deepest of all AWSA wells could lead to the assumption that the ^{3}He originates from high Li content in that depth, but, as outlined above, this possibility is very unlikely. Therefore, the most probable explanation is that the mantle helium originates from even deeper layers, but somehow circumvents the middle aquifer. The Azraq Oasis and its surrounding are crossed by many fault lines, some of which might go deep and be hydraulically conductive. The map in figure 6.2 gives an overview of the most prominent faults in the area. Most striking of all are the Fuluq Fault with its up to 3000 m vertical displacement, running about 10 km NE of the AWSA well field in NW-SE direction, and the parallel Sirhan Fault, about 10 km SW of the well field. These two faults form the eastern and western boundary of the Hamza Graben system, in which Azraq is located. The finding of an obvious mantle helium signature in NDW5 generally supports the assumption of the deep, conductive faults in the area of the central Azraq depression.

The fact that the middle aquifer well NDW7 is not affected by an upstream of mantle influenced water can only be read as that groundwater flow in this aquifer is towards the conductive fault(s). On the other hand, the presence of mantle helium in the shallow Sabkha water and the well field speaks for a flow towards the central area. This groundwater flow scheme is sketched in figure 6.19. As outlined in this drawing the deep water ascends most likely through the Fuluq Fault, because of two reasons. First, groundwater in the middle aquifer flows in eastern to northeastern direction beneath the oasis. Hence, if one of the other main faults is strongly conductive, mantle helium would be found in NDW7. Second, the fact that the Fuluq Fault experienced very strong tectonic forces over a long period of time (consider the distinct dip of the layers west of the fault, as depicted in the geologic cross-section of Margane *et al.* [2002] in figure 6.4) renders it in all probability a well conductive zone, at least at some places.

As the upwelling deep water distributes preferably in the deeper part of the conductive aquifer rock, it can be assumed that a gradient of mantle helium concentration establishes within the shallow aquifer, i. e. the deep part of the aquifer contains a larger amount of mantle influenced water than the more shallow regime, which is compatible with only the deepest wells are being affected by salt as well as ^{3}He.

Groundwater mixing pattern in the AWSA well field

In order to explain the groundwater mixing mechanisms within the AWSA well field, one has to take a detailed look at the local hydrogeology setting, as it is sketched in figure 6.19. Most AWSA wells, like described in chapter 6.3, are drilled to roughly 200 m deep into the B4 aquifer, piercing the basalt shield completely. Because they are open over the whole depth, it can be expected they draw water from all depths of the lithologic profile. However, the transmissivities vary widely along the depth profile. As described in chapter 4.3, the hydraulic conductivity is much better within the fractured basalt aquifer than in the underlying B5 (considered an aquitard in the well field area) and the B4 formations. This means, that by far most water is abstracted from the basaltic part of the aquifer – as long as there is water in this layer.

The transmissivity, which, under steady state conditions, is governed by the water flow inside the basalt shield, however, decreases the more the groundwater table is lowered, simply because there are less well permeable fractures available for water transport the less the basalt is saturated. Additionally, the pumping creates a cone of depression around a well, where the water table can locally be lowered by several meters, depending on the discharge rate and the hydraulic transmissivity of the surrounding rock. This initially small cone of depression in the borehole itself will surely increase the more the basalt is being depleted.

The transmissivity reduction does not necessarily need to be uniform, it strongly depends on the individual environment in a well. If, for example, the groundwater table falls below a very conductive fracture, transmissivitiy steeply drops. Values for drawdown and transmissivity of the AWSA wells listed in table 6.1, therefore, need to be considered to be valid only at the time of well drilling. Today, however, the conditions have certainly changed.

As soon as the groundwater surface in the well field area falls below the basalt, the transmissivity decreases rapidly due to the lower conductivities of the B4/5 unit, and, following, the cone of depression get much deeper. In this case, much more water is abstracted from the deeper layers of the aquifer than it has been the case before.

This situation is depicted in figure 6.20. As long as the water table within the borehole is in the basalt aquifer, the water is abstracted almost exclusively from there. As the water table falls, the basalt gets less conductive and more water is drawn from the deeper layers of the shallow aquifer.

As the groundwater table in the (unpumped) observation well AZ-12 is only roughly 15 m above the basalt base in AWSA 12, 13 and 15, it is easily conceivable that the basalt aquifer already fell dry at those locations and a substantial amount of water is today abstracted from the deeper part of the aquifer system, i. e. mainly from the B4.

Assuming, that the deeper layers of the shallow aquifer contain distinct amounts of terrigenic helium, as proposed before, and that they are considerably higher mineralized than the water in the basalt aquifer, then, in combination with the groundwater level drop process just exemplified, one could indeed explain the very local occurrence of salinization as well as mantle helium in the AWSA field. As one can see in figure 6.7, the base of the basalt shield in wells No 12, 13 and 15 is at around 473 masl, while No 4, 5, 6 and 11 have the base
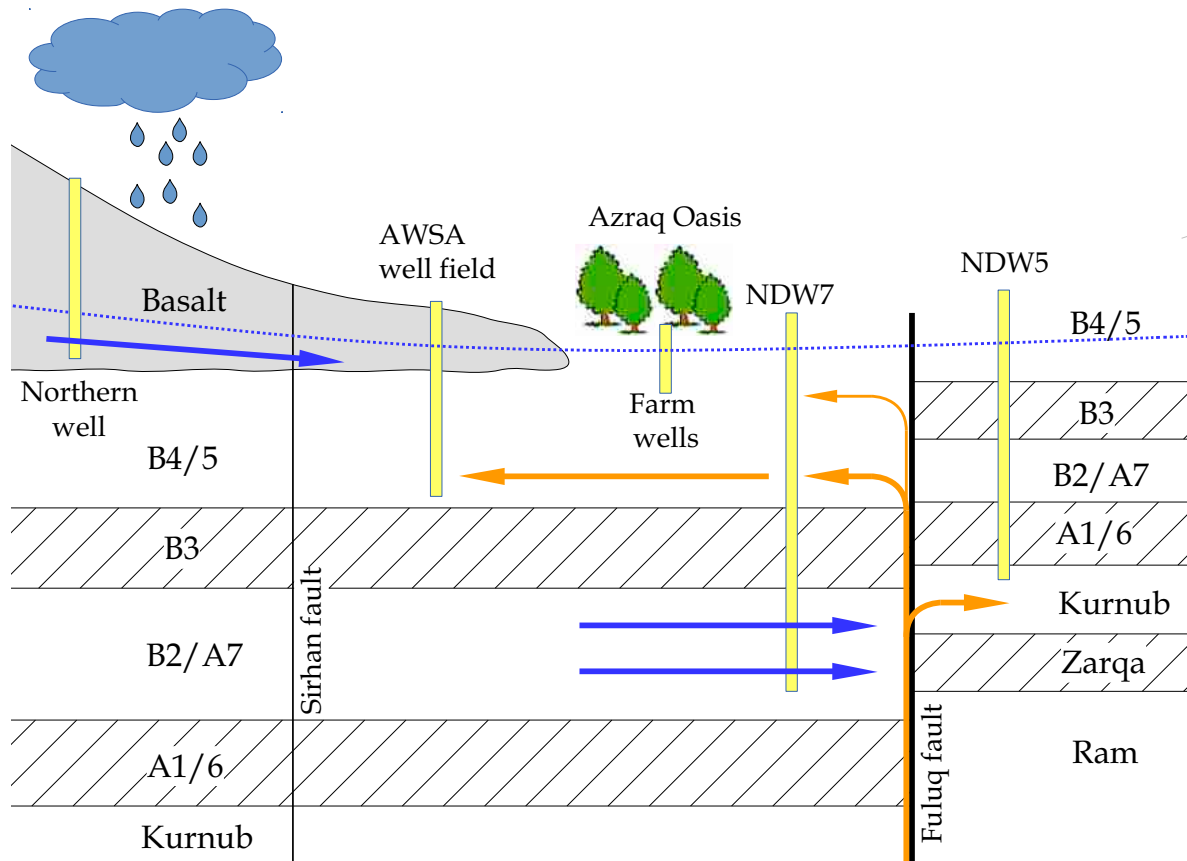
Figure 6.19: This sketch shows the proposed groundwater flow scheme in the Azraq Oasis. Water from the deep aquifer system, loaded with mantle helium, ascends along the Fuluq Fault. Because groundwater flow in the B2/A7 west of the fault is towards it, NDW7 is not affected by mantle gases. At some parts of the Fuluq Fault mantle gases may be transported into the Kurnub east of the fault. In the shallow aquifer the flow direction is reverse and mantle helium containing water stratifies mainly into the deep part of the shallow aquifer. The AWSA wells potentially abstract low lying, saline water from the basalt aquifer and deep, saline and mantle helium containing water from the B4 unit.
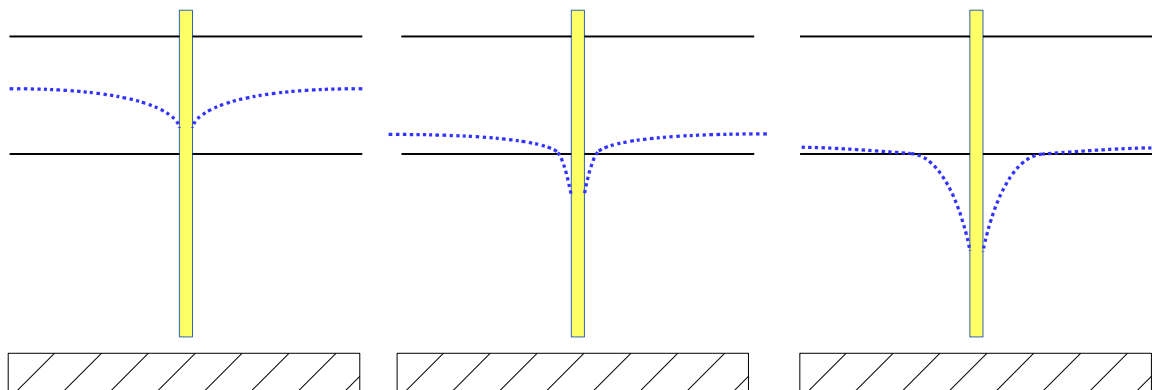
Figure 6.20: Proposed temporal development of the water abstraction in the AWSA wells. The left sketch shows the initial condition, where all water is drawn from the basalt aquifer. When the water table within the borehole decreases and eventually falls into less conductive material below the basalt, the cone of depression gets deeper and more water is abstracted from the B4/5.

10 to 30 m deeper. It is therefore clear, that under the same conditions the basaltic material falls dry earlier in the first mentioned wells than in the latter ones.

However, one exception has to be noted. In AWSA 3, the well containing most mantle helium, the base of the basalt is considerably lower than in the other saline wells. The initial AWSA 3 transmissivity of $17\,539\,\text{m}^2/\text{day}$ was among the highest of all AWSA wells and suggests merely a small cone of depression. But this situation may be owed to a highly permeable fracture in the upper part of the basalt. As AWSA 3 is located very close to the Al-Bayda Fault, an impact to the initially good transmissivity is likely. The assumed massive drawdown, however, may be attributed to the situation that groundwater conducted by this fracture is no longer available and a massive local cone may have established as a consequence. Unfortunately, no information about the true water level in the pumped boreholes is available.

The wells of cluster II, AWSA 4, 5 and 6, are not affected by a rising salt content, but show a slightly elevated ^{4}He concentration as well as a notably mantle helium influence. As the bottom of the basalt aquifer in these wells is located deeper than in the affected wells, one can assume there is still a saturated zone within the basalt. As these wells locate quite close to each other (they are all within 500 m from each other), and are not far from the Al-Bayda Fault, they possibly draw groundwater from a deeper layer connected by the fault. This would, however, mean, there is a water body between the basalt and the deep, saline water source, which is impacted by terrigenic helium, but at the same time has a low mineralization. Admittedly, the explanation that these three wells draw water from an additional reservoir is somewhat far-fetched, but the behavior of the wells is not easily interpreted.

AWSA 15 plays a special role. It is the only well classified as cluster IV due to its helium and salinity pattern being different from all other wells. Following the aforementioned reasoning, from the high mineralization one would also expect a high terrigenic helium content. AWSA 15 shows, indeed, signs of mantle influence, i.e. some water from the deep layer of

the shallow aquifer is incorporated to the final mixture, but compared to the other saline wells it is much higher mineralized. The high salt content suggests that this well feeds from an additional source, which is even more saline than the deep part of the shallow aquifer. However, the mixing calculation performed using the water chemistry data revealed that AWSA 15 is at least not well described by a mixture of B2/A7, Sabkha and unaffected water. But one has to consider, that especially the water type of the farm area may falsely be defined by the mere two wells selected as prototype of the Sabkha water. Although Al-Momani *et al.* [2006] reported the hydraulic gradient to be towards the playa, strong pumping in connection with conductive fractures might lead to a very local flow from the central saltwater body toward well AWSA 15. Another possiblity regards the observation of gypsum dissolution signs in AWSA 15 found by Al-Momani *et al.* [2006] which is confirmed by the new data. Therefore, the possibility that AWSA 15 taps an additional, highly mineralized water source can not be ruled out.

The wells unaffected by rising salinity, AWSA 11, 16, 18 and 20, have in common that they do not go as deep as the other AWSA wells. AWSA 11 is the shallowest AWSA well (62 m) and penetrates the B5 just a few meters. It is therefore comprehensible that this well does not abstract deep water. AWSA 18 is 171 m deep and, moreover, has the highest level of the basalt base. It therefore seems to be a good candidate for salinization. The fact this well still shows no signs of it may be explained by the presence of a highly conductive fracture at the bottom of the basalt layer which still feeds AWSA 18 and prevents it from drawing detectable mounts from deeper layers. Unfortunately no lithologic data could be obtained for AWSA 16 (160 m) and 20 (117 m).

Small variations of salt content over time against the general trend of increasing salt content, as shown figure 6.5, can be attributed in the presented salinization scenario to variations of the groundwater table due to strong recharge events, or to temporarily lower abstraction rates of the well field wells. Such variations occur, like the water table development in figure 6.1 displays.

The presence of different groundwater reservoirs, as concluded from the noble gases, is supported by all other measured tracers. δ^{13}C isotopy, ^{14}C and radon activities suggest the presence of more than one groundwater reservoir feeding the AWSA well field. The water chemistry data shown in the Piper plot suggest an admixing of a different source into the affected AWSA wells, too. Most notable, the hypothesis of a saline, mantle helium containing reservoir in the deep part of the shallow aquifer is supported by the recorded physical parameters (compare figure 6.9). The lower pH values of the salinization affected wells and also those with only an elevated terrigenic helium content (cluster II) suggest they at least incorporate water which does not originate from the alkaline basalt aquifer. The higher water temperatures of these wells are a sign of a deeper source as well. Last but not least, the much lower oxygen content of these samples point to older, and hence deeper water.

The deep well NDW5 differs from all other wells sampled in Azraq. It contains the most significant mantle helium content of all sampled well in the Azraq basin, but at the same time has only a small content of dissolved minerals. It is located east of the Fuluq Fault, where the lithologic structure is not affected by the formation of the Hamza Graben system, i. e. the depth to the geologic units is much smaller than on the other side of the fault. NDW5

therefore abstracts water from the B2/A7 and the Kurnub aquifer. The mantle helium suggests that these aquifers incorporate deep water ascending at the Fuluq Fault. An admixing of B2/A7 water traveling eastwards across the fault, as indicated in figure 6.19, however, is negligible due to the low mineralization. Moreover, it can not be excluded that the water in NDW5 is totally independent of the processes occurring in the Azraq Oasis and that even the mantle helium source lies far away.

Conclusion

The verification of the hypothesis of a deep source within the B4 aquifer spoiling the water quality at some points of the AWSA well field is difficult, because information about water in the deeper parts of the shallow aquifer is scarce. The only hint is found in [Abu-Jaber *et al.*, 1998], where a well close to the central playa is reported, which taps the deep Umm Rijam formation. This well, whose name or well ID is unfortunately not stated, has a high salinity of about $2373\,mg/L$ and is rich in magnesium, calcium and chloride, but has a low sodium concentration (although the IBE of $-19.6\,\%$ is very high). This might be indicative for an admixing of this kind of water into AWSA 3, 13 an 15, because they, too, contain significantly more Mg and Ca than the other wells (compare the dolomite dissolution plot in figure 6.13).

As the presented data propose the existence of (at least) two groundwater reservoirs contributing to the AWSA wells, no constraint can be made about the mineralization level of the saline water source. Therefore, an investigation targeting specifically the deeper part of the shallow aquifer in Azraq is advised. Most important, this could reveal valuable information about the potential upper limit of future mineralization of the AWSA wells. This would be an important assessment of how vulnerable the prospective supply with good quality drinking water from the Azraq Oasis is.

7 Thermal waters along the Dead Sea Transform

Thermal water, especially in springs, is often associated with recent magmatic or tectonic activity, where hot magma bodies reach close to the Earth's surface and warm up the surrounding rock and thereby the contained groundwater. Another mechanism of hot springs is the heating of deeply circulating groundwater as a consequence of the local geothermal gradient. If this water rises quickly, usually in a well conductive fracture, it partly preserves its gained temperature and discharges as a hot spring.

The temperature of a thermal spring, which is essentially the surface manifestation of geothermal heat, is controlled by several factors. In case of heating by a recently formed volcanic source, the distance to the magma body determines the temperature of the rock and, thus, also the groundwater temperature. In case of deep circulation, several aspects govern the final discharge temperature of the spring. First, of course, the temperature of the original reservoir, i.e. the depth from where the water ascends to the surface in combination with the local geothermal gradient. Second, the upstream velocity, determined by the conductivity of the fracture and the hydrostatic pressure. And, finally, ascending hot water can be diluted by addition of cold, ambient groundwater. An overview of these controlling factors is depicted in figure 7.1. Warm water discharging from a deep borehole is essentially warmed the same way, but the borehole replaces the conductive fracture. In both cases, heating by magmatic activity or deep circulation, it can be assumed that gases from the mantle are incorporated into the ambient groundwater.

Thermal waters are found in several locations in Jordan and Israel. Most of them emerge as springs along the Dead Sea Transform Valley. In the presented study, 29 thermal springs and also wells between Wadi Arava in the south and the Hermon Mountains in the north are analyzed. In Israel, some samples were collected in Wadi Arava, at the coast of the Dead Sea, the Yarmouk Gorge and around Lake Kinneret, including boreholes in the Golan heights and the adjacent Hula basin. Thermal waters in Jordan are found mostly along the deeply cut side wadis of the rift escarpment. They distribute from south of the Dead Sea all the way north to the Yarmouk River. Figure 7.2 gives a summary of all sampled locations, where green dots indicate thermal springs and red ones wells discharging hot water. These two colors are used in all presented diagrams and maps to differentiate between springs and wells.

The data presented in this work are combined from two field trips. Wells and springs on the Jordanian side of the rift valley were sampled on my own field trip in March and April 2012, while the Israeli side was covered within the scope of the master's thesis of Neta Tsur [2013], where sampling took place in December 2012. The focus of the analysis lies on the
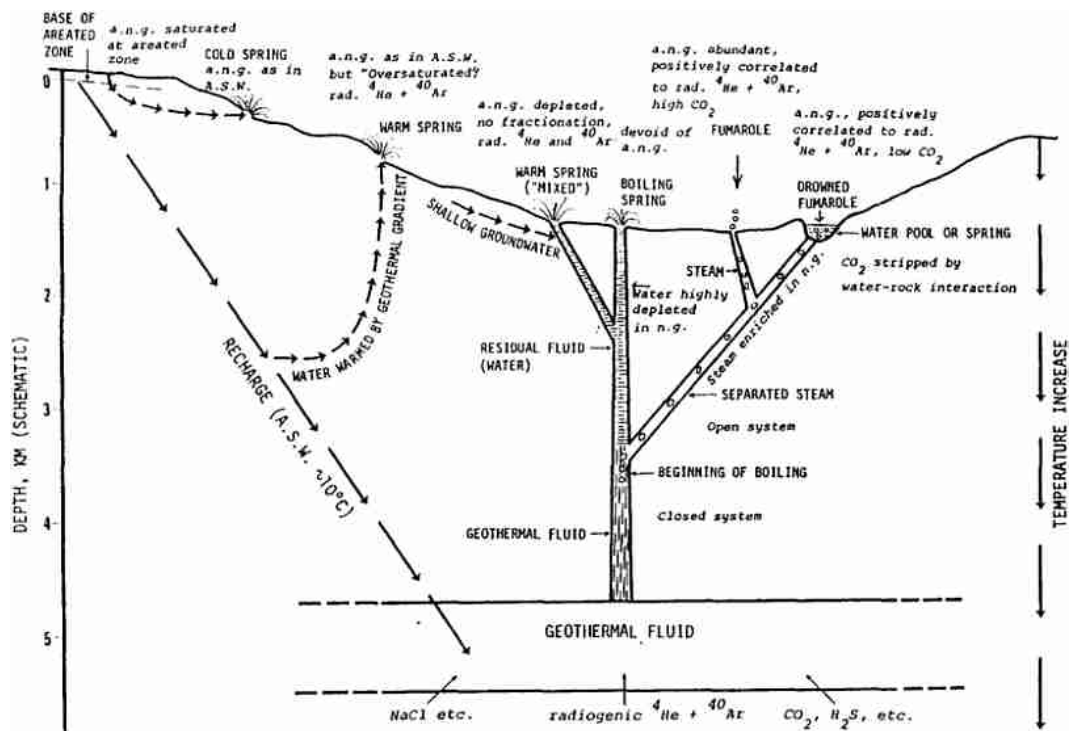
Figure 7.1: Principle structure of a natural thermal system heated by geothermal heat and its expected noble gas composition. a.n.g. stands for atmospheric noble gases. Other possible discharge mechanisms like fumaroles are presented, too. From Mazor *et al.* [1988].

determination of helium isotope ratios, but also other environmental tracers are applied like stable isotopes, δ^{13}C, radon and water chemistry.

Helium isotopes are very good means to determine magmatic and tectonic activity that causes elevated temperatures in thermal water. As outlined in chapter 2.3.6, the ^{3}He/^{4}He ratios of the Earth's reservoirs mantle, crust and atmosphere vary widely and, hence, enables the differentiation between them. The ^{3}He/^{4}He ratio is thereby reported in multiples of the atmospheric ratio, denoted by R_A.

Many scientists have applied helium isotope ratios to charaterize continental rift and fault zones before. The Rhine Graben in central Europe was investigated by Hooker *et al.* [1985] and Griesshaber *et al.* [1992], who found helium ratios up to $6\,R_A$ in thermal groundwater, but no immediate correlation to local tectonic activity. The San Andreas Fault in California exhibits mantle helium up to $4\,R_A$ [Kennedy *et al.*, 1997; Wiersberg and Erzinger, 2007], and Kennedy and van Soest [2007] could delineate a correlation of the extent of crustal deformation and mantle influence in faults related to the San Andreas Fault, which argues for a deformation-enhanced permeability of mantle fluids. Polyak [2003] discovered mantle helium ratios of up to $8\,R_A$ in the Baikal Rift Zone and deduced that continental rifting is radically different from oceanic spreading insofar that mantle activity is not the cause but the consequence of deformation.
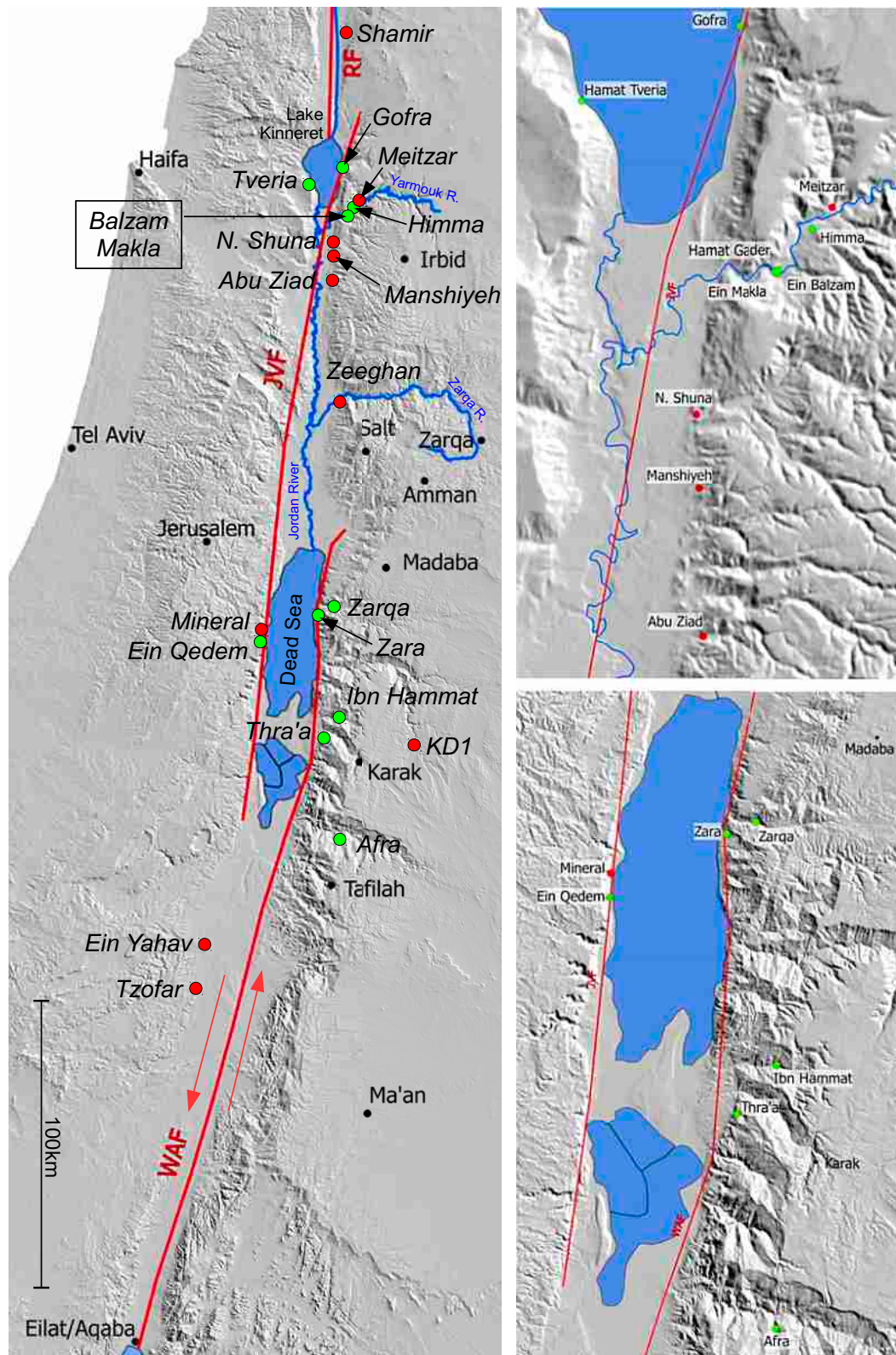
Figure 7.2: Locations of the sampled thermal springs (green) and wells (red). More detailed maps of the Lake Kinneret and the Dead Sea areas are shown on the right. The left-lateral motion of the main faults of the DST is indicated by arrows. WAF: Wadi Arava Fault, JVF: Jordan Valley Fault, RF: Rachaiya Fault.

The southern extension of the DST, the Syrian-African Rift Zone, exhibit mantle helium influence over wide distance as well. Darling *et al.* [1995] found values of up to $8\,R_A$ in Kenya, while Pik *et al.* [2006] published helium ratios of up to $16\,R_A$ along the Rift Zone and conclude an additional mantle plume impact. The spreading ridge of the Red Sea is also strongly imprinted by mantle helium, including a mantle hotspot [Lupton *et al.*, 1977; Moreira *et al.*, 1996]. To the north, the DST joins the vast Anatolian Rift system, where also high helium ratios are found, especially in East Turkey [Güleç *et al.*, 2002; Kipfer *et al.*, 1994, among others].

In can be concluded that mantle volatiles are presumably found in all continental, tectonically young features as is the Dead Sea Transform examined in this study.

Several scientists analyzed groundwater from the Jordan Rift Valley for noble gases before. Notably, the overall first study that obtained paleotemperatures from noble gases in groundwater was carried out by Mazor [1972] on geothermal springs in Israel. However, they measured only the total noble gas amounts, but no ^{3}He/^{4}He ratios. The same holds for Herzberg and Mazor [1979], who determined the recharge origin of cold springs in Israel by NGTs. The Kinneret-10 borehole at the western shore of Lake Kinneret was analyzed by Bergelson *et al.* [1999], who found high total helium concentration and a ^{3}He/^{4}He ratio of $1.45\,R_A$. The reason of salinization of springs in the Jericho area in the Jordan Valley was addressed by Lange *et al.* [2008] applying helium and neon isotopes. They found the highest total ^{4}He and mantle helium (up to $1.01\,R_A$) in springs in the vicinity of faults.

Just recently, Torfstein *et al.* [2013] published an extensive data set of ^{3}He/^{4}He ratios in thermal springs and wells, which covers the Israeli part of the DST. They collected samples around Lake Kinneret and the Yarmouk Gorge, at the Dead Sea, and in Wadi Arava. They found a gradient from high helium isotope ratios of about $2\,R_A$ in the north to more crustal signatures at the Dead Sea ($0.5\,R_A$ to $1\,R_A$) and in the south (below $0.4\,R_A$) and conclude that there is no correlation between tectonic activity, which is essentially similar around Lake Kinneret and the Dead Sea. Torfstein *et al.* attribute the higher mantle component in the north to the northward thinning of the crust and hence a shallower depth of the Moho boundary. In addition, they propose an intermediate, ubiquitous reservoir with a mantle signature of about $2\,R_A$, and lower helium ratios are attributed to a certain degree of admixed water having a crustal, radiogenic imprint.

The Jordanian side of the rift is much less covered by noble gas data. The only data published is from Eraifej [2006], who analyzed the thermal wells Mokhybeh in the Yarmouk Valley ($1.91\,R_A$), Waqas ($1.62\,R_A$, located between North Shuna hot well and Abu Ziad) and two boreholes on the Lisan peninsula between the northern and southern part of the Dead Sea (TA1 and TA2, both found to have $0.11\,R_A$).

Subsequently, at first the analytical results are presented, followed by a detailed view at the local hydrogeologic conditions at each sampling location, and conclusive remark at the end.

7.1 Results

The analysis of the presented samples is performed as described in chapter 3. The sampling procedure, especially of the thermal springs, was quite individual and needed adaption to the local setting. General aspects of sampling are treated in chapter 5.1, while appendix A.3 offers a description of the particular sampling procedure of each Jordanian spring and well. Information about the localities in Israel is found in the master's thesis of Neta Tsur [2013]. Basic information about all springs and wells is compiled in table 7.1. Because many localities have rather long names which would collide in the presented graphs, they are labeled by short forms, also listed in the table.

7.1.1 Basic observations

The sampled thermal waters exhibit a wide range of temperatures and salt contents. Especially in case of springs, water temperature is either an evidence of a heat source close to the ground surface (which induces an elevated geothermal gradient), or points to highly conductive fractures which facilitate a rapid upstream of water heated in a great depth. High salinity, on the other hand, is often an indicator of old water, which had enough time to interact with the surrounding rock. The presence of salt bodies may be another possibility to find brines.

The distribution of discharge temperatures and salinities along the DST is visualized in figure 7.3, the underlying data is listed in table 7.1. Higher temperatures and salt contents, respectively, are illustrated as bigger dots, as categorized in the given legend. The highest temperatures are found in the Meitzar 2 well in the Yarmouk Gorge and the Zarqa Ma'in 1 spring, the hottest one of the Zarqa Ma'in spring field. However, no general trend regarding the geographic location is obvious. As the discharge temperature of wells depends in general on the well depth (or more specifically, the depth from where the majority of the water is abstracted due to the highest aquifer transmissivitiy), one should not ascribe too much importance to the temperature pattern of the wells. Nevertheless, the overall hottest water temperature of well Meitzar 2, which is by far not the deepest of all wells, indicates an elevated thermal gradient in the Yarmouk Valley. More interesting with respect to geothermal activity is the distribution of spring temperatures, with Zarqa Ma'in 1 being the most prominent example. The high discharge temperature of this spring is in good accord with an extraordinary high heat flow exceeding $400\,\mathrm{mW/m^2}$ in the area [Galanis Jr. *et al.*, 1986] and the finding of magnetic anomalies, indicating rather recent magma intrusion in the area [Frieslander and Ben-Avraham, 1989]. But also around Lake Kinneret and especially in the Yarmouk Gorge thermal anomalies are found [Shalev *et al.*, 2013] which can explain the high Meitzar 2 and Hamat Trevia temperatures.

Salinity is also distributed heterogeneously along the valley. Most notable, Ein Qedem and Mineral, located just off the shore of the Dead Sea, exhibit an extreme degree of mineralization and an E. C. of almost 150 mS/cm. Most likely, both discharge hypersaline Dead Sea water which has intruded the subsurface beyond the shoreline, where a transition zone from brine to fresh water exists. The highest E. C. in Dead Sea water measured by Akkawi [2006]

(a) Temperature distribution

(b) Salinity distribution
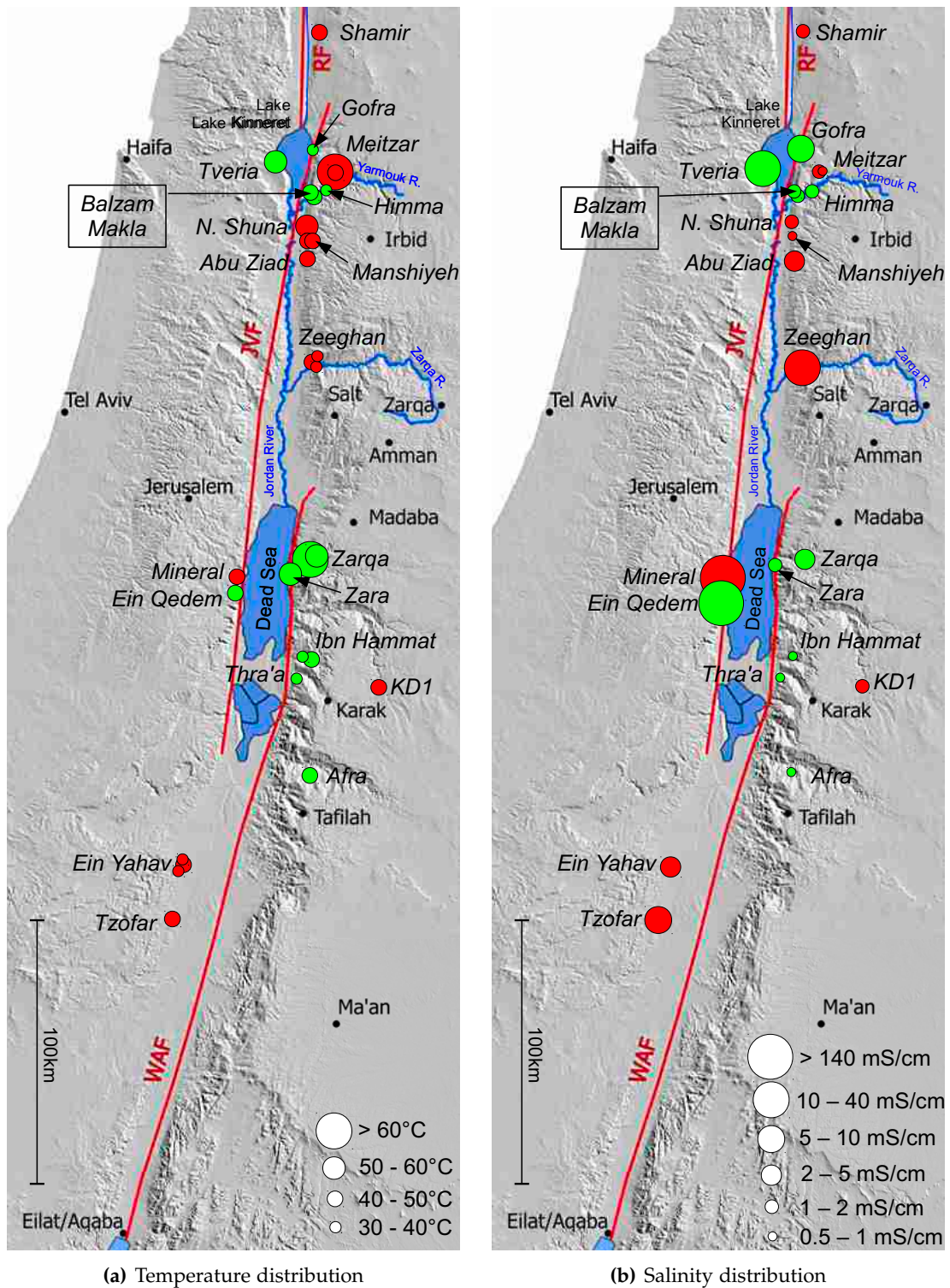
Figure 7.3: Temperature and Salinity distribution along the DST. Red dots denote wells, green dots thermal springs. The hottest water is found in the Meitzar 2 well and the Zarqa Ma'in 1 spring. No general trend regarding the discharge temperatures is visible. Salinity is highest on the western Dead Sea coast, but other centers of high mineralization are present. However, as noted for the temperature, no trend is recognizable.

Table 7.1: Location coordinates and other information of all sampled thermal waters. In case of wells the depth and tapped lithological unit is given, and, if present, information about the location of the screen. The Short names are used in the figures. ID referres to the internal well ID of the WAJ. Also listed is the discharge temperature and E.C.. Israeli data from Tsur [2013].

Name	Short name	ID	Northern	Eastern	Altitude [m]	Lithology	Depth [m]	Screen [m]	E.C. [µS/cm]	Temp. [°C]
Jordan										
Wells										
North Shuna Hot Well	Shuna	AB1138	32°36'46.6''	35°36'59.9''	-178	B2/A7	967	330–967	1327	53.3
Abu Ziad	Ziad	AB1367	32°30'14.5''	35°37'14.2''	-120	B2/A7	1126	600–1126	2100	47.3
Manshiyeh 1	Man1	AB1355	32°34'35.8''	35°37'6.6''	-140	B2/A7	1100	800–1100	739	48.4
Manshiyeh 2	Man2	AB3003	32°33'58.8''	35°37'14.6''	-120	B2/A7 + A4	1183		685	48.8
Zeeghan 4	Zee4	AL3677	32°11'12.1''	35°38'27.9''	-200	K + Z	400		12100	40.5
Zeeghan 14	Zee14	AL3843	32°10'28.0''	35°37'52.1''	-178	Z	200		15200	31.6
Zeeghan 15	Zee15	AL3858	32°10'50.9''	35°38'6.0''	-207	Z	226		11730	34.4
KD1	KD1	CD3411	31°13'12.2''	35°53'24.2''	665	K + RAM	1001		1240	47.4
Springs										
Himma	Himma		32°42'16.6''	35°41'3.9''	-104	B2/A7 + B			1098	37.7
Zarka Ma'in 1	Zarqa1		31°36'37.7''	35°36'50.7''	-33	K			2690	61.3
Zarka Ma'in 2	Zarqa2		31°36'40.6''	35°36'51.1''	-2	K			2700	54.7
Zara	Zara		31°35'44.9''	35°34'8.2''	-272	K			1490	51.6
Ibn Hammat 1	Ibn1		31°17'59.7''	35°37'34.3''	59	K			742	39.0
Ibn Hammat 2	Ibn2		31°18'8.1''	35°38'41.8''	163	K			825	40.2
Afra	Afra		30°58'2.5''	35°38'33''	319	K			538	46.4
Thra'a	Thra'a		31°14'23.1''	35°35'2.0''	47	K			676	32.0
Israel										
Wells										
Shamir	Shamir		33°10'23.0''	35°39'49.8''	245	Limestone	1420	1162–1420	1237	45.4
Meitzar 2	Mei2		32°42'54''	35°41'46''	-90	Dolomite	807	448–807	1835	65.3
Meitzar 3	Mei3		32°42'54''	35°41'46''	-90	Bitum. chalk	336	80–336	660	40.2
Ein Yahav 6	Y6		30°40'32''	35°13'3''	-80	Sandstone	904	765–884	2690	43.5
Ein Yahav 16	Y16		30°40'32''	35°13'3''	-80	Limestone	509	255–509	2780	35.0
Ein Yahav 116	Y116		30°40'32''	35°13'3''	-80	Flint	190	136–171	2170	31.0
Tzofar	Tzofar		30°33'13''	35°10'40''	18	Sandstone	1010	836–1007	9630	43.3
Mineral	Mineral		31°32'45''	35°23'47''	-386				148100	42.7
Springs										
Gofra	Gofra		32°48'14.5''	35°38'31.8''	-183				6840	30.8
Ein Balzam	Balzam		32°41'0.3''	35°39'47.4''	-163	L.S. + Basalt			1393	41.7
Ein Makla	Makla		32°40'56.1''	35°39'52.3''	-163	L.S. + Basalt			1895	48.5
Hamat Tveria	Tveria		32°46'1.9''	35°32'0.0''	-183				37800	58.9
Ein Qedem	Qedem		31°30'55.5''	35°23'43.3''	-404				148500	43.8

along depth profiles is 202 mS/cm at a salinity of 267 g/L, although he discovered that even higher mineralization resulted in lower E.C., which makes it impossible to calculate the fresh water fraction admixed in the discharged water from the E.C. alone. The saline springs on the western coast of Lake Kinneret are thought to feed on brines evolved from the remnant of evoparation of Pliocene and Pleistoncene lakes [Rosenthal *et al.*, 2008]. The saline wells of the Abu Zeeghan well field pump water which originates mainly from lateral groundwater flow towards the rift valley in the Zarka aquifers. Thereby, evaporites and gypsum present in the aquifer matrix are dissolved [Salameh, 2001]. All other thermal waters are only low to medium saline.

7.1.2 Noble gases

Data preparation

The Jordanian samples' raw data are analyzed in WUCEM together with the Azraq samples, collected at the same sampling campaign. The only exception from the normal routine are the ^{3}He measurements of Abu Ziad and Zeeghan 15, because in these cases the ^{3}He signal lies outside the range of calibration measurements. As described in chapter 3.6.2, a linear fit using only the two biggest calibration sizes is taken. In case of the Israeli Ein Balzam is treated the same way, but using a constant fit. The results of all noble gas isotope concentrations is found in table 7.2.

The total element concentrations used for the noble gas temperature fitting routine are listed in table A.6 on page 184. Some samples show an elevated ^{40}Ar/^{36}Ar (Zeeghan 4, 14, 15, Zarqa Ma'in 2, Ein Makla, Hamat Tveria and Ein Qedem), in these cases the total atmospheric argon content is calculated from ^{36}Ar only, as mentioned in chapter 3.6.4.

Inverse NGT fitting proves to be complicated in some cases. Initial application of the UA excess air model reveals the Jordanian samples Abu Ziad, Zarqa Ma'in 1 and 2, Zara and Ibn Hammat 2 to be degassed. Therefore, they are fitted by the CE model in degassing mode, initialized by $F = 2$, while for all other samples the initial F is 0.5. Due to default of good knowledge about the recharge altitude, it is assumed that all waters equilibrated at 800 m, i.e. at $p = 0.92$ atm. This is reasonable since Bajjali *et al.* [1997] estimated the thermal water found in north Jordan to be recharged in the Jordan highlands. The springs east of the Dead Sea discharge from the Kurnub Sandstone which is assumed to be recharged mainly at its outcrop along the southern escarpment, where an altitude of 800 m is reasonable as well, though less constrained. The initial fitting temperature is 18 °C for all samples.

In case of the Israeli samples, the UA model indicated degassing at Gofra, Ein Balzam, Ein Makla, Meitzar 2, Tzofar, Hamat Tveria, Mineral and Ein Qedem; fitting of all these samples is therefore initialized by $F = 2$, the others by $F = 0.5$. Infiltration altitudes are estimated from the outcrop of the discharging hydrological units. Gofra, Meitzar 3, Tzofar and all Ein Yahav wells: 400 m, Shamir: 650 m, Ein Balzam and Ein Makla: 800 m, Meitzar 3: 1500 m, Hamat Tveria: 220 m, and Mineral and Ein Qedem are assumed to be former Dead Sea water (see discussion below) and therefore an equilibration altitude of −400 m is assumed. 18 °C is chosen as initial value of the fitting parameter T.

Table 7.2: Noble gas isotope results of all sampled thermal localities. All data are given in ccSTP/g water. Israeli data from Tsur [2013].

	^{3}He	Δ^3He	^{4}He	Δ^4He	^{20}Ne	Δ^{20}Ne	^{22}Ne	Δ^{22}Ne	^{36}Ar	Δ^{36}Ar	^{40}Ar	Δ^{40}Ar	^{84}Kr	Δ^{84}Kr	^{132}Xe	Δ^{132}Xe
Jordan																
Himma	5.842E-12	2.350E-13	1.984E-06	1.874E-08	1.861E-07	6.759E-10	1.902E-08	7.182E-11	1.084E-06	1.753E-08	3.119E-04	1.014E-06	3.935E-08	3.377E-10	2.479E-09	4.651E-11
North Shuna	5.746E-12	2.261E-13	1.636E-06	1.533E-08	2.177E-07	7.446E-10	2.229E-08	8.397E-11	1.221E-06	1.962E-08	3.565E-04	1.156E-06	4.659E-08	4.184E-10	3.180E-09	5.579E-11
Abu Ziad	9.031E-11	3.096E-12	3.175E-05	3.150E-07	1.430E-07	5.203E-10	1.462E-08	5.618E-11	9.744E-07	1.505E-08	2.803E-04	9.282E-07	3.672E-08	3.716E-10	2.506E-09	4.177E-11
Manshiyeh 1	1.621E-13	5.886E-15	1.843E-07	1.710E-09	2.018E-07	7.765E-10	2.071E-08	8.526E-11	1.153E-06	1.754E-08	3.392E-04	1.123E-06	4.292E-08	3.796E-10	2.882E-09	5.010E-11
Manshiyeh 2	1.341E-13	4.758E-15	1.659E-07	1.522E-09	2.127E-07	7.299E-10	2.175E-08	8.073E-11	1.172E-06	1.780E-08	3.478E-04	1.128E-06	4.419E-08	3.741E-10	2.869E-09	5.188E-11
Zeeghan 4	2.667E-09	6.498E-11	3.948E-04	3.899E-06	2.809E-07	9.653E-10	2.853E-08	1.009E-10	1.423E-06	2.172E-08	4.790E-04	1.547E-06	5.006E-08	4.530E-10	3.100E-09	6.009E-11
Zeeghan 14	4.430E-10	1.844E-11	1.285E-04	1.212E-06	1.670E-07	5.650E-10	1.698E-08	6.056E-11	9.407E-07	1.459E-08	2.997E-04	9.639E-07	3.563E-08	3.635E-10	2.216E-09	4.566E-11
Zeeghan 15	8.513E-10	2.982E-11	2.457E-04	2.436E-06	1.888E-07	6.718E-10	1.920E-08	7.112E-11	1.039E-06	1.724E-08	3.551E-04	1.144E-06	3.849E-08	3.074E-10	2.427E-09	4.049E-11
Zarka Ma'in 1	2.889E-11	1.172E-12	1.421E-05	1.325E-07	7.211E-08	2.472E-10	7.378E-09	2.890E-11	5.614E-07	9.919E-09	1.711E-04	5.580E-07	2.413E-08	2.218E-10	1.674E-09	2.578E-11
Zarka Ma'in 2	1.642E-11	6.100E-13	9.277E-06	8.292E-08	7.973E-08	2.702E-10	8.145E-09	3.329E-11	5.756E-07	1.027E-08	1.648E-04	5.331E-07	2.290E-08	2.361E-10	1.523E-09	2.727E-11
Zara	6.004E-12	2.146E-13	1.439E-05	1.349E-07	1.406E-07	4.934E-10	1.432E-08	5.361E-11	7.389E-07	1.438E-08	2.348E-04	7.541E-07	2.957E-08	2.822E-10	1.896E-09	3.172E-11
Ibn Hammat 1	1.652E-13	5.849E-15	6.132E-07	6.301E-09	1.554E-07	5.430E-10	1.586E-08	5.647E-11	8.254E-07	1.310E-08	2.381E-04	7.762E-07	3.132E-08	2.994E-10	2.030E-09	3.905E-11
Ibn Hammat 2	1.232E-12	4.718E-14	6.791E-07	5.926E-09	2.405E-07	8.176E-10	2.463E-08	8.841E-11	1.163E-06	1.759E-08	3.411E-04	1.106E-06	4.335E-08	4.101E-10	2.786E-09	5.715E-11
Afra	1.518E-13	5.552E-15	5.785E-07	5.799E-09	1.627E-07	5.754E-10	1.664E-08	6.207E-11	9.402E-07	1.466E-08	2.738E-04	8.898E-07	3.604E-08	3.533E-10	2.315E-09	4.420E-11
Thra'a	1.621E-12	6.085E-14	5.795E-06	5.004E-08	1.906E-07	6.742E-10	1.945E-08	7.187E-11	1.010E-06	1.557E-08	3.012E-04	9.812E-07	3.907E-08	3.565E-10	2.454E-09	4.473E-11
KD1	1.494E-12	5.630E-14	7.562E-06	7.151E-08	2.147E-07	1.200E-09	2.197E-08	1.432E-10	1.060E-06	2.686E-08	3.175E-04	9.855E-07	4.085E-08	9.175E-10	2.657E-09	1.040E-10
Israel																
Gofra	3.378E-12	1.426E-13	1.424E-06	8.651E-09	1.256E-07	5.044E-10	1.282E-08	6.023E-11	9.681E-07	2.384E-08	2.742E-04	6.667E-07	3.675E-08	7.037E-10	2.350E-09	4.715E-11
Shamir	7.963E-12	3.457E-13	2.046E-06	1.054E-08	2.218E-07	8.902E-10	2.268E-08	9.487E-11	1.254E-06	2.680E-08	3.704E-04	8.528E-07	4.950E-08	8.281E-10	3.227E-09	7.230E-11
Meitzar 3	1.105E-12	4.920E-14	4.614E-07	2.464E-09	1.976E-07	8.184E-10	2.018E-08	9.710E-11	1.116E-06	2.430E-08	3.339E-04	7.869E-07	5.016E-08	7.537E-10	2.587E-09	4.770E-11
Meitzar 2	4.328E-11	1.889E-12	1.515E-05	8.904E-08	1.680E-07	6.890E-10	1.720E-08	7.924E-11	1.303E-06	2.977E-08	3.881E-04	8.646E-07	5.016E-08	8.369E-10	3.132E-09	6.520E-11
Ein Balzam	1.525E-11	7.721E-13	5.068E-06	3.596E-08	1.612E-07	7.135E-10	1.654E-08	7.656E-11	1.014E-06	2.464E-08	2.982E-04	7.565E-07	3.897E-08	7.143E-10	2.463E-09	4.941E-11
Ein Makla	2.501E-11	1.036E-12	9.880E-06	5.963E-08	1.483E-07	6.222E-10	1.520E-08	6.816E-11	1.030E-06	2.314E-08	3.074E-04	7.325E-07	4.026E-08	7.325E-10	2.506E-09	4.996E-11
Ein Yahav 116	1.241E-12	4.728E-14	2.376E-06	1.234E-08	2.360E-07	9.945E-10	2.412E-08	1.109E-10	1.111E-06	2.443E-08	3.299E-04	7.554E-07	4.024E-08	7.207E-10	2.511E-09	6.149E-11
Ein Yahav 6	6.204E-12	2.430E-13	9.235E-06	5.569E-08	2.212E-07	9.280E-10	2.266E-08	9.742E-11	1.172E-06	2.541E-08	3.494E-04	7.975E-07	4.079E-08	7.648E-10	2.444E-09	4.898E-11
Ein Yahav 16	3.670E-12	1.457E-13	6.772E-06	4.224E-08	2.067E-07	8.481E-10	2.111E-08	9.041E-11	1.082E-06	2.394E-08	3.112E-04	7.217E-07	3.744E-08	7.231E-10	2.354E-09	5.355E-11
Tzofar	9.174E-12	3.564E-13	1.567E-05	8.122E-08	1.521E-07	6.079E-10	1.560E-08	7.080E-11	8.088E-07	1.987E-08	2.449E-04	6.108E-07	2.849E-08	6.293E-10	1.753E-09	3.418E-11
Hamat Tveria	4.120E-11	1.839E-12	2.826E-05	1.494E-07	9.213E-08	3.789E-10	9.439E-09	5.136E-11	6.494E-07	1.758E-08	2.087E-04	5.663E-07	2.871E-08	6.120E-10	1.868E-09	3.783E-11
Ein Qedem	7.729E-12	2.918E-13	9.132E-06	5.518E-08	3.961E-08	1.756E-10	4.027E-09	3.546E-11	2.054E-07	2.048E-08	1.060E-04	3.730E-07	1.366E-08	4.590E-10	8.737E-10	2.156E-11
Mineral	3.322E-14	1.339E-15	2.786E-08	2.840E-10	6.767E-08	2.832E-10	6.918E-09	3.962E-11	3.009E-07	1.162E-08	8.424E-05	3.489E-07	9.614E-09	4.526E-10	5.142E-10	1.465E-11

For some samples it was not possible to obtain a good fit. Zara, Ibn Hammat 1, Meitzar 2, and to a lesser extent Afra, Thra'a, Ein Makla and Ein Qedem exhibit a bad χ^2, indicating a general problem with the noble gas concentrations. Nevertheless, their resulting noble gas temperature seem to be more or less reasonable.

Many samples exhibit the limiting case, where $|F|$ becomes very high and the CE model becomes a quasi-UA model (see chapter 3.6.2). All samples are therefore further processed by Monte Carlo simulations; for each sample 100 000 simulations are done. The final results of the calculated NGTs, the CE model parameters A and F, the modeled atmospheric ^{3}He and ^{4}He concentrations and the distribution of χ^2 from the Monte Carlo analyses are presented in table 7.3. In case only a subset of Monte Carlo simulations was regarded, the respective selection is shown on page 192.

Analysis

Most resulting NGTs are more or less reasonable and lie between 12 and 23 °C. Cool NGTs may reflect recharge at high altitudes (Shamir, Ein Makla) or during the last Glacial (North Shuna, both Manshiyeh wells, Zeeghan 4, Ein Makla), whereas temperatures above 20 °C in the springs discharging from the Kurnub indicate recharge in the warmer south of Jordan. However, the NGTs of Zarqa Ma'in 2 (27.4 °C), Zara (32.6 °C), Ibn Hammat 1 (30.4 °C), Tzofar (31.2 °C) and Hamat Tveria (26.4 °C) exceed the local temperature regime. Most likely the high calculated temperatures are owed to degassing effects which are badly quantified by the CE model, and therefore the model assumes a too low equilibrated noble gas concentration, which is equivalent to a higher temperature. The difficulty to fit the noble gas data is also reflected in bad χ^2 values of the latter two samples. Meitzar 2 exhibits a very low NGT of only 2.6 °C, which might be reasonable at the peak of Mount Hermon, but the bad χ^2 suggests a fitting problem. The same holds for Ein Qedem (calculated NGT 21.5 °C). However, as the solubility of helium is only weakly dependent on temperature, these fitting problems do not significantly affect the determination of the terrigenic ^{3}He and ^{4}He content as well as the ^{3}He/^{4}He ratio. Summarizing, the NGT analysis reveals that all thermal waters along the rift valley have a meteoric background and none of them has a direct mantle origin.

The consideration of the neon excess (ΔNe, defined in equation 2.27), listed in table 7.4, reveals that some samples are obviously degassed, most of them are springs (Zarqa Ma'in 1 and 2, Gofra, Ein Makla, Hamat Tveria and Ein Qedem). Abu Ziad is the only well that shows signs of degassing. Several other localities exhibit high ΔNe values, indicating a distinct excess air contribution to the total noble gas concentrations.

Most of the sampled thermal waters along the rift valley exhibit a significant mantle helium component, as shown in figure 7.4 (explanation of this plot is found in figure 2.14). The underlying data is compiled in table 7.4. Almost all samples plot on or close to the vertical mixing line of crustal and mantle helium isotopic composition, indicating only minor atmospheric contamination. The strongest mantle signal is found in the well Zeeghan No 4, which contains a helium isotope ratio almost five times the atmospheric value (4.9 R_A). The other two samples from this well field have high ratios as well, as do the springs and wells in or near to the Yarmouk Valley (springs: Himma, Ein Balzam and Makla, wells: Meitzar 2, North Shuna, Abu Ziad, all exhibit helium ratios between 2 and 3 R_A). Also Shamir, situated

Table 7.3: The results of the inverse fitting of noble gas concentration with the CE excess air model using Monte Carlo simulations. Beside the mean and standard deviation of NGT and the other model parameters, the resulting atmospheric component of ³He and total He is presented. χ^2 describes the mean and standard deviation of the χ^2 distribution of all considered Monte Carlo simulations. Very high values of $|F|$ in combination with extremely small values of A indicate the limiting case outlined in chapter 3.6.4. Israeli results from Tsur [2013].

	NGT [°C]	Δ NGT [°C]	A [ccSTP/g]	Δ A [ccSTP/g]	F	Δ F	³He^mod [ccSTP/g]	Δ³He^mod [ccSTP/g]	He^mod [ccSTP/g]	ΔHe^mod [ccSTP/g]	χ^2	$\Delta\chi^2$
Jordan												
Himma	18.58	0.36	3.30E-03	2.01E-03	-0.14	1.43	6.942E-14	4.487E-16	5.086E-08	3.078E-10	1.70	2.18
North Shuna Hot Well	12.54	0.15	1.38E-06	2.82E-05	-3634.11	128.16	8.333E-14	4.192E-16	6.078E-08	2.978E-10	11.86	6.60
Abu Ziad	18.02	0.54	2.87E-02	1.58E-02	1.14	0.04	5.124E-14	2.361E-16	3.766E-08	1.723E-10	1.79	2.32
Manshiyeh 1	14.80	0.36	1.36E-03	1.73E-03	-1263.73	1611.85	7.578E-14	6.955E-16	5.542E-08	4.679E-10	3.36	3.31
Manshiyeh 2	14.37	0.43	2.12E-03	1.86E-03	-629.40	1360.93	8.043E-14	8.729E-16	5.878E-08	5.788E-10	1.14	1.53
Zeeghan 4	14.36	0.72	2.21E-02	2.85E-03	0.38	0.02	1.045E-13	5.064E-16	7.650E-08	3.570E-10	1.03	1.45
Zeeghan 14	22.61	0.20	2.40E-05	3.28E-04	-1883.73	217.70	6.277E-14	2.875E-16	4.600E-08	2.062E-10	9.03	5.67
Zeeghan 15	19.43	0.44	2.22E-03	2.33E-03	-778.29	1319.88	7.122E-14	5.629E-16	5.213E-08	3.776E-10	1.49	1.91
Zarka Ma'in 1	23.58	0.91	1.58E-02	2.62E-03	2.71	0.08	2.583E-14	1.129E-16	1.902E-08	8.342E-11	2.31	2.69
Zarka Ma'in 2	27.39	1.24	1.97E-02	4.75E-03	2.22	0.07	2.935E-14	1.416E-16	2.159E-08	1.056E-10	2.67	2.94
Zara	32.62	0.28	7.87E-02	1.02E-03	1.01	0.00	5.334E-14	1.807E-16	3.914E-08	1.317E-10	221.97	29.19
Ibn Hammat 1	30.41	0.21	4.10E-07	7.53E-09	-1657.04	50.69	5.978E-14	2.736E-16	4.380E-08	1.965E-10	132.28	22.96
Ibn Hammat 2	14.95	0.43	-2.97E-03	9.86E-04	1.98	0.80	1.073E-13	5.564E-15	7.693E-08	3.387E-09	1.39	1.90
Afra	22.84	0.19	4.10E-07	8.04E-09	-1627.97	53.91	6.079E-14	2.892E-16	4.457E-08	2.078E-10	40.91	12.60
Thra'a	19.93	0.17	5.83E-07	1.75E-06	-3100.23	30.56	7.288E-14	3.544E-16	5.327E-08	2.531E-10	22.75	9.35
KD1	17.96	0.86	2.48E-03	2.11E-02	-1598.27	1098.20	8.513E-14	1.463E-15	6.207E-08	9.554E-10	2.60	2.70
Israel												
Gofra	19.24	0.42	1.88E-03	1.61E-03	5.04	5.36	4.386E-14	2.471E-16	3.233E-08	1.733E-10	1.86	2.32
Shamir	11.09	0.18	1.22E-04	5.28E-04	-3042.89	990.83	8.460E-14	5.643E-16	6.171E-08	3.900E-10	5.27	4.15
Meitzar 3	18.80	0.90	1.43E-02	7.22E-03	-2.97	99.86	7.294E-14	4.090E-16	5.349E-08	2.857E-10	3.41	3.40
Ein Balzam	17.60	0.16	-7.83E-07	1.83E-06	996.26	342.66	5.866E-14	3.275E-16	4.305E-08	2.357E-10	3.83	3.30
Meitzar 2	2.64	0.11	1.04E-04	4.90E-03	958.94	88.72	5.671E-14	3.133E-16	4.169E-08	2.256E-10	159.07	25.21
Ein Makla	14.80	0.14	4.03E-07	1.05E-08	1485.74	79.72	5.196E-14	2.717E-16	3.823E-08	1.963E-10	19.32	8.71
Ein Yahav 116	20.13	0.64	1.20E-03	1.45E-03	-1418.95	1879.02	9.449E-14	1.158E-15	6.877E-08	7.540E-10	1.34	1.68
Ein Yahav 6	23.95	1.39	4.28E-02	1.22E-02	0.63	0.01	8.313E-14	4.492E-16	6.097E-08	3.312E-10	1.06	1.50
Ein Yahav 16	22.39	0.87	3.84E-03	2.95E-03	-331.52	981.37	7.968E-14	7.302E-16	5.825E-08	4.792E-10	1.21	1.64
Tzofar	31.24	0.35	6.84E-03	8.12E-03	150.35	564.19	5.847E-14	2.748E-16	4.289E-08	1.982E-10	3.88	4.40
Hamat Tveria	26.37	1.01	4.37E-03	1.87E-03	25.44	387.51	3.296E-14	1.661E-16	2.431E-08	1.188E-10	1.43	1.93
Mineral	21.88	1.90	-3.07E-03	1.66E-03	102.16	334.55	2.662E-14	2.415E-15	1.948E-08	1.539E-09	2.34	2.66
Ein Qedem	-2.42	0.64	6.63E-04	9.39E-04	819.42	1055.09	1.496E-14	1.390E-16	1.108E-08	9.307E-11	53.20	14.42

Table 7.4: Helium isotope ratios of all sampled thermal springs and wells. The absolute ³He/⁴He ratios is given first, then the ratio relative to the atmospheric value, R_A, followed by the extrapolated, corrected helium ratio, as explained in the text and in figure 7.5. The Ne/⁴He ratio used in figure 7.4 is listed and finally the neon excess values, ΔNe. Israeli data from Tsur [2013].

	³He/⁴He	Δ(³He/⁴He)	³He/⁴He [R_A]	Δ(³He/⁴He) [R_A]	(³He/⁴He)_corr [R_A]	Δ(³He/⁴He)_corr [R_A]	Ne/He	Δ(Ne/He)	ΔNe [%]	Δ(ΔNe) [%]
Jordan										
Himma	2.883E-06	1.193E-07	2.083	0.086	2.110	0.088	0.104	0.001	19.65%	0.56%
North Shuna	3.512E-06	1.421E-07	2.538	0.103	2.594	0.106	0.147	0.001	32.92%	0.49%
Abu Ziad	3.049E-06	1.201E-07	2.203	0.087	2.204	0.087	0.005	0.000	-8.46%	0.52%
Manshiyeh 1	8.798E-07	3.297E-08	0.636	0.024	0.488	0.033	1.210	0.012	25.77%	0.62%
Manshiyeh 2	8.085E-07	2.963E-08	0.584	0.021	0.372	0.032	1.417	0.014	31.99%	0.68%
Zeeghan 4	6.755E-06	2.678E-07	4.881	0.194	4.882	0.194	0.001	0.000	74.23%	1.25%
Zeeghan 14	3.448E-06	1.472E-07	2.492	0.106	2.492	0.106	0.001	0.000	10.78%	0.41%
Zeeghan 15	3.802E-06	1.497E-07	2.747	0.108	2.747	0.108	0.001	0.000	22.14%	0.61%
Zarka Ma'in 1	2.033E-06	8.461E-08	1.469	0.061	1.470	0.061	0.006	0.000	-51.80%	0.37%
Zarka Ma'in 2	1.770E-06	6.763E-08	1.279	0.049	1.279	0.049	0.009	0.000	-45.23%	0.52%
Zara	4.172E-07	1.542E-08	0.301	0.011	0.300	0.011	0.011	0.000	0.07%	0.40%
Ibn Hammat 1	2.672E-07	9.863E-09	0.193	0.007	0.136	0.008	0.278	0.003	8.97%	0.41%
Ibn Hammat 2	1.814E-07	7.126E-09	0.131	0.005	0.123	0.005	0.039	0.000	50.02%	0.76%
Afra	2.632E-07	1.000E-08	0.190	0.007	0.125	0.008	0.312	0.003	8.12%	0.41%
Thra'a	2.798E-07	1.077E-08	0.202	0.008	0.195	0.008	0.036	0.000	23.86%	0.47%
KD1	2.035E-07	1.134E-08	0.147	0.008	0.141	0.008	0.032	0.000	39.35%	1.06%
Israel										
Gofra	2.371E-06	1.011E-07	1.713	0.073	1.730	0.075	0.097	0.001	-21.55%	0.39%
Shamir	3.893E-06	1.702E-07	2.813	0.123	2.866	0.127	0.120	0.001	33.34%	0.55%
Meitzar 2	2.856E-06	1.258E-07	2.063	0.091	2.067	0.091	0.012	0.000	23.03%	1.00%
Meitzar 3	2.394E-06	1.074E-07	1.730	0.078	1.823	0.087	0.473	0.003	2.98%	0.42%
Ein Balzam	3.008E-06	1.538E-07	2.173	0.111	2.183	0.112	0.035	0.000	4.64%	0.45%
Ein Makla	2.531E-06	1.059E-07	1.829	0.077	1.832	0.077	0.017	0.000	-6.02%	0.38%
Ein Yahav 6	6.718E-07	2.661E-08	0.485	0.019	0.482	0.019	0.026	0.000	48.45%	0.94%
Ein Yahav 16	5.419E-07	2.177E-08	0.392	0.016	0.387	0.016	0.034	0.000	43.26%	1.56%
Ein Yahav 116	5.224E-07	2.008E-08	0.377	0.015	0.361	0.015	0.110	0.001	32.28%	1.00%
Tzofar	5.853E-07	2.293E-08	0.423	0.017	0.421	0.017	0.011	0.000	3.63%	0.46%
Hamat Tveria	1.458E-06	6.553E-08	1.053	0.047	1.053	0.047	0.004	0.000	-40.69%	0.48%
Ein Qeden	8.463E-07	3.236E-08	0.611	0.023	0.611	0.023	0.005	0.000	-25.70%	0.41%
Mineral	1.192E-06	4.959E-08	0.862	0.036	0.616	0.100	2.684	0.030	19.17%	0.70%
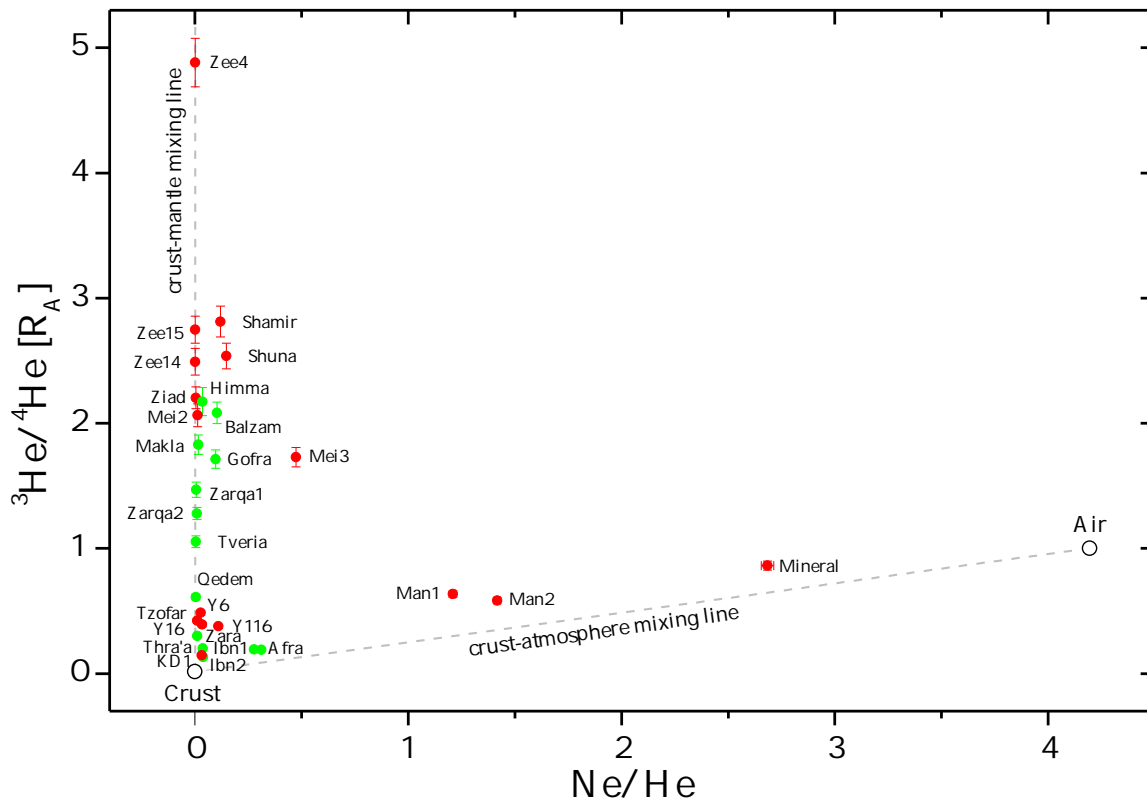
Figure 7.4: Helium isotope ratio plot as explained in figure 2.14. Most thermal water samples exhibit a significant mantle helium component.

at the eastern flanks of the Hula Basin has $2.8\,R_A$. The samples from the shore of Lake Kinneret, Hamat Tveria and Gofra, are a bit less influenced by mantle helium, but still above atmospheric ^{3}He/^{4}He ratio. Also in the same range are the samples from the hot springs in Zarqa Ma'in. All thermal waters in the south of the Dead Sea exhibit only a pretty small mantle helium amount. Overall, the helium isotope ratios are well consistent with those published by Torfstein *et al.* [2013].

Some of the samples, however, plot away from the crust–mantle mixing line, they are shifted towards more atmospheric composition. This indicates either admixing of young, almost atmospherically coined groundwater to the mantle influenced water, or air contamination during sampling. This holds especially for Mineral, both Manshiyeh wells and Meitzar 3. The water of Mineral definitely experienced gas exchange with the atmosphere during sampling, as the water was collected from the outlet of a vessel in which an air phase was present. Therefore, the noble gas analysis for this sample has to be treated with caution. The case is not so clear regarding the Manshiyeh wells. Both are deep, artesian wells and it is unlikely that they incorporate shallow groundwater. Sampling of both wells happened without any visible air bubbles, so direct contamination during sampling is not likely as well. ΔNe, also listed in table 7.4, is a little bit high, but not conspicuous in comparison with the other samples. What also speaks against contamination during sampling is the fact that both

Manshiyeh wells plot close to each other, indicating the atmospheric component is already present within the reservoir. The presence of little tritium content (see table 7.7) in both Manshiyeh wells argues for relatively young water contributing to the discharge despite the depth of these wells. In case of Meitzar 3 bubble formation was observed during sampling and could not totally be inhibited. However, as this well is artesian, the bubbles are more likely due to degassing instead of being air contamination. The atmospheric contamination of Afra and Wadi Ibn Hammat 1 springs is easy to explain. In both cases the water is utilized in a spa center and the spring itself is cased. The samples were collected as close as possible to the spring's discharge opening, but the water is channeled a few meters through pipes where the gases in the water certainly exchange with the atmosphere. Himma spring forms a deep pool, where the water resides for a while, before it flows away. Although care was taken to sample the water as deep as possible, it cannot be excluded that atmospheric gases influenced also the deeper layers of the pool, especially as cooling at the pool's surface leads to a descent of water which exchanged its gases with the atmosphere. Because the discharge rate is high (up to $1000\,\mathrm{L/s}$) not too much atmospheric influence is expected. However, Himma contains a considerable tritium content (11 TU), an indication of admixing of young groundwater. Ein Yahav 6, although being the deepest of the well field, contains some tritium as well, but shows no significant atmospheric contribution in its noble gases.

However, the original helium ratio can be determined in these cases by the assumption that the measured data point falls on a mixing line in the ^{3}He/^{4}He vs. Ne/He isotope plot between atmospheric and the original composition. Hence, where this line meets the crust–mantle mixing line (i. e. where Ne/He $= 0$), the original ^{3}He/^{4}He ratio is found. The according error is calculated using the theorem of intersecting lines, which results in a multiplication of the measurement error with the factor $[1 - (\mathrm{Ne}/{}^4\mathrm{He})_{\mathrm{sample}}/(\mathrm{Ne}/{}^4\mathrm{He})_{\mathrm{air}}]^{-1}$. Figure 7.5 visualizes this procedure and the corrected helium ratios are listed as $({}^3\mathrm{He}/{}^4\mathrm{He})_{\mathrm{corr}}$ in table 7.4. An additional correction for the Ne/He error is omitted since this error is minuscule for all samples. In the further discussion it is always referred to the corrected ^{3}He/^{4}He ratios.

The spatial distribution of the corrected ^{3}He/^{4}He ratios is shown in figure 7.6. Generally, the samples in the north of the DST are more enriched in mantle helium than the southern samples. However, it also reveals the clear north–south trend found by Torfstein *et al.* [2013] considering only the Israeli part of the DST is not that evident on the eastern side.

The ^{3}He against ^{4}He plot in figure 7.7 (which is elucidated in the Azraq chapter on page 111) exhibits the wide range of absolute helium isotope concentrations in groundwater along the rift valley. Those samples obviously contaminated by air have the least isotope amount due to degassing. Notably, Mineral shows helium concentrations even below atmospheric values. The highest concentration in both helium isotopes is found in Zeeghan 4, in which ^{4}He exceeds atmospheric concentration by almost four orders of magnitude, and ^{3}He by even 5×10^4. Also the other two samples from the Zeeghan well field contain a lot of both helium isotopes. None of the samples experienced pure radiogenic development, which would locate them on the crustal evolution line. Even those samples classified as almost crustal in the helium ratio plot above contain ^{3}He contents which are several times above the crustal evolution line.
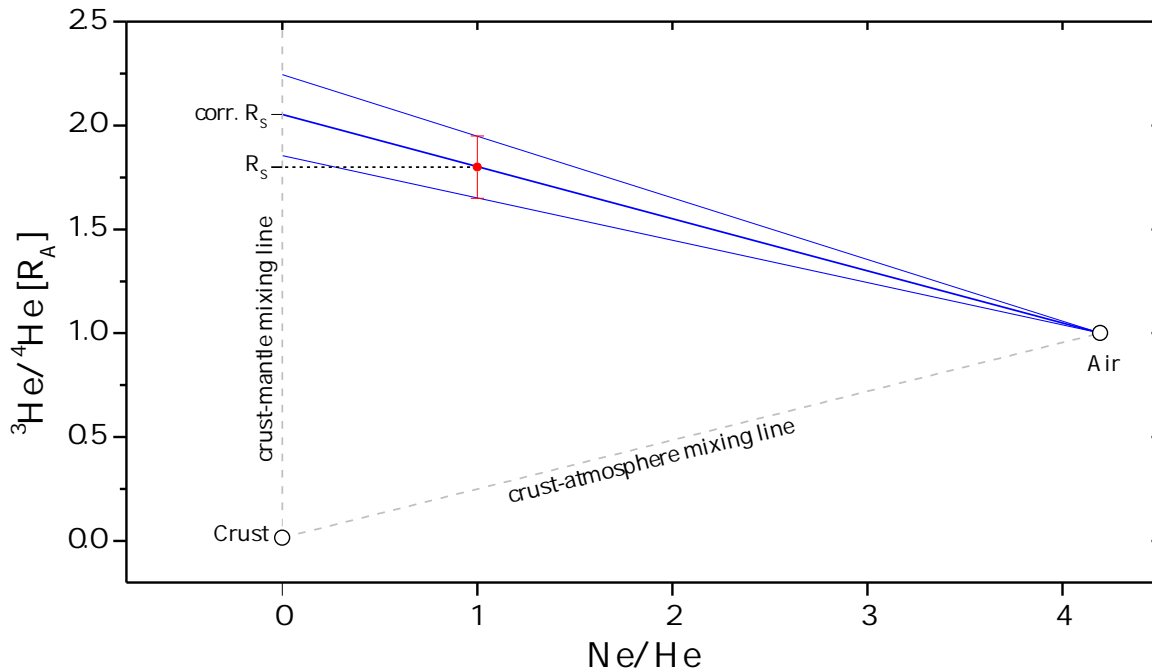
Figure 7.5: Illustration of the reconstruction of the original ^{3}He/^{4}He isotope ratio, here denoted "corr. R_S", of a sample with measured ^{3}He/^{4}He $= R_S$ and a Ne/He ratio of 1, indicating atmospheric contamination. The according error of the corrected ratio results from the theorem of intersecting lines.

Starting from the helium isotope data, the relative contributions of the three endmembers atmosphere, crust and mantle are calculated according to the scheme introduced in chapter 2.3.6.3. The result is presented in table 7.5 and visualized in figure 7.8 (which is essentially an equilateral form of the triangle drawn into the isotope ratio plot in figure 2.18). The relative shares are calculated using the "canonical" ratios for the three endmembers crust (2×10^{-8}), mantle (1.1×10^{-5}) and atmosphere (1.384×10^{-6}). The mantle ratio of $R_M = 8\,R_A$ is considered despite Torfstein *et al.* [2013] published a local mantle ratio of $(6.6 \pm 0.7)\,R_A$ derived from basalt rock samples from the Golan Heights. However, they measured only very few rock samples from a very spatially limited area, which might lead to an overinterpretation if one applies this mantle endmember for the whole DST. Moreover, the highest value obtained by these authors is $(7.83 \pm 0.19)\,R_A$, which suggests an upper mantle source with $8\,R_A$ is present in the region and basalt samples containing lower helium ratios are possibly contaminated. Independently, when using $6.6\,R_A$ as the mantle endmember composition, the relative mantle helium contribution of Zeeghan 4, the most mantle impacted of all samples and therefore the one with the most distinct shift by a variation of R_M, changes to 74 % instead of 61 %, which results from the assumption of $8\,R_A$ being the mantle endmember. Altogether, assuming a different mantle helium composition leads to slightly different relative contributions of the distinct reservoirs, but the basic statement stays the same.

As said, the highest relative mantle helium contribution of 61 % is found in Zeeghan 4, while it is 20 % to 40 % at several localities, and negligible in others. As shown in figure 7.8,

(a) Mantle helium distribution **(b)** δ^{13}C distribution
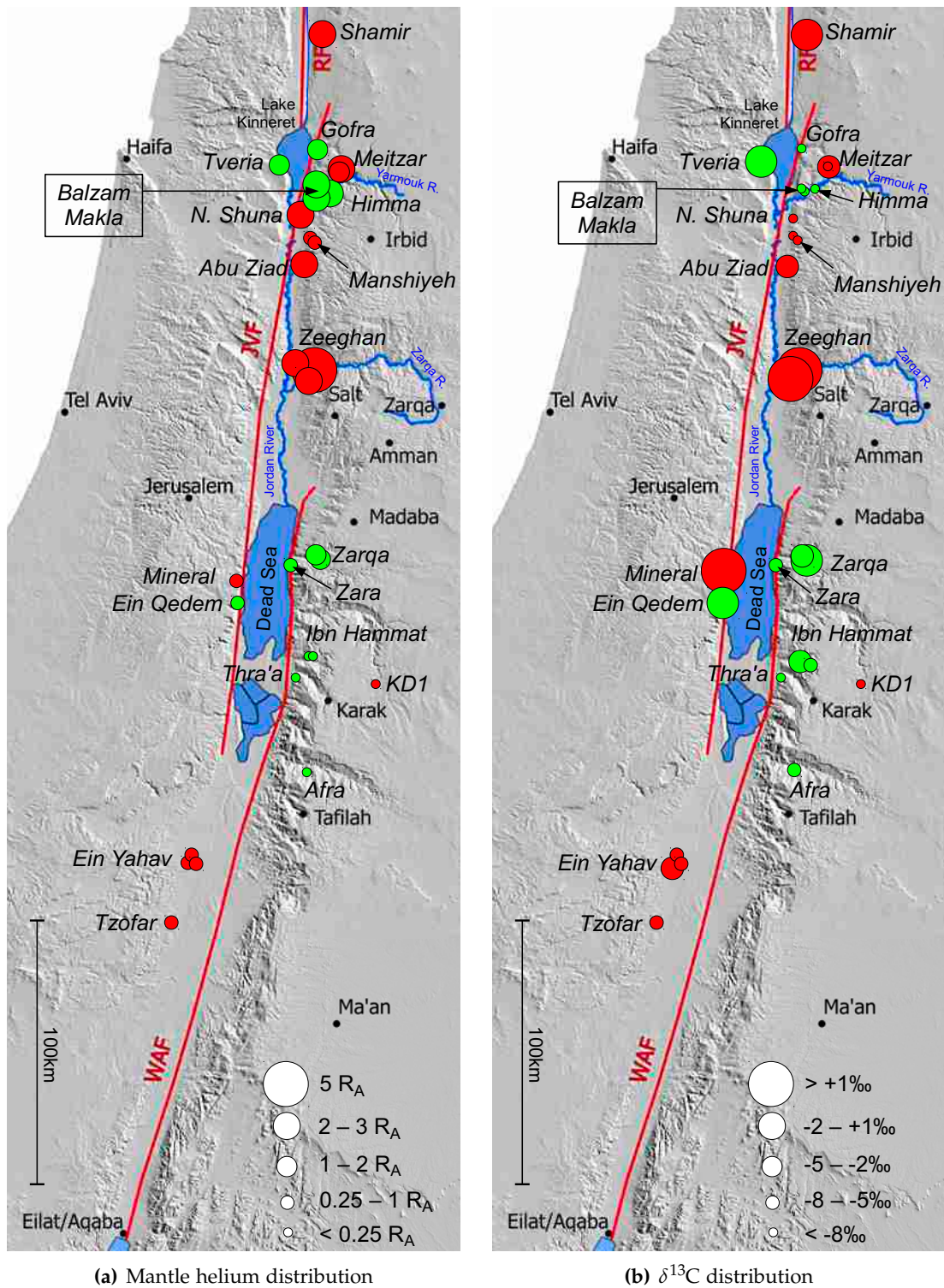
Figure 7.6: Distribution of mantle helium influence and δ^{13}C on springs (green) and wells (red) along the Dead Sea Transform. The size of the dots represents the ^{3}He/^{4}He ratio and ^{13}C isotopy, respectively, as declared in the legend.

Table 7.5: The relative contributions of ^{3}He and ^{4}He to the total measured concentration of the DST samples. Note the huge difference regarding the mantle shares of ^{3}He and ^{4}He, resulting from widely differing isotope ratios in the endmember reservoirs. All values in %. Israeli data from Tsur [2013].

	^{4}He$_A$	Δ^4He$_A$	^{4}He$_M$	Δ^4He$_M$	^{4}He$_C$	Δ^4He$_C$	^{3}He$_A$	Δ^3He$_A$	^{3}He$_M$	Δ^3He$_M$	^{3}He$_C$	Δ^3He$_C$
Jordan												
Himma	2.56	0.03	26.32	1.10	71.12	1.13	1.20	0.05	98.31	5.79	0.48	0.02
North Shuna	3.72	0.04	31.35	1.29	64.94	1.33	1.46	0.06	98.17	5.66	0.37	0.02
Abu Ziad	0.12	0.00	25.71	0.92	74.17	0.93	0.06	0.00	99.42	5.04	0.52	0.02
Manshiyeh 1	30.07	0.38	4.09	0.25	65.83	0.63	47.31	1.87	51.19	3.70	1.50	0.06
Manshiyeh 2	35.44	0.48	2.78	0.21	61.79	0.69	60.66	2.37	37.81	3.18	1.53	0.06
Zeeghan 4	0.02	0.00	61.34	1.62	38.64	1.62	0.00	0.00	99.88	3.72	0.11	0.01
Zeeghan 14	0.04	0.00	31.22	1.34	68.75	1.34	0.01	0.00	99.59	6.03	0.40	0.02
Zeeghan 15	0.02	0.00	31.38	1.15	68.60	1.15	0.01	0.00	99.60	5.14	0.40	0.02
Zarka Ma'in 1	0.13	0.00	18.32	0.77	81.55	0.77	0.09	0.00	99.11	5.86	0.80	0.03
Zarka Ma'in 2	0.23	0.00	15.91	0.62	83.86	0.62	0.18	0.01	98.87	5.38	0.95	0.04
Zara	0.27	0.00	3.58	0.14	96.14	0.14	0.90	0.03	94.49	5.08	4.61	0.17
Ibn Hammat 1	7.14	0.08	1.38	0.08	91.47	0.16	36.70	1.41	56.51	3.89	6.79	0.25
Ibn Hammat 2	1.13	0.05	1.33	0.06	97.54	0.11	8.64	0.52	80.61	4.76	10.75	0.42
Afra	7.70	0.09	1.25	0.08	91.05	0.17	40.64	1.61	52.42	3.90	6.94	0.26
Thra'a	0.92	0.01	2.25	0.10	96.83	0.11	4.55	0.18	88.53	5.12	6.92	0.27
KD1	0.82	0.01	1.57	0.10	97.61	0.11	5.55	0.32	84.85	7.25	9.59	0.53
Israel												
Gofra	2.27	0.02	21.13	0.92	76.60	0.94	1.32	0.06	98.03	5.98	0.65	0.03
Shamir	3.02	0.02	34.90	1.55	62.09	1.58	1.07	0.05	98.61	6.15	0.32	0.02
Meitzar 3	11.59	0.09	20.18	0.99	68.22	1.08	6.70	0.30	92.73	6.16	0.57	0.03
Meitzar 2	0.28	0.00	25.79	1.15	73.92	1.15	0.14	0.01	99.34	6.22	0.52	0.02
Ein Balzam	0.82	0.01	27.11	1.40	72.07	1.41	0.38	0.02	99.14	7.21	0.48	0.03
Ein Makla	0.39	0.00	22.82	0.97	76.79	0.97	0.21	0.01	99.18	5.90	0.61	0.03
Ein Yahav 116	2.89	0.04	4.22	0.19	92.89	0.22	7.67	0.31	88.78	5.21	3.56	0.14
Ein Yahav 6	0.66	0.01	5.85	0.24	93.49	0.25	1.36	0.06	95.86	5.50	2.78	0.11
Ein Yahav 16	0.86	0.01	4.65	0.20	94.49	0.21	2.20	0.09	94.32	5.54	3.49	0.14
Tzofar	0.27	0.00	5.11	0.21	94.61	0.21	0.65	0.03	96.12	5.44	3.23	0.13
Hamat Tveria	0.09	0.00	13.08	0.60	86.83	0.60	0.08	0.00	98.73	6.32	1.19	0.05
Ein Qedem	0.20	0.02	7.50	0.30	92.30	0.32	0.32	0.04	97.49	5.37	2.18	0.08
Mineral	39.79	0.53	5.73	0.52	54.48	1.04	46.18	2.01	52.90	5.25	0.91	0.04
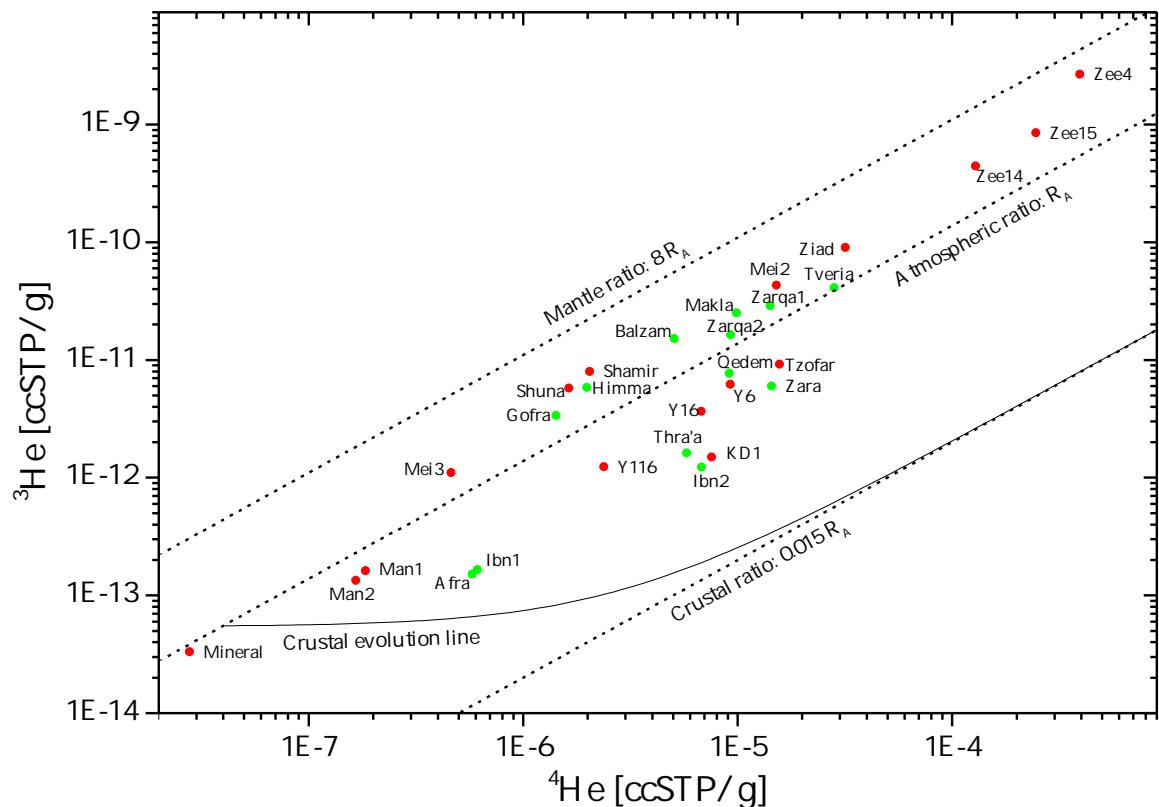
Figure 7.7: The ^{3}He vs. ^{4}He plot for the thermal waters exhibits a wide range of absolute concentrations of these isotopes.

only the Manshiyeh wells and Mineral exhibit a substantial atmospheric component, but most other samples have atmospheric shares below 5 %, indicating a predominant mixing between crustal and mantle reservoirs.

Note the big difference between the mantle contributions of ^{3}He and ^{4}He to the final composition in the sampled water. In all samples, by far most ^{3}He has its origin in the mantle, regardless of the total He contribution (which is essentially ^{4}He). This results from the big difference in helium compositions of the three reservoirs, as outlined in chapter 2.3.6.3.

Figure 7.9 shows the absolute ^{3}He and ^{4}He concentrations related to the relative mantle contribution. This diagram allows the examination of the mantle source that affects the thermal water. Regarding ^{3}He (bottom) and, to a slightly minor degree, also ^{4}He, a rough trend is observed, indicating that samples having a stronger mantle imprint also contain absolutely more ^{3}He as well as ^{4}He, although many exceptions contradict this trend. A high mantle contribution, like in Zeeghan 4, can only establish in an environment where a weak radiogenic ^{4}He production prevails, like in basalt, or where the flow velocity is high enough from the mantle source to the discharge location that radiogenic production can be neglected. Another option would be a massive ascent of volatiles from the mantle source, whose contribution exceeds the radiogenic helium production considerably. The fact that Zeeghan 4 is about twice as deep as the other two wells sampled in close vicinity and contains notably
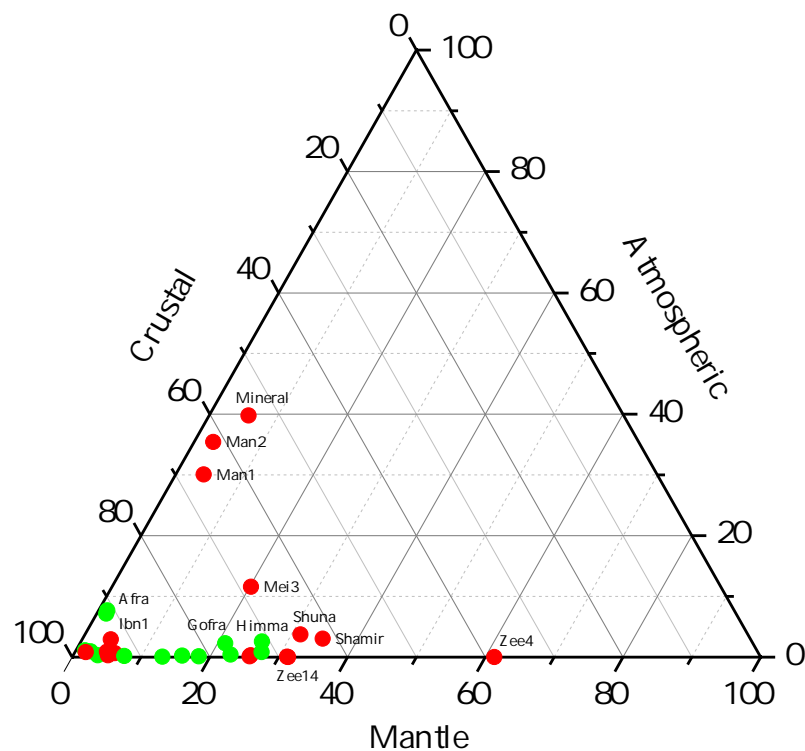
Figure 7.8: The relative contributions of the reservoirs crust, atmosphere and mantle to the total helium content. Except the Manshiyeh wells and Mineral, all samples exhibit a small or infinitesimal atmospheric fraction, indicating a predominant mix between crustal and mantle reservoirs.

more mantle derived helium argues for a young magma body under the well field relatively close to the surface, or it is in direct contact with a deep and highly conductive fault feeding it with mantle gases. The circumstance that Zeeghan 15, which is a few meters deeper than No 14, shows a somewhat higher mantle contribution than the latter one, strengthens the assumption of a shallow magma body inducing a mantle influence gradient. Moreover, the steep temperate gradient of almost 100 K/km (assuming an equal water contribution along the whole borehole and therefore the discharge temperature equals the same at the middle of the screen of the borehole) argues for a strong heat source, presumably a magma diapir below the Zeeghan well field.

The situation is similar for the Abu Ziad well and the two sampled Zarqa Ma'in springs. They are more affected by crustal, radiogenic ^{4}He imprint, suggesting their mantle source is located a bit deeper or further away compared to the Zeeghan area.

Himma, North Shuna, Shamir and others, in contrast, show a rather high relative mantle contribution, although their absolute ^{3}He and ^{4}He content is rather low. This argues for young water which exchanged with a strong mantle source quite quickly, because otherwise the radiogenic ^{4}He would be much more pronounced. The rather young age is supported by Bajjali *et al.* [1997], who estimated these waters to have recharged during the Holocene.
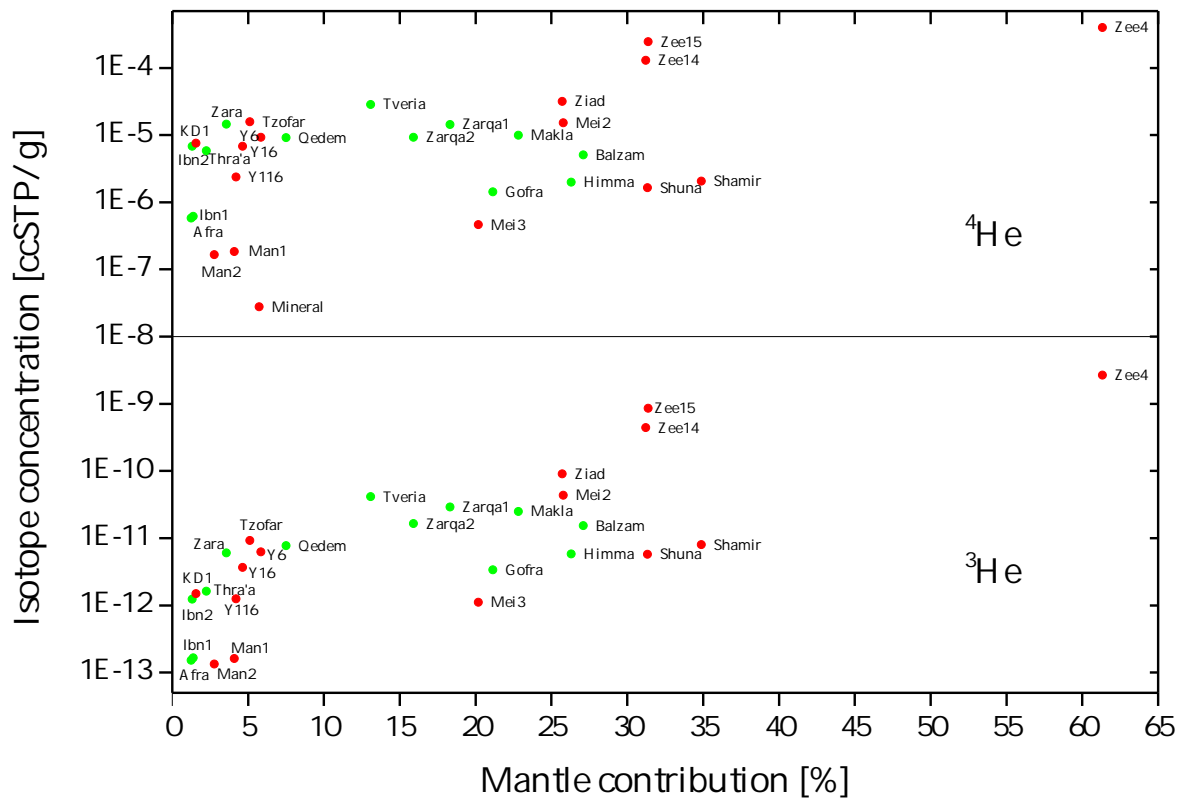
Figure 7.9: The relation of total ^{3}He and ^{4}He concentrations to the relative mantle contribution gives evidence for the distance between mantle source and discharge location as well as for the mantle imprint history. See text for details.

On the other hand there are samples with considerable ^{3}He content, but in total a small amount of mantle helium contributing to the total helium content. This indicates either a weak or distant mantle source, where crustal helium production dominates, or, more likely, the water once passed a strong and locally limited mantle source, but is exposed to crustal conditions before and/or afterwards. This seems to be the case for Ibn Hammat 2, Thra'a, KD1, Zara and the wells in Wadi Arava, which contain even as much ^{3}He as Himma or North Shuna.

One may infer from these observations that the link between a geothermal heat source and the mantle helium ratio would result in a correlation of discharge temperature and the (corrected) ^{3}He/^{4}He ratio. This relation is displayed in figure 7.10. However, no overall tendency is discernible, indicating the discharge temperature and the magnitude of mantle helium imprint are independent. This observation coincides with the data published by Torfstein *et al.* [2013], who likewise found no correlation between ^{3}He/^{4}He ratio and discharge temperature. This notice disagrees with the interpretation above, that mantle helium content is related to the distance from a magmatic heat source, but rather argues either for mantle volatile ascending independently from groundwater movement (i. e. in form of gas bubbles), or for a differently mantle imprinted, local reservoir. The latter would contrast the concept of an uniform reservoir suggested by Torfstein *et al.* [2013].
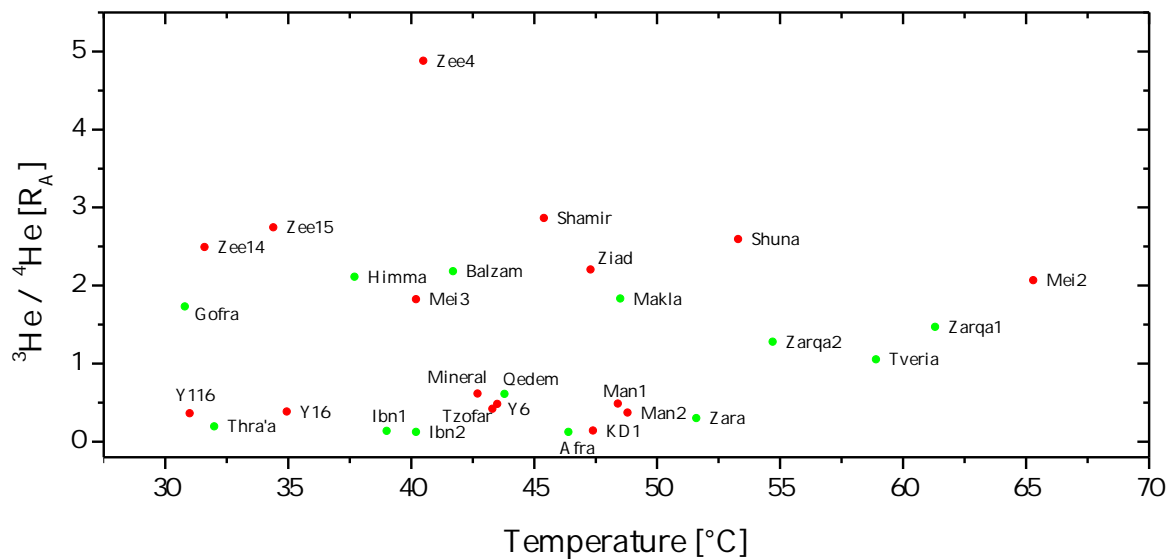
Figure 7.10: No overall tendency is recognizable in the ^{3}He/^{4}He ratio against discharge temperature plot. The trend within the Zeeghan well field (data points labeled Zee4, 14 and 15) suggests a strong mantle source beneath the well field which establishes a gradient of heat and mantle influence. The thermal gradient in this locality can roughly be determined to about 100 K/km.

Other noble gas isotope ratios were found to vary in the reservoirs air and mantle. Some of these isotope ratios are determined in this study. The according endmember composition is listed in table 7.6 and figure 7.11 presents the ratios ^{20}Ne/^{22}Ne, ^{3}He/^{22}Ne and ^{3}He/^{36}Ar, in every plot relative to the ^{40}Ar/^{36}Ar ratio. The dashed lines indicate the mixing line between the atmospheric and the MORB-like mantle reservoir. No clear trend is discernible in all diagrams, which may partly be due to large inaccuracies of the data. But more important is that the noble gas isotope data of the sampled thermal waters all plot very close to atmospheric values compared to MORB-mantle ratios. Even if OIB-mantle values would be considered, the image would not change considerably. Therefore, scattering seems to be predominant over real mixing trends.

It is, however, not so obvious, why the mantle signature is that more pronounced in helium isotopes than in the other mentioned ratios. Since helium has a better solubility in magmatic melts than the heavier noble gases [Carroll and Webster, 1994], partitioning during degassing of the melt under decreased pressure would favor the heavy noble gases to be found in mantle affected groundwater, especially as the heavy noble gases in turn have better solubilities in water. The strongest effect of the other isotope ratios should, hence, be seen in the argon ratio, since it varies most notably among the two reservoirs. The fact that the mantle signature is by far best pronounced in helium isotopes may result from much higher diffusivity of helium compared to the other noble gases. Burnard [2004] modeled the fractionation between argon and helium ascending in fractures up to one order of magnitude, while Torgersen and O'Donnell [1991] calculated the (crustal) noble gas release flux from immediate rock fracturing to be fractionated between He and Ar up several orders of
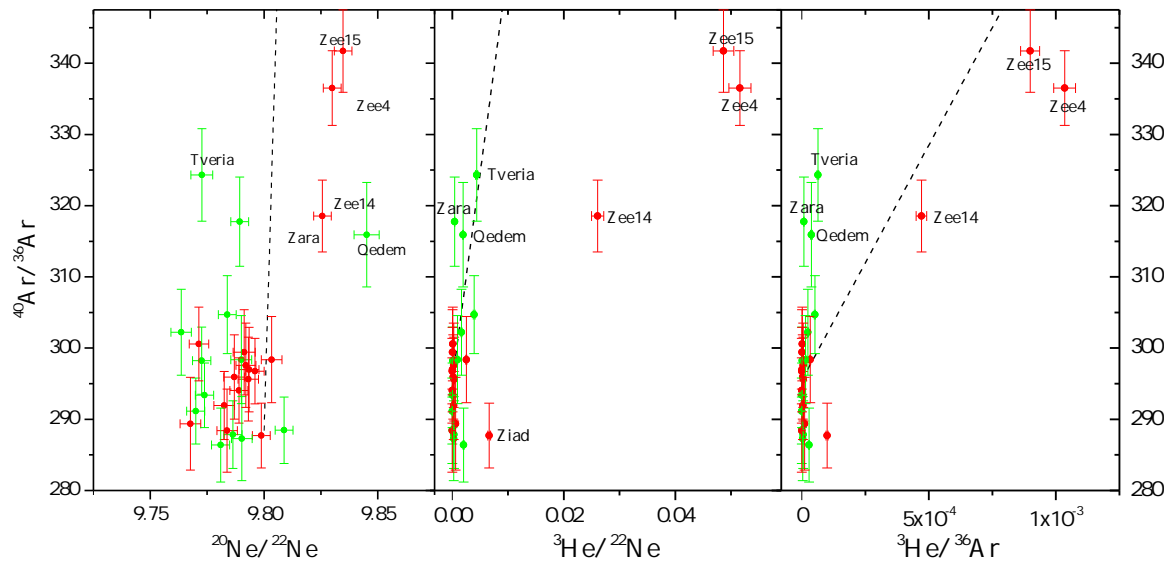
Figure 7.11: Other noble gas isotope ratio plots indicating possible mantle influence. The dashed lines are mixing lines between atmospheric and MORB composition, as compiled in table 7.6. No clear tendency is visible in all plots.

magnitude. However, whether these effects can solely explain the observed effects remains uncertain.

In case of argon another explanation is possible. Since this noble gas is by far the most abundant in the atmosphere, a mantle argon signature would be masked by the atmospheric component if the absolute argon concentration within the mantle is considerably lower than in the atmosphere. Unfortunately, only argon isotope ratios, but no absolute argon contents in magmatic minerals are published, but Nakai *et al.* [1997] measured absolute argon concentrations in CO_2-CH_4 rich gas samples from Etna, Italy, to be about 15 times smaller than atmospheric ones. As neon occurs at roughly the same concentration in the atmosphere as helium, such a masking effect can not explain the absence of mantle neon signatures in samples with high helium isotope ratios typical for mantle sources. Possibly this results simply from the merely small difference regarding the neon isotope composition in air and MORB.

Table 7.6: Other noble gas isotope ratios in air, MORB and different OIBs [Moreira and Kurz, 2013, and references therein].

Reservoir	$^3He/^4He$ [R_A]	$^{40}Ar/^{36}Ar$	$^{20}Ne/^{22}Ne$	$^3He/^{22}Ne$	$^3He/^{36}Ar$
Air	1	295.5	9.8	~0	~0
MORB	8	~30 000	12.6	5.1	0.45
OIB (Galapagos)	23	~3000	12.6	2.3 ± 0.5	0.35
OIB (Iceland)	17.5	~5000	12.6	2.5 ± 0.3	0.4

However, $^{40}Ar/^{36}Ar$ ratios in other hydrothermal systems, compiled by Sano and Fischer [2013], reveal that in most cases the ratio is close to the atmospheric value of 295.5, as it is found in the presented study. In samples from Vulcano, Italy, elevated argon ratios above 1000 are found [Magro and Pennisi, 1991], but a crustal neon systematic revealed by Tedesco and Nagao [1996] suggests the high argon ratios result from crustal ^{40}Ar production rather than from a mantle source at this locality. On the other hand, in case of samples from Etna, Italy [Nakai *et al.*, 1997], as well as from the continental rift zone in the Eiffel, Germany [Aeschbach-Hertig *et al.*, 1996], high argon ratios are associated with stronger mantle influenced neon signatures and, therefore, are interpreted to be an evidence for a mantle source.

Overall, the mantle influence is much less expressed in noble gas isotope ratios other than the $^3He/^4He$ ratio in most hydrothermal occurrences and their relative intensity compared to the helium isotope ratio seems to vary widely. Therefore, the $^3He/^4He$ ratio is by far the most sensitive mantle impact indicator among the noble gases.

Following, the other tracers determined in this study are compared to the helium ratio data in order to reveal any correlation between them and the mantle helium signals.

7.1.3 $\delta^{13}C$ isotopy

The carbon isotopy of the sampled thermal waters is listed in table 7.7 and varies widely from $-12\,‰$ to $+5\,‰$. Most samples show a rather enriched $\delta^{13}C$ level compared to values typically found in groundwater (compare figure 2.7). The most ^{13}C depleted thermal water is tendentially found in the springs and wells in and around the Yarmouk Gorge, namely Himma, North Shuna, Meitzar 2, both Manhiyeh wells, Gofra and, a little bit more enriched, Ein Balzam and Ein Makla, with $\delta^{13}C$ values between -7 and $-11\,‰$. However, in the same area the more shallow well Meitzar 3 is obviously enriched ($-3.40\,‰$), as is Shamir ($-1.54\,‰$), located north of Lake Kinneret, and Hamat Tveria ($-1.85\,‰$), west of the lake. Unfortunately, no $\delta^{13}C$ value for Zeeghan 4, the sample with the highest $^3He/^4He$ ratio, is available, because the sample bottle broke during shipment.

The wells and springs along the eastern side of the central Jordan Valley, from Abu Ziad south to the Zarqa Ma'in spring cluster, are highly enriched, the Zeeghan wells reaching positive $\delta^{13}C$ values. Further south, the $\delta^{13}C$ isotopy tendentially attains medium depleted values of $-7\,‰$ to $-4\,‰$. The map in figure 7.6 visualizes the $\delta^{13}C$ distribution along the DST, with bigger circles representing samples more enriched in ^{13}C.

The outstanding high $\delta^{13}C$ value of $+5.5\,‰$ found in the Mineral well at the Dead Sea, in combination with its very high salinity, suggests that this well feeds on inland intruding Dead Sea water, which is reported to have $\delta^{13}C$ up to $+4\,‰$ in the uppermost 20 m (although this value fluctuates between $+0.5\,‰$ and the mentioned $+4\,‰$) [Barkan *et al.*, 2001]. The same explanation is reasonable for the sampled spring at the Dead Sea shore, Ein Qedem, which has a $\delta^{13}C$ value of $-1.1\,‰$. The indication of Dead Sea water found at these localities is supported by the stable isotopes of the water molecules, as shown below. The high $\delta^{13}C$ values of the Zarqa Ma'in springs, located about 400 m above the Dead Sea, however, are unlikely explained by an upstream of Dead Sea derived water, because highly mineralized

Table 7.7: Compiled analysis results for δ^2H, $\delta^{18}O$, $\delta^{13}C$, tritium, radon and alkalinity for all thermal water samples along the DST. Israeli data from Tsur [2013].

Locality	δ^2H ‰	$\Delta\delta^2H$ ‰	$\delta^{18}O$ ‰	$\Delta\delta^{18}O$ ‰	$\delta^{13}C$ ‰	$\Delta\delta^{13}C$ ‰	Tritium TU	Δ Tritium TU	Rn Bq/m³	Δ Rn Bq/m³	Alkalinity meq/L
Jordan											
Wells											
North Shuna	-5.68	0.01	-27.53	0.09	-10.02		—	—	2693	396	6.84
Abu Ziad	-5.74	0.04	-28.09	0.21	-3.08		2.27	0.97	17228	672	4.72
Manshiyeh 1	-5.50	0.12	-26.05	0.40	-10.45		4.03	0.93	25865	870	6.26
Manshiyeh 2	-5.36	0.26	-25.74	0.68	-10.71		2.70	0.98	16352	821	6.38
Zeeghan 4	-6.58	0.06	-41.34	0.09	0.00		—	—	2873	281	23.00
Zeeghan 14	-5.81	0.04	-35.77	0.09	1.19		—	—	27174	590	18.24
Zeeghan 15	-6.82	0.04	-43.20	0.34	2.05		—	—	1896	418	23.00
KD1	-7.01	0.05	-39.21	0.26			b.d.	—			3.85
Springs											
Himma	-5.86	0.03	-29.55	0.32	-9.75		11.14	1.04	41487	1212	6.24
Zarka Ma'in 1	-4.11	0.01	-32.78	0.05	-3.46		—	—	5340	346	4.90
Zarka Ma'in 2	-4.09	0.05	-32.30	0.20	-0.92		b.d.	—	34277	1458	5.02
Zara	-5.35	0.08	-39.73	0.06	0.00		b.d.	—	78211	1952	3.08
Ibn Hammat 1	-6.91	0.17	-43.83	0.56	-4.85		—	—	176095	3144	3.53
Ibn Hammat 2	-6.99	0.06	-40.18	0.10	-6.50		—	—	6461	408	3.30
Afra	-6.50	0.05	-36.27	0.21	-6.55		—	—	9604	555	2.50
Thra'a	-6.70	0.05	-38.85	0.19	0.00		—	—	5944	373	2.62
Israel											
Wells											
Shamir	-7.03	0.07	-36.02	0.11	-1.54		b.d.				
Meitzar 2	-5.69	0.10	-28.68	0.41	-11.79		b.d.				
Meitzar 3	-7.02	0.15	-36.63	0.90	-3.40		b.d.				
Ein Yahav 6	-7.51	0.11	-47.83	0.66	-5.71		6.52	1.1			
Ein Yahav 16	-6.91	0.10	-42.38	0.54	-3.40		b.d.				
Ein Yahav 116	-6.60	0.06	-39.56	0.45	-6.20		b.d.				
Tzofar	-8.38	0.05	-57.58	0.13	-7.15		b.d.				
Mineral	1.08	0.06	-4.24	0.40	5.54		3.34	1.09			
Springs											
Gofra	-4.60	0.07	-21.84	0.12	-8.38		b.d.				
Ein Balzam	-5.93	0.09	-30.74	0.56	-8.45		b.d.				
Ein Makla	-6.04	0.12	-31.41	0.53	-7.63		b.d.				
Hamat Tveria	-3.57	0.10	-16.00	0.50	-1.85		b.d.				
Ein Qedem	0.92	0.10	-4.49	0.57	-1.10		b.d.				

water contributing to these springs is not in accord with the rather low salinity found in both sampled Zarqa Ma'in springs.

As summarized in figure 2.7, the enriched carbon-13 found along the DST may in principle result from mantle CO_2, freshwater carbonates and metamorphic CO_2. A significant mantle source of CO_2 can be excluded due to two reasons: First, it is unlikely that it can explain $\delta^{13}C$ values above $-3\,‰$. Second, a correlation between mantle helium and $\delta^{13}C$ isotopy would be expected. Griesshaber *et al.* [1992], for example, found clear positive correlations between the helium isotope ratios and $\delta^{13}C$ of CO_2 degassing from thermal waters from the several localities in the Rhine Graben and concluded a mantle source of the carbon dioxide.

As shown in figure 7.12, $\delta^{13}C$ of the DST water samples does not correlate with the $^3He/^4He$ ratios. Therefore, a substantial mantle CO_2 contribution to the thermal waters along the Jordan Rift Valley can be excluded. However, a slight correlation of $\delta^{13}C$ and the absolute measured ^3He and ^4He concentration is discernible. Mineral, which seems to represent a special case (see above), can be omitted in this consideration. Also the wells of the Zeeghan well field may need a separate treatment. They are strongly degassing, and the extremely high alkalinity and the absence of any smell (H_2S) suggest that mostly CO_2 gas escapes. Therefore, these wells might be affected by additional Rayleigh-like fractionation further enriching the ^{13}C isotopy of the water phase, as Evans *et al.* [2008] suggest to explain extraordinarily high $\delta^{13}C$ values of up to $+13\,‰$ in Himalayan hot springs. This would imply the Zeeghan samples would plot further left in the diagrams in figure 7.12 if no additional carbon fractionation would take place. Therefore, if the Zeeghan wells and Mineral are excluded from this analysis, no trend in the plots $\delta^{13}C$ versus ^3He or ^4He, respectively, is visible anymore.

Freshwater carbonates are not found in the DST, as most of the sedimentation occurred under saline conditions, when the precursors of the Dead Sea evaporated. However, Katz *et al.* [1977] report $\delta^{13}C$ of -7.7 up to $+3.4\,‰$ for aragonites of the Lisan formation, the sedimentary remnant of the former saline, Pleistocene Lake Lisan. Generally, groundwater bodies leaching evaporites from this formation have a high salinity, but are found only in the valley depression itself, as for example reported by Salameh [2001]. Sources of salinity in waters entering the Jordan Valley from its eastern escarpment, however, are the Jurassic and Triassic sandstone rocks (Kurnub and Ram aquifers). This means carbon isotopy of the springs in the side-wadis of the Jordan Valley is unlikely to be affected by carbonates from the Lisan formation. Deeply drilled wells and the springs at Lake Kinneret, in contrast, cannot be ruled out to incorporate Lisan formation carbonate.

In case the dissolution of Lisan evaporites would influence the tested thermal waters, the process takes place within in the crust and therefore no correlation between the $^3He/^4He$ ratio and $\delta^{13}C$ should be observed, as is the case for the presented localities. However, if dissolution of carbon from the Lisan formation is the governing process, a correlation between salinity and $\delta^{13}C$ should be discernible, at least among the wells (because most springs are somewhat elevated above the bottom of the Jordan Valley, yet an upstream is not principally impossible). This relation is depicted in figure 7.13. Only a very rough trend is observed, but especially those locations with E. C. below 3000 µS/cm are widely scattered with no pattern. Even more, no general difference between springs and wells can be recognized.
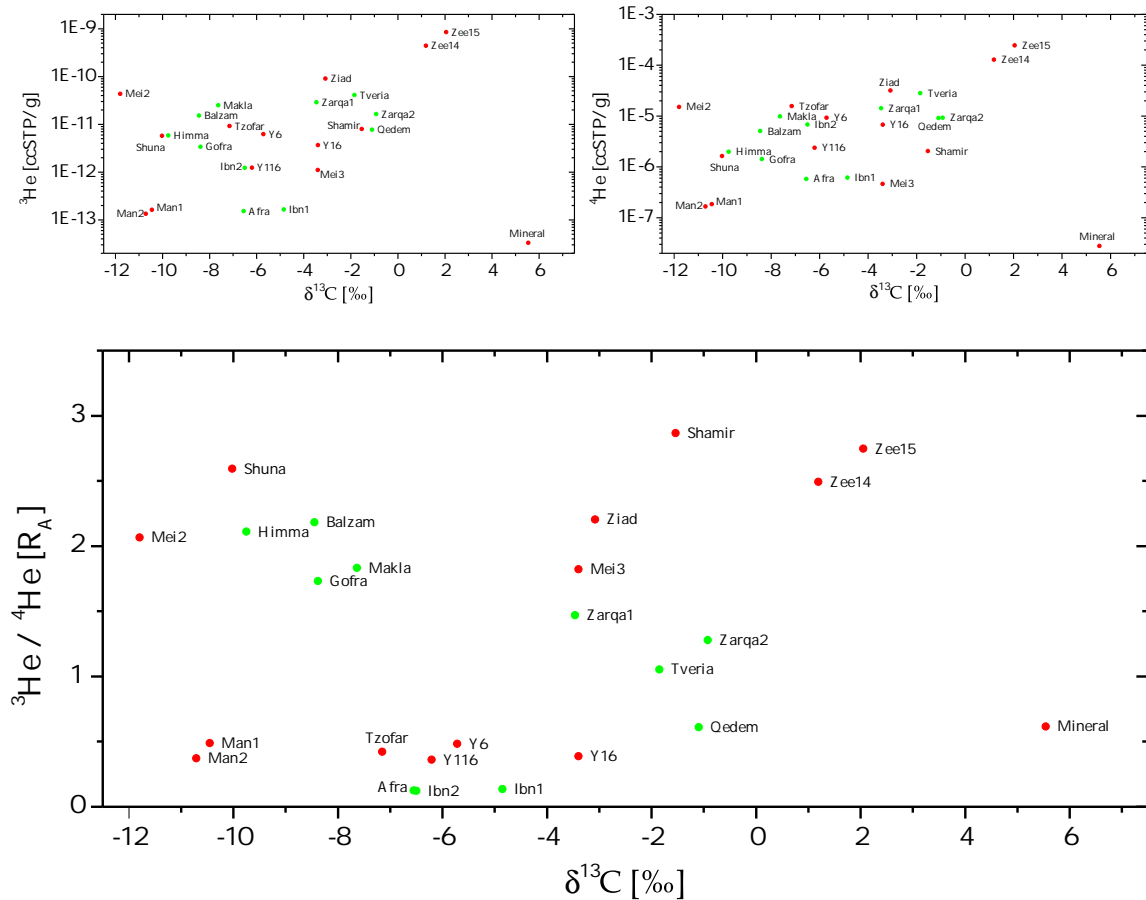
Figure 7.12: No correlation between the corrected $^3\mathrm{He}/^4\mathrm{He}$ ratio and $\delta^{13}C$ can be recognized, excluding a mantle source of carbon in the DST groundwater samples. The slight trends visible in $^3\mathrm{He}$, respectively $^4\mathrm{He}$, against $\delta^{13}C$ disappear, when the Zeeghan and Mineral samples are discarded (see text for details).

These findings suggest that neither mantle CO_2 nor dissolution of evaporites are the reason for the distinctly enriched $\delta^{13}C$ isotopy along the Jordan Rift Valley. The incorporation of ascending CO_2 from metamorphic decarbonation is therefore the most likely explanation for it.

In general, however, the $\delta^{13}C$ isotopy is no good indicator of mantle induced processes, because the signatures of the different carbon sources can not easily be distinguished from each other and ambiguity remains. A better differentiation between a mantle and a crustal carbon source can be obtained by considering the $CO_2/^3\mathrm{He}$ ratio in addition to the $^3\mathrm{He}/^4\mathrm{He}$ ratio [Sano and Fischer, 2013]. However, no CO_2 concentration in thermal waters and volatiles escaping from them was determined during this study. Torfstein *et al.* [2013], on the contrary, published $CO_2/^3\mathrm{He}$ ratios for many thermal waters in Israel and concluded that crustal carbon dissolution and precipitation are the controlling factors regarding the carbon content along the DST.
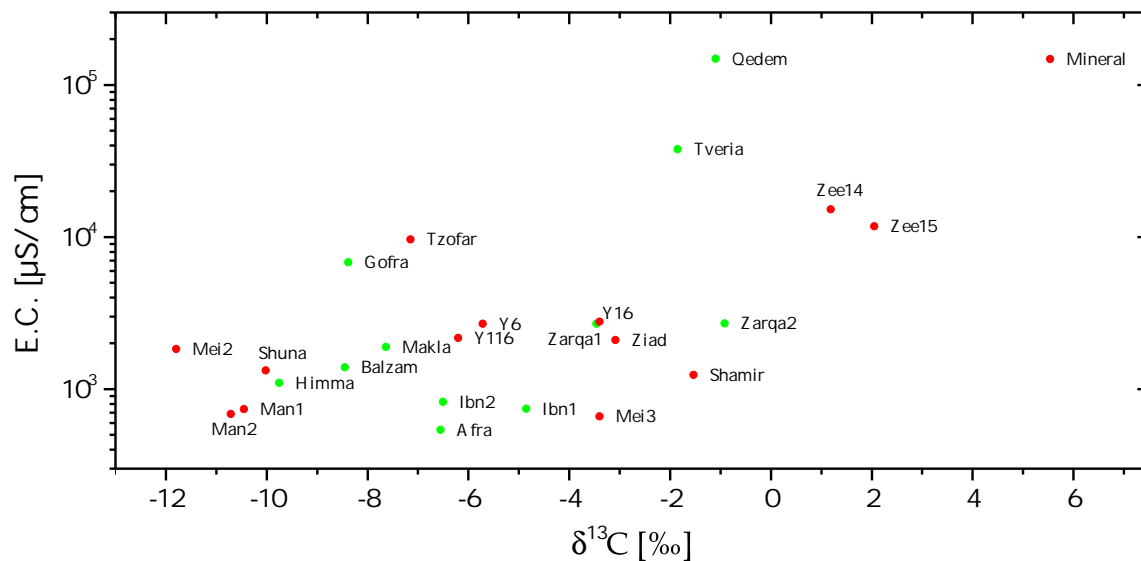
Figure 7.13: A rough correlation between the E. C. and the carbon isotopy is recognizable, but especially low mineralized waters scatter widely regarding their δ^{13}C. This indicates the dissolution of carbonates is not the dominating factor governing the δ^{13}C isotopy in the DST.

7.1.4 Stable isotopes

Stable isotopes of thermal waters have been studied over a long time in Jordan [Salameh and Rimawi, 1984; Bajjali *et al.*, 1997; Möller *et al.*, 2006, among others] and Israel [Mazor *et al.*, 1980; Rosenthal, 1994; Möller *et al.*, 2006, and others] and basically agree with our analyses. The new data is presented in figure 7.14 and listed in table 7.7. All sampled waters fall below the LMWL, regardless if the Jordan Meteoric Water Line (JMWL) or the Eastern Mediterranean Water Line (EMWL) is considered, which is indicative of evaporative processes during percolation. This matches the interpretation already made regarding the stable isotope data presented in the Azraq study.

In general, the stable isotope data span a wide range, indicating different recharge altitudes or even different climatic conditions at the time of recharge. The samples most depleted, i. e. which recharged at the coolest conditions, are Tzofar and Ein Yahav 6 in Wadi Arava, the most enriched ones are Ein Qedem and Mineral at the Dead Sea coast. The latter confirm the assumption obtained from the δ^{13}C isotopy, that these waters are former Dead Sea water, which has δ^{18}O values at the surface mostly around $+4\,\permil$ (a minimum is reported to be $+1.6\,\permil$ during a steep water level rise), indicating the strong imprint of evaporative conditions of the Dead Sea terminal lake. Associated δ^2H values are between -8 and $+5\,\permil$ [Gat and Dansgaard, 1972].

Except of the Dead Sea influenced samples, the springs at the shore of Lake Kinneret are most enriched, whereas the northernmost Shamir well is considerably more depleted, indicating a higher recharge altitude. The locations in and around the Yarmouk Gorge cluster quite close to each other, indicating a similar recharge history. As Bajjali *et al.* [1997] infers,
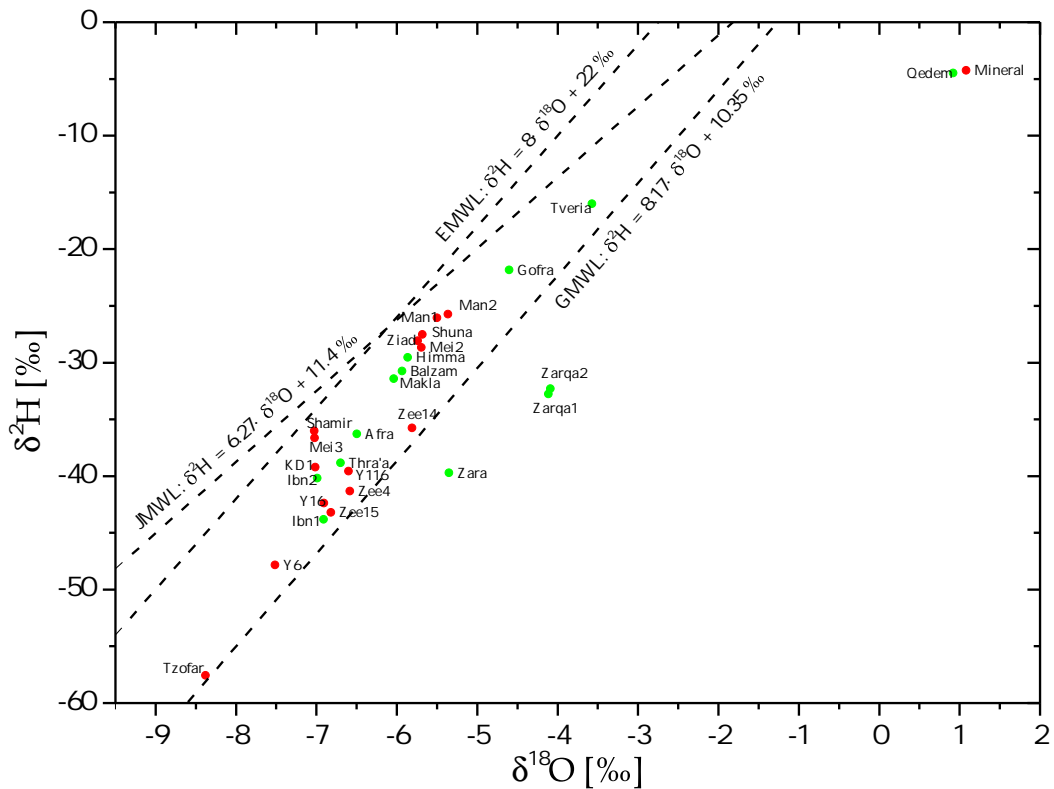
Figure 7.14: Stable isotope plot of all sampled thermal waters. All samples fall below the local meteoric water lines, indicating evaporative processes in the top soil. The springs of the Zarqa Ma'in/Zara cluster are significantly shifted towards less depleted ^{18}O, signaling the original hot water reservoir exceeded temperatures of $100\,^{\circ}$C, where oxygen exchange reactions with the surrounding aquifer matrix occur.

recharge of this cluster of waters took place in the Jordan highlands and the opposing Golan Heights, except Ein Maqla whose water originates from higher altitudes, presumably from Mount Hermon at the Syrian-Libanese border. Ein Balzam is, according to the mentioned publication, assumed to be a mixture of the water body feeding Ein Maqla with water found in the other springs in the area, an interpretation that can be confirmed by the presented stable isotope data. Also the 800 m deep Meitzar 2 well fits into this cluster, whereas the more shallow Meitzar 3 well plots closer to the water found more to the south of the Jordan Valley.

The stable isotope pattern changes south of the Abu Ziad well, where the Zeeghan wells and the springs in the side-wadis southeast of the Dead Sea cluster loosely together and are more depleted than the northern water types. Also the Ein Yahav wells 16 and 116 and the more inland located KD1 well belong to this cluster. It is actually not surprising that KD1 has a similar isotopic imprint than Afra, Thra'a and the two Ibn Hamat springs, because they all discharge from the Lower Cretaceous Kurnub sandstone aquifer. In total, a general trend is observable since waters in the north of the study area are less depleted in stable isotopes than those found in the south.

An exception of the water group of the eastern Dead Sea escarpment are the springs of Zarqa Ma'in and Zara. These are distinctly more enriched in $\delta^{18}O$, expressed also in a very low deuterium excess, which plots them far away from the meteoric water lines. This points to interaction of the oxygen in the water molecules with oxygen incorporated in the rock material. According to Clark and Fritz [1997], oxygen containing minerals have positive $\delta^{18}O$ values (carbonate rock ~+29‰, granitic rock ~+10‰, basalt ~+8‰). As exchange rates at low temperatures are much too slow to considerably influence the oxygen isotopy of groundwater within typical residence times, the case is different in geothermal systems. The exchange rate is notably increased at temperatures above 100 °C and therefore water percolating through the rock at such high temperatures gets enriched in $\delta^{18}O$. At the same time δ^2H stays virtually the same, simply because most minerals do not contain any hydrogen [Clark and Fritz, 1997]. The right-shift in the δ^2H–$\delta^{18}O$ diagram of groundwater interacting with the rock matrix at high temperatures is found in many geothermal systems around the world [Truesdell and Hulston, 1980] and can explain the δ^2H–$\delta^{18}O$ composition of the Zarqa and Zara springs. Moreover, it shows that no juvenile or magmatic water, which is estimated to have $\delta^{18}O$ between +6 and +9‰, but δ^2H between −40 and −80‰ [White, 1974], contributes to the sampled thermal waters. The thermal anomaly with very high geothermal gradients found in the Zarqa Ma'in/Zara area (compare chapter 4.2) is in good accordance with the finding of temperature induced oxygen exchange between rock and water molecules.

A slight influence of the temperature effect on $\delta^{18}O$ can not principally be excluded for the other waters, but the effect of a hot reservoir would be much less compared to the Zara and Zarqa springs.

The question of a relation between mantle helium influence and stable isotopes is answered by the graphs in figure 7.15: there is no relation recognizable between $^3He/^4He$ ratio, ^3He or ^4He and $\delta^{18}O$. Therefore, $\delta^{18}O$ cannot be taken as an additional tracer for mantle influenced fluids.

7.1.5 Water chemistry and radon

Water chemistry

The major ion analysis of the thermal waters of Jordan is presented in a Piper plot in figure 7.16 and the underlying data is compiled in table A.7 on page 185. The samples from Israeli localities were not analyzed for water chemistry. Some water groups can be distinguished. First, the two Manshiyeh wells form a solitary group, where bicarbonate and Ca/Mg dominate. Second, the water from the Zeeghan wells and the spring field of Zarqa Ma'in and Zara are similar in their mineralization pattern, with Cl being the dominant anion and Na the most abundant cation. Most notable, however, the wells and springs around the Yarmouk Valley, carrying much mantle helium, and those springs furthest south with predominant crustal signature exhibit a very similar ionic composition and cannot be distinguished from each other. Therefore, the ionic pattern of the thermal waters in Jordan is not suitable to differentiate the tectonic behavior and the mantle gas input along the DST.
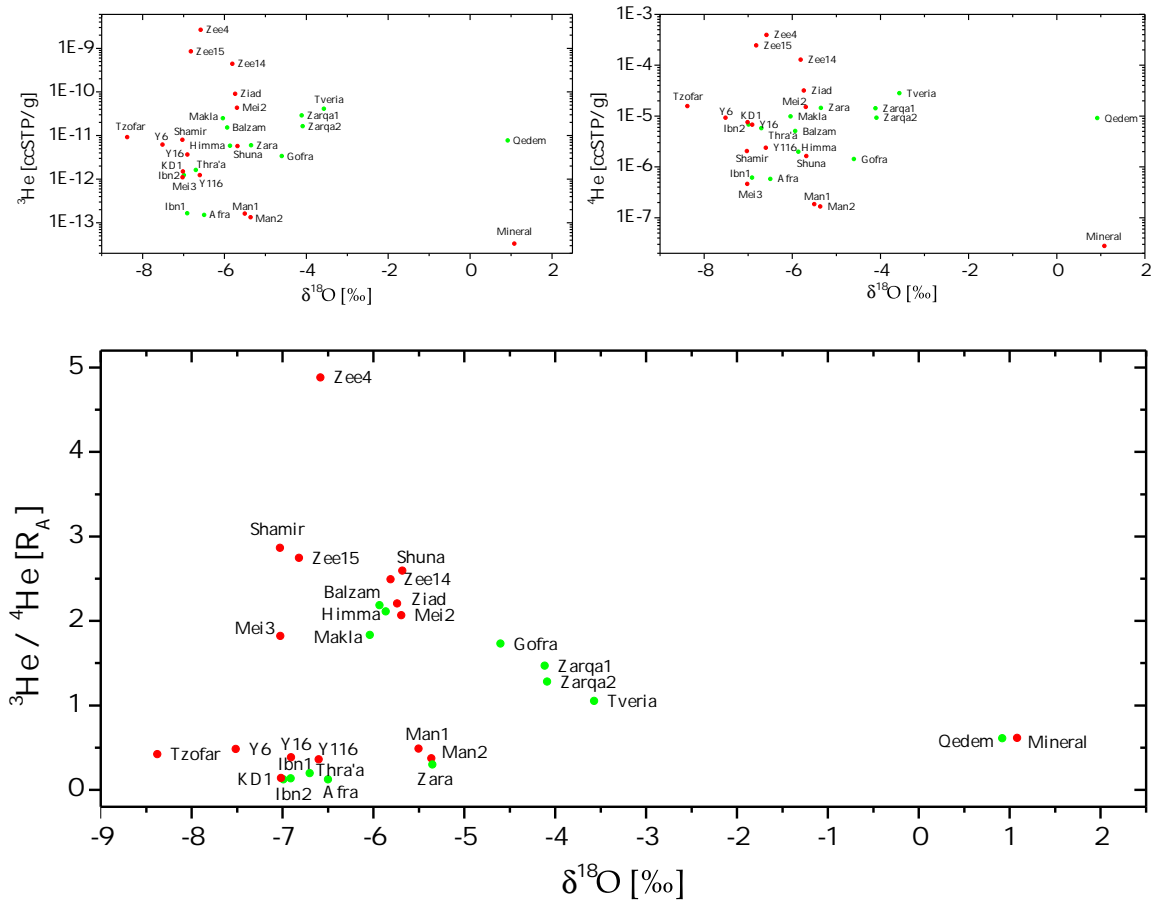
Figure 7.15: No correlation between the corrected ^{3}He/^{4}He ratio, ^{3}He or ^{4}He and δ^{18}O can be recognized.

The origin of thermal waters can be studied with a ternary diagram of relative Cl, SO$_4$ and HCO$_3$ content, as shown in figure 7.17, and which is in principle the anion triangle of the Piper diagram, but uses the ion concentrations in mg/L instead of in meq/L (after Giggenbach and Goguel [1989], cited according to Powell and Cumming [2010]). According to this plot, water can be classified into four types: 1) HCO$_3$ rich, peripheral, i. e. meteoric water with no or only little geothermal influence, 2) steam heated, SO$_4$ rich water, 3) volcanic water which is rich in SO$_4$ and Cl, originating from absorption of H$_2$S carrying volcanic gases, and 4) mature or geothermal water, dominated by Cl.

The samples from north Jordan plot all more or less in the bicarbonate dominated corner, while the samples from the Zarqa Ma'in/Zara spring cluster and the Zeeghan well field are located tendentially towards the mature water vertex. All samples contain sulphate to a certain extent. Abu Ziad, where H$_2$S smell was perceptible at sampling, contains most SO$_4$, followed by Zeeghan 4 and 15. The latter wells showed extreme degassing, but H$_2$S was not noticeable at the sites. On the other hand, North Shuna well has a quite low SO$_4$ content, but exhibited obvious H$_2$S smell. In total, however, none of the samples can be referred to as real volcanic water.

Figure 7.16: The Piper plot of thermal waters in Jordan shows, that the water of the northern location (green) and those from the southern side wadis (cyan) have a very similar mineralization pattern. Therefore, the water chemistry is not appropriate to distinguish between predominant mantle and crustal character of the thermal waters.

Figure 7.17: Ternary diagram of the thermal waters in Jordan, in which a volcanic or a deep geothermal source can be distinguished. None of the samples can be considered as true volcanic water.

Figure 7.18: No correlation between the radon activity and the mantle influence is observed.

Radon

Radon is often used as a tool to detect fault locations [Crenshaw *et al.*, 1982; Toutain and Baubron, 1999, and references therein], as these may facilitate the fast ascent of volatile gases from deep, radium rich reservoirs (especially the crystalline basement) to the surface. Provided the geothermal reservoirs have a similar Rn production rate up to the point of discharge, one should expect a correlation between the ^{3}He/^{4}He ratio and the radon activity in the sampled water, as both gases are assumed to take the same pathway towards the surface.

The relation between the corrected ^{3}He/^{4}He and the ^{222}Rn activity is presented in figure 7.18. Radon data of Israeli springs and wells is taken from Moise *et al.* [2000], who analyzed most of the Israeli localities treated in this study. No obvious trend, however, is visible between the mantle helium and Rn concentration. The wide range of Rn activities argues for very differently Rn producing minerals, or at least strong variability of conductive fractures down to the basement. Interestingly, all thermal wells feature Rn activities below 30 000 Bq/m^3, whereas the activity of many thermal springs is much higher, reaching almost 300 000 Bq/m^3 in Ein Qedem. This indicates that many springs are connected to deep, Ra rich layers, but also that the transport of mantle gases is more or less independent from the Rn gas conveyance.

The Rn activity varies also on a very local level, as springs situated in close vicinity, like Ein Maqla, Ein Balzam and Himma, or the two springs in Wadi Ibn Hammat, vary widely in their radon content. Radon activity can therefore not be applied as an additional tracer of mantle impact in the DST.

7.2 Detailed analysis of the geothermal localities

Following, the different localities of thermal water occurrence are considered in detail and the individual conditions leading to elevated water temperatures are tried to deduce in view of the new data and other sources.

In and around the Yarmouk Gorge

The thermal waters in the Yarmouk Gorge were intensively studied. They are situated between the structural depression of the Golan Heights and the anticline of the Ajloun Dome. Most of the groundwater originates from the Ajloun ridge [Bajjali *et al.*, 1997; Margane *et al.*, 2002], but stable isotopes in some sources indicate also a fraction being recharged at the slopes of Mount Hermon in the north [Arad and Bein, 1986; Bajjali *et al.*, 1997]. Figure 7.19 shows a hydrogeologic cross-section along a north–south line from the Hermon Mountain Ridge in Lebanon across the Golan Heights and the Ajloun dome to the Zarqa River Valley in the south, including assumed hot and cold groundwater flow and its ascent through a supposed zone of enhanced conductivity in the Yarmouk Gorge.

Both, Galanis Jr. *et al.* [1986] and Shalev *et al.* [2013] report an elevated heat flow in the area of the lower Yarmouk Gorge, where the springs are located. This heat flow anomaly seems to be a very local phenomenon, as Dafny *et al.* [2006] found no heat anomaly beneath the Golan Heights, and Galanis Jr. *et al.* [1986] and Bajjali [1994] reported no evidence for a deviation from the normal Jordanian heat flow at the Ajloun Ridge. This would be an indication of a fast upstream of deep, hot groundwater. However, no evidence for major fractures is reported in the Yarmouk Valley [Roded *et al.*, 2013], only the presence of hot springs in the valley is interpreted as an indication of deep faulting beneath the Yarmouk Gorge [Levitte and Eckstein, 1978]. Additionally, no significant volcanic activity has been reported for the Ajloun Dome, but the Golan area is covered by basalts originating form the Harrat ash-Shaam volcanic field which has its center several hundred kilometer eastwards at Jabal ad-Druze. The youngest basalts on the Golan are dated to ages of 0.5 Ma and younger [Horowitz, 2001].

The approximately uniform distribution of helium isotope ratios of around $2\,R_A$ to $2.5\,R_A$ in the Yarmouk Gorge and the wells nearby along the Jordan Rift escarpment southward argue for a source of mantle volatiles not directly related to recent Harrat ash-Shaam volcanic activity. This would imply a groundwater flow from the north crossing the Yarmouk Gorge in the subsurface towards the wells at the flanks of the Ajloun Ridge, which is rather unlikely due to the updoming of the strata south of the gorge, as depicted in figure 7.19. Instead, Roded *et al.* [2013] assume two separated deep reservoirs which are recharged at the Hermon and the Ajloun Mountains, respectively, and which are heated under a normal geothermal gradient. The water of these reservoirs, as it percolates, interacts with mantle fluids or volatiles rising through permeable fractures opened by the deformation leading to the syncline of the Golan Heights and the updoming of the Ajloun Ridge. As hot springs can always be considered to be a mixture of thermal water with cool, shallow water, the original reservoir can be expected to have a higher helium isotope ratio than observed at the surface.
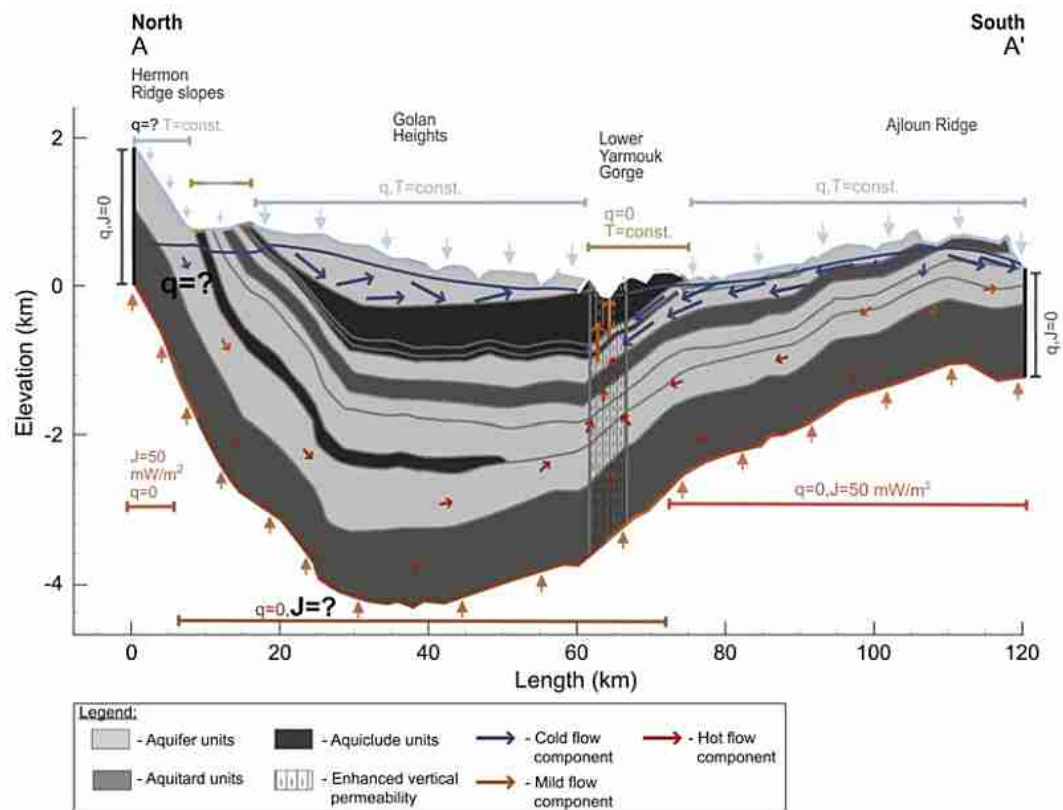
Figure 7.19: Conceptual cross-section of the hydrogeologic setting from the Hermon Mountains in the north and across the lower Yarmouk Gorge and south to the Zarqa River, including assumed groundwater flow and an ascent of hot water in conductive faults in the Yarmouk area. From Roded *et al.* [2013].

The presented data is overall in accordance with this concept, but it needs to be assumed that both the contributions from north and south contain approximately the same ^{3}He/^{4}He ratio. Furthermore, the Manshiyeh wells, showing only a minor mantle gas imprint (around $0.4\,R_A$) are located between two approximately equally deep wells (North Shuna and Abu Ziad), which both exhibit a rather strong mantle helium configuration (2.6 and 2.2 R_A, respectively). If one considers also the high helium ratio of $1.62\,R_A$, found by Eraifej [2006] in the Waqas well, situated between Manshiyeh and Abu Ziad, the distance of the two high mantle reservoirs is restricted to maximal 10 km, yet, they are separated by a low mantle regime in between. Therefore, instead of the imagination of a wide-spread reservoir supplying the whole area, a more local view is prompted to describe the hydrologic setting with respect to mantle influences.

Around Lake Kinneret

The Lake Kinneret basin is a pull-apart within the DST. It is bounded by two NS-trending major fault systems and several small fractures are present below the lake, as shown in figure 7.20. Heat flow measurements resulted in a normal flow of $36\,\text{mW}/\text{m}^2$ in the Zemah-1
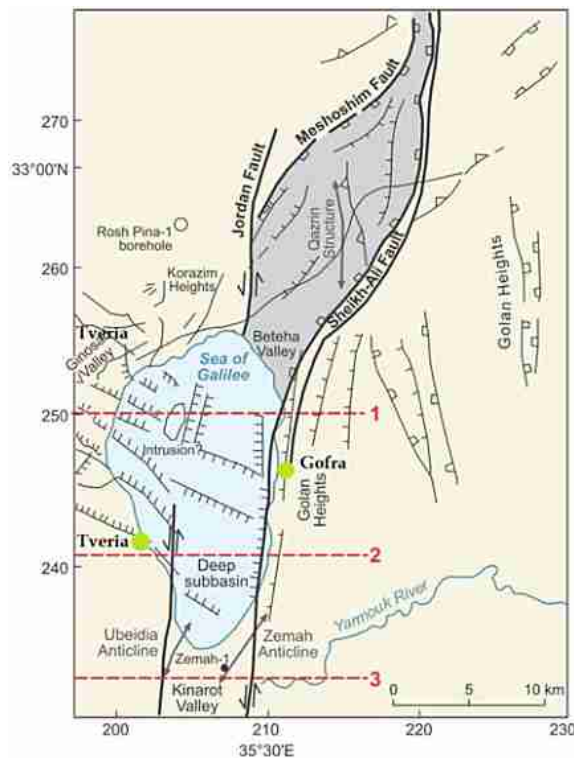
Figure 7.20: Structural map of Lake Kinneret. The lake is bounded by two main faults and several structural features are present below the lake. The two sampled springs, Gofra and Hamat Tveria, are drawn in. Adapted from Ben-Avraham *et al.* [2008].

borehole (4249 m) at the southern tip of the lake [Eckstein and Maurath, 1995, cited after Roded *et al.* [2013]], but Ben-Avraham *et al.* [1978] obtained an elevated average heat flow through Lake Kinneret itself of 75 mW/m^2. Local basalt outcrops are dated to ages of 3.5 Ma to 5 Ma [Mor, 1993], and dating of deep occurrences observed in boreholes drilled around the lake resulted in ages of around 9 Ma [Heimann and Steinitz, 1989, after Horowitz [2001]].

Hamat Tveria on the west coast of Lake Kinneret discharges hydrochemically different water from Gofra, located on the eastern side [Möller *et al.*, 2012, and references therein] and presumably not much exchange takes place between the two reservoirs. Although Hamat Tveria is distinctly warmer than Gofra (59 °C versus 31 °C), the latter spring has a significantly higher helium isotope ratio (1.56 R_A, whereas Hamat Tveria has only 1.13 R_A). A magmatic heat source, however, would increase both the temperature and the ^{3}He/^{4}He ratio. Such a heat source at Lake Kinneret can be excluded due to the high ages of the basalt bodies around and beneath the lake. Therefore, deep circulation and ascent through conductive fractures is most likely to be the reason of thermal waters at Lake Kinneret. This would, however, imply that the reservoir feeding Gofra is considerably more enriched in mantle helium than the one supplying Hamat Tveria, as the higher temperature of the latter indicates either a faster ascent or less admixed shallow groundwater. Both possibilities would result in a higher helium ratio in Hamat Tveria, if the helium composition of the reservoirs would be the same. This finding, again, contradicts the common reservoir proposed by Torfstein *et al.* [2013].

Shamir well

Shamir well, 1420 m deep and located on the eastern margin of the Hula basin, the northernmost pull-apart in Israel, has a high helium ratio of $2.83\,R_A$, yet, the water temperature indicates a normal thermal gradient at the well location, although an elevated gradient of 40 K/km was detected within the basin [Bein and Feinstein, 1988]. In this case the observation of mantle helium is apparently not connected to a geothermal anomaly as found in the systems explained above.

Western Dead Sea coast

The noble gas interpretation of Mineral is problematic. The well did not facilitate good sampling conditions and atmospheric contamination occurred, which needed profound correction. The extremely low ^{3}He and ^{4}He content below atmospheric values indicates even more strong degassing prior to sampling. Ein Qedem seems to be reasonable, although the NGT fit had bad χ^2 values. Its proximity to the crust–mantle mixing line in plot 7.4 indicates no major atmospheric contamination.

Despite sampling difficulties, both samples show very similar ^{3}He/^{4}He ratios of $0.6\,R_A$, which agree with data published by Torfstein *et al.* [2013] and Lange *et al.* [2008], the latter found samples with up to $1\,R_A$ a few kilometers further north. Although located close to the western fault comprising the Dead Sea pull-apart, the mantle influence in these localities is rather low.

Zeeghan well field

Not much detailed information is available on the structural geology of the Zeeghan area. The Zeeghan wells are drilled where the Zarqa River Gorge enters the Jordan Valley. This gorge is cut into the uplifted rock of the Ajloun dome. Information on deep faults in this anticline is inconsistent. Salameh and Rimawi [1984] show a N–S cross-section through highlands, where no relevant faults are present at the site, whereas Bajjali [1994] displays extensive faulting at the Ajloun ridge. The database of WAJ [2010] contains only a few lineaments and faults in the well field area, but no information about displacement is given. The closest basalt occurrence, dated to around 3 Ma, is found somewhat further away from the rift, at the headwaters of Zarqa River [Baubron *et al.*, 1985, after Horowitz [2001]]. The magnetic survey of Frieslander and Ben-Avraham [1989] did not suggest a magma body at shallow depth in the well field area, whereas Ben-Avraham and Ginzburg [1990] indicate a slight magnetic anomaly a little bit further east, but their presented map has a large scale and details are hard to figure out.

The presence of the very high geothermal gradient discovered by a very rough estimation in this study has not been reported before and indicates the influence of a strong heat source, either being quite close to the surface, or an upstream of huge amounts of deep, mantle impacted groundwater over an area of several km^2 occupied by the Zeeghan well field. The observation of a high helium isotope ratio of up to $5\,R_A$ supports the discovery a strong mantle reservoir. A favored transport of mantle gases by metamorphic CO_2 bubbles seems very likely.

Zarqa Ma'in/Zara spring cluster

The area around the spring fields of Zarqa Ma'in and Zara are considered to have the most favorable geothermal potential in Jordan and are therefore studied most extensively of all thermal spring systems in the country. Extensive surface volcanism is found in the area and magmas are dated to ages between 0.6 and 3.4 Ma [Duffield *et al.*, 1988]. Moreover, the area is traversed by deep faults, most prominent the shearing Zarqa Ma'in Fault which extends more than 200 km eastwards to Saudi Arabia (compare figure 4.6). Heat flow in the area is found to be very high. Galanis Jr. *et al.* [1986] reports heat flows of up to $472\,mW/m^2$ and a temperature gradient of 175 K/km for the Zara springs area and an almost as high geothermal gradient of 165 K/km in the Zarqa Ma'in spring cluster, where the heat flow is $255\,mW/m^2$. That this enhanced heat flow is a local phenomenon and not directly related to the pull-apart of the Dead Sea basin is documented by Ben-Avraham *et al.* [1978], who determined a rather low heat flow of only $29\,mW/m^2$ on average through the Dead Sea (although it should be noted they did not measure off the Jordanian coast). However, Sawarieh [2005] assumes this heat reservoir also supplies the shallow, hot wells in Jiza, located further inland, about 30 km south of Amman.

Duffield *et al.* [1988] state that the magma bodies found in the area are too old to considerably contribute to the heat anomaly in Zarqa Ma'in and Zara, as they should have already cooled down. The discharge of hot water in these springs is therefore attributed to deep circulating water in an environment of an enhanced geothermal gradient. Hakki and Teimeh [1981, cited after Sawarieh [2005]] related the hottest springs to the highest shearing intensity in the area. This means the high temperature gradient is owned to quickly rising hot water from great depths instead of a shallow heat source being responsible for warming up the water. An initial reservoir temperature of $> 100\,°C$ is indicated by $\delta^{18}O$.

The presented helium isotope data support the assumption of deep water being in contact with mantle fluids rising through permeable fault segments. However, this mantle imprint is very local and not related to the heat flow, because Zara spring, located where the highest heat flow was recorded, has a much more crustal signature than the Zarqa Ma'in springs. The deep reservoir discharging at the Zara springs is hence less affected by mantle volatiles.

Other localities along the eastern side of the Dead Sea and in Wadi Arava

The same explanation as for the Zara spring can be assumed to apply to the springs in the other side-wadis at the Dead Sea, i.e. the springs in Wadi Ibn Hammat, Afra, and Thra'a. They feed on deep reservoirs heated under a possibly elevated geothermal gradient (no heat flow data in this area is available), but these reservoirs are only very weakly affected by mantle fluids. The same holds for the wells in Wadi Arava, where Eckstein and Simmonsi [1977] report a temperature gradient of about 16 K/km and a heat flow of $45\,mW/m^2$ at shallow depths of the Ein Yahav well nest. There, the discharged water temperature corresponds to the wells' screen interval depth and almost no mantle impact is present. The only magmatic occurrence in Wadi Arava is found close to Ein Yahav and yielded ages around 6 Ma [Horowitz, 2001], which is obviously too old to significantly influence the groundwater in Ein Yahav wells today. The observation that the thermal groundwater south of the Dead Sea

is only weakly impacted by mantle volatiles is supported by Eraifej [2006], who reported helium isotope ratios of 0.11 R_A in two wells located at the southern end of the Dead Sea. It should, however, be noted that the sampled wells at the margins of Wadi Arava have a higher helium ratio than those localities in the southern side-wadis. The general low interaction with mantle gases corresponds to the inferior seismic and tectonic activity in Wadi Arava [Ambraseys, 2006].

7.3 Conclusions

An extensive data set of helium isotopes in thermal waters along the Dead Sea Transform, covering both the Jordanian and the Israeli part of the valley, is presented, accompanied by other hydrological tracers. A wide range of ^{3}He/^{4}He ratios from crustal signature to high mantle influence is found in hot springs and wells along the margins of the Jordan Valley. Helium isotope ratios prove to be the only reliable tracer of interaction of thermal groundwaters with a mantle reservoir, as no other tracer shows a credible relation to the mantle helium content. Only in a few cases the stable isotopes of carbon and oxygen reveal deeper insight in the mantle gas origin or the heat history of the thermal water.

The samples collected along the Jordanian part of the DST yield a significantly higher spatial resolution than the Torfstein *et al.* [2013] data set, where mantle helium information is gathered in three locations only, namely the Lake Kinneret/Yarmouk area, the western Dead Sea and the central Wadi Arava, with no data available in between. In contrast, thermal waters in Jordan are distributed more widely and therefore give a more detailed and finer resolved picture of mantle gas impact along the valley.

The general north–south trend of mantle gas influence reported by Torfstein *et al.* [2013] is not reproduced in the clarity claimed by those authors when the thermal waters along the Jordanian part of the rift escarpment are considered, too. In figure 7.21 the north–south distribution of the ^{3}He/^{4}He ratio, ^{4}He and ^{3}He is illustrated versus the distance from the Gulf of Aqaba (GOA). It is the same configuration Torfstein *et al.* [2013] used in their figure 8. As already mentioned by the same authors, the ^{3}He/^{4}He distribution pattern is not reflected if only ^{3}He or ^{4}He is considered, rendering the ^{3}He/^{4}He ratio a unique marker for mantle influence.

The illustration shows that, indeed, the samples coined most strongly by a crustal environment are collected south of the Dead Sea and most of the locations in the north exhibit a typical mantle signature, but two exceptions exist: 1) the Zeeghan wells, located midway between Lake Kinneret and the Dead Sea, and especially Zeeghan 4, exhibit the highest mantle component of all tested waters (4.9 R_A), exceeding the highest ratio found by Torfstein *et al.* by a factor of 2.5; and 2) the Manshiyeh wells which show a minor mantle gas imprint only (around 0.4 R_A), yet, they are closely neighbored by two approximately equally deep wells that exhibit a rather strong mantle helium configuration.

The presented observations, therefore, do not permit the straightforward explanation of the mantle influence distribution given by Torfstein *et al.* [2013], where the gradual thinning of the crust from south to north is responsible for a more developed fracture system there
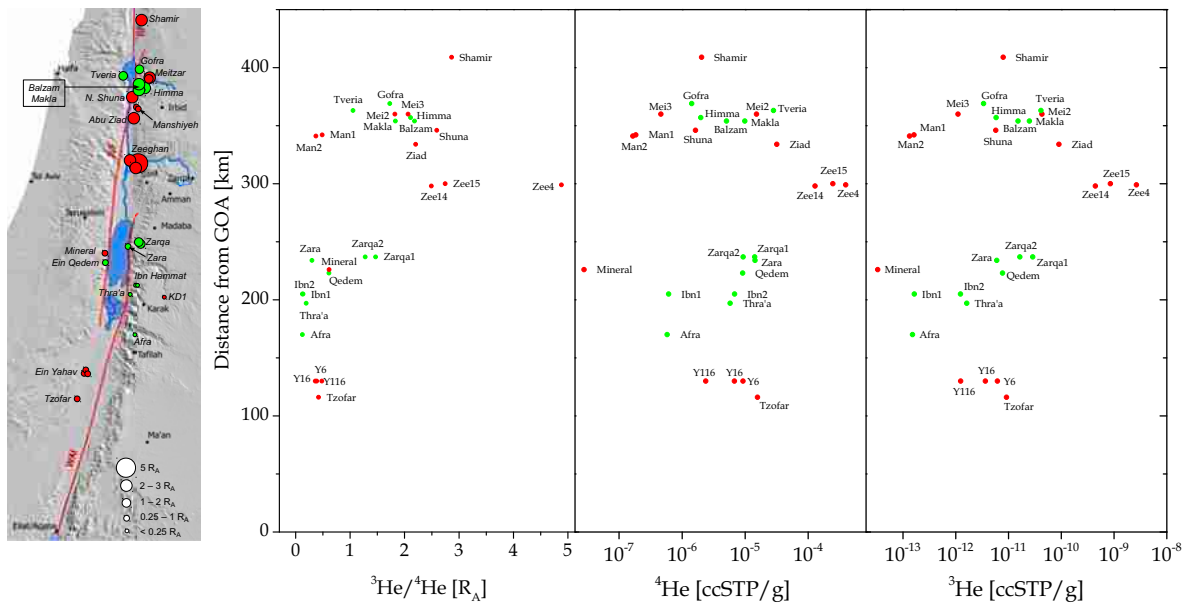
Figure 7.21: Spacial pattern of the ^{3}He/^{4}He ratio as well as ^{4}He and ^{3}He concentrations as functions of the distance from the Gulf of Aqaba (GOA). The clear north–south trend inferred by Torfstein *et al.* [2013] is not reproduced when samples of the Jordanian part of the DST are considered, too. The distribution pattern found for the ^{3}He/^{4}He ratio is not reproduced by ^{3}He or ^{4}He alone.

and, hence, the elevated mantle influence around Lake Kinneret and the Yarmouk Gorge. To the contrary, a much more localized view needs to be inferred, including single fractures which affect the groundwater often in close vicinity only. This becomes especially apparent along the rift flanks south of where the Yarmouk Gorge meets the Jordan Valley. The case of the Manshiyeh wells, having only a slight mantle influence, but being enclosed by two significantly mantle coined wells, indicate the localities north and south of Manshiyeh are supplied by (at least) two different mantle helium containing reservoirs which are separated by groundwater masses less affected.

Instead of a north–south tendency of mantle gas influence the present data set rather suggests a difference between the eastern and the western margin of the Dead Sea Transform. This might be an indicator that recent shearing took place predominantly along the eastern bounding fault system, creating more or better conductive fractures. However, helium isotope data density is only low on the western rift side, and more samples should be collected to confirm or disprove this hypothesis.

Furthermore, the existence of a sub-continental, wide-spread, intermediate mixing reservoir, where mantle and crustal endmembers mix to a local endmember of $\approx 2\,R_A$, probably at the base of the crust, and which is then further diluted by shallow groundwater on its way to the surface [Torfstein *et al.*, 2013], is not supported by the new data. If this would be the case, a correlation between water temperature and mantle component should be visible, because, in general, it can be assumed that slowly ascending groundwater, which has further

cooled down when reaching the discharge location, is also stronger admixed by shallow, crust-impacted water. Moreover, this deep uniform reservoir, from which all thermal water sources are supplied, would need to have a helium isotope ratio of at least $4.9\,R_A$ to be capable to explain the helium data of Zeeghan 4.

Present-day knowledge of heat flow pattern beneath Jordan and Israel, as displayed in the heat maps on pages 178 and 179, meets very well with the presented observation of mantle helium amount in case of the Yarmouk/Kinneret and the Zarqa Ma'in areas, but due to the lack of high resolution temperature–depth data in Jordan, the observed heat anomaly at the Zeeghan well field is not yet captured. Borehole logging should be undertaken in this area to complete the knowledge about geothermal heat distribution in this location. A first, very rough estimation of the local geothermal gradient of $100\,K/km$ in the Zeeghan well field area is found from discharge temperature in this thesis, which is comparable to the gradient found in the Zarqa Ma'in locality [Galanis Jr. *et al.*, 1986]. Together with the remarkably high $^3He/^4He$ ratios found in the Zeeghan wells this area is probably the most promising locality for geothermal energy usage, maybe even including electric power generation.

8 Summary

Two case studies are presented in this work where noble gases and especially the helium isotope ratio in Jordanian groundwaters are applied in very diverse contexts and for totally different purposes.

In the Azraq study dissolved noble gases are used to uncover a complex groundwater mixing scheme, which has not been understood before and which causes creeping salinization of groundwater reserves in the Azraq Oasis. The new approach includes the determination of noble gas contents in three well types found in Azraq: The AWSA well field wells, mostly around 200 m deep, abstract water from the uppermost of three aquifer systems, which lie on top of each other and are separated by poorly permeable layers, shallow agricultural wells, and two deep wells tapping the middle aquifer. It is found that those wells which are affected by a rising salt content feature the presence of mantle helium, expressed as elevated ^{3}He/^{4}He ratios, which indicate an upstream of deep groundwater. However, the middle aquifer is virtually free of mantle helium, so the ascent needs to occur from even deeper aquifers through deep and permeable fractures. To my knowledge, such a hydrological setting has not been reported before and is interpreted as groundwater in the middle aquifer flowing towards the deep reaching, conductive fault, whereas it is directed opposed towards the sampled wells in the shallow aquifer.

The observation that those wells of the well field containing a considerable amount of mantle helium are the same affected by rising salinity is interpreted in terms of an increasing share of groundwater from deeper parts of the shallow aquifer contributing to the discharged water. It is made plausible that water at the bottom part of this aquifer seems to be both saline and to contain some mantle imprint, although several assumptions are made to infer this. Due to the continuous drawdown the water table in some wells left the highly conductive regime of the basalt rock lying on top and therefore the deeper aquifer layers are considerably more involved, resulting in both increased salinity and mantle helium content.

The second study investigates geothermal systems along the central Dead Sea Transform system, the continental break-up zone of the African and the Arabian plates, where the ^{3}He/^{4}He ratio proved to be a valuable tracer for tectonic activity. For the first time a comprehensive data set, covering both the Jordanian and the Israeli part of the transform valley, is presented. ^{3}He/^{4}He ratios observed lie in the range from clear crustal signature to almost $5\,R_A$, R_A being the atmospheric ratio. The new data contradict the interpretation of Torfstein *et al.* [2013] who examined thermal localities on the Israeli side only for mantle helium. While they inferred a general north–south trend in the distribution of mantle influence and attributed this to the gradual thinning of the crust northwards, the new data suggest that each thermal manifestation needs to be looked at on a very local scale. Instead of a universal intermediate reservoir with about $2\,R_A$, which is diluted in different degrees to generate the

observed ^{3}He/^{4}He ratio, as proposed by Torfstein *et al.* [2013], the thermal springs discharge water which circulated deep in the crust under a local geothermal gradient. Whether this water is affected by mantle gases, however, depends on the presence or absence of deep, conductive fractures in the close vicinity. Therefore, the simple model of Torfstein *et al.* [2013] needs to be replaced by a concept regarding more the individual tectonic surroundings of the thermal localities.

A Appendix

A.1 Solubility coefficients

The temperature and salinity dependency of the solubility is described by the Bunsen coefficient β. It is given as

$$\ln\beta(T,S) = t_1 + t_2 \left(\frac{100\,\text{K}}{T} \right) + t_3 \ln \left(\frac{T}{100\,\text{K}} \right) + S \left[s_1 + s_2 \left(\frac{T}{100\,\text{K}} \right) + s_3 \left(\frac{T}{100\,\text{K}} \right)^2 \right] \quad \text{(A.1)}$$

with T being the water temperature in K and S its salinity in ‰. Weiss [1971] gives constants for helium and neon, Weiss [1970] for argon, Weiss and Kyser [1978] for krypton (table A.1).

Table A.1: The Bunsen solubility coefficients for all noble gases from fitting equation A.1 to experimental data. Reference are given in the text.

	t_1	t_2	t_3	s_1	s_2	s_3
He	-34.6262	43.0285	14.1391	-0.04234	0.022624	-0.003312
Ne	-39.1971	51.8013	15.7699	-0.124695	0.078374	-0.0127972
Ar	-55.6578	82.0262	22.5929	-0.036267	0.016241	-0.0020114
Kr	-57.2596	87.4242	22.9332	-0.008723	-0.002793	0.0012398
Xe	-74.7398	105.21	27.4664			
Rn	-90.5481	130.026	35.0047			

For Xe and Rn the temperature dependent Bunsen solubility coefficient is given by the same temperature dependency term as for the other noble gases [Clever, 1979b; Kipfer *et al.*, 2002]. The coefficients are listed in the table A.1. In order to introduce the influence of dissolved salt, however, the Setschenow equation [Smith and Kennedy, 1983] is applied:

$$\ln \left(\frac{\beta(T,0)}{\beta(T,S)} \right) = M \cdot K_M(T). \quad \text{(A.2)}$$

M is the NaCl molarity and K_M the empirical salting coefficient, which can be approximated by

$$K_M(T) = B_1 + B_2 \left(\frac{100\,\text{K}}{T} \right) + B_3 \ln \left(\frac{T}{100\,\text{K}} \right) \quad \text{(A.3)}$$

with the coefficients $B_1 = -14.1338$, $B_2 = 21.8772$, and $B_3 = 6.5527$ for Xe. The only available data on radon solubility in dependence of the salinity is found in Clever [1979b] (who in turn
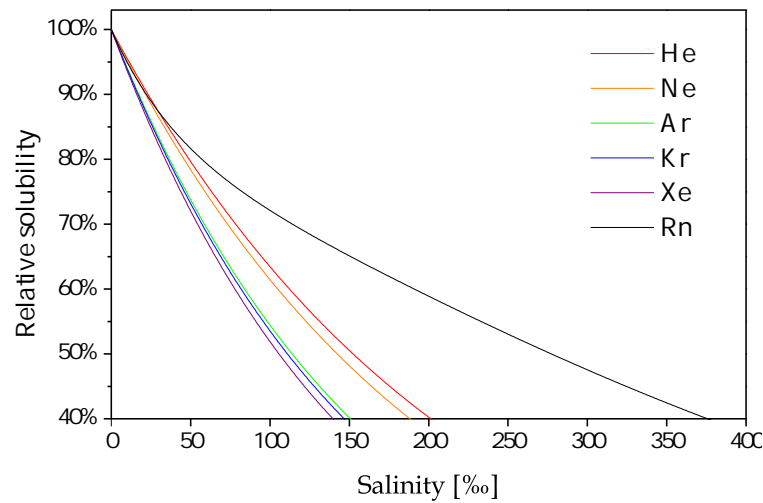
Figure A.1: The radon solubility in dependence of salt content is shown. Since the calculated solubility is derived from data between 12 and 362 g/kg salt concentration [Kofler, 1913], the fit is questionable at low concentrations. The other noble gases are shown as well in the same salinity range, but their fits are optimized for low salt concentration in the range of seawater.

cites Kofler [1913]) for a fixed temperature of 18 °C. The Rn curve in the right plot of figures 2.16 and A.1 is created by performing an exponential fit $K_M(S) = C_1 + C_2 \cdot \exp(-S/C_3)$ to the data for $K_M(18)$ given in Clever [1979b]. The resulting coefficients are $C_1 = 0.14116, C_2 = 0.18364$, and $C_3 = 76.7217$.

Since the radon solubility dependence on salinity is derived from data between 12 and 362 g/kg salt concentration – contrary to the other noble gases which are optimized for salt contents in the range of seawater – the fit is questionable at a low salinity. Figure A.1 gives the relative solubilities of Rn in a much wides range. The plots for the other noble gases are included as well, but are in turn questionable at higher salt concentrations.

A.2 Experiences applying diffusion samplers in the field

Since diffusion samplers of the kind developed in our group [Wieser, 2006] had never been applied in a field campaign, I summarize the experiences gained during my field trip in 2012 in Jordan.

- The first apprehension that this design does not withstand the high hydrostatic pressure in deep wells lead to a construction where the PVC tube was not spanned between two copper tubes, but tightly covered a perforated part of one longer copper tube (compare figure 5.1 on page 69). This promised a more stable built as the squeezed PVC tube cannot be incised by the rims of the copper tubes. However, the normal diffusion sampler design proved to be very sturdy under high pressure and even the

deepest sampler at 569 m was retrieved obviously undamaged. The newly constructed samples with the perforated copper tube, in contrast, leaked much more often, which leads to the recommendation to use the normal diffusion sampler design but to locate several samplers, at least two, at the same depth to raise the chance of getting at least one undamaged sample.

- A considerable amount of (normal) diffusion samplers broke during transport. As they are fast and easy to assemble they should be put together in the field just right before usage.

- We first tried to use a fishing line to lower the diffusion samplers into the boreholes, as it is light and easy to transport. However, the fishing line we used formed knots very easily, in the first attempt a big clutter swam upon the groundwater surface and the samplers not even submerged into the water. A stronger, more heavy string in combination with an additional weight at the bottom proved to be much more reliable. However, even with this string knots occurred, presumably because the samplers were lowered too fast. Thus, it should be taken care of a permanent tension in the string that the string with the samplers can not get caught somewhere on its way down.

- To prevent the diffusion samplers from moving much and being stuck in the borehole, both ends were fixed to the string. As the closed outer ends of the copper tubes are quite sharp they were wrapped with duct tape that they cannot cut the string.

- Afterwards, I think the approach of putting all diffusion samplers on one single string is the right strategy when sampling a depth profile. The use of separate strings for each sampler would in all likelihood lead to knotting together of the strings. Especially when retrieving the samples as a pair, the retrieving speed is not significantly lower when one person closes the copper tubes while the other continues pulling up the samples.

- The usage of the simple diffusion sampler design applied during this thesis in cold water gives rise to the assumption that the closing with the pneumatic pliers is unreliable under these circumstances. During a test of the samplers in the water of a frozen lake nearly all samplers appeared to leak. Maybe the copper is not as smooth at wintry temperatures as it usually is and the galling does not work.

A.3 Description of the sampled wells and springs

In this chapter a detailed description of the sampled springs and wells is given.

Azraq project

AWSA well field

All wells of the AWSA well field are productive wells which operate day and night. The water is pumped to Amman for drinking water purposes. Some wells where visited more

than once in the different campaigns. In every case it was possible to connect the sampling hoses via a hose coupling. For the connection itself the pump was stopped for some minutes by an employee of the WAJ. The pressure was high at all wells. All wells have a casing and the screen covers the whole length.

Figure A.2: Well AWSA 3 as a typical example for wells in the AWSA well field.

Farming wells

Private wells of farmers in the Azraq Oasis are simpler constructions compared to the governmental production wells. Beside drilled wells also dug wells exist with depths of around ten meters. The bottom of these holes with diameters of several meters is filled with groundwater, which is supplied to the fields by a pump. Contact with the atmosphere is evident in these cases.

F3975

The accompanying employee of the WAJ had to manipulate the well's flow meter since the owner did not want to pay for the "wasted" water during sampling. No flushing of the borehole before sampling was possible since the owner offered only five minutes of sampling time. Pressure was usable, equipment connected at a tap.

F3731

A dug well, about eight meters deep. The pump was started for the sampling procedure. I connected the equipment with a rubber plug to the installed plastic tubing system. Just before I took the second noble gas sample the well ran dry and I waited for about 20 minutes for the water to return to the well hole, killing the time with a tea offered by the farmer. Sampling pressure was poor, but usable.

Figure A.3: Well head with flow meter and sampled tap of F3975

F3960

The pump of this drilled well was not working anymore, though it still hung in the borehole. It was damaged by the saline water, they told me. The depth of the well is 35 m, the water table at 16 m below surface. Diffusion samplers were placed at 27 m below surface on 8 April 2012 at 5pm and collect the following day at 6pm. I dared to only collect water with the deep sampler once, because it almost stuck at the pump.

F3741

A drilled well. The pump was started for the time of sampling, but no long flushing was possible. Connection with a rubber plug, the pressure was usable.

Mohammeds well

This well was drilled just recently and no pump was installed yet. The well was quite disturbed since the owner let down a rock on a rope down the borehole beforehand. Water level was about 20 m. Samples were collected from a depth of 53 m below surface and diffusion samplers installed at the same depth on 7 April 2012, 4:15pm. Retrieval on 9 April 2012, 7pm.

B2/A7 wells

Since the B2/A7 aquifer in the Azraq area consists of saline water, no production wells exist. The only two wells which enabled me to sample water from this aquifer were abandoned monitoring wells. The NDW 5 (733 m deep) and NDW7 (970 m deep, according to WAJ data base) were drilled in 1992 as geological exploration wells, are constructed in the same way

Figure A.4: The 8 m deep dug well F3731.

and haven't been used since then. Thus, noble gas samples were collected at different depth with diffusion samplers, while anion, cation, tritium, carbon and stable isotope samples were obtained using a deep sampler provided by the WAJ (description in chapter 5.2). Detailed information about the construction was not available. A farmer who participated in the drilling of NDW 7 remembered that this wells had a full length casing and the screen starts at 400 m below surface (he remembered the depth of 973 m correctly so I assume the other facts are right as well). The piezometric head was at 101 m below surface in NDW 5 and at 26 m below surface in NDW 7.

Because the lack of experience of the physical stability of the classical diffusion samplers [Wieser, 2006] another type, which was thought of being more robust against high pressure (see chapter 5.2 for details), was applied at depth below about 300 m in addition to the classical ones.

Diffusion samplers were positioned in NDW 5 in depths of 310, 444 and 684 m on 9 March 2012 at around 2pm using a fishing line and retrieved on 30 March 2012 at 11:30am. Unfortunately only one (classical) DS from 684 m was undamaged, all others leaked. Possibly the 684 m was not at that depth because for the last about 200 m the thread tension was lower than before and the sampler might have lain at the bottom (this would imply a wrong depth information or a partial collapse of the borehole). Water samples were collected from 250 m below surface. Chemical treatment took place at 10:30am the following day.

Noble gas samples from NDW 7 were planned to be collected in depths of 50, 100, 150, 200, 250, 300, 450, 600, and 800 m. A strong PVC thread with a weight at the bottom end was used and all diffusion samplers were lined up according to their depth. Due to the formation of knots between the 250 and 300 m samples (a loss of about 6 m), between 300 and 450 m (a loss of about 50 m) and another one between the two deepest samples (a loss of about 175 m) the depths correct to 50, 100, 150, 200, 250, 294, 394, 544 and 569 m. These depths hold provided

Figure A.5: Mohammeds well. There was no pump installed yet. Well F3960 was of the same type as this one.

the rope was straight except the knotty sections. Diffusion samplers were positioned in the borehole on 13 March 2012 at 1:30pm and retrieved on 30 March 2012. All DS except the classical DS at 394 m were undamaged, and the 569 m sampler was inflated from the high gas pressure in that depth. Anyway some samplers displayed some fogging inside the PVC tube. Water samples were collected at depth of 50, 100, 150, 200 and 250 m, the maximum depth achievable with the deep sampler. Due to problems with the deep sampler at 250 m only one volume of 500 ml was pulled up and distributed to the small bottles, the ion samples being filtered. The remaining 250 ml was treated with only 0.5 ml $AgNO_3$ solution to produce the same concentration as the other ^{14}C samples. Like the NDW 5 samples, chemical treatment was conducted the following morning.

Wells in Northern Azraq

Three wells in the Northern Part of the Azraq basin were sampled, two governmental (KM 140 and Mukefteh 2) and one private farming well (Jordan Modern Farm). Sampling pressure was good and the connection of the tubing was easy. Thickness of the unsaturated zone is more than 100 m in this part of the country (275 m at the KM 140 well).

(a) My College Florian Freundt sampling NDW7 using a deep sampler.

(b) Lowering the deepest diffusion sampler, an additional weight is attached.

(c) The 569 m diffusion sampler was inflated after being retrieved to the surface.

Figure A.6: Sampling NDW7

Thermal waters project

Thermal waters were sampled from thermal springs and wells. They distribute along the Jordan Valley and its side wadis from the Syrian border in the North and Wadi al-Karak South of the Dead Sea.

Thermal springs

Zara Ma'in spring

This spring complex is situated at the Dead Sea. Several springs discharge within about one kilometer. The sampled spring forms a small cave with a little pool in it. A hose was moved as deep as possible into the cave and weighted down with a small rock to collect water for noble gas analysis from as far away from atmospheric influences as possible. A small downhill gradient was exploited to let the water flow into the copper tubes. Bottled samples were filled from the pool.

Figure A.7: The cave pool of Zara Ma'in spring close to the Dead Sea shore.

Zarqa Ma'in springs

The Zarqa Ma'in spring complex is situated in a deeply cut side wadi of the Dead Sea close to the Zara Ma'in springs and nowadays feeds a famous public spa center. Water samples were collected at two discharge spots. The first, labeled Zarqa Ma'in I, forms a small pool of very hot water (61 °C) and gloves had to be filled with cool water to prevent skin burning to fill the sample bottles, especially the radon sample, underwater. Heavy degassing was obvious as gas bubbles ascended; it smelled of H_2S. Because no downward gradient could be utilized, NG samples needed to be collected with the suction technique introduced in chapter 5.1. For this my partner stood about 1.5 m above the spring pool. Oxygen content could not be recorded since the CellOx 325 sensor refuses to work at temperatures above 50 °C.

The second sampled discharge point, labeled Zarka Ma'in II, is located about 100 m from the first one and some meters higher. The discharge rate is very low. The inlet tubing was located in the tiny pond using the weight of small rocks and a small gradient made the water flow through the copper tubes. Water samples were taken from the exit of the tubing system. No degassing could be observed here. Again no oxygen could be measured due to the water temperature above 50 °C.

(a) Heavy degassing of the Zarka Ma'in I hot spring.

(b) Hauling of the hose in Zarka Ma'in II.

(c) A hot waterfalls feeds the spa center of Zarka Ma'in.

Hemme spring

Hemme spring, located in the lower Yarmouk Valley, was used as a public swimming pool years ago. It discharges into an 18 m deep pool with a rate of around $1000\,\mathrm{m^3/h}$. Influx into the pool takes place from the Western side. In order to take NG samples from as deep as possible from the influx location the end of the sampling hose was weighted with a rock which allowed to draw samples from a depth of about 3 to 4 m. The several NG samples were taken from different spots. The suction technique was applied. Samples in bottle were

taken from about 40 cm below the water surface. A couple of ascending gas bubbles indicate degassing accompanied by a H$_2$S smell.

Figure A.8: Hemme spring

Afra spring

Afra spring in Wadi Hasa south of the Dead Sea is used as a spa retreat as well. The spring itself is cased, and samples were drawn from the discharging pipe. The sampling hose was telescoped about 60 cm into it. No H$_2$S smell was recognized.

Figure A.9: The sampling tube was telescoped into the discharge pipe at Afra spring.

Springs in Wadi Ibn Hammat

In Wadi Ibn Hammat there are two thermal springs. Water from the first one, named Ibn Hammat I, is used in a spa facility. The spring itself is cased and, like at Afra spring, access was only possible through a pipe. This pipe was inside a manhole. The sampling hose was telescoped 60 cm into the pipe and blocked with a rock. This setup dammed up the water

and minimal contact to the atmosphere guaranteed. NG samples were taken by the suction technique.

The second spring, Ibn Hammat 2, is located about two kilometers upstream of the first one. It discharges into a pond and is used for relaxation by people who do not like to or cannot afford the entrance fee of the spa downstream. The hose was telescoped as far as possible into the discharging opening, but a little exchange with the atmosphere can not be excluded. NG samples were taken by suction, bottles were filled from the pool water close to the discharge hole. Emerging gas bubbles indicate some degassing, but no H_2S could be smelled. The sampling took about two hours because it was Friday (puplic holiday in the Arab world). A lot of families enjoyed their leisure time and invited me for lunch and drinks several times.

(a) The manhole of Ibn Hammat I

(b) Discharge pipe of Ibn Hammat I

(c) Pool of Ibn Hammat II. The spring is under the rock in the upper right corner.

(d) Jordanian hospitality

Thra'a

Thra'a spring is situated in Wadi al-Thra'a, a side wadi of Wadi al-Karak. The discharge is located at the sandy floor of a 1 m deep artificial pool. I collected NG samples with suction while I hold the hose end at the ground with my foot. Bottles were filled at the pool's bottom as well.

Thermal wells

North Shuna Hot Well

North Shuna Hot Well at the mouth of Wadi al-Arab is an artesian well and is utilized in a spa facility. It was easy to connect the sampling equipment to this 967 m deep well. H_2S was present. The cation sample changed color to yellow upon acidification with nitric acid, while the carbon sample changed color to brown instead of the usual purple upon addition of silver nitrate solution. Oxygen content could not be recorded due to water temperature of 53.3 °C. Sampling pressure was high.

Figure A.10: Sampling the thermal well in North Shuna.

Abu Zeeghan well field

Highly saline thermal water from the Abu Zeeghan well field is being desalinized and treated and contributes to the water supply of Irbid. The brine is dumped into the Jordan River. Three wells were sampled.

All sampled wells showed a heavy degassing, No 14 the least (but still more than any other sampled spring or well in Jordan), No 4 degassed extremely. However, there was no smell of H_2S. All waters tasted of iron which was also visible at leaks. At well No 15 there were no bubbles visible inside the sampling hose after closing the NG copper tubes, however,

Figure A.11: Precipitated iron oxide on the ground at well Abu Zeeghan No 4

after removal of the hoses foamily water dripped out. Chemical treatment of the carbon and cation sample was done after all the samples had been collected.

Alkalinity was far beyond the working range of the alkalinity test kit at all Abu Zeeghan well. Even at quadruplicated concentration, which is not supported by this test kit officially, the exact alkalinity could not be determined for wells No 4 and 15. No further dilution was done, but as it was obvious that the threshold was almost reached and a value of 23 meq/L is assumed for these wells. The good result in the ion balance justify this assumption. The well No 14 alkalinity value was within range of the quadruplicated test, thus providing a possibly arguable value.

During the Radon measurement the Abu Zeeghan samples exhibited a foamy behavior. The bubbles at the surface even ascended into the tubing system and a little bit into the Dririte cartridge of the first radon analysis (Zeeghan No 4). The bottle was detached from the closed system and a small gulp was discarded, thus additional contact to the ambient air was established and also part of the radon which was already degassed into the tubing system got lost. In the case of the other two samples I poured out a gulp of about 5 to 10 mL before I connected them to the closed system.

Figure A.12: Heavy degassing occurred during sampling and foam formation at the radon measurement of the Zeeghan wells

Mashiyeh 1 and 2

Both Manshiyeh wells used to be pumped wells, but the pumps do not work anymore. Anyway, together they yield about $50\,\text{m}^3/\text{h}$ as they are artesian wells. The water was iron bearing and was said to contain H_2S but this was not smellable. In both cases the sampling tube could be telescoped a few centimeter into small openings. At Manshiyeh 1 no bubbles were visible, at Manshiyeh 2 some were in the sampling bucket but not in the sampling hoses while the copper tube were being closed.

(a) Sampling hose connection at Manshiyeh 1
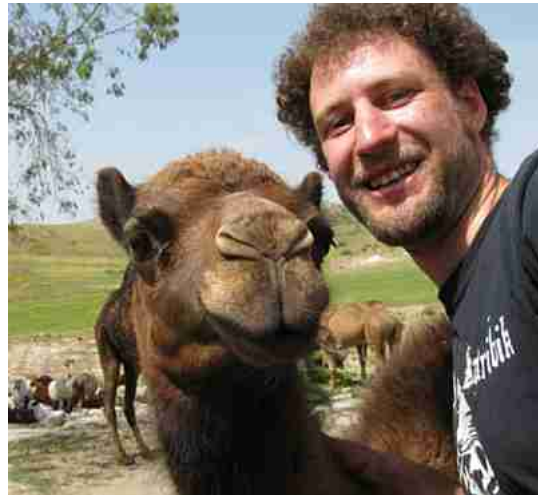
(b) Making new friends

Abu Ziad

This thermal well in the Wadi Abu Ziad is an artesian well, too and used for irrigation purposes. The sampling hose was telescoped about $4\,\text{m}$ deep into the borehole, thus contamination with atmospheric gases can be ruled out. H_2S was present, but no strong degassing was noticeable. The hoses revealed no air bubbles, only inside the carbon bottle a few very small ones were visible.

(c) Abu Ziad Thermal Well

(d) I can't complain about a lack of courtesy during sampling

175

Lajjun KD1

This well was sampled in the scope of the attempted groundwater recharge study in the Karak area in 2010 and is now included into the thermal waters study due to its characteristics. Sampling was problem-free. Pressure was low, but no bubble formation was observable.

A.4 Additional figures
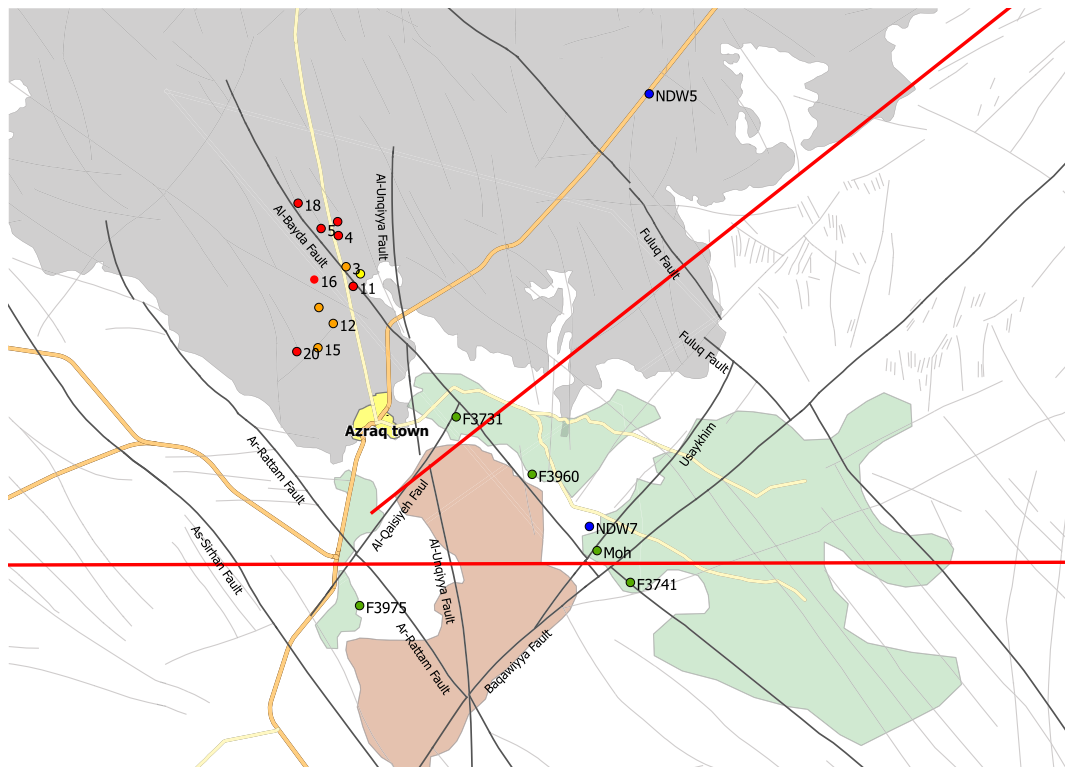
Figure A.13: The location of the cross-sections published by Margane *et al.* [2002] (W–E direction) and Dottridge and Abu Jaber [1999] (NE direction, starting from the Azraq Oasis).
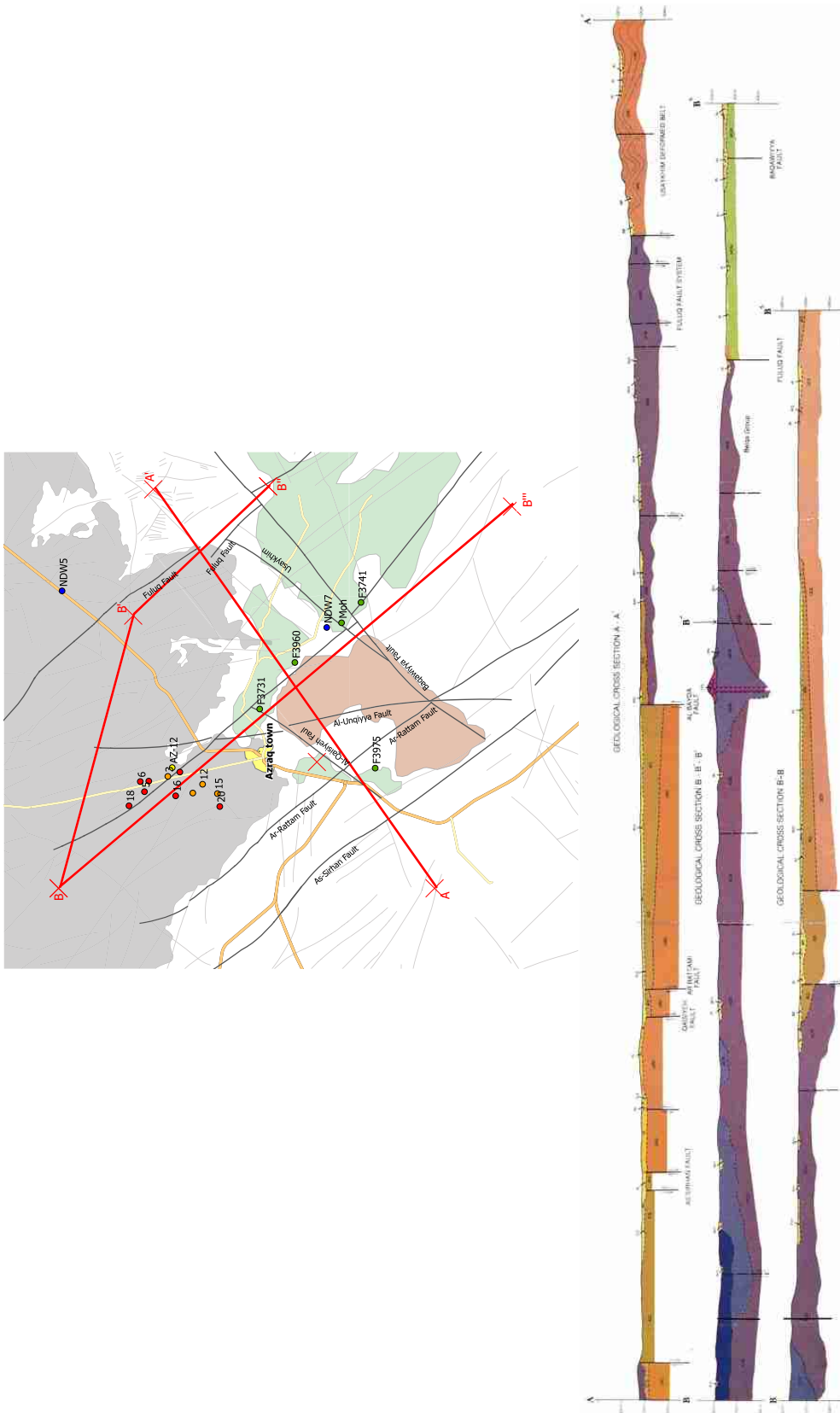
Figure A.14: Three cross-section of the central shallow aquifer in Azraq. The upper one goes from A–A′, the middle cross-section B–B′–B″ and the last is B–B‴. The positions and the way of tectonic movement at the faults is indicated. Purple color indicates basalt, brown the B4/5 and the Sirhan formation, green the east of the Fuluq Fault ourcropping B3. From Ibrahim [1993].
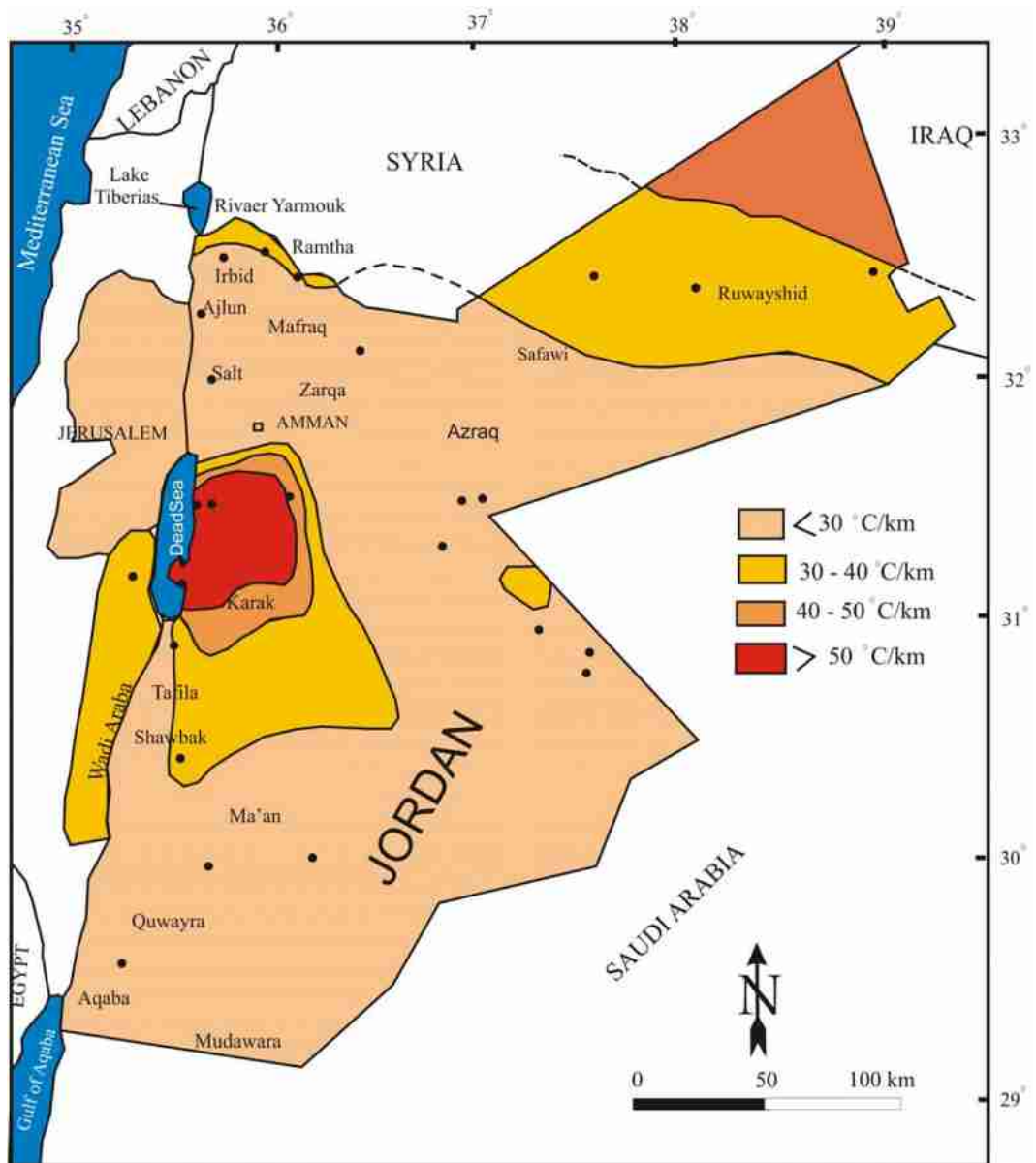
Figure A.15: Heat map of Jordan, after Gharaibeh [2008], based on data from Galanis Jr. *et al.* [1986].
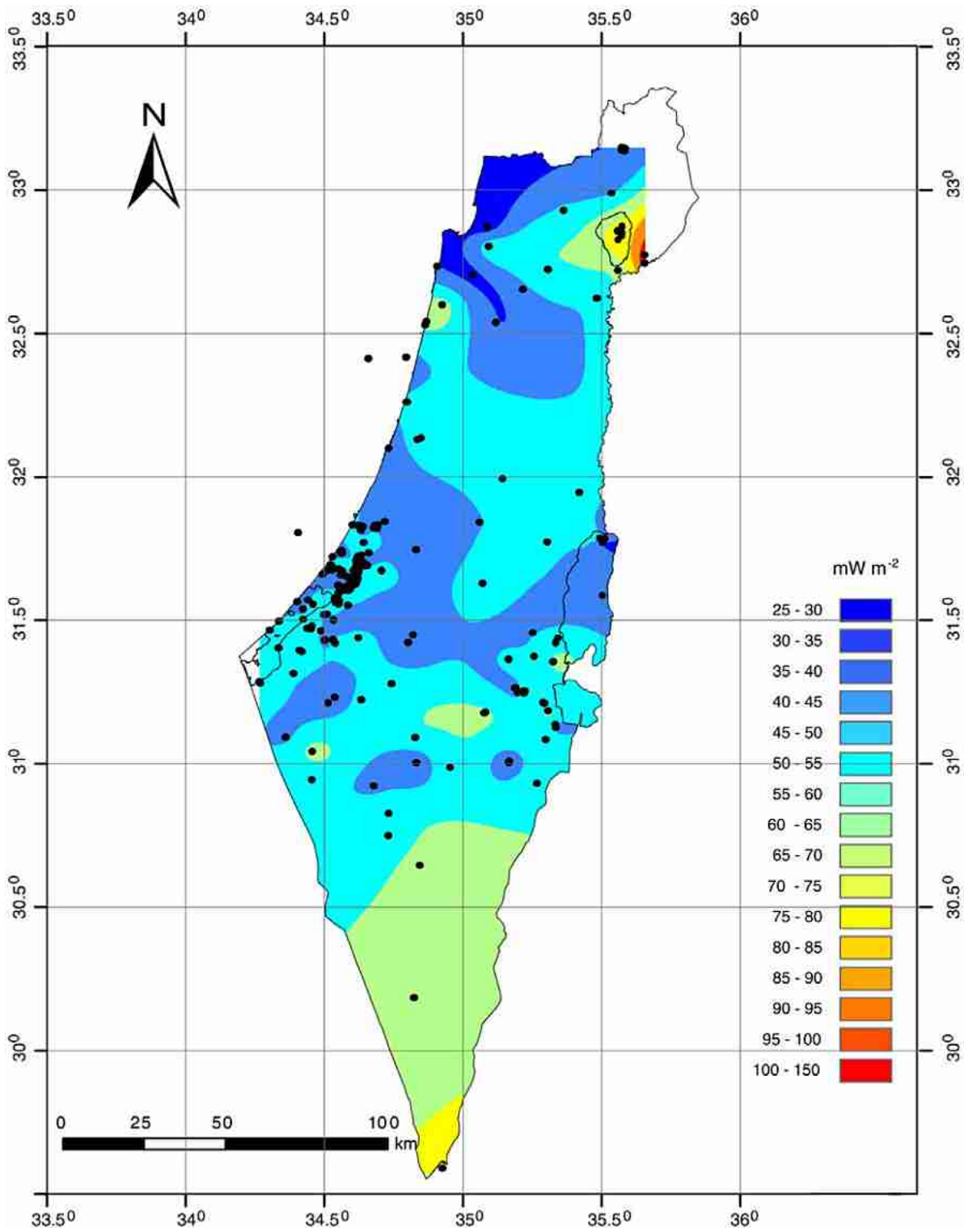
Figure A.16: Heat map of Israel, from Shalev *et al.* [2013].

A.5 Additional tables

Table A.2: The lithologic data for all sampled well in the Azraq basin where this information could be obtained. All numbers indicate the bottom of the respective layer. All heights are given in meters above sea level. Data from WAJ [2010].

	Altitude	Aluvium	Basalt	B4/5	B3	B2/A7	A1/6	Kurnub
AWSA 3	521	520	457	311				
AWSA 4	536	535	462	330				
AWSA 5	541	541	444	337				
AWSA 6	549	546	464	343				
AWSA 11	517	514	463	455				
AWSA 12	528	526	474	319				
AWSA 13	532	530	473	322				
AWSA 15	524	522	472	314				
AWSA 18	553	548	488	382				
NDW5	598	598	523	not present	445	308	-6	-135
NDW7	515	513	401	200	-195	-455		

Table A.3: Helium components of Azraq wells sampled in 2012. All concentrations in ccSTP/g.

	^{3}He$_{meas}$	Δ^3He$_{meas}$	^{4}He$_{meas}$	Δ^4He$_{meas}$	^{3}He$_{mod}$	Δ^3He$_{mod}$	^{4}He$_{mod}$	Δ^4He$_{mod}$	R_S	ΔR_S
AWSA 3	2.895E-13	1.072E-14	2.437E-07	2.321E-09	5.884E-14	3.106E-16	4.315E-08	2.233E-10	1.188E-06	4.541E-08
AWSA 4	1.028E-13	3.562E-15	1.152E-07	1.019E-09	5.848E-14	3.105E-16	4.288E-08	2.231E-10	8.921E-07	3.190E-08
AWSA 5	7.499E-14	2.789E-15	1.018E-07	8.915E-10	5.846E-14	3.090E-16	4.287E-08	2.221E-10	7.370E-07	2.816E-08
AWSA 6	7.605E-14	2.662E-15	9.370E-08	8.175E-10	5.723E-14	2.982E-16	4.199E-08	2.146E-10	8.116E-07	2.928E-08
AWSA 13	1.830E-13	6.533E-15	2.404E-07	2.281E-09	5.929E-14	3.070E-16	4.347E-08	2.207E-10	7.614E-07	2.812E-08
AWSA 15	1.610E-13	5.695E-15	1.677E-07	1.547E-09	1.376E-13	1.850E-15	9.960E-08	1.200E-09	9.605E-07	3.510E-08
AWSA 16	6.193E-14	2.270E-15	5.037E-08	4.300E-10	5.835E-14	3.197E-16	4.281E-08	2.299E-10	1.230E-06	4.628E-08
F3731	6.526E-14	2.418E-15	5.016E-08	4.274E-10	6.903E-14	5.333E-16	5.058E-08	3.605E-10	1.301E-06	4.947E-08
F3975	7.323E-14	2.643E-15	1.135E-07	1.012E-09	5.828E-14	3.104E-16	4.276E-08	2.231E-10	6.452E-07	2.399E-08
F3741	1.272E-13	4.551E-15	3.215E-07	3.133E-09	6.055E-14	3.279E-16	4.441E-08	2.345E-10	3.957E-07	1.467E-08
F3960	8.676E-14	3.584E-15	7.215E-08	8.869E-10	5.903E-14	5.739E-16	4.334E-08	4.147E-10	1.202E-06	5.182E-08
Mohammed	1.080E-13	3.859E-15	1.866E-07	2.164E-09	5.655E-14	6.388E-16	4.154E-08	4.615E-10	5.788E-07	2.174E-08
NDW5 684m	2.227E-12	8.910E-14	2.231E-06	4.146E-08	4.820E-14	9.514E-16	3.542E-08	6.881E-10	9.982E-07	4.403E-08
NDW7 50m	1.469E-13	5.740E-15	4.654E-07	9.185E-09	6.025E-14	8.958E-16	4.424E-08	6.524E-10	3.157E-07	1.382E-08
NDW7 100m	1.673E-13	6.612E-15	6.162E-07	1.325E-08	6.079E-14	1.042E-15	4.462E-08	7.536E-10	2.715E-07	1.222E-08
NDW7 150m	1.785E-13	1.399E-14	7.268E-07	1.382E-08	6.024E-14	1.077E-15	4.421E-08	7.769E-10	2.455E-07	1.981E-08
NDW7 200m	1.790E-13	1.381E-14	9.872E-07	2.095E-08	6.420E-14	1.289E-15	4.711E-08	9.289E-10	1.813E-07	1.451E-08
NDW7 250m	1.572E-13	1.414E-14	1.339E-06	2.878E-08	6.243E-14	1.292E-15	4.581E-08	9.302E-10	1.174E-07	1.086E-08
NDW7 300m	1.568E-13	1.461E-14	3.070E-06	6.921E-08	5.591E-14	8.917E-16	4.109E-08	6.437E-10	5.106E-08	4.895E-09
NDW7 544m	1.695E-13	6.893E-15	2.892E-06	5.444E-08	4.831E-14	9.823E-16	3.558E-08	7.120E-10	5.861E-08	2.626E-09
NDW7 569m	1.364E-13	5.941E-15	2.796E-06	5.188E-08	5.051E-14	9.997E-16	3.715E-08	7.233E-10	4.879E-08	2.310E-09

Table A.4: The results of the ion analysis of the 2012 Azraq samples. The total cation and anion concentration is found to the right, together with the ion balance error (IBE) after equation 2.18. b. d. means below detection limit.

	Ca meq/L	Fe µeq/L	K meq/L	Mg meq/L	Mn µeq/L	Na meq/L	Sr µeq/L	F µeq/L	Cl meq/L	Br µeq/L	NO3 µeq/L	SO4 meq/L	HCO3 meq/L	∑ Cations meq/L	∑ Anions meq/L	IBE
AWSA 3	2.03	1.53	0.25	1.70	b.d.	9.20	11.05	11.52	9.59	6.15	67.33	1.42	2.16	13.18	13.26	-0.53%
AWSA 4	0.93	0.32	0.22	0.73	b.d.	3.45	4.61	15.22	2.45	3.03	71.53	0.84	2.28	5.34	5.65	-5.53%
AWSA 5	0.90	0.39	0.13	0.72	b.d.	2.98	4.76	17.36	1.91	2.33	52.04	0.73	2.11	4.74	4.81	-1.62%
AWSA 6	0.80	0.49	0.10	0.61	b.d.	2.26	3.74	13.87	1.12	1.61	60.34	0.56	2.16	3.78	3.92	-3.57%
AWSA 13	2.05	1.22	0.46	1.79	0.15	8.54	14.61	37.55	8.41	6.43	9.08	2.00	2.16	12.86	12.62	1.94%
AWSA 15	7.24	1.54	0.57	7.57	0.93	17.75	48.85	9.87	20.68	5.22	403.99	10.06	2.05	33.17	33.21	-0.10%
AWSA 16	0.80	0.23	0.13	0.91	b.d.	3.49	5.48	7.94	2.17	2.45	192.26	1.62	1.78	5.33	5.77	-7.51%
F3731	26.20	b.d.	0.38	17.94	b.d.	46.76	129.65	5.92	71.46	34.64	51.52	15.33	7.64	91.41	94.52	-3.29%
F3975	8.81	b.d.	4.39	17.40	b.d.	171.81	162.06	53.88	164.11	72.70	70.03	34.42	5.02	202.57	203.75	-0.57%
F3741	10.78	2.39	6.39	19.26	1.50	138.54	151.11	61.30	161.36	34.14	50.16	9.72	3.46	175.12	174.69	0.25%
F3960	18.76	b.d.	1.01	18.76	6.22	29.84	204.06	19.93	65.00	21.74	68.78	1.63	1.32	68.59	68.05	0.79%
Mohammed	29.19	132.51	11.34	54.31	58.43	486.30	249.94	b.d.	527.48	143.42	349.35	48.44	2.85	581.59	579.26	0.40%
NDW5 684m	1.06	0.49	0.44	3.40	7.79	5.70	9.94	59.15	5.94	4.50	0.17	3.84	1.13	10.61	10.97	-3.24%
NDW7 50m	8.78	0.79	2.21	9.87	12.56	48.89	122.80	36.42	64.73	29.27	b.d.	7.62	0.33	69.89	72.74	-3.92%
NDW7 100m	8.04	b.d.	2.14	8.41	9.25	49.93	118.69	58.01	63.97	33.10	b.d.	7.30	0.33	68.66	71.69	-4.23%
NDW7 150m	7.47	b.d.	2.36	7.13	7.72	53.15	115.96	66.33	62.56	32.78	2.48	6.95	0.33	70.23	69.94	0.42%
NDW7 200m	6.81	0.90	2.50	6.30	8.23	57.76	109.56	48.19	66.82	31.61	b.d.	7.12	0.37	73.49	74.39	-1.20%
NDW7 250m	7.14	b.d.	2.41	6.83	6.74	56.72	111.39	51.56	66.06	35.76	b.d.	7.19	0.33	73.22	73.66	-0.60%

Table A.5: The absolute elemental noble gas concentrations of the Azraq samples used for the fitting routine. All concentrations are given in ccSTP/g.

	He	ΔHe	Ne	ΔNe	Ar	ΔAr	Kr	ΔKr	Xe	ΔXe
2009										
AWSA 3	2.433E-07	1.989E-09	1.714E-07	8.208E-10	2.604E-04	8.804E-07	5.707E-08	1.032E-09	7.548E-09	1.291E-10
AWSA 4	1.056E-07	9.208E-10	1.698E-07	7.914E-10	2.616E-04	9.018E-07	5.606E-08	9.986E-10	7.455E-09	1.296E-10
AWSA 12	2.377E-07	1.944E-09	1.725E-07	8.608E-10	2.625E-04	8.880E-07	5.701E-08	1.030E-09	7.750E-09	1.343E-10
AWSA 13	1.893E-07	1.793E-09	1.729E-07	8.090E-10	2.690E-04	9.332E-07	6.030E-08	1.019E-09	7.811E-09	1.303E-10
AWSA 18	4.523E-08	3.722E-10	1.695E-07	7.867E-10	2.744E-04	9.393E-07	5.974E-08	1.072E-09	7.884E-09	1.377E-10
AWSA 20	6.057E-08	5.064E-10	1.727E-07	8.511E-10	2.810E-04	9.982E-07	6.195E-08	1.056E-09	8.191E-09	1.423E-10
Mkeifteh 2	4.839E-08	3.990E-10	1.700E-07	7.796E-10	2.681E-04	8.891E-07	6.122E-08	1.066E-09	7.970E-09	1.364E-10
KM 140	4.484E-08	3.688E-10	1.639E-07	7.700E-10	2.400E-04	8.126E-07	5.167E-08	9.638E-10	6.907E-09	1.196E-10
F1381	4.508E-08	3.711E-10	1.718E-07	7.950E-10	2.592E-04	8.806E-07	5.653E-08	1.016E-09	7.715E-09	1.317E-10
2010										
AWSA 3	2.398E-07	2.087E-09	1.684E-07	1.008E-09	2.564E-04	8.090E-07	5.599E-08	1.456E-09	6.856E-09	2.690E-10
AWSA 4	1.082E-07	8.690E-10	1.663E-07	1.120E-09	2.450E-04	7.555E-06	5.557E-08	1.486E-09	6.946E-09	2.747E-10
AWSA 5	1.192E-07	9.606E-10	1.701E-07	9.713E-10	2.600E-04	7.880E-07	5.730E-08	1.559E-09	7.468E-09	2.966E-10
AWSA 6	8.729E-08	6.994E-10	1.627E-07	9.822E-10	2.495E-04	7.998E-07	5.476E-08	1.368E-09	7.193E-09	2.785E-10
AWSA 11	5.537E-07	4.214E-09	1.900E-06	7.261E-09	1.300E-03	3.659E-06	1.850E-07	2.633E-09	1.620E-08	4.549E-10
AWSA 12	2.065E-07	1.791E-09	1.691E-07	9.979E-10	2.593E-04	7.848E-07	5.576E-08	1.473E-09	7.739E-09	3.144E-10
AWSA 13	2.054E-07	1.755E-09	1.703E-07	1.023E-09	2.640E-04	9.321E-07	5.845E-08	1.438E-09	8.229E-09	3.321E-10
AWSA 15	1.602E-07	1.327E-09	1.708E-07	1.024E-09	2.697E-04	9.645E-07	5.986E-08	1.413E-09	7.298E-09	2.982E-10
AWSA 16	5.772E-08	4.613E-10	1.814E-07	1.013E-09	2.776E-04	9.818E-07	6.181E-08	1.539E-09	8.509E-09	3.390E-10
AWSA 18	4.506E-08	3.517E-10	1.667E-07	9.825E-10	2.612E-04	6.659E-06	6.027E-08	1.573E-09	7.865E-09	3.098E-10
2012										
AWSA 3	2.437E-07	2.321E-09	1.716E-07	5.986E-10	2.564E-04	8.384E-07	5.626E-08	5.341E-10	7.596E-09	1.397E-10
AWSA 4	1.152E-07	1.019E-09	1.705E-07	5.975E-10	2.556E-04	8.339E-07	5.569E-08	5.261E-10	7.367E-09	1.240E-10
AWSA 5	1.018E-07	8.915E-10	1.704E-07	5.962E-10	2.554E-04	8.370E-07	5.561E-08	5.860E-10	7.355E-09	1.396E-10
AWSA 6	9.370E-08	8.175E-10	1.676E-07	5.717E-10	2.549E-04	8.479E-07	5.585E-08	6.304E-10	7.647E-09	1.332E-10
AWSA 13	2.404E-07	2.281E-09	1.732E-07	5.876E-10	2.599E-04	8.869E-07	5.662E-08	4.776E-10	7.833E-09	1.263E-10
AWSA 15	1.677E-07	1.547E-09	3.563E-07	1.235E-09	3.505E-04	1.149E-06	6.867E-08	6.751E-10	8.994E-09	1.538E-10
AWSA 16	5.037E-08	4.300E-10	1.728E-07	6.245E-10	2.703E-04	8.941E-07	6.023E-08	6.019E-10	7.995E-09	1.517E-10
F3731	5.016E-08	4.274E-10	2.034E-07	7.336E-10	3.035E-04	9.916E-07	6.625E-08	6.357E-10	8.658E-09	1.506E-10
F3975	1.135E-07	1.012E-09	1.731E-07	6.037E-10	2.734E-04	9.048E-07	6.037E-08	5.604E-10	8.232E-09	1.406E-10
F3741	3.215E-07	3.133E-09	1.810E-07	6.192E-10	2.895E-04	9.558E-07	6.509E-08	5.793E-10	8.775E-09	1.555E-10
F3960	7.215E-08	8.869E-10	1.773E-07	1.369E-09	2.926E-04	2.238E-06	6.415E-08	7.312E-10	8.519E-09	1.693E-10
Mohammed	1.866E-07	2.164E-08	1.718E-07	1.331E-09	2.905E-04	2.222E-06	6.451E-08	7.706E-10	8.748E-09	1.541E-10
NDW5 684m	2.231E-06	4.146E-08	1.399E-07	2.284E-09	2.128E-04	3.467E-06	4.586E-08	8.463E-10	5.928E-09	1.464E-10
NDW7 50m	4.654E-07	9.185E-09	1.806E-07	2.277E-09	2.959E-04	3.304E-06	6.531E-08	1.075E-09	8.511E-09	2.173E-10
NDW7 100m	6.162E-07	1.325E-08	1.812E-07	2.663E-09	2.962E-04	3.986E-06	6.544E-08	1.176E-09	8.438E-09	2.142E-10
NDW7 150m	7.268E-07	1.382E-08	1.806E-07	2.649E-09	2.945E-04	3.957E-06	6.539E-08	1.181E-09	8.686E-09	2.354E-10
NDW7 200m	9.872E-07	2.095E-08	1.917E-07	3.277E-09	3.097E-04	4.974E-06	6.647E-08	1.320E-09	8.906E-09	2.465E-10
NDW7 250m	1.339E-06	2.878E-08	1.877E-07	3.204E-09	3.083E-04	4.932E-06	6.589E-08	1.314E-09	9.314E-09	2.721E-10
NDW7 300m	3.070E-06	6.921E-08	1.756E-07	3.030E-09	3.250E-04	5.181E-06	7.175E-08	1.462E-09	9.407E-09	2.500E-10
NDW7 544m	2.892E-06	5.444E-08	1.515E-07	2.495E-09	3.017E-04	4.959E-06	6.868E-08	1.257E-09	8.951E-09	2.219E-10
NDW7 569m	2.796E-06	5.188E-08	1.529E-07	2.476E-09	2.742E-04	4.426E-06	6.081E-08	1.126E-09	7.755E-09	1.775E-10

Table A.6: The absolute elemental noble gas concentrations of the thermal waters used for the fitting routine. All concentrations are given in ccSTP/g. Israeli data from Tsur [2013].

	He	ΔHe	Ne	ΔNe	Ar	ΔAr	Kr	ΔKr	Xe	ΔXe
Jordan										
Himma	1.984E-06	1.874E-08	2.057E-07	7.498E-10	3.132E-04	1.032E-06	6.904E-08	5.925E-10	9.219E-09	1.730E-10
North Shuna	1.636E-06	1.533E-08	2.406E-07	8.308E-10	3.579E-04	1.177E-06	8.174E-08	7.341E-10	1.183E-08	2.075E-10
Abu Ziad	3.175E-05	3.150E-07	1.581E-07	5.780E-10	2.815E-04	9.438E-07	6.442E-08	6.519E-10	9.318E-09	1.553E-10
Manshiyeh 1	1.843E-07	1.710E-09	2.231E-07	8.641E-10	3.405E-04	1.142E-06	7.529E-08	6.660E-10	1.072E-08	1.863E-10
Manshiyeh 2	1.659E-07	1.522E-09	2.351E-07	8.128E-10	3.492E-04	1.146E-06	7.753E-08	6.562E-10	1.067E-08	1.929E-10
Zeeghan 4	3.948E-04	3.899E-06	3.103E-07	1.069E-09	4.231E-04	1.570E-06	8.783E-08	7.947E-10	1.153E-08	2.235E-10
Zeeghan 14	1.285E-04	1.212E-06	1.845E-07	6.273E-10	2.796E-04	9.791E-07	6.250E-08	6.378E-10	8.242E-09	1.698E-10
Zeeghan 15	2.457E-04	2.436E-06	2.085E-07	7.449E-10	3.089E-04	1.162E-06	6.752E-08	5.393E-10	9.025E-09	1.506E-10
Zarka Ma'in 1	1.421E-05	1.325E-07	8.812E-08	3.043E-10	1.655E-04	5.437E-07	5.188E-08	4.952E-10	5.662E-09	9.587E-11
Zarka Ma'in 2	9.277E-06	8.292E-08	8.812E-08	2.768E-10	1.669E-04	5.683E-07	4.234E-08	4.142E-10	6.224E-09	1.014E-10
Zara	1.439E-05	1.349E-07	1.553E-07	5.485E-10	2.196E-04	7.690E-07	4.017E-08	3.891E-10	7.051E-09	1.180E-10
Ibn Hammat 1	6.132E-07	5.926E-08	1.717E-07	6.011E-10	2.391E-04	7.898E-07	5.494E-08	5.252E-10	7.549E-09	1.452E-10
Ibn Hammat 2	6.791E-06	6.301E-09	2.658E-07	9.084E-10	3.425E-04	1.124E-06	7.604E-08	7.195E-10	1.036E-08	2.125E-10
Afra	5.785E-07	5.799E-09	1.798E-07	6.392E-10	2.749E-04	9.050E-07	6.323E-08	6.198E-10	8.611E-09	1.644E-10
Thra'a	5.795E-06	5.004E-08	2.106E-07	7.481E-10	3.024E-04	9.974E-07	6.854E-08	6.254E-10	9.126E-09	1.663E-10
KD1	7.602E-06	1.412E-08	2.407E-07	8.592E-10	3.154E-04	1.383E-05	7.127E-08	8.416E-10	9.612E-09	2.384E-10
Israel										
Gofra	1.424E-06	8.651E-09	1.388E-07	5.183E-10	2.754E-04	6.939E-07	6.448E-08	1.235E-09	8.739E-09	1.754E-10
Shamir	2.046E-06	1.054E-08	2.451E-07	9.144E-10	3.719E-04	8.936E-07	8.684E-08	1.454E-09	1.200E-08	2.690E-10
Meitzar 3	4.614E-07	2.464E-09	2.184E-07	8.400E-10	3.352E-04	8.210E-07	7.444E-08	1.323E-09	9.620E-09	1.775E-10
Ein Balzam	5.068E-06	3.596E-08	1.782E-07	7.306E-10	2.994E-04	7.870E-07	6.837E-08	1.254E-09	9.158E-09	1.839E-10
Meitzar 2	1.515E-05	8.904E-08	1.857E-07	7.083E-10	3.897E-04	9.104E-07	8.800E-08	1.470E-09	1.165E-08	2.426E-10
Ein Makla	9.880E-06	5.963E-08	1.639E-07	6.386E-10	3.063E-04	6.880E-07	7.063E-08	1.286E-09	9.321E-09	1.859E-10
Ein Yahav 116	2.376E-06	1.234E-08	2.608E-07	1.019E-09	3.312E-04	7.898E-07	7.060E-08	1.265E-09	9.337E-09	2.288E-10
Ein Yahav 6	9.235E-06	5.569E-08	2.445E-07	9.515E-10	3.508E-04	8.362E-07	7.156E-08	1.343E-09	9.091E-09	1.823E-10
Ein Yahav 16	6.772E-06	4.224E-08	2.284E-07	8.702E-10	3.125E-04	7.555E-07	6.568E-08	1.270E-09	8.754E-09	1.992E-10
Tzofar	1.567E-05	8.123E-08	1.681E-07	6.253E-10	2.458E-04	6.362E-07	4.997E-08	1.105E-09	6.521E-09	1.272E-10
Hamat Tveria	2.826E-05	1.494E-07	1.018E-07	3.899E-10	1.930E-04	5.227E-06	5.037E-08	1.074E-09	6.947E-09	1.408E-10
Mineral	2.786E-08	2.840E-10	7.479E-08	2.904E-10	8.459E-05	3.454E-06	1.687E-08	7.941E-10	1.912E-09	5.448E-11
Ein Qedem	9.132E-06	5.518E-08	4.376E-08	1.818E-10	6.107E-05	3.797E-07	2.396E-08	8.053E-10	3.249E-09	8.021E-11

Table A.7: The results of the ion analysis of the Jordanian thermal waters samples. The total cation and anion concentration is found to the right, together with the ion balance error (IBE) after equation 2.18. No water chemistry analysis was done for the Israeli samples. b. d. means below detection limit.

	Ca meq/L	Fe µeq/L	K meq/L	Mg meq/L	Mn µeq/L	Na meq/L	Sr µeq/L	F µeq/L	Cl meq/L	Br µeq/L	NO$_3$ µeq/L	SO$_4$ meq/L	HCO$_3$ meq/L	Σ Cations meq/L	Σ Anions	IBE
Himma	5.44	0.21	0.22	2.72	b.d.	3.48	41.20	51.81	3.82	16.54	b.d.	2.49	6.24	11.91	12.61	-5.61%
North Shuna	4.29	1.55	0.14	3.77	0.18	5.57	27.39	37.81	5.00	11.95	4.54	2.18	6.84	13.80	14.08	-1.99%
Abu Ziad	8.13	8.27	0.65	4.71	0.43	9.18	73.27	37.27	8.94	13.99	b.d.	5.04	4.72	22.75	18.74	21.36%
Manshiyeh 1	3.74	70.91	0.05	3.21	1.58	1.41	14.27	28.06	1.16	2.14	b.d.	1.03	6.26	8.50	8.48	0.34%
Manshiyeh 2	3.74	34.56	0.05	3.07	0.78	1.12	11.87	26.20	0.85	1.60	b.d.	0.88	6.38	8.03	8.13	-1.30%
Zeeghan 4	37.18	107.80	4.32	10.78	2.51	87.21	336.68	155.99	86.80	111.98	32.55	34.25	23.00	139.94	144.35	-3.05%
Zeeghan 14	35.93	b.d.	5.47	33.49	1.95	93.30	261.36	97.54	132.75	649.43	275.55	28.40	18.24	168.46	180.42	-6.63%
Zeeghan 15	32.19	99.20	4.77	17.82	2.89	82.86	263.64	141.77	83.31	156.86	b.d.	35.23	23.00	138.00	141.83	-2.70%
Zarka Ma'in 1	6.39	b.d.	1.14	2.16	26.47	16.31	79.89	31.02	18.67	32.04	2.74	3.65	4.90	26.11	27.28	-4.30%
Zarka Ma'in 2	6.64	6.95	1.13	2.31	27.70	15.70	78.75	35.32	17.94	32.59	b.d.	3.57	5.02	25.89	26.60	-2.66%
Zara	4.42	b.d.	0.63	1.42	22.02	7.33	62.89	18.56	8.51	18.16	8.06	2.65	3.08	13.88	14.28	-2.81%
Ibn Hammat 1	2.59	0.42	0.19	1.52	b.d.	3.31	16.43	14.59	1.77	2.60	b.d.	1.28	3.53	7.63	6.59	15.70%
Ibn Hammat 2	2.33	12.82	0.16	1.51	3.02	3.89	11.53	26.17	2.79	5.05	b.d.	1.40	3.30	7.91	7.52	5.22%
Afra	2.39	21.49	0.06	1.54	2.02	1.64	9.34	15.04	1.82	3.04	b.d.	1.32	2.50	5.67	5.66	0.28%
Thra'a	2.57	43.69	0.14	1.51	5.75	2.35	13.24	7.79	1.97	3.69	b.d.	1.48	2.62	6.63	6.08	9.08%
KD1	2.24	0.73	0.19	1.56	1.58	5.02	10.44	21.15	4.05	5.13	11.64	1.45	3.85	9.02	9.38	-3.88%

Table A.8: Noble gas isotope concentrations of samples collected on the Karak plateau. All data in ccSTP/g. In the bottom table the determined isotope ratios are listed.

	3He	Δ3He	4He	Δ4He	20Ne	Δ20Ne	22Ne	Δ22Ne	36Ar	Δ36Ar	40Ar	Δ40Ar	84Kr	Δ84Kr	132Xe	Δ132Xe
Swaqa 1	7.415E-14	2.946E-15	7.175E-08	5.639E-10	1.941E-07	1.123E-09	1.981E-08	1.244E-10	1.054E-06	2.217E-08	3.098E-04	9.246E-07	3.824E-08	9.106E-10	2.356E-09	8.824E-11
Swaqa 5A	7.247E-14	2.810E-15	5.546E-08	4.400E-10	1.851E-07	1.026E-09	1.888E-08	1.213E-10	1.233E-06	2.644E-08	3.222E-04	9.478E-07	4.041E-08	9.505E-10	2.469E-09	9.073E-11
Swaqa 23	6.645E-14	2.650E-15	5.766E-08	4.533E-10	1.625E-07	9.448E-10	1.664E-08	1.112E-10	9.430E-07	2.403E-08	2.821E-04	8.456E-07	3.636E-08	8.994E-10	2.119E-09	8.023E-11
Swaqa 24	6.499E-14	2.513E-15	1.360E-07	1.111E-09	1.617E-07	8.817E-10	1.645E-08	1.073E-10	9.444E-07	2.177E-08	2.831E-04	8.400E-07	3.674E-08	8.831E-10	2.343E-09	8.872E-11
Swaqa 25	7.223E-14	2.683E-15	6.233E-08	4.886E-10	1.615E-07	9.377E-10	1.645E-08	1.055E-10	9.665E-07	2.127E-08	2.835E-04	8.223E-07	3.572E-08	8.733E-10	2.355E-09	9.232E-11
Swaqa 27	7.788E-14	3.071E-15	6.810E-08	5.355E-10	1.979E-07	1.139E-09	2.025E-08	1.299E-10	1.019E-06	2.106E-08	3.201E-04	1.096E-06	3.970E-08	8.945E-10	2.455E-09	9.281E-11
Swaqa 28	8.192E-14	3.169E-15	7.556E-08	5.976E-10	2.174E-07	1.250E-09	2.217E-08	1.020E-10	1.020E-06	3.190E-08	3.376E-04	1.118E-06	4.246E-08	9.152E-10	2.578E-09	1.001E-10
Swaqa 29	5.683E-14	2.181E-15	7.257E-08	5.716E-10	1.556E-07	8.716E-10	1.591E-08	1.122E-10	7.236E-07	3.362E-08	2.749E-04	9.756E-07	3.661E-08	8.688E-10	2.374E-09	9.296E-11
Qatraneh 8	3.724E-13	1.379E-14	2.951E-07	2.637E-09	8.513E-07	5.293E-09	8.666E-08	5.914E-10	2.263E-06	3.822E-08	6.631E-04	1.995E-06	6.128E-08	1.324E-09	3.151E-09	1.201E-10
Qatraneh 12	7.170E-14	2.982E-15	8.009E-08	6.355E-10	1.661E-07	1.050E-09	1.709E-08	1.127E-10	9.682E-07	2.668E-08	2.931E-04	9.029E-07	3.889E-08	8.928E-10	2.424E-09	8.980E-11
Qatraneh 26	5.973E-14	2.376E-15	6.487E-08	5.129E-10	1.563E-07	9.506E-10	1.601E-08	1.019E-10	9.489E-07	2.153E-08	2.778E-04	8.261E-07	3.703E-08	9.470E-10	2.055E-09	7.933E-11
KSH 1	2.221E-13	8.245E-15	1.900E-07	1.600E-09	6.644E-07	3.769E-09	6.778E-08	4.350E-10	2.198E-06	4.008E-08	6.597E-04	1.979E-06	6.842E-08	1.413E-09	4.297E-09	1.725E-10
KSH 8	5.654E-13	2.179E-14	5.116E-07	4.741E-09	1.445E-06	8.695E-09	1.486E-07	1.108E-09	3.843E-06	6.406E-08	1.157E-03	3.374E-06	1.001E-07	1.966E-09	4.428E-09	1.798E-10
KD 1	1.494E-12	5.630E-14	7.562E-06	7.151E-08	2.147E-06	1.200E-08	2.197E-07	1.432E-09	9.648E-07	2.675E-08	2.849E-04	9.855E-07	4.085E-08	9.175E-10	2.657E-09	1.040E-10
KD 5	7.071E-14	2.722E-15	6.588E-08	5.155E-10	1.595E-06	9.395E-09	1.636E-07	1.101E-09	9.160E-07	2.500E-08	2.802E-04	8.431E-07	3.705E-08	8.904E-10	2.450E-09	9.633E-11
Lajjun 7A	6.408E-13	2.476E-14	4.943E-07	4.569E-09	1.551E-06	8.803E-09	1.594E-07	1.116E-09	4.767E-06	7.977E-08	1.424E-03	4.259E-06	1.241E-07	2.588E-09	5.473E-09	2.578E-10
Ghuwair 3	5.808E-13	2.216E-14	4.207E-07	3.844E-09	1.323E-06	7.488E-09	1.354E-07	8.910E-10	3.217E-06	7.488E-08	9.656E-04	2.792E-06	8.450E-08	1.672E-09	3.620E-09	1.418E-10
Shihan	7.316E-14	3.116E-15	1.107E-07	8.850E-10	1.743E-07	9.699E-10	1.785E-08	1.152E-10	1.101E-06	2.321E-08	3.249E-04	1.087E-06	4.224E-08	1.022E-09	3.005E-09	1.129E-10

	3He/4He	Δ3He/4He	20Ne/22Ne	Δ20Ne/22Ne	40Ar/36Ar	Δ40Ar/36Ar
Swaqa 1	1.033E-06	4.185E-08	9.799	0.006	292.20	4.40
Swaqa 5A	1.307E-06	5.171E-08	9.783	0.005	258.36	3.99
Swaqa 23	1.153E-06	4.685E-08	9.764	0.006	277.32	4.45
Swaqa 24	4.777E-07	1.888E-08	9.799	0.006	303.89	4.61
Swaqa 25	1.159E-06	4.400E-08	9.793	0.006	288.68	5.26
Swaqa 27	1.144E-06	4.598E-08	9.781	0.006	315.18	4.76
Swaqa 28	1.084E-06	4.260E-08	9.823	0.007	305.50	5.38
Swaqa 29	7.832E-07	3.068E-08	9.776	0.006	338.57	6.80
Qatraneh 8	1.262E-06	4.808E-08	9.804	0.006	293.59	4.32
Qatraneh 12	8.952E-07	3.791E-08	9.736	0.006	291.05	4.95
Qatraneh 26	9.208E-07	3.735E-08	9.773	0.006	298.30	4.52
KSH 1	1.169E-06	4.451E-08	9.777	0.007	301.98	4.52
KSH 8	1.105E-06	4.380E-08	9.758	0.006	299.47	4.43
KD 1	1.976E-07	7.676E-09	9.768	0.005	295.32	4.72
KD 5	1.073E-06	4.224E-08	9.779	0.006	305.85	4.94
Lajjun 7A	1.296E-06	5.151E-08	9.748	0.006	295.09	4.38
Ghuwair 3	1.381E-06	5.417E-08	9.800	0.008	300.63	4.43
Shihan	6.610E-07	2.865E-08	9.793	0.005	295.92	4.38

A.6 Overview of the NG measurement runs

Noble gas measurements are always executed in so-called runs, i. e. several samples are measured together with several calibrations of each size. Data evaluation takes place for a whole run at once.

Run 53: Samples of 2009 campaign
Run 55: Double-samples of 2009 campaign
Run 60: Azraq samples 2010
Run 62: Karak samples 2010
Run 65: Double-sample of the 2010 campaign
Run 71: Samples of 2012 campaign
Run 72: continuance of run 71, most of the 2012 samples were measured in run 72

A.7 Used software

- This document is prepared using LaTeX with the MikTeX 2.9 distribution. The development environment is Texmaker.

- Plots are created using OriginPro 9.0.

- Geographical maps are prepared using Quantum GIS, most of the georeferenced data is from WAJ [2010].

- Piper diagrams are plotted using the freeware GW_Chart, published by the USGS (http://water.usgs.gov/nrp/gwsoftware/GW_Chart/GW_Chart.html).

- Microsoft Excel is in charge of the data management.

- Data preparation was done with the group-own programs introduced in the text, WUCEM and PANGA.

A.8 Panga data evaluation diagrams

Following, the relevant Monte Carlo plots used in the analysis. The simulations within the white array are the selected one, all others are omitted in the analysis. This approach is justified in chapter 3.6.4. In case no Panga plots are shown there were not made any selections of Monte Carlo simulations.
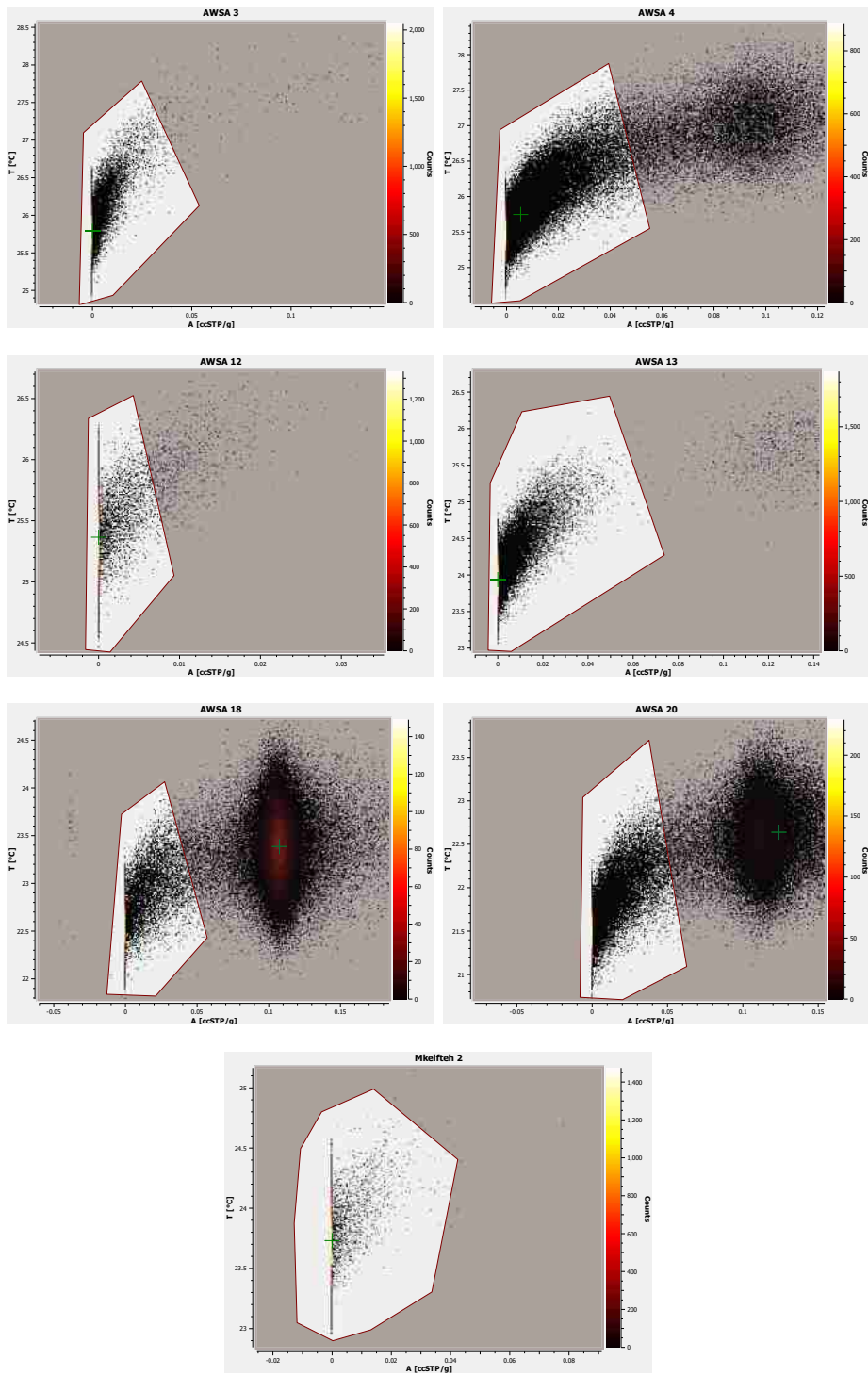
Figure A.17: Panga plots of the Azraq 2009 samples.
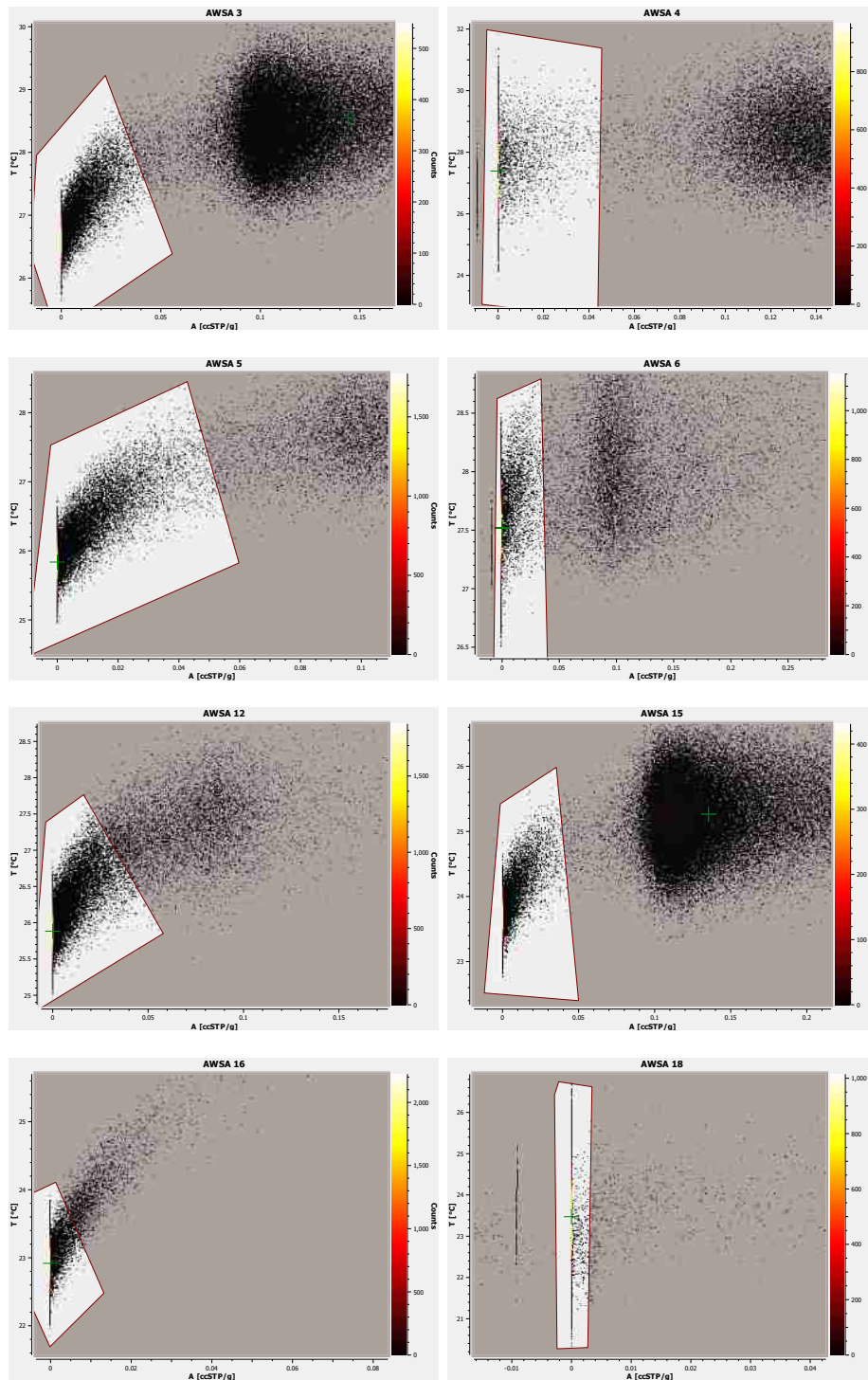
Figure A.18: Panga plots of the Azraq 2010 samples.
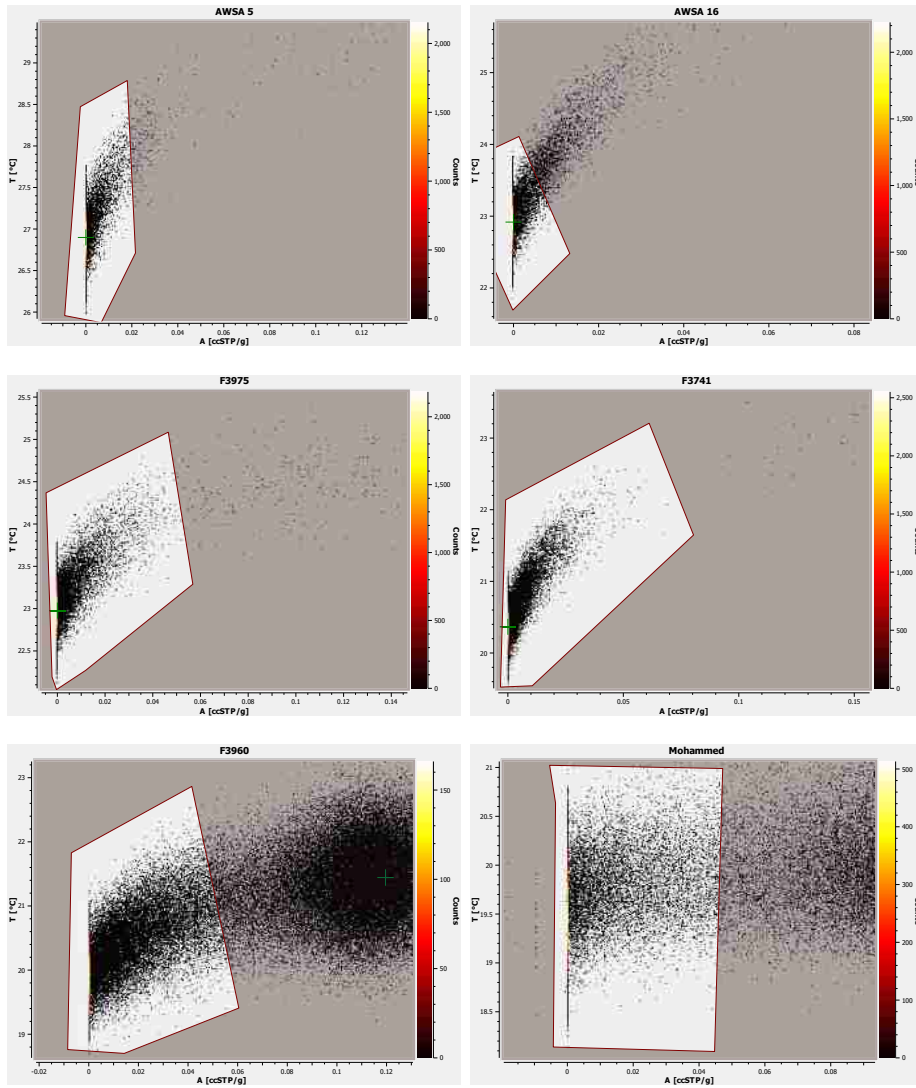
Figure A.19: Panga plots of the AWSA and Farm well 2012 samples.
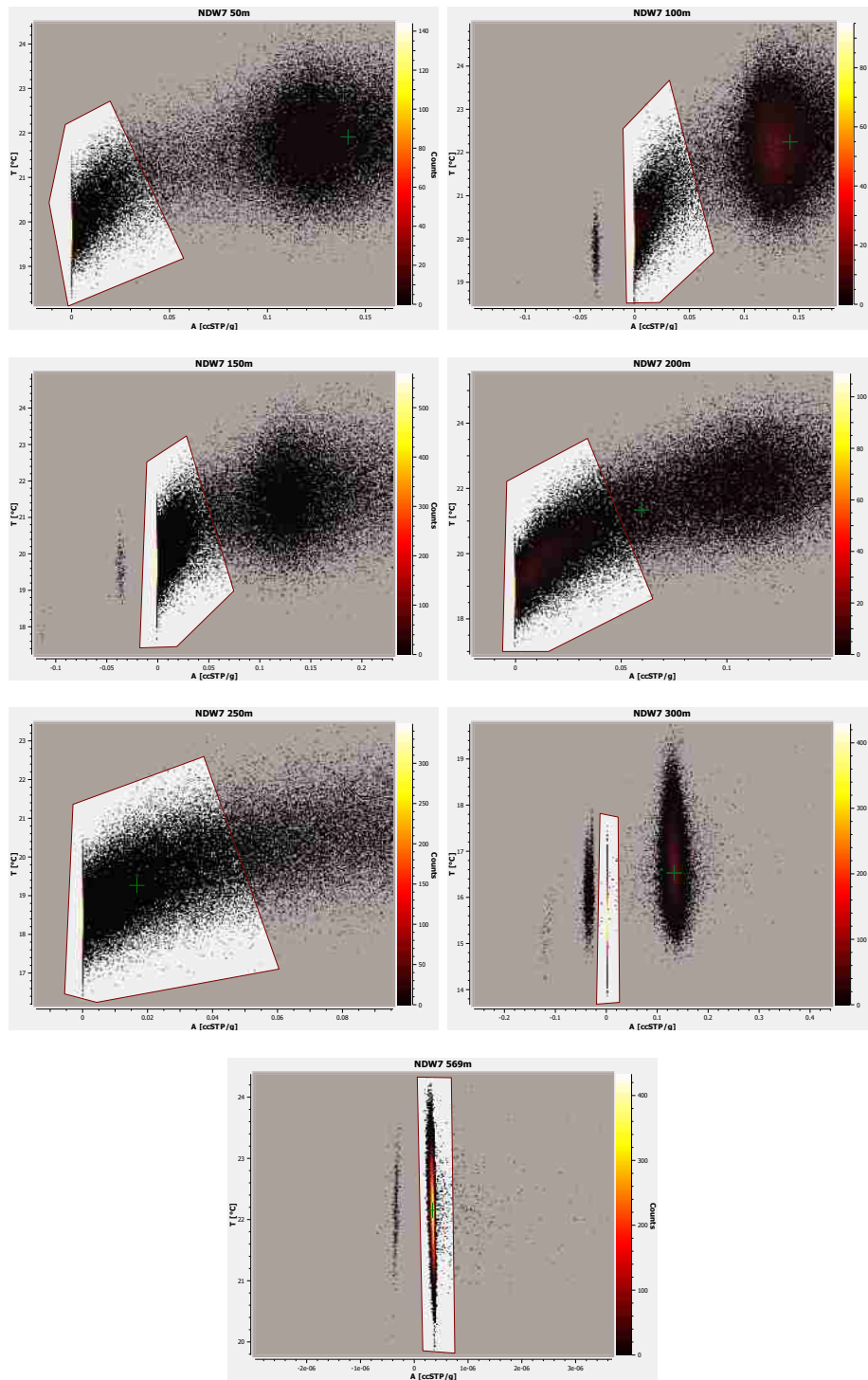
Figure A.20: Panga plots of the NDW7 samples.
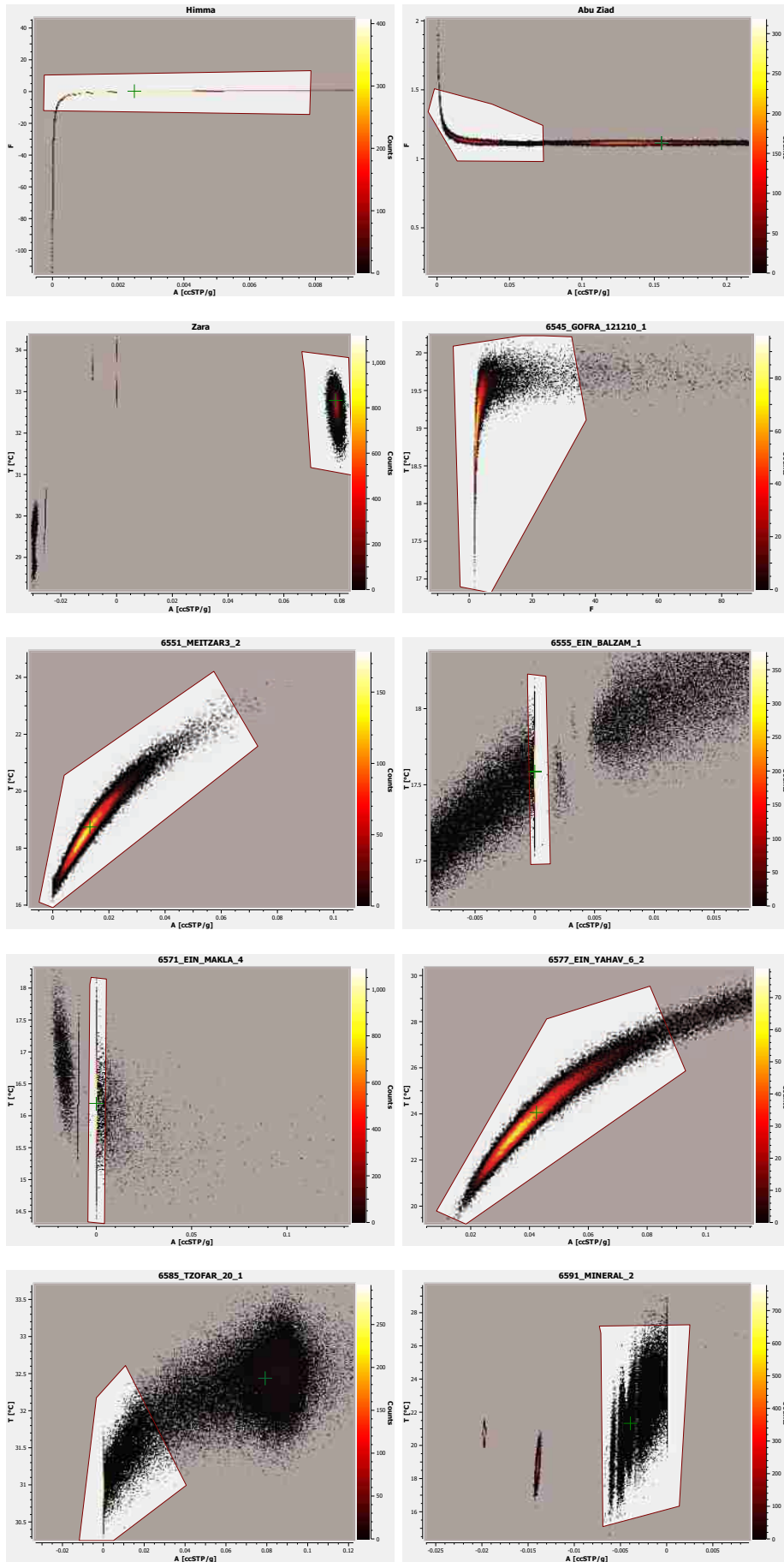
Figure A.21: Panga plots of Thermal waters.

A.9 Abbreviations

AWSA	Amman Water and Sewage Authoriy
CE	Closed-system equilibration excess air model
DS	Diffusion sampler
DST	Dead Sea Transform
EA	Excess air
EMWL	Eastern Mediterranean Water Line
GMWL	Global Meteoric Water Line
JMWL	Jordanian Meteoric Water Line
LMWL	Local Meteoric Water Line
masl	Meters above sea level
mbsl	Meters below sea level
MORB	Mid-Ocean Ridge Basalt
NGT	Noble Gas Temperature
OIB	Ocean Island Basalt
UA	Unfractionated Air excess air model

List of Figures

List of Tables

Acknowledgments – Danksagung

Bibliography

ABDULLA FA, AL-KHATIB MA, AL-GHAZZAWI ZD (2000) Development of groundwater modeling for the Azraq basin, Jordan. *Environmental Geology* 40(1-2)

ABU-EL-SHA'R WY, RIHANI JF (2007) Application of the high performance computing techniques of parflow simulator to model groundwater flow at Azraq basin. *Water Resource Management* 21: 409–425

ABU-JABER NS, ALI AJ, AL-QUDAH K (1998) Use of solute and isotopic composition of ground water to constrain the ground water flow system of the Azraq area, Jordan. *Groundwater* 36(2): 361–365

AESCHBACH-HERTIG W (2005) A comment on "Helium sources in passive margin aquifers – new evidence for a significant mantle ^{3}He source in aquifers with unexpectedly low in situ ^{3}He/^{4}He production" by M. C. Castro [Earth Planet. Sci. Lett. 222 (2004) 897-913]. *Earth Planetary Science Letters* 240: 827–829

AESCHBACH-HERTIG W, SOLOMON DK (2013) Noble gas thermometry in groundwater hydrology. In: BURNARD P (Ed.), The noble gases as geochemical tracers, Advances in isotope geochemistry, 81–122. Springer, Berlin, Heidelberg

AESCHBACH-HERTIG W, KIPFER R, HOFER M, IMBODEN DM, WIELER R, SIGNER P (1996) Quantification of gas fluxes from the subcontinental mantle: The example of Laacher See, a maar lake in Germany. *Geochimica et Cosmochimica Acta* 60(1): 31–41

AESCHBACH-HERTIG W, PEETERS F, BEYERLE U, KIPFER R (1999) Interpretation of dissolved atmospheric noble gases in natural waters. *Water Resource Research* 35(9): 2779–2792

AESCHBACH-HERTIG W, PEETERS F, BEYERLE U, KIPFER R (2000) Palaeotemperature reconstruction from noble gases in ground water taking into account equilibration with entrapped air. *Nature* 405: 1040–1044

AESCHBACH-HERTIG W, STUTE M, CLARK J, REUTER R, SCHLOSSER P (2002) A paleotemperature record derived from dissolved noble gases in groundwater of the Aquia Aquifer (Maryland, USA). *Geochimica et Cosmochimica Acta* 66(5): 797–817

AESCHBACH-HERTIG W, EL-GAMAL H, WIESER M, PALCSU L (2008) Modeling excess air and degassing in groundwater by equilibrium partitioning with a gas phase. *Water Resource Research* 44: W08449

AJAMIEH M (1998) Water Quality Improvement and Conservation Project – Assessment of Brackish Groundwater in Jordan. Tech. rep., USAID

AKKAWI EJ (2006) Locating Zones and Quantify the Submarine Groundwater Discharge into the Eastern Shores of the Dead Sea-Jordan. *PhD Thesis*, University of Göttingen

AL-EISAWI D (1996) Vegetation in Jordan. Tech. rep., UNESCO - Cairo Office, Regional Office for Science and Technology for the Arab States

AL-KHARABSHEH A (2000) Ground-water modelling and long-term management of the Azraq basin as an example of arid area conditions (Jordan). *Journal of Arid Environments* 44: 143–153

AL-MOMANI MR (1994) Environmental isotope and hydrochemical study of the shallow and deep groundwater in the Azraq basin, Jordan. In: IAEA TecDoc 890, 75–101

AL-MOMANI MR, AMRO H, KILANI S, EL-NAQA A, RIMAWI O, KATBEH H, TUFFAHA R (2006) Isotope response to hydrological systems for long term exploitation, case of Azraq basin, Jordan. In: IAEA TecDoc 1507, 177–211

ALJAZZAR TH (2003) Groundwater recharge modeling in the Azraq basin considering the unsaturated flow components. *Master's Thesis*, Jordan University of Science and Technology, Irbid

AMBRASEYS NN (2006) Comparison of frequency of occurrence of earthquakes with slip rates from long-term seismicity data: the cases of Gulf of Corinth, Sea of Marmara and Dead Sea Fault Zone. *Geophysical Journal International* 165(2): 516–526

ANDERSON DL (1993) Helium-3 from the mantle: Primordial signal or cosmic dust? *Science* 261: 170–176

ANDREWS J I (1992) Cretaceous and Paleogene Lithostratigraphy in the subsurface of Jordan, vol. 5 of *Subsurface Geology Bulletin*. Subsurface Geoloy Division, NRA, Amman, Jordan

ANDREWS JN, LEE DJ (1979) Inert gases in groundwater from the Bunter Sandstone of England as indicators of age and palaeoclimatic trends. *Journal of Hydrology* 41: 233–252

APPELO CAJ, POSTMA D (2005) Geochemistry, groundwater and pollution. A. A. Balkema Publishers, Leiden, London, New York, Philadelphia, Singapore

ARAD A, BEIN A (1986) Saline- versus freshwater contribution to the thermal waters of the northern Jordan Rift Valley, Israel. *Journal of Hydrology* 83(1-2): 49–66

AYED R (1996) Hydrological and Hydrogeological study of the Azraq Basin, Jordan. *PhD Thesis*, University of Baghdad, Iraq

BACK W (1966) Hydrochemical facies and ground-water flow patterns in northern part of Atlantic Coastal Plain. *USGS Prof Paper* 498-A

BAERTSCHI P (1976) Absolute ^{18}O content of standard mean ocean water. *Earth and Planetary Science Letters* 31: 341–344

BAJJALI W (1994) Recharge and regional circulation of thermal groundwater in northern Jordan using isotope geochemistry. *PhD Thesis*, University of Ottawa

BAJJALI W (2012) Spatial variability of environmental isotope and chemical content of precipitation in Jordan and evidence of slight change in climate. *Applied Water Science* 2: 271–283

BAJJALI W, CLARK ID, FRITZ P (1997) The artesian thermal groundwaters of northern Jordan: insights into their recharge history and age. *Journal of Hydrology* 192(1-4): 355–382

BALLENTINE CJ, BURNARD PG (2002) Production, release and transport of noble gases in the continental crust. In: PORCELLI D, BALLENTINE C, WIELER R (Eds.), Noble gases in geochemistry and cosmochemistry, vol. 47 of *Reviews in Mineralalogy and Geochemistry*, 481–538. Mineralogical Society of America, Geochemical Society, Washington, DC

BALLENTINE CJ, HALL CM (1999) Determining paleotemperature and other variables by using an error-weighted, nonlinear inversion of noble gas concentrations in water. *Geochimica et Cosmochimica Acta* 63(16): 2315–2336

BARD E, HAMELIN B, FAIRBANKS RG, ZINDLER A (1990) Calibration of the ^{14}C timescale over the past 30,000 years using mass spectrometric U-Th ages from Barbados corals. *Nature* 345: 405–410

BARKAN E, LUZ B, LAZAR B (2001) Dynamics of the carbon dioxide system in the Dead Sea. *Geochimica et Cosmochimica Acta* 65(3): 355 – 368

BARTOV Y, STEIN M, ENZEL Y, AGNON A, RECHES Z (2002) Lake Levels and Sequence Stratigraphy of Lake Lisan, the Late Pleistocene Precursor of the Dead Sea. *Quaternary Research* 57: 9–21

BASFORD JR, DRAGON JC, PEPIN RO, COSCIO JR MR, MURTHY VR (1973) Krypton and xenon in lunar fines. *Proc 4th Lunar Sci Conf* 2: 1915–1955

BAUBRON JC, BESANÇON J, COPELAND L, HOURS F, MACAIRE JJ, SANLAVILLE P (1985) Évolution de la moyen vallée du Zarqa (Jordanie) au Néogène et au Quaternaire. *Rév Géol Dyn Géog Phys* 26(5): 273–283

BECKER B, KROMER B (1993) The continental tree-ring record – absolute chronology, ^{14}C calibration and climatic change at 11 ka. *Palaeogeography, Palaeoclimatology, Palaeoecology* 103(1-2): 67–71

BEIN A, FEINSTEIN S (1988) Late Cenozoic thermal gradients in Dead Sea Transform system basins. *Journal of Petroleum Geology* 11(2): 185–192

BEISER A (1957) Variations in the Geomagnetic Dipole in the past 15,000 Years. *Journal of Geophysical Research* 62(2): 235–239

BEN-AVRAHAM Z, GINZBURG A (1990) Displaced terranes and crustal evolution of the Levant and the eastern Mediterranean. *Tectonics* 9(4): 613–622

BEN-AVRAHAM Z, HÄNEL R, VILLINGER H (1978) Heat flow through the Dead Sea rift. *Marine Geology* 28(3-4): 253–269

BEN-AVRAHAM Z, GARFUNKEL Z, LAZAR M (2008) Geology and evolution of the southern Dead Sea Fault with emphasis on subsurface structure. *Annual Review of Earth and Planetary Science* 36: 357–387

BENDER F (1968) Geologie von Jordanien. Beiträge zur regionalen Geologie der Erde. Gebrüder Borntraeger, Berlin, Stuttgart. An English translation was released by the same publisher in 1974 under the title "Geology of Jordan"

BENSON BB, KRAUSE JR D (1976) Empirical laws for dilute aqueous solutions of nonpolar gases. *Journal of Chemical Physics* 64(2): 689–709

BENSON BB, KRAUSE JR D (1980) Isotopic fractionation of helium during solution: A probe for the liquid state. *Journal of Solution Chemistry* 9(12): 895–909

BERGELSON G, NATIV R, BEIN A (1999) Salinization and dilution history of ground water discharging into the Sea of Galilee, the Dead Sea Transform, Israel. *Applied Geochemistry* 14(1): 91–118

BEYERLE U, AESCHBACH-HERTIG W, IMBODEN DM, BAUR H, GRAF T, KIPFER R (2000) A mass spectrometric system for the analysis of noble gases and tritium from water samples. *Environtal Science & Technology* 34(10): 2042–2050

BEYERLE U, RUEEDI J, LEUENBERGER M, AESCHBACH-HERTIG W, PEETERS F, KIPFER R, DODO A (2003) Evidence for periods of wetter and cooler climate in the Sahel between 6 and 40 kyr BP derived from groundwater. *Geophysical Research Letters* 30(4): 1173

BLASER PC, KIPFER R, LOOSLI HH, WALRAEVENS K, VAN CAMP M, AESCHBACH-HERTIG W (2010) A 40 ka record of temperature and permafrost conditions in northwestern Europe from noble gases in the Ledo-Paniselian Aquifer (Belgium). *Journal Quaternary Science* 25(6): 1038–1044

BLICHER-MATHIESEN G, MCCARTY GW, NIELSEN LP (1998) Denitrification and degassing in groundwater estimated from dissolved dinitrogen and argon. *Journal of Hydrology* 208: 16–24

BONN T (2013) Strategische Ressourcenwahrheiten – Interaktion zwischen Behörden und Geberorganisationen in der jordanischen Wasserpolitik. *PhD Thesis*, Heidelberg University

BOOM G (1968) Zur Petrogenese der Plateaubasalte Nordostjordaniens. In: Geologisches Jahrbuch, vol. 85, 489–496. Bundesamt für Bodenforschung und Geologische Landesämter der Bundesrepublik Deutschland

BURNARD P (2004) Diffusive fractionation of noble gases and helium isotopes during mantle melting. *Earth and Planetary Science Letters* 220(3-4): 287–295

CARROLL MR, WEBSTER JD (1994) Solubilities of sulphur, noble gases, nitrogen, chlorine, and fluorine in magmas. In: CARROLL MR (Ed.), Volatiles in magmas, vol. 30 of *Reviews in Mineralogy and Geochemistry*, 231–279. Mineralogical Society of America

CERLING TE, SOLOMON DK, QUADE J, BOWMAN JR (1991) On the isotopic composition of carbon in soil carbon dioxide. *Geochimica et Cosmochimica Acta* 3403–3405

CHEBAANE M, EL-NASER H, FITCH J, HIJAZI A, JABBARIN A (2004) Participatory groundwater management in Jordan: Development and analysis of options. *Hydrogeology Journal* 12: 14–32

CHIODINI G, FRONDINI F, PONZIANI F (1995) Deep structures and carbon dioxide degassing in Central Italy. *Geothermics* 24(1): 81–94

CHOUBEY VW, RAMOLA RC (1997) Correlation between geology and radon levels in groundwater, soil and indoor air in Bhilangana Valley, Garhwal Himalaya, India. *Environmental Geology* 32(4): 258–262

CLARK ID, FRITZ P (1997) Environmental Isotopes in Hydrogeology. CRC Press, Boca Raton, New York

CLARKE WB, JENKINS WJ, TOP Z (1976) Determination of tritium by mass spectrometric measurement of ^{3}He. *International Journal of Applied Radiation and Isotopes* 27: 515–522

CLASS C, GOLDSTEIN SL (2005) Evolution of helium isotopes in the Earth's mantle. *Nature* 436: 1107–1112

CLEVER HL (1979a) Helium and neon – gas solubilities, vol. 1 of *Solubility data series*. Pergamon Press, Oxford

CLEVER HL (1979b) Krypton, xenon and radon – gas solubilities, vol. 2 of *Solubility data series*. Pergamon Press, Oxford

CLEVER HL (1980) Argon, vol. 4 of *Solubility data series*. Pergamon Press, Oxford

COLLINS WD (1923) Graphic representation of water analyses. *Industrial and Engineering Chemistry* 15(4): 394

CORNOG R, LIBBY WF (1941) Production of Radioactive Hydrogen by Neutron Bombardment of Boron and Nitrogen. *Physical Review* 59: 12

CRAIG H (1957) Isotopic standards for carbon and oxygen and correction factors for massspectrometric analysis of carbon dioxide. *Geochimica et Cosmochimica Acta* 12: 133–149

CRAIG H (1961) Isotopic variations in meteoric water. *Science* 133: 1702–1703

CRAIG H, CLARKE WB, BEG MA (1975) Excess ^{3}He in deep water on the East Pacific Rise. *Earth and Planetary Science Letters* 26: 125–132

CRENSHAW WB, WILLIAMS SN, STOIBER RE (1982) Fault location by radon and mercury detection at an active volcano in Nicaragua. *Nature* 300: 345–346

CROWE C (1958) Carbon-14 Activity during the past 5,000 Years. *Nature* 182: 470–471

DAFNY E, BURG A, GVIRTZMAN H (2006) Deduction of groundwater flow regime in a basaltic aquifer using geochemical and isotopic data: The Golan Heights, Israel case study. *Journal of Hydrology* 330(3-4): 506–524

DAMON PE, CHENG SL, LINICK TW (1989) Fine and Hyperfine Structure in the Spectrum of Secular Variations of Atmospheric ^{14}C. *Radiocarbon* 31(3): 704–718

DANSGAARD W (1964) Stable isotopes in precipitation. *Tellus* 16(4): 436–468

DAOUD R, NABER H, ABU TARBUSH M, QUOSSOUS R, SALMAN A, KARABLIEH E (2006) Environmental Issues of Water Resources. In: HADDADIN MJ (Ed.), Water resources in Jordan – Evolving policies for development, the environment, and conflict resolution, 88–115. Resources for the Future, Washington

DARLING WG, GRIESSHABER E, ANDREWS JN, ARMANNSSON H, O'NIONS RK (1995) The origin of hydrothermal and other gases in the Kenya Rift Valley. *Geochimica et Cosmochimica Acta* 59(12): 2501–2512

Davis SN, DeWiest RJM (1966) Hydrogeology. John Wiley & Sons, New York, London, Sydney

de Wit JC, van der Straaten CM, Mook WG (1980) Determination of the absolute hydrogen isotopic ratio of V-SMOW and SLAP. *Geostandards Newsletter* 4(1): 33–36

Deshpande RD, Gupta SK (2013) Groundwater helium: An indicator of active tectonic regions along Narmada River, central India. *Chemical Geology* 344: 42–49

DeWayne Cecil L, Green JR (2000) Radon-222. In: Cook P, Herczeg AL (Eds.), Environmental tracers in subsurface hydrology, 175–194. Kluwer Academic Publishers, Boston

Diabat A (2004) Structural map of Jordan. Unpublished report, Natural Resources Authority, Amman, Jordan

Dottridge J, Abu Jaber N (1999) Groundwater resources and quality in northeastern Jordan: safe yield and sustainability. *Applied Geography* 19: 313–323

Duffield WA, McKee EH, El Salem F, Teimeh M (1988) K-Ar ages, chemical composition and geothermal significance of cenozoic basalt near the Jordan rift. *Geothermics* 17(4): 635–644

Durridge (2000) RAD7 radon detector – Owner's manual. http://www.durridge.com/product_manuals.shtml

Durridge (2001) RAD7 RAD-H$_2$O – Radon in water accessory – Owner's manual. http://www.durridge.com/product_manuals.shtml

Eckstein Y, Maurath G (1995) Heat flow and the hydrologic cycle: examples from Israel. In: Gupta ML, Yamano M (Eds.), Terrestrial heat flow and geothermic energy in Asia, 1–21. Oxford & IBH Publishing, New Delhi, Bombay, Calcutta

Eckstein Y, Simmonsi G (1977) Measurement and interpretation of terrestrial heat flow in Israel. *Geothermics* 6(3-4): 117–142

Ehleringer JR, Philips SL, Schuster WSF, Sandquist DR (1991) Differential utilization of summer rains by desert plants. *Oecologia* 88: 430–434

El-Isa Z, Mechie J, Prodehl C (1987a) Shear velocity structure of Jordan from explosion seismic data. *Geophysical Journal of the Royal Astronomical Society* 90(1): 265–281

El-Isa Z, Mechie J, Prodehl C, Makris J, Rihm R (1987b) A crustal structure study of Jordan derived from seismic refraction data. *Tectonophysics* 138(2-4): 235–253

El-Naqa A (2010) Study of saltwater intrusion in the upper aquifer in Azraq basin. Tech. rep., IUCN

El-Naqa A, Al-Momani M, Kilani S, Hammouri N (2007) Groundwater deterioration of shallow groundwater aquifers due to overexploitation in northeast Jordan. *Clean* 35(2): 156–166

El-Waheidi MM, Merlanti F, Pavan M (1992) Geoelectrical resistivity survey of the central part of the Azraq basin (Jordan) for identifying saltwater/freshwater interface. *Journal Applied Geophysics* 29: 125–133

Eraifej N (2006) Gas geochemistry and isotopic signatures in the deep thermal waters in Jordan. *Freiberg Online Geology* 16

Evans MJ, Derry LA, France-Lanord C (2008) Degassing of metamorphic carbon dioxide from the Nepal Himalaya. *Geochemistry, Geophysics, Geosystems* 9(4): Q04021

Fairbanks RG, Mortlock RA, Chiu TC, Cao L, Kaplan A, Guilderson TP, Fairbanks TW, Bloom AL, Grootes PM, Nadeau MJ (2005) Radiocarbon calibration curve spanning 0 to 50,000 years BP based on paired ^{230}Th/ ^{234}U/ ^{238}U and ^{14}C dates on pristine corals. *Quaternary Science Reviews* 24: 1781–1796

Fairbridge RW, Oliver JE (2005) Lapse rate. In: Oliver JE (Ed.), Encyclopedia of world climatology, 448–450. Springer, Dordrecht, Berlin, Heidelberg

FALKENMARK M, LUNDQVIST J, WIDSTRAND C (1989) Macro-scale water scarcity requires micro-scale approaches: Aspects of vulnerability in semi-arid development. *Natural Resources Forum* 13(4): 258–267

FAYBISHENKO BA (1995) Hydraulic behavior of quasi-saturated soils in the presence of entrapped air: Laboratory experiments. *Water Resourse Research* 31(10): 2421–2435

FETTER CW (2001) Applied Hydrogeology. Prentice-Hall, New Jersey, 4 edn.

FITTS CR (2002) Groundwater science. Academic Press, London

FLORKOWSKI T (1985) Sample preparation for hydrogen isotope analysis by mass spectrometry. *International Journal of Applied Radiation and Isotopes* 36(12): 991–992

FONTES JC (1991) Évaluation de la production naturelle in situ d'argon-36 via le chlore-36 : implications géochimiques et géochronologiques. *Comptes rendus de l'Académie des sciences Série 2* 313(6): 649–654

FONTES JC, GARNIER JM (1979) Determination of the initial ^{14}C activity of the total dissolved carbon: A review of the existing models and a new approach. *Water Resource Research* 15(2): 399–413

FREEZE RA, CHERRY JA (1979) Groundwater. Prentice-Hall, New Jersey, USA

FREUND R, GARFUNKEL Z, ZAK I, GOLDBERG M, WEISSBROD T, DERIN B, BENDER F, WELLINGS FE, GIRDLER RW (1970) The Shear along the Dead Sea Rift [and Discussion]. *Philosophical Transactions of the Royal Society of London A* 267(1181): 107–130

FREUNDT F, SCHNEIDER T, AESCHBACH-HERTIG W (2013) Response of noble gas partial pressures in soil air to oxygen depletion. *Chemical Geology* 339: 283 – 290

FRIEDRICH R (2007) Grundwassercharakterisierung mit Umwelttracern: Erkundung des Grundwassers der Odenwald-Region sowie Implementierung eines neuen Edelgas-Massenspektrometersystems. *PhD Thesis*, Heidelberg University

FRIESLANDER U, BEN-AVRAHAM Z (1989) Magnetic field over the Dead Sea and vicinity. *Marine and Petroleum Geology* 6(2): 148–160

FRISCH W, MESCHEDE M, BLAKEY R (2011) Plate tectonics – Continental drift and mountain building. Springer, Berlin, Heidelberg

FÖRSTER A, FÖRSTER HJ, MASARWEH R, MASRI A, TARAWNEH K (2007) The surface heat flow of the Arabian Shield in Jordan. *Journal of Asian Earth Sciences* 30(2): 271–284

FÖRSTER HJ, FÖRSTER A, OBERHÄNSLI R, STROMEYER D (2010) Lithospheric composition and thermal structure of the Arabian Shield in Jordan. *Tectonophysics* 481(1-4): 29–37

FRY VA, SELKER JS, GORELICK SM (1997) Experimental investigations for trapping oxygen gas in saturated porous media for in situ bioremedation. *Water Resource Research* 33(12): 2687–2696

GALANIS JR SP, SASS JH, MUNROE RJ, ABU-AJAMIEH M (1986) Heat flow at Zerqa Ma'in and Zara and a geothermal reconnaissance of Jordan. *USGS Open File Report* 86(631)

GALLI P (1999) Active tectonics along the Wadi Araba-Jordan Valley transform fault. *Journal of Geophysical Research: Solid Earth* 104(B2): 2777–2796

GARFUNKEL Z (1981) Internal structure of the Dead Sea leaky transform (rift) in relation to plate kinematics. *Tectonophysics* 80: 81–108

GARFUNKEL Z, BEN-AVRAHAM Z (1996) The structure of the Dead Sea basin. *Tectonophysics* 266: 155–176

GARRARD AN, HARVEY P, HIVERNEL F, BYRD B (1985) The environmental history of the Azraq Basin. *Studies in the History and Archaeology of Jordan* 2: 109–115

GASCOYNE M, SHEPPARD MI (1993) Evidence of terrestrial discharge of deep groundwater of the Canadian Shield from helium in soil gases. *Environtal Science & Technology* 27: 2420–2426

GAT JR (1987) Effect of climate changes on the precipitation patterns and isotopic composition of water in a climate transition zone: Case of the Eastern Mediterranean Sea area. In: Proceedings of the Vancouver Symposium, August 1987: The influence of climate change and climatic variability on the hydrologic regime and water resources, 168, 513–523. IAHS

GAT JR, CARMI I (1970) Evolution of the Isotopic Composition of Atmospheric Waters in the Mediterranean Sea Area. *Journal of Geophysical Research* 75(15): 3039–3048

GAT JR, DANSGAARD W (1972) Stable isotope survey of the fresh water occurrences in Israel and the Northern Jordan Rift Valley. *Journal of Hydrology* 16(3): 177 – 211

GEYH M (2000) Groundwater – Saturated and unsaturated zone. In: MOOK WG (Ed.), Environmental Isotopes in the hydrological cycle; principles and applications, vol. 4. UNESCO, Paris

GEYH MA, MICHEL G (1982) Isotopical differentiation of groundwater of different hydrogeologic origin. *Journal of Hydrology* 59(1–2): 161–171

GHARAIBEH AAJ (2008) Heat source study and geothermal reservoir assessment for the Zarqa Ma'in – Dab'a area, central Jordan. In: United Nations University, Geothermal Trainng Programm, 221–246

GIGGENBACH WF, GOGUEL RL (1989) Collection and analysis of geothermal and volcanic water and gas discharges. DSIR report CD 2401, 4. edition. Department of Scientific and Industrial Research, Pentone, New Zealand

GILL AE (1982) Atmosphere-Ocean Dynamics. International Geophysics Series. Academic Press

GINGRICH JE (1984) Radon as a geochemical exploration tool. *Journal of Geochemical Exploration* 21(1-3): 19–39

GINZBURG A, BEN-AVRAHAM Z (1997) A seismic refraction study of the north basin of the Dead Sea, Israel. *Geophysical Research Letters* 24(16): 2063–2066

GIRDLER RW (1990) The Dead Sea transform fault system. *Tectonophysics* 180: 1–13

GÜLEÇ N, HILTON DR, MUTLU H (2002) Helium isotope variations in Turkey: relationship to tectonics, volcanism and recent seismic activities. *Chemical Geology* 187(1?2): 129–142

GODWIN H (1962) Half-life of Radiocarbon. *Nature* 195: 984

GOMEZ F, KARAM G, KHAWLIE M, MCCLUSKY S, VERNANT P, REILINGER R, JAAFAR R, TABET C, KHAIR K, BARAZANGI M (2007) Global Positioning System measurements of strain accumulation and slip transfer through the restraining bend along the Dead Sea fault system in Lebanon. *Geophysical Journal International* 168(3): 1021–1028

GONFIANTINI R (1986) Environmental isotopes in lake studies. In: FRITZ P, FONTES JC (Eds.), Handbook of Environmental Isotope Geochemistry, vol. 2, 113–168. Elsevier, Amsterdam

GRAHAM DW (2002) Noble gas isotope geochemistry of mid-ocean ridge and ocean island basalts: Characterization of mantle source reservoirs. In: PORCELLI D, BALLENTINE C, WIELER R (Eds.), Noble Gases in Geochemistry and Cosmochemistry, vol. 47 of *Rev. Mineral. Geochem.*, 247–317. Mineralogical Society of America, Geochemical Society, Washington, DC

GRIESSHABER E, O'NIONS RK, OXBURGH ER (1992) Helium and carbon isotope systematics in crustal fluids from the Eifel, the Rhine Graben and Black Forest, F.R.G. *Chemical Geology* 99(4): 213–235

GRÜNTHAL G, WAHLSTRÖM R (2012) The European-Mediterranean Earthquake Catalogue (EMEC) for the last millennium. *Journal of Seismology* 16(3): 535–570

GROTHE J (1992) Datenerfassung und Datenauswertung am Heidelberger Low-Level-Tritium-Messsystem. *Diploma Thesis*, Heidelberg University

GUBA I, MUSTAFA H (1988) Structural control of young basaltic fissure eruptions in the plateau basalt area of the Arabian plate, northeastern Jordan. *Journal of Volcanology and Geothermal Research* 35: 319–334

HAKKI W, TEIMEH M (1981) The geology of Zarqa Ma'in and Zara areas. Tech. rep., NRA, Amman

HALL CM, CASTRO MC, LOHMANN KC, MA L (2005) Noble gases and stable isotopes in a shallow aquifer in southern Michigan: Implications for noble gas paleotemperature reconstructions for cool climates. *Geophysical Research Letters* 32: L18404

HAN W, DI L, ZHAO P, SHAO Y (2012) DEM Explorer: An online interoperable DEM data sharing and analysis system. *Environmental Modelling & Software* 38: 101–107

HEATON THE, VOGEL JC (1981) "Excess air" in groundwater. *Journal of Hydrology* 50: 201–216

HEIMANN A, STEINITZ G (1989) ^{40}Ar/^{39}Ar total gas ages of basalts from Notera #3 well, Hula Valley, Dead Sea Rift: stratigraphic and tectonic implications. *Israel Journal of Earth Sciences* 38: 173–184

HENRY W (1803) Experiments on the quantity of gases absorbed by water, at different temperatures, and under different pressures. *Philosophical Transactions of the Royal Society of London* 93: 29–42+274–276

HERZBERG O, MAZOR E (1979) Hydrological applications of noble gases and temperature measurements in underground water systems: Examples from Israel. *Journal of Hydrology* 41: 217–231

HILL RA (1940) Geochemical patterns in Coachella Valley. *Transactions American Geophysical Union* 21: 46–53

HOLDEN W (1998) Modelling and isotope study of the Azraq basin. In: DUTTON RW, CLARKE JI, BATTICKI A (Eds.), Arid land resources and their management: Jordan's desert margin, 87–93. Kegan Paul International, London

HOLMÉN K, LISS P (1984) Models for air-water gas transfer: An experimental investigation. *Tellus* 36B(2): 92–100

HOLOCHER J, PEETERS F, AESCHBACH-HERTIG W, HOFER M, BRENNWALD M, KINZELBACH W, KIPFER R (2002) Experimental investigations on the formation of excess air in quasi-saturated porous media. *Geochimica et Cosmochimica Acta* 66(23): 4103–4117

HOLOCHER J, PEETERS F, AESCHBACH-HERTIG W, KINZELBACH W, KIPFER R (2003) Kinetic model of gas bubble dissolution in groundwater and its implications for the dissolved gas composition. *Environtal Science & Technology* 37: 1337–1343

HOOKER PJ, O'NIONS RK, OXBURGH ER (1985) Helium isotopes in North Sea gas fields and the Rhine rift. *Nature* 318: 273–275

HOROWITZ A (2001) The Jordan Rift Valley. A. A. Balkema Publishers, Lisse, Abingdon, Exton (PA), Tokyo

HOYT DV, KYLE HL, HICKEY JR, MASCHHOFF RH (1992) The Nimbus 7 solar total irradiance – A new algorithm for its derivation. *Journal of Geophysical Research* 97(A1): 51–63

HSI (1994) Groundwater Investigations in the Hammad and Sirhan Basin, Vol. 1. Unpublished Report, Ministry of Water and Irrigation, Amman, Jordan

HUGHEN K, LEHMAN S, SOUTHON J, OVERPECK J, MARCHAL O, HERRING C, TURNBULL J (2004) ^{14}C activity and global carbon cycle changes over the past 50,000 years. *Science* 303: 202–207

HUGHEN K, SOUTHON J, LEHMAN S, BERTRAND C, TURNBULL J (2006) Marine-derived ^{14}C calibration and activity record for the past 50,000 years updated from the Cariaco Basin. *Quaternary Science Reviews* 25: 3216–3227

HUMPHREYS AND SONS (1982) Azraq well-field evaluation, Hydrochemistry and monitoring. Tech. rep., Amman Water and Sewerage Authority, Amman, Jordan

IAEA/WMO (2006) Global Network of Isotopes in Precipitation database. Accessible at: www.iaea.org/water

IBRAHIM KM (1993) Geologic map, sheet Al-Azraq, by the Geologic Mapping Division, NRA, Jordan

ILANI S, HARLAVAN Y, TARAWNEH K, RABBA I, WEINBERGER R, IBRAHIM K, PELTZ S, STEINITZ G (2001) New K-Ar ages of basalts from the Harrat Ash Shaam volcanic field in Jordan: Implications for the span and duration of the upper-mantle upwelling beneath the western Arabian plate. *Geology* 29(2): 171–174

INGRAM RGS, HISCOCK KM, DENNIS PF (2007) Noble gas excess air applied to distinguish groundwater recharge conditions. *Environtal Science & Technology* 41: 1949–1955

IOLR (2013) Monitoring the Dead Sea. Israel Oceanographic & Limnological Research. http://isramar.ocean.org.il. Viewed 30/09/2013

JAMES RH, PALMER RP (2000) The lithium isotope composition of international rock standards. *Chemical Geology* 166(3-4): 319–326

JONES MD, RICHTER T (2011) Paleoclimatic and archeological implications of Pleistocene and Holocene environments in Azraq, Jordan. *Quaternary Research* 363–372

JORDAN TIMES (2013) Red Sea project dropped, gov't ready with alternatives. http://jordantimes.com/red-sea-project-dropped-govt-ready-with-alternatives. Viewed 30/09/2013

JUNG M (2013) PANGA: A new tool for the evaluation of noble gas data. Goldschmidt Conference Abstract. http://goldschmidt.info/2013/abstracts/finalPDFs/1412.pdf

JUNG M, WIESER M, VON OEHSEN A, AESCHBACH-HERTIG W (2013) Properties of the closed-system equilibration model for dissolved noble gases in groundwater. *Chemical Geology* 339: 291–300

KASHAI EL, CROKER PF (1987) Structural geometry and evolution of the Dead Sea-Jordan rift system as deduced from new subsurface data. *Tectonophysics* 141: 33–60

KATZ A, KOLODNY Y, NISSENBAUM A (1977) The geochemical evolution of the Pleistocene Lake Lisan-Dead Sea system. *Geochimica et Cosmochimica Acta* 41(11): 1609–1626

KECK L (2001) Climate significance of stable isotope records from Alpine ice cores. *PhD Thesis*, Heidelberg University

KENNEDY BM, VAN SOEST MC (2007) Flow of mantle fluids through the ductile lower crust: Helium isotope trends. *Science* 318: 1433–1436

KENNEDY BM, REYNOLDS JH, SMITH SP (1988) Noble gas geochemistry in thermal springs. *Geochimica et Cosmochimica Acta* 52(7): 1919–1928

KENNEDY BM, KHARAKA YK, EVANS WC, ELLWOOD A, DEPAOLO DJ, THORDSEN J, AMBATS G, MARINER RH (1997) Mantle fluids in the San Andreas Fault System, California. *Science* 278(5341): 1278–1281

KIPFER R, AESCHBACH-HERTIG W, BAUR H, HOFER M, IMBODEN DM, SIGNER P (1994) Injection of mantle type helium into Lake Van (Turkey): The clue for quantifying deep water renewal. *Earth and Planetary Science Letters* 125: 357–370

KIPFER R, AESCHBACH-HERTIG W, PEETERS F, STUTE M (2002) Noble gases in lakes and ground waters. In: PORCELLI D, BALLENTINE C, WIELER R (Eds.), Noble gases in geochemistry and cosmochemistry, vol. 47 of *Rev. Mineral. Geochem.*, 615–700. Mineralogical Society of America, Geochemical Society, Washington, DC

KLINGER Y, AVOUAC JP, ABOU KARAKI N, DORBATH L, BOURLES D, REYSS JL (2000) Slip rate on the Dead Sea transform fault in the northern Araba Valley (Jordan). *Geophysical Journal International* 142: 755–768

KLUGE T, ILMBERGER J, VON ROHDEN C, AESCHBACH-HERTIG W (2007) Tracing and quantifying groundwater inflow into lakes using a simple method for radon-222 analysis. *Hydrology and Earth System Sciences* 11: 1621–1631

KLUMP S, GRUNDL T, PURTSCHERT R, KIPFER R (2008) Groundwater and climate dynamics derived from noble gas, ^{14}C, and stable isotope data. *Geology* 36(5): 395–398

KNÖDEL K, LANGE G, VOIGT HJ (2007) Environmental Geology – Handbook of field methods and case studies. Springer, Berlin, Heidelberg, New York

KOFLER M (1913) Mitteilungen aus dem Institut für Radiumforschung. XXXIII. *Monatshefte für Chemie und verwandte Teile anderer Wissenschaften* 34(2): 389–400

KOULAKOV I, SOBOLEV SV (2006) Moho depth and three-dimensional P and S structure of the crust and uppermost mantle in the Eastern Mediterranean and Middle East derived from tomographic inversion of local ISC data. *Geophysical Journal International* 164(1): 218–235

KRAUSE JR D, BENSON BB (1989) The solubility and isotopic fractionation of gases in dilute aqueous solution. IIa. Solubilities of the noble gases. *Journal of Solution Chemistry* 18(9): 823–873

KREUZER A (2007) Paläotemperaturstudie mit Edelgasen im Grundwasser der Nordchinesischen Tiefebene. *PhD Thesis*, Heidelberg University

KRIENITZ MS, HAASE KM, MEZGER K, SHAIKH-MASHAIL MA (2007) Magma Genesis and Mantle Dynamics at the Harrat Ash Shamah Volcanic Field (Southern Syria). *Journal of Petrology* 48(8): 1513–1542

KROMER B (2007) Radiokohlenstoffdatierung. In: WAGNER GA (Ed.), Einführung in die Archäometrie, 3–10. Springer, Berlin/Heidelberg

KULONGOSKI JT, HILTON DR, SELAOLO ET (2004) Climate variability in the Botswana Kalahari from the late Pleistocene to the present day. *Geophysical Research Letters* 31: L10204

KULONGOSKI JT, HILTON DR, IZBICKI JA, BELITZ K (2009) Evidence for prolonged El Nino-like conditions in the Pacific during the Late Pleistocene: A 43 ka noble gas record from California groundwaters. *Quaternary Science Reviews* 28: 2465–2473

LACHNIET MS (2009) Climatic and environmental controls on speleothem oxygen-isotope values. *Quaternary Science Reviews* 28: 412–432

LANGE T, HAMMERSCHMIDT K, FRIEDRICHSEN H, MAREI A, WEISE SM (2008) Groundwater in the shallow aquifer of the Jericho area, Jordan Valley – Noble gas evidence for different sources of salinization. In: ZEREINI F, HÖTZL H (Eds.), Climatic changes and water resources in the Middle East and North Africa, 469–495. Springer, Berlin, Heidelberg

LEHMANN BE, LEHMANN M, NEFTEL A, TARAKANOV SV (2000) Radon-222 monitoring of soil diffusivity. *Geophysical Research Letters* 27(23): 3917–3920

LEVENBERG K (1944) A method for the solution of certain problems in least squares. *Quarterly of Applied Mathematics* 2: 164–168

LEVIN I, NAEGLER T, KROMER B, DIEHL M, FRANCEY RJ, GOMEZ-PELAEZ AJ, STEELE LP, WAGENBACH D, WELLER R, WORTHY DE (2010) Observations and modelling of the global distribution and long-term trend of atmospheric $^{14}CO_2$. *Tellus* 62B: 26–46

LEVITTE D, ECKSTEIN Y (1978) Correlation between the silica concentration and the orifice temperature in the warm springs along the Jordan–Dead Sea Rift Valley. *Geothermics* 7(1): 1–8

LIBBY W (1946) Atmospheric Helium Three and Radiocarbon from Cosmic Radiations. *Physical Review* 69: 11–12

LIPPMANN J, STUTE M, TORGERSEN T, MOSER DP, HALL JA, LIN L, BORCSIK M, BELLAMY RES, ONSTOTT TC (2003) Dating ultra-deep mine waters with noble gases and ^{36}Cl, Witwatersrand Basin, South Africa. *Geochimica et Cosmochimica Acta* 67(23): 4597–4619

LOTT DE (2001) Improvements in noble gas separation methodology: A nude cryogenic trap. *Geochemistry Geophysics Geosystems* 2: 2001GC000202

Lucas LL, Unterweger MP (2000) Comprehensive review and critical evaluation of the half-life of Tritium. *Journal of Research of NIST* 105(4): 541–549

Lupton JE, Craig H (1981) A major helium-3 source at 15°S on the East Pacific Rise. *Science* 214(4516): 13–18

Lupton JE, Weiss RF, Craig H (1977) mantle helium in the Red Sea brines. *Nature* 266: 244–246

Magro G, Pennisi M (1991) Noble gases and nitrogen: mixing and temporal evolution in the fumarolic fluids of Vulcano, Italy. *Journal of Volcanology and Geothermal Research* 47(3–4): 237–247

Mallast U, Siebert C, Wagner B, Sauter M, Gloaguen R, Geyer S, Merz R (2013) Localisation and temporal variability of groundwater discharge into the Dead Sea using thermal satellite data. *Environmental Earth Sciences* 69(2): 587–603

Mamyrin BA, Tolstikhin IN (1984) Helium isotopes in nature. Elsevier, Amsterdam

Marco S (2007) Temporal variation in the geometry of a strike-slip fault zone: Examples from the Dead Sea Transform. *Tectonophysics* 445(3?4): 186–199

Margane A, Hobler M, Al-Momani M, Subah A (2002) Contributions to the hydrogeology of northern and central Jordan. *Geologisches Jahrbuch* C 68: 3–52

Marquardt DW (1963) An algorithm for least-squares estimation of nonlinear parameters. *Journal of the Society for Industrial and Applied Mathematics* 11(2): 431–441

Mazor E (1972) Paleotemperatures and other hydrological parameters deduced from gases dissolved in ground-waters, Jordan Rift Valley, Israel. *Geochimica et Cosmochimica Acta* 36: 1321–1336

Mazor E, Levitte D, Truesdell AH, Healy J, Nissenbaum A (1980) Mixing models and ionic geother-mometers applied to warm (up to 60°C) springs: Jordan Rift Valley, Israel. *Journal of Hydrology* 45(1-2): 1–19

Mazor E, Dubois J, Fluck J, Jaffé F (1988) Noble gases as tracers identifying geothermal components in regions devoid of surface geothermal manifestations: A case study in the Baden springs area, Switzerland. *Chemical Geology: Isotope Geoscience Section* 72(1): 47 – 61

Merkel BJ, Planer-Friedrich B (2005) Groundwater geochemistry. Springer, Berlin, Heidelberg

Meshik AP, Hohenberg CM, Pravdivtseva OV (2004) Record of Cycling Operation of the Natural Nuclear Reactor in the Oklo/Okelobondo Area in Gabon. *Physical Review Letters* 93(18): 182302

Möller P, Dulski P, Salameh E, Geyer S (2006) Characterization of the sources of thermal spring- and well water in Jordan by rare earth element and yttrium distribution and stable isotopes of H_2O. *Acta Hydrochimica et Hydrobiologica* 34(1-2): 101–116

Möller P, Siebert C, Geyer S, Inbar N, Rosenthal E, Flexer A, Zilberbrand M (2012) Relationship of brines in the Kinnarot Basin, Jordan-Dead Sea Rift Valley. *Geofluids* 12(2): 166–181

Moise T, Starinsky A, Katz A, Kolodny Y (2000) Ra isotopes and Rn in brines and ground waters of the Jordan-Dead Sea Rift Valley: enrichment, retardation, and mixing. *Geochimica et Cosmochimica Acta* 64(14): 2371–2388

Mook WG (1980) Carbon-14 in hydrogeological Studies. In: Fritz P, Fontes JC (Eds.), Handbook of Environ-mental Isotope Geochemistry, vol. 1, 49–74. Elsevier, New York

Mook WG (2000) Environmental Isotopes in the hydrological cycle; principles and applications, vol. 1: Intro-duction: Theory, Methods, Review. UNESCO, Paris

Mor D (1993) A time-table for the Levant Volcanic Province, according to K-Ar dating in the Golan Heights, Israel. *Journal of African Earth Sciences (and the Middle East)* 16(3): 223–234

Moreira M, Valbracht PJ, Staudacher T, Allègre C (1996) Rare gas systematics in Red Sea ridge basalts. *Geophysical Research Letters* 23(18): 2453–2456

MOREIRA MA, KURZ MD (2013) Noble gases as tracers of mantle processes and magmatic degassing. In: BURNARD P (Ed.), The noble gases as geochemical tracers, Advances in isotope geochemistry, 371–391. Springer, Heidelberg, New York

MORRISON P, PINE J (1955) Radiogenic origin of the helium isotopes in rock. *Annals of the New York Acadamy of Sciences* 62(3): 71–92

MÜNNICH KO, VOGEL JC (1958) Durch Atomexplosionen erzeugter Radiokohlenstoff in der Atmosphäre. *Naturwissenschaften* 45(7): 327–329

MUSCHELER R, KROMER B, BJÖRCK S, SVENSSON A, FRIEDRICH M, KAISER KF, SOUTHON J (2008) Tree rings and ice cores reveal ^{14}C calibration uncertainties during the Younger Dryas. *Nature Geoscience* 1: 263–267

MWI (2009a) Disi-Mudawarra to Amman water conveyance system – environmental & social management plan part 2 (ESMP 2). Tech. rep., Ministry of Water and Irrigation

MWI (2009b) National Water Master Plan 2: Water resources in Jordan. Tech. rep., Ministry of Water an Irrigation. 2nd edition

MWI (2009c) Water for life: Jordan's water strategy 2008–2022. Tech. rep., Ministry of Water and Irrigation

NAKAI S, WAKITA H, NUCCIO MP, ITALIANO F (1997) MORB-type neon in an enriched mantle beneath Etna, Sicily. *Earth and Planetary Science Letters* 153(1–2): 57–66

NELSON JB (1985) Azraq – A case study. In: HADIDI A (Ed.), Studies in the history and archaeology of Jordan, vol. 2, 39–44. Routledge, London

NEUBERT R (1998) Messung der stabilen Isotopomere des atmosphärischen Kohlendioxids. *PhD Thesis*, Heidelberg University

OEHSEN VON A (2008) Parameter estimation and model validation for models of dissolved noble gas conentrations in groundwater. *Diploma Thesis*, Heidelberg University

OPENSTREETMAP FOUNDATION (2013) http://www.openstreetmap.org. Downloaded 02/10/2013

OXBURGH ER, O'NIONS RK (1987) Helium loss, tectonics, and the terrestrial heat budget. *Science* 237(4822): 1583–1588

OZIMA M, PODOSEK FA (2002) Noble gas geochemistry. Cambridge University Press, Cambridge, 2. edn.

PEARSON JR FJ (1965) Use of C-13/C-12 ratios to correct radiocarbon ages of material initially diluted by limestone. In: Radiocarbon and Tritium Dating, Proceedings of Sixth International Conference on Radiocarbon, 357–366. Pullman, Washington

PEISKER M (1984) Modellvorstellungen zur Kohlenstoff-Isotopendiskriminierung bei der Photosynthese von C_3- und C_4-Pflanzen. *Kulturpflanze* 32: 35–65

PEIXÓTO JP, OORT AH (1983) The atmospheric branch of the hydrological cycle and climate. In: STREET-PERROTT A, BERAN M, RATCLIFFE R (Eds.), Variations in the global water budget, 5–65. Reidel Publishing Company, Dordrecht

PIK R, MARTY B, HILTON DR (2006) How many mantle plumes in Africa? The geochemical point of view. *Chemical Geology* 226(3?4): 100–114

PIPER AM (1944) A graphic procedure in the geochemical interpretation of water analyses. *Transactions American Geophysical Union* 25: 914–928

POLYAK BG (2003) Helium Isotopes in the ground fluids of the Baikal Rift and its surrounding, contribution to continental rifting geodynamics. *Russian Journal of Earth Sciences* 5(1): 45–66

PORCELLI D, BALLENTINE CJ, WIELER R (Eds.) (2002) Noble gases in geochemistry and cosmochemistry, vol. 47 of *Reviews in mineralogy & geochemistry*. Mineralogical Society of America, Geochemical Society

Powell T, Cumming W (2010) Spreadsheets for geothermal water and gas geochemistry. In: 35. Workshop on geothermal reservoir engineering. Stanford University. Proceedings

Pyle DM (1993) Graphical analysis of rare gas mixing systematics in geothermal systems. *Geochemical Journal* 27: 125–129

Quennell AM (1958) The structural and geomorphic evolution of the Dead Sea rift. *Quarterly Journal of the Geological Society of London* 114: 1–24

Raddat K (2005) Water supply and water use statistics in Jordan. In: IWG-Env, International Work Session on Water Statistics. Vienna

Raven JA, Edwards D (2001) Roots: evolutionary origins and biogeochemical significance. *Journal of Experimental Botany* 52: 381–401

Reichel T (2009) Optimierung eines Verfahrens zur Radonmessung in Wasser. *Diploma Thesis*, Heidelberg University

Reilinger R, McClusky S, Vernant P, Lawrence S, Ergintav S, Cakmak R, Ozener H, Kadirov F, Guliev I, Stepanyan R, Nadariya M, Hahubia G, Mahmoud S, Sakr K, ArRajehi A, Paradissis D, Al-Aydrus A, Prilepin M, Guseva T, Evren E, Dmitrotsa A, Filikov SV, Gomez F, Al-Ghazzi R, Karam G (2006) GPS constraints on continental deformation in the Africa-Arabia-Eurasia continental collision zone and implications for the dynamics of plate interactions. *Journal of Geophysical Research: Solid Earth* 111(B5): 26

Reimer PJ, Baillie MGL, Bard E, Baylis A, Beck JW, Blackwell PG, Bronk Ramsey C, Buck CE, Burr GS, Edwards RL, Friedrich M, Grootes PM, Kromer B, McCormac FG, Manning SW, Reimer RW, Richards DA, Southon JR, Talamo S, Turney CSM, Plicht Jvd, Weyhenmeyer CE (2009) Intcal09 and Marine09 radiocarbon age calibration curves 0 – 50,000 years cal BP. *Radiocarbon* 51(4): 1111–1150

Rimawi O, Udluft P (1985) Natural water groups and their origin of the shallow aquifers complex in Azraq-depression/Jordan. *Geologisches Jahrbuch* C 38: 17–38

Roded R, Shalev E, Katoshevski D (2013) Basal heat-flow and hydrothermal regime at the Golan-Ajloun hydrological basins. *Journal of Hydrology* 476: 200–211

Rosenthal E (1994) The hydrogeothermal provinces of Israel. In: Risler JJ, Simmers I (Eds.), Hydrogeothermics (International contributions to hydrogeology), 113–135. A A Balkema Publishers, Leiden, London, New York, Philadelphia, Singapore

Rosenthal E, Flexer A, Möller P (2008) The hydrochemical history of the Rift. In: Hötzl H, Möller P, Rosenthal E (Eds.), The Water of the Jordan Valley – Scarcity and deterioration of groundwater and its impact on the regional development, 75–82. Springer, Berlin

Rozanski K, Gonfiantini R, Araguás-Araguás L (1991) Tritium in the global atmosphere: Distribution patterns and recent trends. *Journal of Physics G: Nuclear and Partical Physics* 17: S523–S536

Rozanski K, Araguás-Araguás L, Gonfiantini R (1993) Isotopic patterns in modern global precipitation. *Geophysical Monograph* 78: 1–36

RSCN – Royal Society for the Conservation of Nature (2013) http://www.rscn.org.jo/. Sighted 07/03/13

Sakaguchi A, Nishimura T, Kato M (2005) The Effect of entrapped air on the quasi-saturated soil hydraulic conductivity and comparison with the unsaturated hydraulic conductivity. *Vadose Zone Journal* 4: 139–144

Salameh E (1996) Water quality degradation in Jordan (Impacts on environment, economy and future generations resources base). Friedrich Ebert Stiftung, Amman

SALAMEH E (2001) Sources of water salinities in the Jordan Valley Area/Jordan. *Acta hydrochimica et hydrobiologica* 29(6-7): 329–362

SALAMEH E (2008) Over-exploitation of groundwater resources and their environmental and socio-economic implications: the case of Jordan. *Water International* 33(1): 55–68

SALAMEH E, BANNAYAN H (1993) Water resources of Jordan – Present status and future potentials. Friedrich Ebert Stiftung, Amman

SALAMEH E, RIMAWI O (1984) Isotopic analyses and hydrochemistry of the thermal springs along the eastern side of the Jordan Dead Sea–Wadi Araba Rift Valley. *Journal of Hydrology* 73(1-2): 129–145

SALAMEH E, UDLUFT P (1985) The hydrodynamic pattern of the central part of Jordan. *Geologisches Jahrbuch* C 38: 40–53

SANDIAS M (2011) The reconstruction of diet and environment in ancient Jordan by carbon and nitrogen stable isotope analysis of human and animal remains. International Hydrology Series. Cambridge University Press

SANFORD WE, SHROPSHIRE RG, SOLOMON DK (1996) Dissolved gas tracers in groundwater: Simplified injection, sampling, and analysis. *Water Resource Research* 32(6): 1635–1642

SANO Y, FISCHER TP (2013) The analysis and interpretation of noble gases in modern hydrothermal systems. In: BURNARD P (Ed.), The noble gases as geochemical tracers, Advances in isotope geochemistry, 249–317. Springer, Berlin, Heidelberg

SANO Y, MARTY M, BURNARD P (2013) Noble gases in the atmosphere. In: BURNARD P (Ed.), The noble gases as geochemical tracers, Advances in isotope geochemistry, 17–31. Springer, Berlin, Heidelberg

SAWARIEH AK (2005) Heat sources of the groundwater in the Zara-Zarqa Ma'in-Jiza area, Central Jordan. *PhD Thesis*, University of Karlsruhe, Germany

SCHLOSSER P, STUTE M, DÖRR C, SONNTAG C, MÜNNICH KO (1988) Tritium/^{3}He-dating of shallow groundwater. *Earth and Planetary Science Letters* 89: 353–362

SCHMIDT G, SUBAH A, KHALIF N (2008) Model investigations on the groundwater system in Jordan – A contribution to the resources management (National Water Master Plan). In: ZEREINI F, HÖTZL H (Eds.), Climatic changes and water resources in the Middle East and North Africa. Springer, Berlin, Heidelberg

SCHOELLER H (1955) Géochimie des eaux souterraines: application aux eaux des gisements de pétrole. Institut Français du Pétrole

SCHOELLER H (1962) Les eaux souterraines. Mason et Cie

SCHULZE ED, BECK E, MÜLLER-HOHENSTEIN K (2005) Plant ecology. Springer, Berlin, Heidelberg

SCHWIENTEK M, MALOSZEWSKI P, EINSIEDL F (2009) Effect of the unsaturated zone thickness on the distribution of water mean transit times in a porous aquifer. *Journal of Hydrology* 373: 516–526

SEGEV A, RYBAKOV M, LYAKHOVSKY V, HOFSTETTER A, TIBOR G, GOLDSHMIDT V, BEN-AVRAHAM Z (2006) The structure, isostasy and gravity field of the Levant continental margin and the southeast Mediterranean area. *Tectonophysics* 425(1-4): 137–157

SEYMOUR RM (2000) Air entrapment and consolidation occuring with saturated hydraulic conductivity changes with intermittent wetting. *Irrigation Science* 20: 9–14

SHACKLETON NJ, OPDYKE ND (1973) Oxygen isotope and palaeomagnetic stratigraphy of Equatorial Pacific core V28-238: Oxygen isotope temperatures and ice volumes on a 10^5 year and 10^6 year scale. *Quaternary Research* 3(1): 39–55

SHALEV E, LYAKHOVSKY V, WEINSTEIN Y, BEN-AVRAHAM Z (2013) The thermal structure of Israel and the Dead Sea Fault. *Tectonophysics* 602: 69–77

SHELDON AL (2002) Diffusion of radiogenic helium in shallow groundwater: Implications for crustal degassing. *PhD Thesis*, University of Utah

SIEGENTHALER U (1979) Stable hydrogen and oxygen isotopes in the water cycle. In: JÄGER E, HUNZIKER JC (Eds.), Lectures in isotope geology, 264–274. Springer, Berlin, Heidelberg, New York

SMITH GD, NEWHALL F, ROBINSON LH, SWANSON D (1964) Soil temperature regimes: Their characteristics and predictability. Tech. Rep. SCS-TP-144, USDA, Soil Conservation Service

SMITH SP, KENNEDY BM (1983) The solubility of noble gases in water and in NaCl brine. *Geochimica et Cosmochimica Acta* 47: 503–515

SOLOMON DK (2000) ^{4}He in groundwater. In: COOK P, HERCZEG AL (Eds.), Environmental tracers in subsurface hydrology, 425–439. Kluwer Academic Publisher, Boston

SOLOMON DK, POREDA RJ, COOK PG, HUNT A (1995) Site characterization using ^{3}H/^{3}He ground-water ages, Cape Cod, MA. *Ground Water* 33(6): 988–996

STANLEY RHR, BASCHEK B, LOTT III DE, JENKINS WJ (2009) A new automated method for measuring noble gases and their isotopic ratios in water samples. *Geochemistry Geophysics Geosystems* 10(5)

STANLEY PRICE NP, GARRARD AN (1975) A survey of prehistoric sites in the Azraq Basin, eastern Jordan. *Paléorient* 3: 109–126

STEPHENSON M, SCHWARTZ WJ, MELNYK TW, MOTYCKA MF (1994) Measurement of advective water velocity in lake sediment using natural helium gradients. *Journal of Hydrology* 154(1-4): 63–84

STUIVER M, POLACH H (1977) Discussion: reporting of ^{14}C data. *Radiocarbon* 19: 355–363

STUIVER M, QUAY PD (1980) Changes in atmospheric carbon-14 attributed to a variable sun. *Science* 207(4426): 11–19

STUTE M, SCHLOSSER P (1993) Principles and applications of the noble gas paleothermometer. In: SWART PK, LOHMANN KC, MCKENZIE J, SAVIN S (Eds.), Climate change in continental isotopic records, vol. 78 of *AGU Geophysical Monograph Series*, 89–100. American Geophysical Union, Washington, DC

STUTE M, CLARK J, SCHLOSSER P, BROECKER W (1995) A 30,000 yr continental paleotemperature record derived from noble gases dissolved in groundwater from the San Juan Basin, New Mexico. *Quaternary Research* 43: 209–220

SUESS H (1955) Radiocarbon concentration in modern wood. *Science* 122: 415

SUN T, HALL CM, CASTRO MC, LOHMANN KC, GOBLET P (2008) Excess air in the noble gas groundwater paleothermometer: A new model based on diffusion in the gas phase. *Geophysical Research Letters* 35: L19401

SUN T, HALL CM, CASTRO MC (2010) Statistical properties of groundwater noble gas paleoclimate models: Are they robust and unbiased estimators? *Geochemistry Geophysics Geosystems* 11(2): Q02002

TAMERS MA (1975) Validity of Radiocarbon Dates on Ground Water. *Geophysical Surveys* 2 217–239

TEDESCO D, NAGAO K (1996) Radiogenic ^{4}He, ^{21}Ne and ^{40}Ar in fumarolic gases on Vulcano: implication for the presence of continental crust beneath the island. *Earth and Planetary Science Letters* 144(3–4): 517–528

TEN BRINK US, BEN-AVRAHAM Z, BELL RE, HASSOUNEH M, COLEMAN DF, ANDREASEN G, TIBOR G, COAKLEY B (1993) Structure of the Dead Sea pull-apart basin from gravity analyses. *Journal of Geophysical Research* 98(B12): 21877–21894

TORFSTEIN A, HAMMERSCHMIDT K, FRIEDRICHSEN H, STARINSKY A, GARFUNKEL Z, KOLODNY Y (2013) Helium isotopes in Dead Sea Transform waters. *Chemical Geology* 352: 188–201

TORGERSEN T (1980) Controls on pore-fluid concentration of ^{4}He and ^{222}Rn and the calculation of ^{4}He/^{222}Rn ages. *Journal of Geochemical Exploration* 13: 57–75

TORGERSEN T (1989) Terrestrial degassing fluxes and the atmospheric helium budget: Implications with respect to the degassing processes of continental crust. *Chemical Geology* 79: 1–14

TORGERSEN T, CLARKE WB (1985) Helium accumulation in groundwater, I: An evaluation of sources and the continental flux of crustal 4He in the Great Artesian Basin, Australia. *Geochimica et Cosmochimica Acta* 49: 1211–1218

TORGERSEN T, O'DONNELL J (1991) The degassing flux from the solid earth: Release by fracturing. *Geophysical Research Letters* 18(5): 951–954

TOUTAIN JP, BAUBRON JC (1999) Gas geochemistry and seismotectonics: a review. *Tectonophysics* 304: 1–27

TRUESDELL AH, HULSTON JR (1980) Isotopic evidence on environments of geothermal systems. In: FRITZ P, FONTES JC (Eds.), Handbook of environmental isotope geochemistry, Vol 1: The terrestrial environment, A, chap. 5, 179–226. Elsevier, Amsterdam, Oxford, New York

TSUR N (2013) Noble gas isotopic signatures in thermal waters of the Dead Sea Transform, Israel. *Master's Thesis*, Heidelberg University

UK GROUNDWATER FORUM (2013) http://www.groundwateruk.org. Downloaded 04/10/2013

UN-ESCWA, BGR (2013) Inventory of Shared Water Resources in Western Asia. Tech. Rep. 10, United Nations Economic and Social Commission for Western Asia and Bundesanstalt für Geowissenschaften und Rohstoffe, Beirut

UNKEL I (2006) AMS-14C-Analysen zur Rekonstruktion der Landschafts- und Kulturgeschichte in der Region Palpa (S-Peru). *PhD Thesis*, Heidelberg University

USAID (2012) A review of water policies in Jordan and recommendations for strategic priorities. Tech. rep., USAID

USGS (1998) EXACT – Overview of Middle East water resources. Tech. rep., U.S. Geological Survey

VOGEL JC (1967) Investigation of groundwater flow with radiocarbon. In: IAEA-SM-83 (Ed.), Isotopes in Hydrology, 355–369. IAEA, Vienna

VOGEL JC (1970) Carbon-14 dating of groundwater. In: Isotope Hydrology, 225–240. Vienna

WADLEIGH MA, VEIZER J (1992) $^{18}O/^{16}O$ and $^{13}C/^{12}C$ in lower Paleozoic articulate brachiopods: Implications for the isotopic composition of seawater. *Geochimica et Cosmochimica Acta* 56: 431–443

WAJ (2010) GIS database of the Water Authority of Jordan

WALDMANN N, STEIN M, ARIZTEGUI D, STARINSKY A (2009) Stratigraphy, depositional environments and level reconstruction of the last interglacial Lake Samra in the Dead Sea basin. *Quarternary Research* 72: 1–15

WATTS BG, BENNETT ME, KOPP OC, MATTINGLY GL (2004) Geochemistry and petrography of basalt grindstones from the Karak Plateau, central Jordan. *Geoarchaeology* 19(1): 47–69

WEBER M, ABU-AYYASH K, ABUELADAS A, AGNON A, ALASONATI-TAŠÁROVÁ Z, AL-ZUBI H, BABEYKO A, BARTOV Y, BAUER K, BECKEN M, BEDROSIAN PA, BEN-AVRAHAM Z, BOCK G, BOHNHOFF M, BRIBACH J, DULSKI P, EBBING J, EL-KELANI R, FÖRSTER A, FÖRSTER HJ, FRIESLANDER U, GARFUNKEL Z, GOETZE HJ, HAAK V, HABERLAND C, HASSOUNEH M, HELWIG S, HOFSTETTER A, HOFFMANN-ROTHE A, JÄCKEL KH, JANSSEN C, JASER D, KESTEN D, KHATIB M, KIND R, KOCH O, KOULAKOV I, LASKE G, MAERCKLIN N, MASARWEH R, MASRI A, MATAR A, MECHIE J, MEQBEL N, PLESSEN B, MÖLLER P, MOHSEN A, OBERHÄNSLI R, ORESHIN S, PETRUNIN A, QABBANI I, RABBA I, RITTER O, ROMER RL, RÜMPKER G, RYBAKOV M, RYBERG T, SAUL J, SCHERBAUM F, SCHMIDT S, SCHULZE A, SOBOLEV SV, STILLER M, STROMEYER D, TARAWNEH K, TRELA C, WECKMANN U, WETZEL U, WYLEGALLA K (2009) Anatomy of the Dead Sea Transform from lithospheric to microscopic scale. *Reviews of Geophysics* 47(2): 44

WEIGEL F (1978) Radon. *Chemiker-Zeitung* 102: 287–299

WEISS RF (1970) The solubility of nitrogen, oxygen and argon in water and seawater. *Deep-Sea Research* 17: 721–735

WEISS RF (1971) Solubility of helium and neon in water and seawater. *Journal of Chemical Engineering Data* 16(2): 235–241

WEISS RF (1974) Carbon dioxide in water and seawater: The solubility of a non-ideal gas. *Marine Chemistry* 2: 203–215

WEISS RF, KYSER TK (1978) Solubility of krypton in water and seawater. *Journal of Chemical Engineering Data* 23(1): 69–72

WEISS W, BULLACHER J, ROETHER W (1979) Evidence of pulsed discharges of tritium from nuclear energy installations in Central European precipitation. In: IAEA (Ed.), Behaviour of tritium in the environment, Proceedings Series, 17–30. IAEA, San Francisco, 16-20 Oct. 1978

WHITE DE (1974) Diverse origins of hydrotehermal ore fluids. *Economic Geology* 69: 954–973

WIERSBERG T, ERZINGER J (2007) A helium isotope cross-section study through the San Andreas Fault at seismogenic depths. *Geochemistry Geophysics Geosystems* 8(1): Q01002

WIESER M (2006) Entwicklung und Anwendung von Diffusionssamplern zur Beprobung gelöster Edelgase in Wasser. *Diploma Thesis*, Heidelberg University

WIESER M (2011) Imprints of climatic and environmental change in a regional aquifer system in an arid part of India using noble gases and other environmental tracers. *PhD Thesis*, Heidelberg University

WILLSON RC, HUDSON HS (1988) Solar luminosity variations in Solar Cycle-21. *Nature* 332(6167): 810–812

WOLFART R (1966) Zur Geologie und Hydrogeologie von Syrien – unter besonderer Berücksichtigung der süd- und nordwestlichen Landesteile. *Beiheft Geologisches Jahrbuch* 68

WÖLFLI W (1987) Advances in accelerator mass spectrometry. *Nuclear Instruments and Methods in Physics Research* 29: 1–13

WÖLFLI W, BONANI G, SUTER M, BALZER R, NESSI M, STOLTER C (1983) Radioisotope dating with the ETHZ-EN-Tandem accelerator. *Radiocarbon* 25(2): 745–753

WORLD BANK (2013) Red Sea – Dead Sea water conveyance study program: Feasibility study. Tech. rep., Coyne-et Bellier in association with Tractebel Engineering and Kema

WORLDBANK (2013) Jordan country overview. http://www.worldbank.org/en/country/jordan/overview. Checked 05/11/2013

YATSEVICH I, HONDA M (1997) Production of nucleogenic neon in the Earth from natural radioactive decay. *Journal of Geophysical Research* 102(B5): 10291–10298

YOGESHWAR P, TEZKAN B, HAROON A (2013) Investigation of the Azraq sedimentary basin, Jordan using integrated geoelectrical and electromagnetic techniques. *Near Surface Geophysics* 11: 283–291

ZAK I, FREUND R (1981) Asymmetry and basin migration in the Dead Sea rift. *Tectonophysics* 80: 27–38

ZAPOROZEC A (1972) Graphical interpretation of water-quality data. *Groundwater* 10(2): 32–43

ZHU C, KIPFER R (2010) Noble gas signatures of high recharge pulses and migrating jet stream in the late Pleistocene over Black Mesa, Arizona, United States. *Geology* 38: 83–86